Constraining the Physics of the X-ray Irradiated Accretion Discs in Low-mass X-ray Binaries with Observations

by

Bailey Elizabeth Tetarenko

A thesis submitted in partial fulfillment of the requirements for the degree of

Doctor of Philosophy

Department of Physics
University of Alberta

Abstract

Recurring outbursts associated with matter flowing onto compact stellar remnants (black holes and neutron stars) in low-mass X-ray binary systems provide constraints on the poorly understood accretion process. Multi-wavelength light-curves and spectra of these bright outbursts provide powerful diagnostics to probe the physics behind the mechanisms driving mass inflow and outflow in these astrophysical systems. Using the population of low-mass X-ray binaries harbouring stellar-mass black holes in our Galaxy as a guide, I have developed an innovative methodology, to decode the physics of disc-accretion, hidden within observational data. In this thesis, I present this methodology, that combines observed X-ray, ultraviolet, optical, and infrared time-series and spectroscopic data, accretion theory, and advanced Bayesian statistical techniques. Using this methodology, I tackle the complex, multi-scale problem of understanding the evolution of accretion disc structure and the X-ray irradiating source heating the accretion discs throughout low-mass X-ray binary outbursts. Given the advanced monitoring capabilities of current ground and space-based observatories, ever-evolving abilities of numerical simulations, and the vast landscape of online multi-wavelength archival databases available, my methodology has the opportunity to open up a new chapter in accretion physics,

one of the most fundamental building blocks of our Universe, responsible for the evolution of objects across astrophysical scales, from new born stars and planets to super-massive black holes at the centre of Galaxies.

Preface

This thesis is a combination of original published (or in the process of being published) and collaborative research done under the supervision of G. R. Sivakoff.

> Chapter 2 is part of the published manuscript: Tetarenko, B. E., Sivakoff, G. R., Heinke, C. O., and Gladstone, J. C. "WATCHDOG: A Comprehensive All-sky Database of Galactic Black Hole X-ray Binaries", ApJ, 222, 15-113 (2016). Sections 3–6 of this manuscript have been adapted for inclusion in this thesis. The remaining parts of this manuscript, not included in this thesis, specifically the catalogue, data products, and details on statistical algorithms used to analyze the data, were presented as my MSc. thesis (2014). I was responsible for data reduction, analysis, and writing the manuscript. All co-authors contributed to interpretation of the data.
>
> Chapter 3 is published as: Tetarenko, B. E., Lasota, J.-P., Heinke, C. O., Dubus, G., and Sivakoff, G. R. "Strong Disk Winds Traced Throughout Outbursts in Black Hole X-ray Binaries", Nature, 554, 69-72 (2018). I performed the analysis of the X-ray data, wrote the Markov-Chain Monte-Carlo light-curve fitting algorithm and performed the light-curve fitting, built the Bayesian hierarchical methodology, and wrote the paper. J.-P. Lasota helped formulate the analytical version of the irradiated-disc instability model that was fit to the X-ray light-curves and assisted in writing the discussion in the paper. G. Dubus assisted in writing the discussion in the paper. C.O. Heinke assisted in the analysis of the X-

ray data and the light-curve fitting process. G.R. Sivakoff assisted with writing the paper. All authors contributed to the interpretation of the data.

Chapter 4 is published as: Tetarenko, B. E., Dubus, G., Lasota, J.-P., Heinke, C. O., and Sivakoff, G. R. "Understanding X-ray Irradiation in Low-mass X-ray Binaries Directly From Their Light-curves", MNRAS, 480, 2-16 (2018). I compiled and reduced the X-ray data, developed and implemented the Bayesian hierarchical methodology used, and wrote the paper. G. Dubus performed all the theoretical light-curve modelling and assisted in interpreting the results. J.-P. Lasota assisted in interpretation of the observed light-curves in the context of the disc-instability model (DIM). C.O. Heinke and G.R. Sivakoff assisted in the analysis and interpretation of the X-ray data. All co-authors assisted in writing the discussion of the paper and contributed to the interpretation of the results.

Chapter 5 has been submitted for publication in MNRAS as: Shaw, A. W., Tetarenko, B. E., Dubus, G., Dincer, T., Tomsick, J. A., Gandhi, P., Plotkin, R. M., and Russell, D. M. "The Curious Case of Swift J1753.5–0127: A Black Hole Low-mass X-ray Binary Analogue to Z Cam Type Dwarf Novae", MNRAS (2018). I was responsible for development and implementation of the data analysis techniques and collection of the archival X-ray data. A.W. Shaw and I co-wrote the submitted manuscript, however the work presented in this thesis is my own. A.W. Shaw and J.A. Tomsick wrote the proposal to obtain the *Swift* data and A.W. Shaw was responsible for the collection and reduction of the *Swift* data. T. Dincer was responsible for the collection and reduction of the *SMARTS* data. G. Dubus assisted in writing the discussion of the paper. All co-authors contributed to the interpretation of the data.

"Quiet people have the loudest minds"

— Stephen Hawking

Dedication

For my Dad,

Acknowledgements

First and foremost, to my supervisor Greg, for giving me the freedom to pursue the science I wanted, and for always giving my many (and often far too ambitious) ideas a chance. Thank you for throwing me in the deep end without a life jacket. I know I am the researcher I am today because of this independence you allowed me to have.

I would also like to thank my collaborators. To Craig, first for all your guidance, support, and direction. I would have been beyond lost (more then a few times) without it. When I received a "fantastic!" from you, I always knew I was on the right track.

To Jean-Pierre and Guillaume, for guiding me through the world of accretion theory. I have learned so much from the two of you in the past few years and our insightful discussions have always lead me in interesting and fruitful directions.

Lastly to Phil, first for your careful read of, and intuitive additions to, this thesis. Second, for all our discussions, that have inspired me to pursue, a path full of imaginative, ambitious, and exciting science.

In addition, I owe a debt of gratitude to the UAlberta Astro Group. First, to Erik, for introducing me to the wonderful world of Bayesian statistics. Second, to Natasha, for all the effort you put toward bridging the gap between "theorist" and "observer" points of view. Lastly, to Sharon for sharing your black hole knowledge and expertise over the years.

Also, to my friends. To Arash, for being my X-ray guru and sounding board. To Eric, by far the best office mate I had over the past four years, for sharing all your python expertise. To Kaylie and Robin, for your friendship and support over the years. Finally, to Kenny and Aarran, for our intensely passionate Flames/Oilers hockey rivalry that got me through some of the most difficult days. I wouldn't have survived without all of you.

Most importantly, to my family, without whom I would not be here. To my dad, whose strength and seemingly unshakable resilience continuously inspires me to keep moving forward, regardless of what is in my way. To my mom, for building me back up when I have been in the darkest of places and raising me to believe I could accomplish anything I set my mind to. To my twin, my carbon copy and the sharer of my unique psychosis, for our intensely competitive (and borderline crazy) relationship which inspires me to strive for greatness (or at the very least, slightly better then you) everyday. Lastly to Ben, my therapy dog, for keeping me on the right side of the insanity line for all these years.

Contents

List of Tables

List of Figures

List of Abbreviations

ADAF	Advection Dominated Accretion Flow
ADIOS	Advection Dominated Inflow/Outflow Solution
AGN	Active Galactic Nuclei
ASM	All-Sky Monitor
BH	Black Hole
BHC	Black Hole Candidate
BH-LMXB	Black Hole Low-mass X-ray Binary
CCD	Charge-coupled Device
CDAF	Convection Dominated Accretion Flow
CV	Cataclysmic Variable
cm	centi-metre
DIM	Disc-instability Model
DN	Dwarf Novae
eV	electron volt
FRED	Fast Rise Exponential Decay
HCS	Hard Comptonized State
HID	Hardness Intensity Diagram
hr	hour
IDIM	Irradiated Disc-instability Model
IMS	Intermediate State
IR	Infrared
ISS	International Space Station
JDAF	Jet Dominated Accretion Flow
K	Kelvin
keV	kilo-electron volt
kpc	kilo-parsec
ks	kilo-second
LMXB	Low Mass X-ray Binary
MCMC	Markov Chain Monte-Carlo

MDAF	Magnetically Dominated Accretion Flow
MRI	Magneto-rotational Instability
NIR	Near-infrared
PDF	Probability Density Function
s	second
SDS	Soft Disc-dominated State
UV	Ultraviolet
XRN	X-ray Novae

Chapter 1

Introduction

1.1 Low-mass X-ray Binaries (LMXBs)

A low-mass x-ray binary (LMXB) is an interacting binary system in which a compact object (black hole or neutron star, the remnants of the most massive stars) accretes from a disc of matter (known as an accretion disc; Pringle & Rees 1972; Shakura & Sunyaev 1973), formed as a result of gravity pulling material from a nearby, low-mass star (see Figure 1.1).

While some of this inward falling material will accrete directly onto the compact object, a portion may also be removed from the system via an outflow in the form of a relativistic plasma jet or an accretion disc wind (Hjellming & Wade, 1971; Blandford & Königl, 1979; Phinney, 1982; White & Holt, 1982; Begelman & Mckee, 1983). See Section 1.2.3 for a discussion on LMXB outflows. For major reviews on LMXBs see Tanaka & Lewin (1995); Tanaka & Shibazaki (1996); Chen et al. (1997); McClintock & Remillard (2006); Remillard & McClintock (2006) and Done et al. (2007).

In LMXBs, the mass-transfer process onto the accretion disc mostly occurs via Roche lobe overflow[1] of the low-mass companion star, with a mass $M_2 \lesssim 1\,M_\odot$ and spectral type A or later (White et al., 1995). Most LMXBs are transient, displaying

---

[1] Roche lobe overflow is the process by which the companion star fills its critical gravitational potential lobe, referred to as the Roche lobe, and as a result, material is transferred onto the accretion disc around the compact object through the inner Lagrangian point $\mathscr{L}_1$.

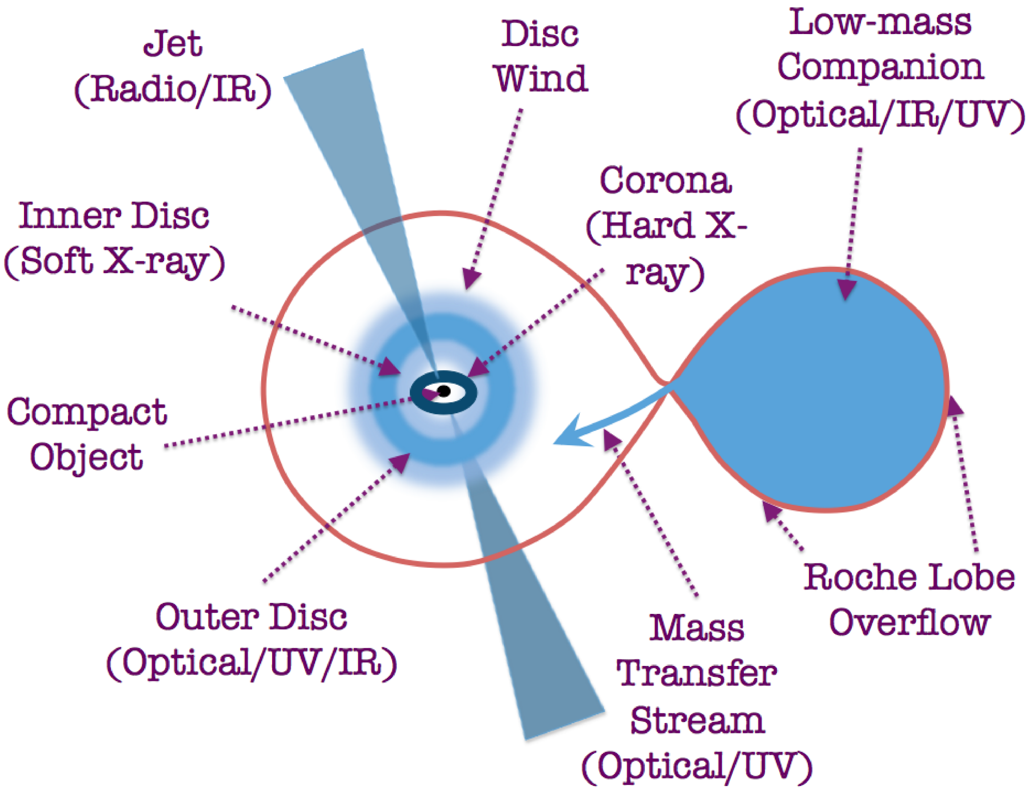

Figure 1.1: Schematic of a LMXB system, displaying each component of the system and the key emission regions. Figure adapted from Tauris & van den Heuvel (2006).

long-term behavior characterized by a cyclical pattern of quiescent and outburst states. This transient behavior is dependent upon the mass-transfer rate onto the compact object (Tanaka & Lewin, 1995).

Transient systems spend most of their time in the quiescent state, characterized by long periods of time, lasting anywhere from a few months to decades. In quiescence, the system is exceptionally faint ($L_X \sim 10^{30} - 10^{33}\,\mathrm{erg\,s^{-1}}$) and very little material is transferred from the accretion disc onto the compact object (McClintock & Remillard, 2006). The transition to the outburst state occurs as a consequence of instabilities, both thermal and viscous in nature, developing in the accretion disc that cause more rapid mass-transfer onto the compact object and lead to bright emission at X-ray, ultraviolet (UV), optical, and infrared (IR) and wavelengths. The physical mechanism causing outbursts in LMXBs can be explained with the disc-instability model (DIM; Meyer & Meyer-Hofmeister 1981; Cannizzo et al. 1995; King & Ritter 1998; Lasota 2001). See Section 1.2.1 for a detailed discussion on the DIM.

Most of our empirical knowledge about stellar-mass black holes (BHs; 5–30 $M_\odot$), comes from LMXB systems. Astronomers have identified ∼64 likely BH-LMXBs in our Galaxy through their bright outbursts, indicative of rapid accretion episodes occurring between the companion star and BH (McClintock & Remillard, 2006; Tetarenko et al., 2016; Corral-Santana et al., 2016; Negoro et al., 2017; Kawamuro et al., 2018; Kawase et al., 2018, and refs therein). Unlike the population of binary BHs, identified via gravitational waves by LIGO/Virgo, BH-LMXBs can be studied via temporal and spectral signatures (see Section 1.2.2), observed across the electromagnetic spectrum (McClintock & Remillard, 2006). Thus, these accreting binary systems offer an accessible window into understanding how compact objects form, grow, evolve, and interact with the environments they live in.

Enumerating the frequency of outbursts in, and quantitatively classifying the wide range of outburst behaviour exhibited by, these systems allow us to quantitatively build statistical distributions of key binary properties (e.g., mass, orbital period, duty cycles, recurrence timescales, peak outburst luminosity) describing the Galactic population as a whole. Building Galactic distributions of these parameters (which are currently sparsely measured) is crucial as they are tracers of the physics responsible for the formation and growth of binary systems (beyond just X-ray binaries). The currently uncertain physics processes include the supernova process, that affects massive stars and forms BHs, and key stages in the binary evolutionary process e.g., natal kicks and the common envelope phase (Belczynski et al., 2002; Ivanova et al., 2013).

Moreover, BH-LMXB systems also offer ideal laboratories to study a causally connected sequence of accretion regimes over astrophysically interesting (i.e., actually observable) timescales. This stands in contrast to the other primary type of accreting BH systems, Active Galactic Nuclei (AGN), where each source can only provide an instantaneous view, due to the (much) longer evolutionary timescales involved. The currently poorly understood accretion process is one of the most fundamental building blocks of our Universe, responsible for evolution of astrophysical objects ranging from newborn stars and planets, to supermassive BHs at the center of galaxies. The recurring (day to year timescale) outbursts in BH-LMXBs give us the unique opportunity to study the physics governing mass transport through, and outflowing matter from, discs in accreting systems, an area where our knowledge is largely fragmented due to both limits of current theoretical methods and missing observational constraints.

For these reasons, this thesis investigates and places observational constraints on the disc-accretion process, through a combination of observational and statistical techniques and accretion theory, using the population of BH-LMXBs in our Galaxy as a guide.

1.2 A Quantitative Description of Active Accretion in BH-LMXBs

1.2.1 The Disc-Instability Model

The disc-instability model (DIM; Osaki 1974; Meyer & Meyer-Hofmeister 1981; Smak 1984; Faulkner et al. 1983; Cannizzo et al. 1985; Cannizzo 1993; Lin & Taam 1984; Huang & Wheeler 1989; Mineshige & Wheeler 1989) was originally developed to explain dwarf novae outbursts in Cataclysmic Variables (CVs; Warner 1995), compact binary systems where a white dwarf accretes from a low-mass companion star.

In quiescence, the accretion disc is in a cool, neutral state. The quiescent disc is built up due to steady mass-transfer from the companion star, as a result of Roche lobe overflow. The temperature of the disc begins to rise as matter accrues in the disc. Eventually at some radius (called the ignition radius) the disc temperature will reach the temperature where hydrogen ionizes ($\sim 10^4$ K). This triggers a thermal-viscous instability within the disc due to the steep temperature dependence of opacity in this temperature range. As a result, the disc will undergo a thermal limit cycle, alternating between a hot, ionized, outburst state and a cold, neutral, quiescent state. The effect that the thermal-viscous instability has on an accretion disc is commonly visualized in the temperature-surface density plane or "S-Curve" (see Figure 1.2).

The cycle begins with the increase in temperature causing an increase in mass-accretion rate through a particular annulus. The reason that this can occur is directly tied to hydrogen ionization causing a viscous instability within the disc. When the hydrogen is (at least partly) ionized, the magnetic field is locked into the disc. As the disc rotates differentially, magnetic field lines that have radial extent are stretched, tending to slow down particles that are closer to the BH (thus making them fall inwards faster) and speed up those that are farther away (making them move outwards). Thus, the viscosity of the disc (i.e., the ability of the disc to move angular-momentum around) increases dramatically; in the hot ionized state, material moves inward rapidly. The mechanism believed to be behind the angular-momentum (and mass) transport described here is known as the magneto-rotational instability (MRI; Balbus & Hawley 1991). See Figure 1.3 and Balbus & Hawley (1998) for a thorough review of this mechanism. In Chapter 3 I present an observational study of the angular-momentum (and mass) transport process in BH-LMXB discs.

The growth of this thermal-viscous instability at the ignition radius ultimately results in two heating fronts, one propagating inwards and one propagating outwards through the disc. This brings the disc into a hot state causing rapid infall of matter onto the compact object, and a bright X-ray, ultraviolet, optical, and infrared outburst. Here, the innermost portions of the inflowing matter are primarily re-

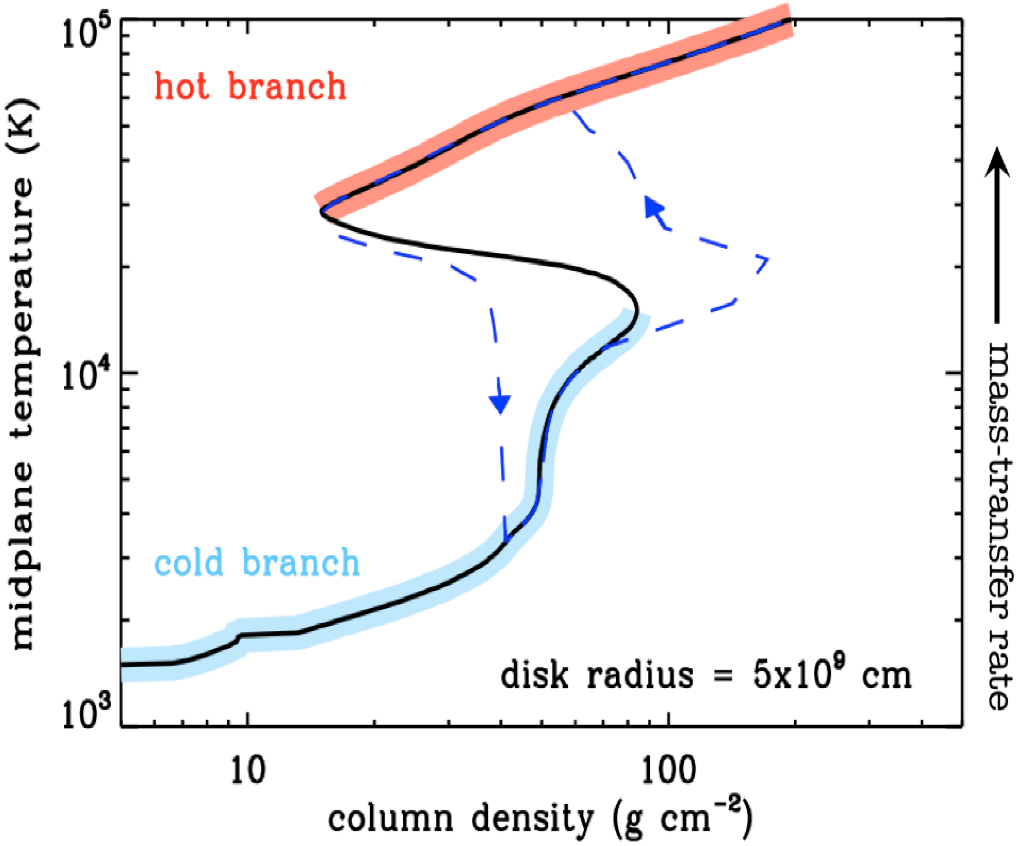

Figure 1.2: The "S-Curve", for a thin annulus in a disc with radius $R = 5 \times 10^9$ cm, depicting the hysteretic limit cycle caused by the thermal-viscous instability in an accretion disc. There is a corresponding "S-Curve" for each choice of disc radius and α-viscosity (the parameter describing the efficiency of angular-momentum transport; see Chapter 3). If the mass-transfer rate is large enough the disc will remain on the hot stable branch. Otherwise, the disc will cycle between the hot and cold branches (i.e., undergo transient outbursts; indicated by the blue dashed lines). Figure courtesy of G. Dubus.

sponsible for X-ray emission, while the ultraviolet, optical, and infrared emission is mainly generated in the outer accretion disc.

As the disc is depleted over time (because mass falls onto the compact object at a higher rate than it is being transferred from the companion star), the temperature and mass-accretion rate in the outer radii will eventually be reduced to the point where hydrogen can recombine. This triggers the formation and propagation of a cooling front that returns the disc to its quiescent (neutral) state.

While this predicted behaviour, characterized by alternating periods of disc-outbursts and quiescence, matches observations of accreting white dwarfs well, the additional parameter of X-ray irradiation must be accounted for to describe the observed outburst behaviour in LMXBs. LMXBs have deeper potential wells and thus undergo brighter X-ray (UV, optical, and IR) outbursts that last longer ($\sim$ tens to hundreds of days), and recur less frequently (recurrence rates $\sim$ 1 year to decades), than dwarf novae. In Chapter 2, I present a two-decade long population study of the outburst properties exhibited by BH-LMXBs in our Galaxy.

The difference between accreting BHs and white dwarfs is attributed to stronger heating of the outer disc by X-rays emitted in the inner regions of the accretion flow in the former. This X-ray irradiation controls the outburst decay toward quiescence by keeping the disc in the hot ionized state. Irradiation only allows the disc to return to quiescence on a viscous timescale, providing a means to produce the longer outburst durations observed across the BH-LMXB population. Furthermore, when the effects of disc evaporation[2] is included along with irradiation, longer recurrence timescales can also be reproduced (Menou et al., 2000; Dubus et al., 2001).

The effect X-ray irradiation has on the accretion discs in LMXBs can be illustrated by comparing the broad-band spectrum of non-irradiated (e.g., like in dwarf novae) and irradiated accretion discs (see Figure 1.4). In general, accretion discs radiate via viscous dissipation of accumulated gravitational potential energy of the infalling matter from the companion star, resulting in a broadband spectrum de-

---

[2] The inner disc will gradually evaporate into a hot, radiatively inefficient accretion flow, often associated with an advection-dominated accretion flows (ADAFs; Narayan & Yi 1994), during the decay from outburst towards quiescence (Esin et al., 1997; Hameury et al., 1997; Narayan et al., 1997). See Section 1.2.2 for a detailed discussion.

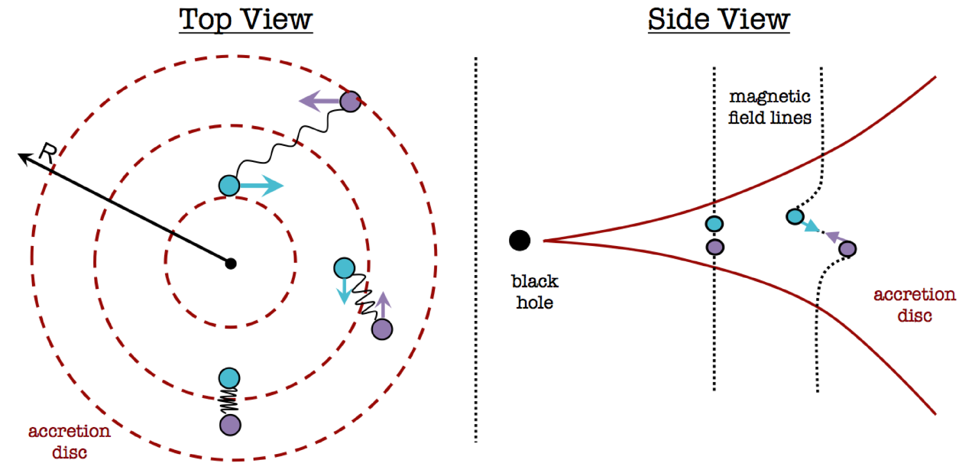

Figure 1.3: A mechanical representation of the magneto-rotational instability (MRI), thought to be the physical mechanism behind angular-momentum transport in accretion discs. (left) Two neighbouring fluid elements in a differentially rotating disc, located in an axial magnetic field, behave like masses connected by a weak massless spring. The inner element (cyan) rotates more rapidly then the outer element (purple), causing the spring to stretch. As spring tension is analogous to magnetic force, only a weak magnetic field is needed to begin with. The spring will force the inner element to slow down, decreasing its angular-momentum and moving it to a lower orbit. At the same time, the spring will also force the outer element to speed up, increasing its angular-momentum, and moving it to a higher orbit. As the elements move further and further apart the spring tension will increase, demonstrating the unstable nature of the MRI. (right) Fluid elements in an accretion disc that carry magnetic field lines (dotted lines) along with them will be increasingly separated, resulting in magnetic forces (arrows) from tension in the field lines. Overall, weak magnetic-fields can cause inward mass flow and outward angular-momentum transport in a differentially rotating disc, substantially altering the stability of the disc as a whole. Figure adapted from Balbus & Hawley (1991, 1998).

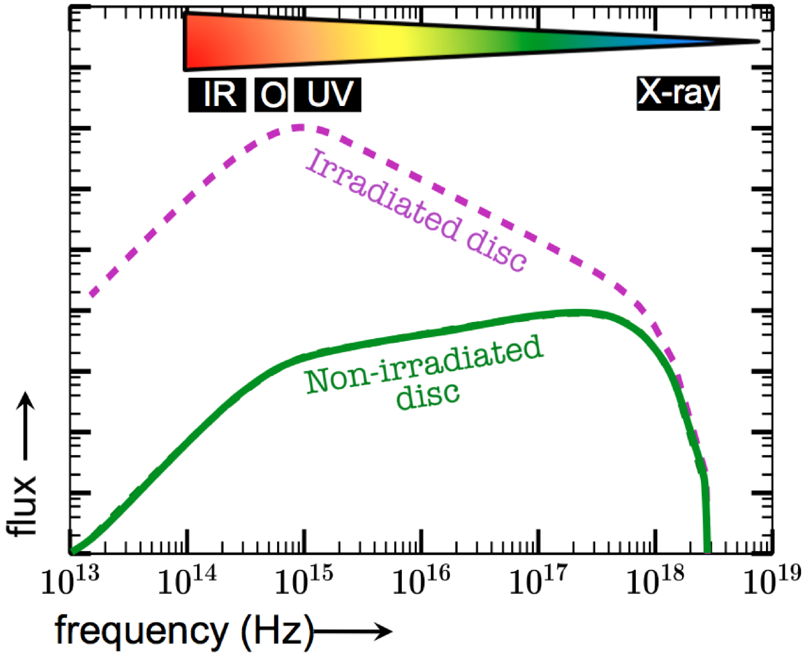

Figure 1.4: The broadband disc-blackbody spectrum with (purple) and without (green) X-ray irradiation. The overlaid one-dimensional accretion disc slice shows approximate disc radii where different wavelengths of radiation are emitted.

scribed by the sum of blackbody emission, radiated at each radius, over the whole disc (disc-blackbody; see Section 1.2.2 for details). In contrast, the spectrum of irradiated discs display a broad optical peak, attributed to reprocessed X-rays heating the outer disc. In Chapter 4, I present an observational study of the properties of the X-ray irradiation heating of BH-LMXB discs.

To first order, the predictions of the DIM+irradiation can explain the global behavior of BH-LMXBs relatively well (Maccarone, 2014).

- First, systems that have high enough mass-transfer rates to keep the disc fully ionized tend to be observed as persistently accreting systems and those that have mass-transfer rates below this threshold tend to be transient (see Section 2.3.1 for details).

- Second, the positive correlation found between peak outburst luminosity and orbital period in transient LMXBs (see Section 2.3.2 for details) agrees roughly with the prediction that outburst peak luminosities should scale with the radius of the accretion disc (King & Ritter, 1998).

- Third, observed outburst durations match relatively well with the viscous timescales of accretion discs in many BH-LMXB systems (see Chapter 3 for details).

- Fourth, with the addition of tidal effects to the DIM (i.e., the tidal instability; Osaki 1996; Truss et al. 2002), sources that show outbursts of varying amplitudes (e.g., "super outbursts"; see Zurita et al. 2008; Maccarone & Patruno 2013) can also possibly be explained by this model. See for example Maccarone (2014) for a detailed discussion of phenomena associated with tidal interactions.

- Lastly, there are a few observed phenomena that provide strong arguments for a mass-transfer instability occurring (i.e., variable mass-transfer from the companion star; Osaki 1985; Hameury et al. 1986, 1987, 1988, 1990) in some systems as well.

Given the observational evidence, it is clear that various other physical processes (e.g., X-ray irradiation of the disc and companion star, inner disc truncation, mass-transfer fluctuations) must be added to the standard DIM to describe the behaviour exhibited by LMXBs adequately. In Chapter 5, I present a thorough study on how the behaviour of the unusual BH-LMXB Swift J1753.5−0127 can be explained in the context of the DIM when irradiation, disc evaporation, and variable mass-transfer from the companion star are taken into account.

1.2.2 Temporal and Spectral Evolution

During the outburst state, BH-LMXB light-curves exhibit a range of morphological types that vary on both a source-by-source basis and between individual outbursts of the same source. While the most prominently observed type is the fast rise exponential decay (FRED) outburst, numerous other features including linear decays, plateaus, multiple peaks, and complex variability have been observed (Chen et al., 1997). In Chapter 4 I present a detailed discussion on BH-LMXB light-curve morphology.

Notable variations in spectral and timing properties are also observed during an outburst, allowing a number of different accretion states to be defined. X-ray accretion states have been known to exist since the early 1970s when Tananbaum et al. (1972) first observed a global spectral change in Cygnus X−1. However, it was largely the multitude of population studies performed throughout the late 1990s and early 2000s (e.g., Tanaka & Lewin 1995; Chen et al. 1997; McClintock & Remillard 2006; Remillard & McClintock 2006) that propelled us beyond the largely phenomenological description of X-ray accretion states and into descriptions more firmly based on physical models (e.g., accretion disc, corona, and jet).

The launches of X-ray satellites with unparalleled capabilities like *RXTE* (1995), *XMM-Newton* (1999), *Chandra* (1999), *MAXI* (2009), and *Swift* (2004), have challenged, and continue to challenge, the prevailing views of X-ray accretion states in LMXBs. Access to large amounts of X-ray observations have made it possible to place observational constraints on accretion flows in strong gravity and has allowed for further theoretical understanding of these systems.

A variety of different models of the changing nature and geometry of accretion flows created over the last few decades have been developed to understand the wide variety and variability of emission observed from these systems. From these models we now have an emerging picture that explains much of the behavior seen from BH-LMXBs (e.g., Remillard & McClintock 2006, Done et al. 2007).

Theoretical Accretion Flow Models

Currently, there are two theoretical stable accretion flow models that are generally thought to explain the majority of observed BH-LMXB spectra. See Figure 1.5.

The thermal disc-blackbody spectral model, typically observed at low energies, is attributed to direct soft photons from a geometrically thin, optically thick disc (Shakura & Sunyaev, 1973; Mitsuda et al., 1984; Makishima et al., 1986). While the hard Comptonized spectral model, typically observed at higher energies, is thought to come from a hot, geometrically thick, optically thin inner coronal flow existing above and around the inner disc. At higher flux levels, the electrons within this flow are thought to (repeatedly) up-scatter a fraction of the lower energy disc photons, producing the observed smooth Comptonized spectrum that extends to high energies (Thorne & Price, 1975; Sunyaev & Truemper, 1979). At lower flux levels, when the disc is truncated further from the BH (see Figure 1.6 and the discussion on accretion states below for details), the spectrum is thought to result from the up-scattering of synchrotron photons self-generated within the coronal flow (Veledina et al., 2013, 2017).

The structure of this flow is now most commonly associated with Advection Dominated Accretion Flows (ADAFs; Ichimaru 1977; Narayan & Yi 1994). However, because the flow is thought to be more complex, other physical processes such as convection (CDAFs; Abramowicz & Igumenshchev 2001), magnetic fields (MDAFs; Meier 2005), winds (ADIOS; Blandford & Begelman 1999), and jets (JDAFs; Falcke et al. 2004) are necessary for a more realistic treatment. Currently, there is still no single model among these that is preferred yet in the literature.

Note that while a number of plausible alternatives for the origin of the Comptonized spectrum exist (e.g., see Malzac & Belmont 2009; Plotkin et al. 2015), this

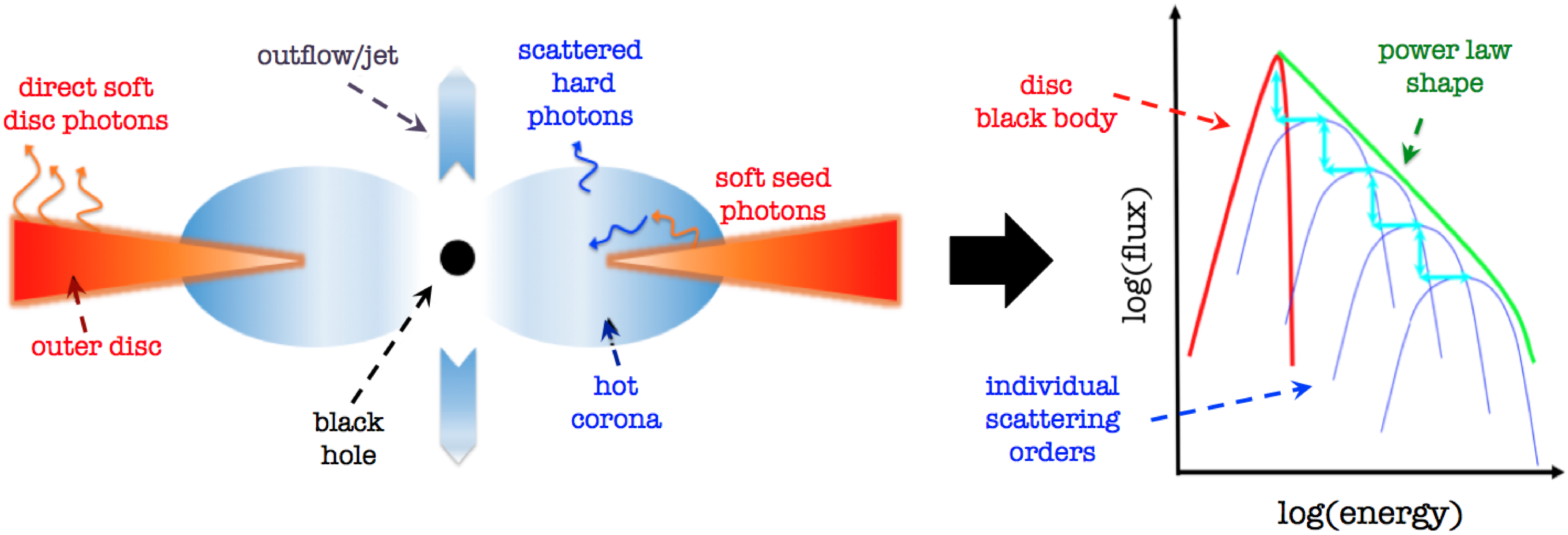

Figure 1.5: Schematic showing the emission mechanisms thought to be responsible for the individual components observed in an X-ray spectrum of an outbursting LMXB. Figure adapted from Zdziarski et al. (2004) and Done (2010).

thesis will focus only on the interpretation discussed above.

Accretion States

The behavioural pattern often observed during BH-LMXBs outbursts (Maccarone & Coppi, 2003; Vadawale et al., 2003) involves the system cycling through a pattern of hard (dominated by Comptonized emission) and soft (dominated by thermal emission) states, where the rise in luminosity at the start of outbursts occurs in the hard state. The peak of the outburst and the initial decline typically occurs in the soft state, while the final stages of the decline occur in the hard state. This pattern, referred to in this thesis as the “turtlehead”, can be clearly observed in a hardness-intensity diagram (HID; see Figure 1.6).

The Hard (Comptonized) State (HCS) is characterized by spectra that are dominated by a power-law (Comptonized) component with a hard photon index of $\Gamma \sim 1.5 - 1.7$ and a high energy cutoff at $\sim$100 keV. This may or may not be supplemented by a weak thermal component (Done, 2010). The HCS typically involves low mass-transfer rates, and is typically associated with lower Eddington-scaled luminosities[3].

In contrast, the Soft (Disc-Dominated) State (SDS) is characterized by spectra with a dominant disc component peaking at $\sim$ 1 keV. This component is accompanied by a weak power-law tail with $\Gamma \sim 2$ that often extends past $\sim$ 500 keV and carries only a small portion of the emitted power (Done et al., 2007). Observationally, the soft state is associated with high mass-transfer rates, and higher Eddington-scaled luminosities.

The situation becomes far more complex during transitions between the hard and soft states. This transitional stage, often collectively referred to as the Intermediate State (IMS), involves an increase in X-ray luminosity and a softer spectrum. The

---

[3] Matter accreting onto a compact object will be subject to radiation pressure from X-rays being emitted from the inner regions of the accretion disc. If the X-ray luminosity of the source is large enough, it is possible for the outward radiation pressure to balance (and exceed) the inward gravitational force of the compact object. This luminosity limit is referred to as the Eddington luminosity and can be parametrized in terms of the mass of the compact object as $L_{\mathrm{edd}} = 1.3 \times 10^{38} (M_c/M_{\odot})\,\mathrm{erg\,s^{-1}}$. Only a few BH-LMXBs are thought to reach super-Eddington luminosities (see Done et al. 2007).

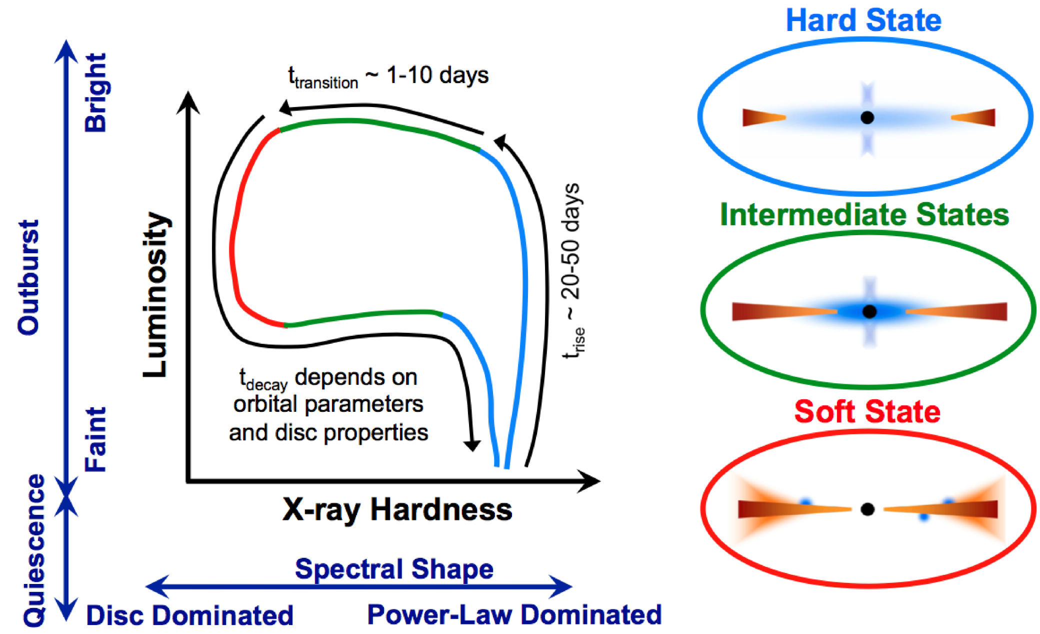

Figure 1.6: Schematic Hardness-Intensity Diagram (HID) showing the “turtle-head” pattern often observed during a BH-LMXB outburst. The source geometry thought to be producing the observed emission in each spectral accretion state is depicted. HCS = hard comptonized state, IMS = intermediate state, SDS = soft disc-dominated state. Source geometries taken from Done (2010).

softening of the spectrum is due to two effects that happen simultaneously; the appearance of a significant thermal disc component and the steepening of the hard power-law component to a photon index of $\Gamma \sim 2.0$–2.5. Observationally, the IMS is associated with high mass-transfer rates. The spectral behavior associated with this state can be observed at both low and high fractions of Eddington. Typically, no clear luminosity change is observed during hard-soft and soft-hard spectral transitions (Maccarone, 2005).

While collectively the intermediate states are known to take place on relatively short time scales (hours to days), much of the physics occurring during this transitional stage is largely unknown (Remillard & McClintock, 2006). The prevalent model (see Esin et al. 1997; Meyer et al. 2007), stipulates that to transition between the hard and soft states, the mass-transfer rate must increase, causing the disc to move inwards. Fewer seed photons are intercepted by the hot inner flow when the disc is truncated far from the BH, leading to a hard spectral component. As the disc moves inwards further underneath the hot flow, the spectrum softens due to the disc component becoming significantly brighter (and more dominant) and a larger fraction of disc seed photons being intercepted, effectively cooling the corona via up-scattering.

This basic "turtlehead" pattern has been modelled after numerous outbursts of well-studied BH-LMXB GX 339−4 (e.g., Zdziarski et al. 2004; Fender et al. 2004; Belloni 2010; Corbel et al. 2013; Debnath et al. 2013b) and can be observed in a multitude of other Galactic sources (McClintock & Remillard, 2006). That being said, not all BH-LMXB systems follow the basic "turtlehead" pattern during outburst. A number of BH-LMXBs systems have been observed to undergo outbursts that do not involve any complete state transitions (i.e., "failed" outbursts). In this case the source either remains in the HCS (Harmon et al., 1994; Hynes et al., 2000; Belloni et al., 2002; Brocksopp et al., 2001, 2004; Aref'ev et al., 2004; Sturner & Shrader, 2005; Brocksopp et al., 2010; Sidoli et al., 2011; Curran & Chaty, 2013) or only transitions as far as the IMS (Wijnands & Miller, 2002; in't Zand et al., 2002; Capitanio et al., 2009; Ferrigno et al., 2011; Reis et al., 2012; Soleri et al., 2013; Zhou et al., 2013; Curran et al., 2014) during outburst, never fully reaching the softer thermally dominant states. In Chapter 2, I present a detailed discussion and analysis of the accretion states during outbursts as observed in the population of BH-LMXBs in our Galaxy.

1.2.3 Outflows

Two different types of outflows have been observed in BH-LMXBs, each predominantly associated with different spectral accretion state(s) observed during outburst.

The first, is a compact, steady jet, that produces a flat to slightly inverted radio spectrum (Hjellming & Wade, 1971; Tananbaum et al., 1972; Fender et al., 2004; Fender, 2010; Russell et al., 2012). This jet is exclusively observed in the hard spectral state. While the soft state lacks any persistent optically thick radio emission (thought to be a result of the quenching of the compact steady radio jet in this regime; Fender et al. 2004), optically thin jet ejecta that propagate out from the compact object are typically detected at radio frequencies early in the soft state or just before the soft state is reached (Fender et al., 2004; Miller-Jones et al., 2012).

The second, is an accretion disc wind. While these winds have been seen recently in high resolution X-ray spectra (e.g., Lee et al. 2002; Miller et al. 2004; Miller et al. 2006; Miller et al. 2006, 2008; King et al. 2012; Neilsen & Homan 2012; Diaz Trigo et al. 2014), evidence for their presence was identified well before high resolution X-ray spectroscopy had ever been undertaken (e.g., V404 Cyg; Oosterbroek et al. 1997). Originating from the outer disc, accretion disc winds have the ability to carry away large amounts of mass, sometimes on the order of, or larger than, the accretion rate onto the BH, $\dot{M}_{\rm BH}$.

These winds have been postulated as a mechanism behind the quenching of the radio jet in the soft state regimes (Neilsen & Lee, 2009; Ponti et al., 2012). These strong mass outflows have only ever been observed in the soft and intermediate states, or in a few special cases at high flux levels ($>10\%$ Eddington) in the hard accretion state, during BH-LMXB outbursts (Miller et al., 2006; Ponti et al., 2012; Neilsen, 2013b). However, a recent study (Tetarenko et al., 2018b, presented as Chapter 3 of this thesis) has suggested that it is likely these winds exist in all accretion states, across a wide range of luminosity regimes.

While it has been suggested that the two outflow regimes of the hard and soft states are most likely not connected by a simple rebalancing of the same outflow power, with the wind carrying more mass but less kinetic power then that of the jet, detailed calculations of quantities such as kinetic energy, mass, and momentum flux in these two types of outflows have not yet been carried out (Fender & Gallo, 2014). As a result the physical interaction between the winds, accretion flows, and jets in these systems are not fully understood. However, given the observationally suggested mass flux and power of these winds, it stands to reason that both jets and winds are perhaps a fundamental component of the accretion phenomenon (Ponti et al., 2012).

1.3 Instrumentation

In this thesis I make use of data from the following telescopes/instruments that observe at X-ray, UV, Optical, and IR wavelengths.

1.3.1 Rossi X-ray Timing Explorer (RXTE)

The *RXTE* (Swank, 1997) satellite, which operated between 1996–2012, was perhaps the most important vehicle for the study of transient phenomena in the last two decades due to the wide-sky coverage of the All-sky Monitor (ASM), high sensitivity of the Proportional Counter Array (PCA), the high-energy coverage of HEXTE, and its overall fast response time (McClintock & Remillard, 2006).

1. The ASM (Levine et al., 1996), made up of three wide-field proportional counters[4], operated in the 1.5–12 keV band and had the ability to cover $\sim 90\%$ of the sky every orbit, which took about 90 minutes, with a sensitivity between

---

[4] Proportional counters contain a windowed gas cell, subdivided into regions of low and high electric fields using electrodes. The signal induced on these electrodes, via photoionization of the gas by X-rays, contains information on arrival times, energies and interaction position of the photons transmitted by the window. For a detailed description of proportional counters see Fraser (2009).

$\sim$10–20 mCrab[5] (integrating all orbits over a full day; McClintock & Remillard 2006).

2. The PCA (Jahoda et al., 1996) consisted of an array of 5 proportional counters, which operated in the 2–60 keV range[6], had a total collecting area of 6500cm^2, a field of view of a square degree[7] and a sensitivity of 1mCrab (estimated from observations; see Heinke et al. 2010). The Galactic Bulge Scan Survey used in Chapter 2, which exclusively used the PCA (Jahoda et al., 1996; Swank & Markwardt, 2001), provided periodic scans of the Galactic bulge region in the 2.5–10 keV energy band between 1999 and 2011. Each scan covered $\sim 8\%$ of the sky with a sensitivity of $\sim$3–7 mCrab (estimated from real observations).

3. HEXTE (Rothschild et al., 1998) provided coverage of the X-ray sky in the 15–250 keV energy band. HEXTE consisted of two clusters of detectors, each of which contained four NaI(Tl)/CsI(Na) phoswich scintillation counters. Each cluster had the ability to "rock" along mutually orthogonal directions, providing background measurements 1.5 or 3.0 degrees away from the source every 16 to 128 s. Overall, HEXTE was capable of measuring a 100 mCrab X-ray source to 100 keV or greater in 10^3 live seconds. The field of view per cluster was 1 degree, and all 8 detectors in both clusters covered a net open area of 1600 cm^2.

1.3.2 Neil Gehrels Swift Observatory

The *Neil Gehrels Swift Observatory*, operating since 2004, consists of three instruments: the (i) Burst Alert Telescope (BAT); (ii) X-ray Telescope (XRT); and (iii) Ultraviolet and Optical Telescope (UVOT).

---

[5] The Crab Nebula is often used as an X-ray calibration source (and baseline unit of flux) due to the fact that it has been observed to be a bright, approximately steady X-ray source producing a constant spectrum.

[6] The energy range and sensitivity of the PCA varied over the instrument lifetime due to gain changes (see, e.g. Shaposhnikov et al. 2012; Garcia et al. 2014) and eventual loss of working counters.

[7] The PCA collimator has a FWHM of 1 degree. While there is some sensitivity to objects more then half a degree away, to first order, the field of view can be approximated as a square degree. See https://heasarc.gsfc.nasa.gov/docs/xte/PCA.html.

1. The BAT X-ray monitor (Krimm et al., 2013) has provided near real time, wide-field coverage of the X-ray sky in the 15–150 keV energy range since 2005. Given its 1.4 steradian field of view and the wide number of sources that *Swift* observes in a given day, the BAT has the ability to observe 80–90% of the sky every day with a sensitivity of 16 mCrab (integrating scans over 1 day) and arcminute positional accuracy. After a detection by BAT, the *Swift* satellite has the ability to "swiftly" ($\lesssim$ 90 s) and autonomously repoint itself to bring the source within the field of view of the more sensitive narrow-field X-ray and UV/optical instruments, XRT and UVOT.

2. XRT (Burrows et al., 2000) is an X-ray CCD imaging spectrometer, with a $110\mathrm{cm}^2$ effective area and 23.6×23.6 arcmin FOV, operating in the 0.2–10 keV band. XRT has the ability to measure light-curves and spectra of X-ray sources, with an energy resolution of 260 eV (FWHM) at 6 keV, and a sensitivity of $4 \times 10^{-13} \mathrm{ergcm}^2\mathrm{s}^{-1}$ for a 1 ks observation. Moreover, it can be operated in imaging, photon counting (PC), or windowed timing (WT) mode, depending on the brightness of the source being observed[8].

3. UVOT (Roming et al., 2004) is a 30cm diameter telescope, with a 17×17 arcmin FOV, covering the UV and optical bands (170-600 nm) with six individual filters available. It has the ability to detect an $m_B = 22.3$ point source in 1 ks using the open (white) filter. UVOT operates simultaneously with XRT.

1.3.3 Monitor of All-Sky Image (MAXI) Telescope

MAXI (Matsuoka et al., 2009), mounted on the International Space Station (ISS) has the ability to scan 85% of the sky every 92 minutes (one orbit/rotation period of the ISS) with its wide field of view (i.e., rectangular FOV of $160° \times 1.5°$) providing near real-time coverage of the X-ray sky with a positional accuracy of < 6 arcminutes and a daily sensitivity of 9 mCrab. The Gas Slit Camera (GSC; Mihara et al. 2011) detector, one of the two ASMs aboard *MAXI*, contains a proportional counter that

---

[8] http://www.swift.ac.uk/analysis/xrt/modes.php.

covers the 2–20 keV energy band with its large detection area (5000 cm^2) and an energy resolution of 18% at 6 keV.

1.3.4 INTErnational Gamma-Ray Astrophysics Laboratory (INTEGRAL)

The INTEGRAL satellite contains three coded mask imagers. One of which is the Integral Soft Gamma-Ray Imager (IBIS/ISGRI; Ubertini et al. 2003), which has a primary energy range of 20–60 keV, an energy resolution of 8% at 100 keV, and a field of view of 8.3×8.0 (66.4 deg^2) fully coded[9]. The other two are the Joint European X-Ray Monitor (JEM-X; Lund et al. 2003) X-ray detectors, which have a primary energy range of 3–35 keV, an energy resolution of 9% and 13% at 30 keV, and a 4.8 degree diameter circular field of view (18 deg^2) fully coded[10]. Note that within each observation, only one JEM-X unit is used at a time. The *INTEGRAL* (Winkler et al., 2003; Kuulkers et al., 2007) Monitoring Program, used in Chapter 2, has provided periodic scans of the Galactic Bulge since 2005. Data is taken approximately every 3 days (the length of one orbit) and is provided in the form of single observations, consisting of 7 pointings in a hexagonal pattern of spacing 2 degrees, and lasting ∼1.8 ksec total. Each observation covers 0.1% of the sky with JEM-X and 2% of the sky with ISGRI, with a sensitivity of 3–9 mCrab.

1.3.5 The Small & Moderate Aperture Research Telescope System (SMARTS)

The *SMARTS Consortium*, located at the Cerro Tololo Inter-American Observatory (CTIO) in Chile, consists of four 1-meter class telescopes that operate at optical and near-infrared wavelengths. This thesis makes use of data from A Novel Dual Imaging CAMera (ANDICAM; DePoy et al. 2003) on the 1.3m *SMARTS* telescope. ANDICAM is a CCD imager that takes both optical and near-infrared data (in

---

[9] http://integral.esac.esa.int/integ_imager_para.html

[10] http://integral.esac.esa.int/integ_jemx_param.html

BVRIJHK filters) simultaneously.

1.4 Bayesian Statistical Analysis Techniques

Throughout this thesis I exclusively make use of Bayesian Markov Chain Monte-Carlo (MCMC) statistical techniques to analyze multi-wavelength data. In this section I introduce briefly the principles behind fitting a model to data in the Bayesian statistical framework with MCMC sampling methods (as outlined in Foreman-Mackey et al. 2013 and Sharma 2017).

Suppose we have a set of parameters θ of some model $f(x, \theta)$, and observed data x with uncertainty σ_x. Defining x^t as a data point generated by the model, the probability of the observed data x given the model and error is,

$$p(x \mid \theta, \sigma_x) = \int f(x^t \mid \theta) p(x \mid x^t, \sigma_x) dx^t, \tag{1.1}$$

where the integral is over true values of x^t, which are unknown. Accordingly, the total probability for the full data set of N data points $X = \{x_1, \cdots, x_N\}$, referred to as the likelihood, is the sum of conditional probabilities such that,

$$p(\theta \mid X, \sigma_x) = \prod_{n=1}^{N} p(x_i \mid \theta, \sigma_{x,i}). \tag{1.2}$$

The foundation of any statistical fitting algorithm is the objective function, which represents a measure of the quality of the fit. In Bayesian statistics, the likelihood acts as this objective function with the goal being to maximize the probability of the observed data given the model, $p(\theta \mid X, \sigma_x)$.

To estimate the best-fit parameters θ, given data D, one can use the Bayes theorem,

$$p(\theta \mid D) = \frac{1}{p(D)} p(\theta) p(D \mid \theta), \tag{1.3}$$

where $p(\theta \mid D)$ is the posterior distribution, $p(\theta)$ is the prior distribution, representing all prior knowledge we have on each parameter, $p(D \mid \theta)$ is the likelihood function, and $p(D)$ is a normalization.

Here, the idea is to sample from, and thus provide a sample approximating, the posterior distribution, $p(\theta \mid D)$, efficiently in any parameter spaces, regardless of the number of parameters in the model. Once sampled, constraints on parameters θ can be estimated using a histogram projected onto the parameter subspace.

To generate the samples, one can use an MCMC algorithm. The MCMC will generate a random walk, and use a set of "walkers" to explore the parameter space. Over time these "walkers" will draw representative samples from the posterior distribution, $p(\theta \mid D)$. The path a "walker" takes through the parameter space, referred to as a trace, is recorded in a chain. Each point in the chain $X(t_i) = [\theta_i]$ depends only on the position of the "walkers" in the previous step $X(t_i - 1)$.

A number of methods exist to advance the "walkers" through the parameter space. The algorithm used in this thesis is a modified version of the Metropolis-Hastings Algorithm. The algorithm works as follows: for a given $P(X)$,

- Place "walker" at initial positions x_0 and evaluate $P(X_0)$
- draw possible next step X_1 from a random walk and evaluate $P(X_1)$.
- If $P(X_1) > P(X_0)$, the walker moves to position X_1.
- If $P(X_1) < P(X_0)$, the walker stays at position X_0.
- Repeat the process until convergence.

The Metropolis-Hastings algorithm will converge to a stationary set of samples as $t \to \infty$. Plotting the traces of each parameter allows one to observe the path each "walker" took through the parameter space to reach the final converged solution.

Convergence can be tested in two different ways. The first, is using the autocorrelation function, which measures the convergence rate by estimating the number of steps needed in the chain to draw independent samples. The second, is using the acceptance fraction a_f, the fraction of proposed steps where the walker moves to a new position. Here, an $a_f = 0$ corresponds to all steps being rejected, while an $a_f = 1$ corresponds to all steps being accepted. Typically, an $a_f = 0.2 - 0.5$ is considered a good indication of convergence.

Detailed applications of the basic principles introduced in this Chapter to observational data can be found in Chapters 3, 4, and 5.

1.5 Outline

In this thesis I present work that uses a combination of time-series and spectral data analysis techniques, accretion theory, and Bayesian statistical algorithms to study the X-ray irradiated accretion discs in LMXB systems harbouring stellar-mass BHs.

In Chapter 2 I present a population study of BH-LMXBs in our Galaxy. Making use of the WATCHDOG project I recently developed, an interactive suite of tools built to use the current suite of wide-field (all-sky), scanning survey, and narrow-field pointed X-ray instruments, to detect, track, and monitor LMXB outburst behaviour over decades of energy and time, I study the long-term temporal and spectral evolution observed in the Galactic BH-LMXB population. In doing so, I am able to (i) characterize nearly two decades of outburst behaviour exhibited by the BH-LMXB population of our Galaxy, (ii) build statistical distributions of a number of outburst properties across the Galactic population, including outburst detection rates, duration, recurrence timescales, duty cycles, total energy radiated during outburst, and peak outburst luminosity, (iii) study observable properties of accretion state transitions, (iv) build a long-term mass-transfer history for the population, and (v) study the relationship between observed outburst properties and the parameters that define the size and mass scales of LMXB systems.

In Chapter 3, I present an innovative methodology, which combines a foundation of Bayesian statistics, the observed X-ray light-curves of LMXBs, and accretion disc theory to characterize the angular-momentum (and mass) transport processes at work in an accretion disc. By applying this methodology to the Galactic BH-LMXB population, I derive the first-ever measurements of the efficiency of the angular-momentum (and mass) transport process (parametrized via α-viscosity) in the X-ray irradiated discs of BH-LMXBs, directly from observations. My results suggest that strong accretion disc winds, with the ability to remove a substantial fraction of the disc mass, must exist in all accretion states throughout outbursts of BH-LMXBs.

In Chapter 4, I continue analysis of Galactic BH-LMXB accretion discs, extending the Bayesian methodology presented in Chapter 3 to investigate the physical properties of the X-ray irradiation heating BH-LMXB discs during outbursts of strong accretion. I find that the disc-instability model (with irradiation) cannot adequately describe the extremely diverse light-curve morphology of BH-LMXBs. In particular, my findings suggest that mass loss through inner disc evaporation to a radiatively-inefficient structure or through a magnetized disc wind may play a prominent role in shaping the outburst light-curves. This is a significant change in paradigm. Further, I show how this complex and varied light-curve morphology observed across the population provides evidence for a likely temporal and spatially varying X-ray irradiation source heating the discs in these systems during transient outbursts. Lastly, I demonstrate how my Bayesian methodology can accurately reproduce the synthetic model light-curves computed from numerical codes built to simulate accretion flows in binary systems.

In Chapter 5, I build on the progress of Chapters 3 and 4, presenting an alternative method to tackle the complex, multi-scale problem of understanding the evolution of accretion disc structure and the X-ray irradiating source heating the discs throughout LMXB outbursts. Using the unusual BH-LMXB Swift J1753.5-0127 as a case study, I use sophisticated modelling of the observed multi-wavelength behaviour of this LMXB system, at different times throughout its ~ 12 yr long outburst, to effectively track the time-series evolution of the accretion disc through three different accretion regimes undergone by this system. Overall, I am able to show that the abnormal long-term behaviour observed bears a striking resemblance to Z Cam type dwarf novae (compact binary systems where the mass-transfer rate from the companion star fluctuates about the critical mass-transfer rate above which the accretion disc is stable). Using this comparison I provide a concrete explanation for the long-term behaviour of Swift J1753.5-0127 in the context of the DIM. This explanation employs the addition of variable mass-transfer from the companion star, which is driven by how the changing irradiation properties of the system affect both the accretion disc and companion star.

In Appendix A, I provide a visual representation and detailed step-by-step description of the process involved in my Bayesian hierarchical methodology, developed and used in Chapters 3–5.

Chapter 2

A Comprehensive All-sky Study of the Galactic BH-LMXB Population

a part of:
Tetarenko, B.E., Sivakoff, G.R., Heinke, C.O., and Gladstone, J.C.
The Astrophysical Journal, 222, 15-113 (2016)

ABSTRACT

With the advent of more sensitive all-sky instruments, the transient Universe is being probed in greater depth than ever before. Taking advantage of available resources, we have established a comprehensive database of black hole (and black hole candidate) X-ray binary (BHXB) activity between 1996 and 2015 as revealed by all-sky instruments, scanning surveys, and select narrow-field X-ray instruments aboard the INTErnational Gamma-Ray Astrophysics Laboratory (INTEGRAL), Monitor of All-Sky X-ray Image (MAXI), Rossi X-ray Timing Explorer (RXTE), and *Swift* telescopes; the Whole-sky Alberta Time-resolved Comprehensive black Hole Database Of the Galaxy or WATCHDOG. Over the past two decades, we have detected 134 transient outbursts, tracked and classified behavior occurring in 49 transient and 8 persistently accreting BHs, and performed a statistical study on a number of outburst properties across the Galactic population. We find that outbursts undergone by BHXBs that do not reach the thermally dominant accretion state make up a substantial fraction ($\sim 40\%$) of the Galactic transient BHXB outburst sample over the past ~ 20 years. Our findings suggest that this “failed” behavior, observed in transient and persistently accreting BHXBs, is neither a rare nor recent phenomenon and may be indicative of an underlying physical process, relatively common among

binary BHs, involving the mass-transfer rate onto the BH remaining at a low level rather than increasing as the outburst evolves. We discuss how the larger number of these “failed” outbursts and detected outbursts in general have significant implications for both the luminosity function and mass-transfer history of the Galactic BHXB population.

2.1 The WATCHDOG Project

2.1.1 The Catalogue, Algorithm, and Online Interface

Population studies remain our best option for understanding the wide range of (currently unknown) physics needed to explain all observed behavior exhibited in BH-LMXBs. To date, there exist numerous catalogues of various types of X-ray binary systems (see Bradt & McClintock 1983; van Paradijs & McClintock 1995; Liu et al. 2001, 2007). However, with the advent of more sensitive all-sky and scanning survey X-ray instruments allowing the transient X-ray Universe to be probed in greater depth, we are detecting a larger number of sources than ever before, culminating in the currently published catalogues quickly becoming dated.

In addition to these catalogues, there also exists a copious amount of comprehensive reviews on LMXBs and X-ray Novae (XRN) in the literature. For large scale reviews see Tanaka & Lewin (1995); Tanaka & Shibazaki (1996); McClintock & Remillard (2006), for a comprehensive study of X-ray properties of BH-LMXBs in the pre-*RXTE* era see Chen et al. (1997) and for more recent global X-ray studies see Gierlinski & Newton (2006); Remillard & McClintock (2006); Dunn et al. (2010); Fender (2010); Belloni (2010); Gilfanov (2010); Yan & Yu (2015). However, the majority of these studies only focus on the “bright” outburst events, and offer only a sampling of the sources exhibiting the well defined canonical (“turtlehead”) behavior as observed by one telescope.

As is evident by the overview of the state of the field presented in Chapter 1, despite the numerous advances over the past 50 years, we still do not have a theoretical framework to explain all the observational behavior exhibited by BH-LMXBs. Thus, I have developed WATCHDOG (Tetarenko et al., 2016), a comprehensive population study of Galactic BH-LMXBs through their outburst activity.

Taking advantage of the suite of wide-field (all-sky), scanning survey, and narrow-field pointed X-ray instruments available over the past two decades, I have established: (i) the most up-to-date catalogue of BH-LMXBs, encompassing our Galaxy and Magellanic clouds; (ii) an outburst history for the Galactic population, encompassing over 20 years and including over 200 outbursts in >60 transient BH-LMXB sources; and (iii) a suite of tools to study the temporal and spectral evolution observed in LMXB sources. These tools include: (i) the "Outburst Tracker", a first of its kind algorithm that detects, tracks, and monitors LMXB outburst behaviour over decades of energy and time; (ii) a quantitative outburst classification scheme; and (iii) a set of unique interactive, online applications to determine accretion state, derive mass-transfer rates, and compute bolometric luminosities of BH-LMXBs during outburst on daily timescales. Built to act as an interactive, multi-purpose, online interface[1], WATCHDOG is available to (and currently being used by) the widespread binary community.

For the complete WATCHDOG catalogue, outburst history, and a detailed description of the algorithm behind WATCHDOG's suite of tools, see Tetarenko et al. (2016), and my MSc. thesis (2014), where this portion of the material was originally presented. For the application of WATCHDOG's suite of tools to the Galactic BH-LMXB population, refer to Sections 2.2 and 2.3 in this Chapter.

2.1.2 Data Compilation

To construct the WATCHDOG project I have incorporated data from the All-Sky Monitors (ASMs), Galactic Bulge Scan Surveys, and select narrow-field X-ray instruments available on four separate telescopes, making it possible to study nearly two-decades of behavior exhibited by the Galactic BH-LMXB population.

ASMs are indispensable in the study of BH-LMXBs as they: (i) provide near real-time coverage of a large percentage of the sky across a wide range of X-ray energies; (ii) operate on short timescales, allowing them to track short-term behavior

---

[1] http://astro.physics.ualberta.ca/WATCHDOG

in known sources and discover new sources; and (iii) accumulate vast databases of activity, which can be used to track outbursts, study evolution and state transitions, and derive a long-term history for numerous sources (e.g., McClintock & Remillard 2006; Krimm et al. 2013).

Scanning surveys observe the Galactic Bulge, a region rich in bright variable high-energy X-ray sources, regularly during all visible periods. These surveys, in addition to the pointed observations from various narrow-field X-ray instruments, provide high sensitivity long-term light curves of numerous X-ray sources to supplement the all-sky coverage.

Data for this study has been acquired from the (i) *INTEGRAL* Galactic Bulge Monitoring Program[2], *MAXI* Archive[3], *RXTE*/PCA data archive, a part of the High Energy Astrophysics Science Archive Research Center (HEASARC) Online Service provided by the NASA/Goddard Space Flight Center[4], Craig Markwardt's (*RXTE*/PCA) Galactic Bulge Survey Webpage[5], and *Swift*/BAT Transient Monitor[6]. See Section 1.3 for details of individual telescopes and instruments.

2.2 The Population Study

2.2.1 Characterization of Long-term Temporal and Spectral Evolution in BH-LMXBs

By combining three of WATCHDOG's unique algorithms — the outburst tracker, accretion state-by-day tool, and outburst classification tool — I have been able to characterize nearly two decades of outburst behaviour exhibited by the BH-LMXB population of our Galaxy.

The outburst tracker is built on, a first of its kind, comprehensive algorithm written to discover and track X-ray outbursts in BH-LMXBs using all-sky, scanning

---

[2] http://integral.esac.esa.int/BULGE/

[3] http://maxi.riken.jp/top/

[4] http://heasarc.gsfc.nasa.gov/

[5] http://asd.gsfc.nasa.gov/Craig.Markwardt//galscan/main.html

[6] http://swift.gsfc.nasa.gov/results/transients/

survey, and pointed X-ray instruments aboard multiple telescopes. This tool allows us to probe the whole-sky at both soft and hard X-ray energies (2–100 keV). The outburst tracker has the ability to detect transient events, occurring at flux levels greater then a few times $10^{-10}\,\mathrm{erg\,cm^{-2}\,s^{-1}}$ (i.e., $\sim 10^{35} - 10^{36}\,\mathrm{erg\,s^{-1}}$ in bolometric luminosity), allowing for the study of both canonical and anomalous behaviour exhibited by the Galactic population.

The accretion state-by-day tool uses the X-ray hardness ratio parameter (defined as the ratio of hard to soft band flux) as a tracer of X-ray spectral properties in outbursting LMXBs (see Section 1.2.2 and Figure 1.6), to determine the accretion state of a source on any given day during outburst.

The outburst classification tool provides a quantitative classification scheme for observable (temporal and spectral) behaviours exhibited by BH-LMXBs during outburst. This tool has the ability to iterate through, and track the spectral evolution of a source, on a daily timescale throughout an outburst. In doing so, this tool can categorize outburst behaviour into two classes, "canonical" (definitive soft state or a full hard-soft state transition is observed) or "failed" (no state transition was observed, remain in the hard state for the duration of the outburst).

Galactic Outburst Detection Rates

Using WATCHDOG's outburst tracker tool, we have computed the overall (and instrument specific) outburst rates for transient BH-LMXB events in the Galaxy during the WATCHDOG time-period (1996 January 6 – 2015 May 14). This is, in and of itself, a non-trivial task as these outburst rates depends on the sky coverage, lifetime, and limiting sensitivity of instruments launched at different times (Chen et al., 1997). To address these issues we begin by estimating outburst rates per year, with quoted 1σ Gehrels errors (Gehrels, 1986), for each individual instrument (see Table 2.1).

We attempt to quantify sky coverage and instrument lifetime by using only the time in which data were being taken by the instrument ($f_{\mathrm{collect}} * t_{\mathrm{active}}$), rather than the total time that the instrument was active (t_{active}) in the calculation of this rate.

Table 2.1: Transient BH-LMXB Outburst Rate per Instrument during the WATCHDOG time-period

Telescope	Instrument	Type	t_{active} [a] (yrs)	f_{collect} [b]	Outbursts Detected	Rate (yr^{-1})
INTEGRAL	JEM-X	scan	10.23	0.19	16	$8.2^{+2.6}_{-2.0}$
	ISGRI	scan	10.23	0.25	24	$10.1^{+2.4}_{-2.0}$
MAXI	GSC	all-sky	5.74	1.0	28	$4.9^{+1.1}_{-0.9}$
RXTE	ASM	all-sky	15.98	0.92	76	$5.2^{+0.7}_{-0.6}$
	HEXTE	pointed	-	-	38	-
	PCA	scan+pointed	12.74	0.59	105	$14.1^{+1.5}_{-1.4}$
Swift	BAT	all-sky	10.25	0.92	62	$6.7^{+1.0}_{-0.8}$

NOTE. – Outburst rates are quoted with 1σ Gehrels errors. Note that, no all-sky monitoring survey was done by HEXTE, thus no outburst rate is calculated.

[a] the amount of time the instrument has been active.

[b] the fraction of time the instrument was taking data over the total time active.

Due to Sun constraints, most X-ray instruments do not point near the Galactic Bulge region (where most of our sources are located) around December every year. To take into account these Sun constraints in the calculation of $f_{\rm collect}$ for *Swift*/BAT and *RXTE*/ASM, we assume that for one month per year of operation the instrument in question was not actively observing, yielding $f_{\rm collect} = 0.92$ in both cases. Given that *MAXI* has no Sun constraint, we assume that the GSC aboard *MAXI* has taken data daily for the full time period it has been active (i.e., $f_{\rm collect} = 1.0$).

The instruments involved in the scanning surveys (as well as those that have pointed observations available) only take data in short consecutive intervals resulting in $f_{\rm collect} \ll 1.0$. To calculate $f_{\rm collect}$ for PCA, ISGRI, and JEM-X we begin by parsing through all available data on an individual source (including the scanning survey and/or pointed observations), checking if data is available from that instrument on a weekly timescale. If the instrument observed the source at least once in any particular week, the full week is counted toward the total time the instrument was observing. If the algorithm finds a time gap greater than a week in which the instrument has no observations of the source, the total duration of this gap is calculated and subsequently not counted toward the total time the instrument was observing. Once the total observation time is calculated for each transient source, an average over all transient sources is calculated. This average is then used to calculate $f_{\rm collect}$ for the instrument in question.

We do not attempt to take into account the differing limiting sensitivities between the instruments used in this study (e.g., PCA is the most sensitive soft instrument and *INTEGRAL* is the most sensitive hard instrument).

Overall, WATCHDOG's outburst tracker has detected 134 outbursts occurring in 49 transient BH-LMXBs during the period of 1996 January 6 – 2015 May 14 (see Figure 2.1). Taking the above mentioned factors into consideration, we estimate that with the current suite of instruments in space we are detecting ∼4–12 BH-LMXB transient events every year, more than a factor of three larger than in the pre-*RXTE* era (Chen et al., 1997).

Note that on 2015 May 14 (the cutoff date for the WATCHDOG analysis), 4U 1630−472 and GX339−4 were both in the decay stage of their most recent outbursts

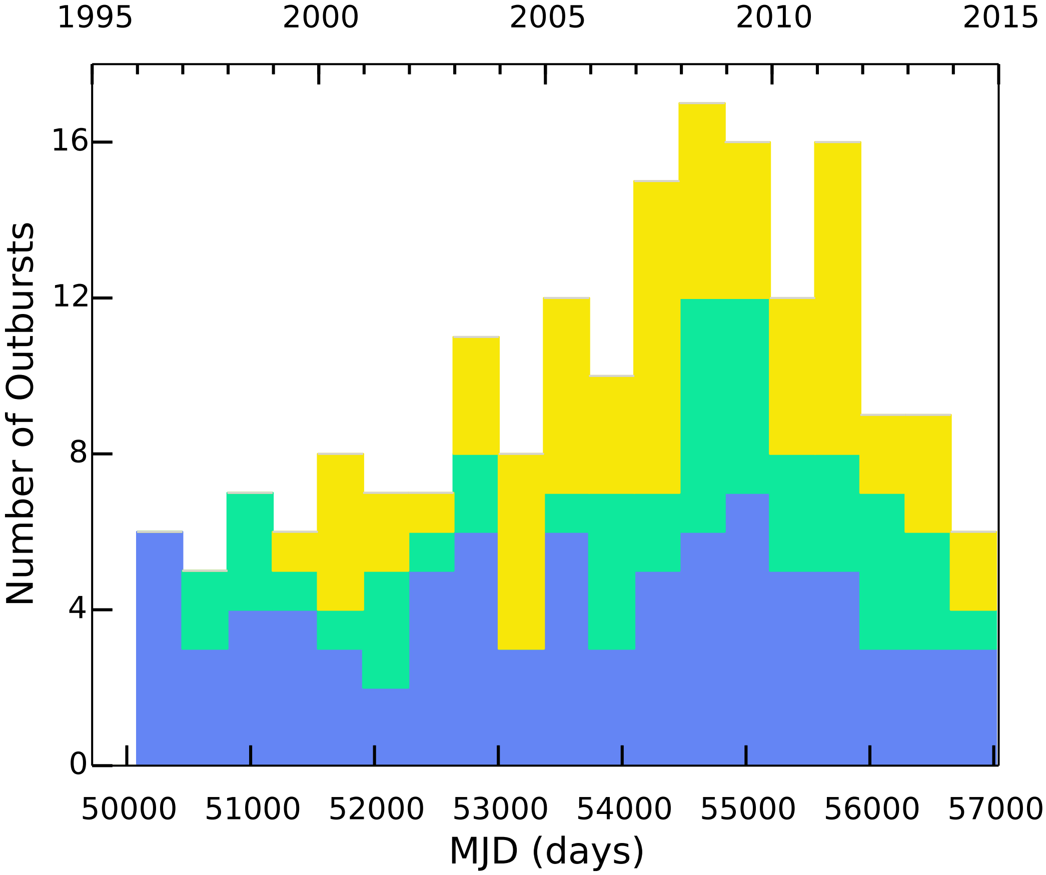

Figure 2.1: Histogram showing transient BH-LMXB outbursts detected by the WATCHDOG algorithm between 1996 January 1 – 2015 May 14. Time bins are one year in length and colors correspond to outburst classification; blue for canonical, green for failed, and yellow for indeterminate.

(and had already reached the soft state during their outburst). As such, these outbursts are included in all of our analyses with the exception of the outburst duration statistics. In addition, during the months of June and July (2015), H 1743−322, GS1354−64, GS 2023+338 (V404 Cyg), and SAX J1819.3−2525 (V4641 Sgr) were all observed in outburst again. These outbursts occurred after the cut-off date, and therefore are not included in our analysis. See Tetarenko et al. (2016) for the full tabulated outburst history of the Galactic BH-LMXB population.

Classification of Outburst Behaviour

WATCHDOG's outburst classification tool categorizes transient outburst behavior into one of two classes: "canonical" or "failed", based on accretion state reached during outburst. See Figure 2.2 for a schematic of each outburst class.

The classification procedure (Tetarenko et al., 2016) works by using WATCHDOG's accretion state-by-day tool, to differentiate daily-averaged X-ray data taken during each outburst into hard, soft, and intermediate accretion states based on critical hard ($C_{\rm hard}$) and critical soft ($C_{\rm soft}$) X-ray hardness ratio values.

As these critical values will differ depending on the telescopes involved in the X-ray hardness ratio, the tool makes use of 10 calibration sources (found in Table 2.2) to set these baseline critical values. These calibration sources have been specifically chosen based on the criteria that they have exhibited (proven via in depth spectral analysis in the literature) either "failed" outbursts, or a combination of "canonical" and "failed" outbursts over the WATCHDOG time-period (1996 January 1 – 2015 May 14).

The literature classification is then used to find the baseline critical values for each of the nine X-ray hardness ratio combinations that are used in this study. See Table 2.3 for the critical values corresponding to each X-ray hardness ratio combination.

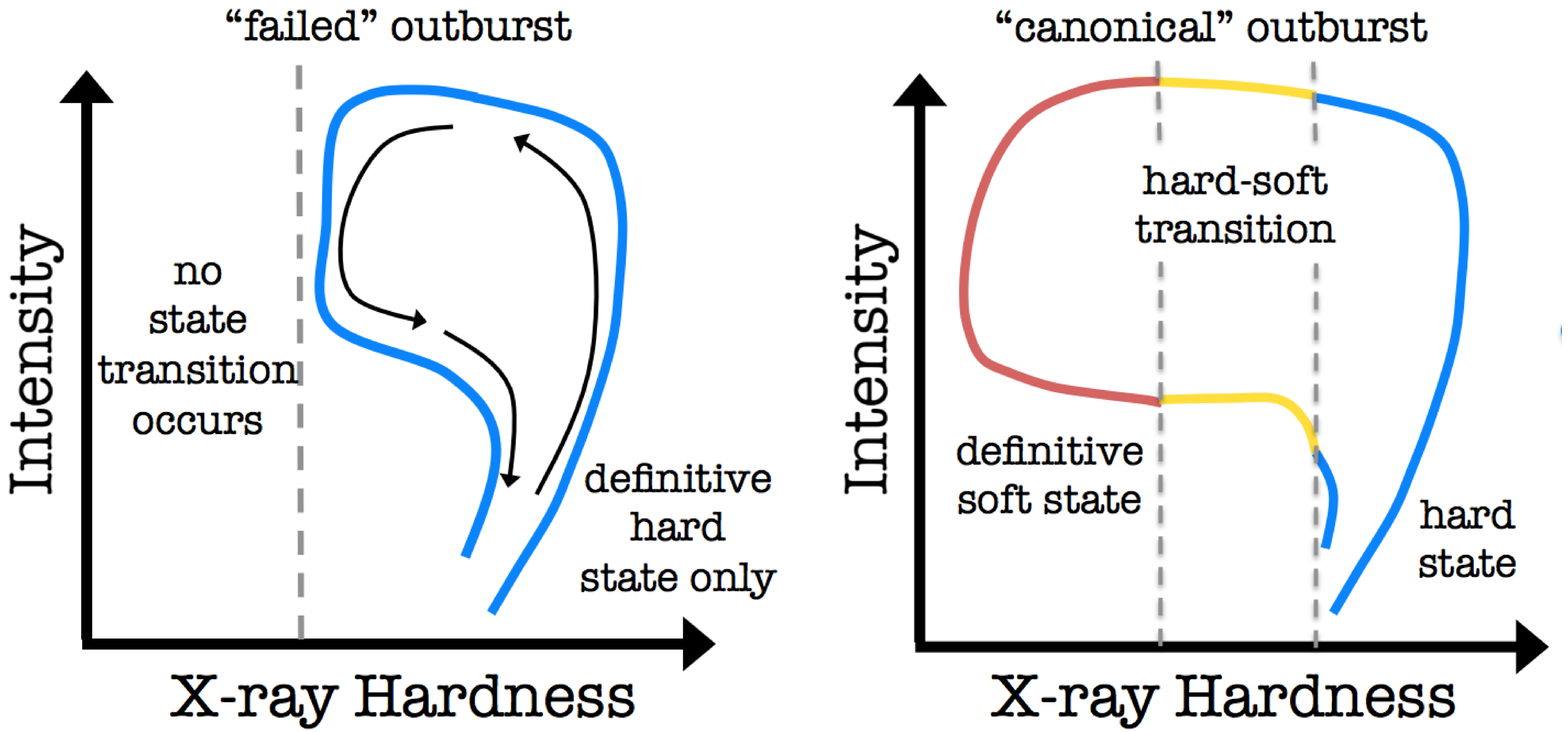

Figure 2.2: Schematic displaying the two different types of outburst behaviour, observed in the Galactic BH-LMXB population, as seen in a hardness-intensity diagram.

There are multiple telescope/instrument pairs involved in this process (between 1–9 separate pairs). Each pair of observations (that is the two bands involved in the X-ray hardness ratio) will indicate whether the source is currently in the hard, soft, or intermediate state, on any given day during an outburst. The accretion state-by-day tool takes into account all possible combinations of state classifications and logically combines them to determine the accretion state of the source on each day during an outburst. If at least one hardness ratio indicates a soft accretion state, the state for that day is classified as soft. Otherwise, if at least one hardness ratio indicates an intermediate accretion state (defined as in between the $C_{\rm soft}$ and $C_{\rm hard}$ limits), the state for that day is classified as intermediate. If all data indicates a hard accretion state, the state for that day is classified as hard.

WATCHDOG's outburst classification tool will parse the daily accretion state information available throughout an individual outburst to determine which accretion states were reached by the source. If all observations during the outburst are found to be in the hard accretion state, then the outburst is classified as "failed". If any observations during the outburst are found to be in the soft accretion state, then the outburst is classified as "canonical". If neither of these conditions are met, the outburst is classified "indeterminate", which indicates that the outburst was detected by the algorithm but that there was not enough data available to confidently determine whether or not the source reached the soft accretion state during the outburst.

Using WATCHDOG's outburst classification tool, we have been able to classify the behavior exhibited during 94 of the 134 total transient BH-LMXB outbursts detected by the WATCHDOG outburst tracker. In contrast to the picture found in much of the large-scale population studies in the literature on BH-LMXB spectral evolution (e.g., Zhang et al. 2007; Dunn et al. 2010), we find that the outbursts undergone by BH-LMXBs that do not complete the "canonical" turtlehead pattern (i.e., undergo a state change), the so-called "failed" outbursts, make up $\sim 40\%$ (i.e., 0.38 ± 0.06) of all outbursts occurring in Galactic transient BH-LMXBs between 1996 January 1 – 2015 May 14. "Failed" outbursts appear to make up a (surprisingly) substantial contribution to the total outburst sample.

Table 2.2: Outburst Behaviour Calibration Source Details

Source Name	Outburst Year	Calibration Type	References
GX 339−4	1996–1999	C	1,2
	2002/2003	C	3
	2004/2005	C	4
	2006	F	5
	2006/2007	C	5,6
	2009–2011	C	7
H 1743−322	2003	C	3,8–11
	2004	C	12
	2005	C	12
	2007/2008	C	13,14
	2008	F	15,16
	2010	C	14,17,18
MAXI J1836−194	2011/2012	F	19–21
XTE J1118+480	1999/2000	F	22–26
GS 1354−64	1997/1998	F	27–29
IGR J17497−2821	2006	F	30–32
XTE J1550−564	1998/1999	C	33–35
	2001	F	36
	2001/2002	F	37
	2003	F	38,39
SAX J1711.6−3808	2001	F	40
IGR J17285−2922	2010	F	41
Swift J174510.8−262411	2012/2013	F	42,43

NOTE.– The calibration type for each outburst is stated: C for “canonical” and F for “failed”.

Refs. – [1] Zdziarski et al. (2004), [2] Belloni et al. (1999), [3] Homan et al. (2005), [4] Belloni et al. (2006), [5] Buxton et al. (2012), [6] Motta et al. (2009), [7] Debnath et al. (2013b), [8] Capitanio et al. (2005), [9] Miller et al. (2006), [10] Kalemci et al. (2006), [11] McClintock et al. (2009), [12] Capitanio et al. (2006), [13] Capitanio et al. (2010), [14] Zhou et al. (2013), [15] Capitanio et al. (2009), [16] Motta et al. (2010), [17] Corral-Santana et al. (2011), [18] Debnath et al. (2013a), [19] Ferrigno et al. (2011), [20] Reis et al. (2012), [21] Russell et al. (2014), [22] Hynes et al. (2000), [23] McClintock et al. (2001), [24] Brocksopp et al. (2010), [25] Frontera et al. (2001), [26] Revnivtsev et al. (2000b), [27] Brocksopp et al. (2001), [28] Brocksopp et al. (2004), [29] Revnivtsev et al. (2000a), [30] Rodriguez et al. (2007), [31] Walter et al. (2007), [32] Paizis et al. (2009), [33] Sobczak et al. (2000), [34] Remillard et al. (2002), [35] Kubota & Makishima (2004), [36] Tomsick et al. (2001b), [37] Belloni et al. (2002), [38] Sturner & Shrader (2005), [39] Aref’ev et al. (2004), [40] in’t Zand et al. (2002), [41] Sidoli et al. (2011), [42] Krimm et al. (2013), [43] Curran et al. (2014)

Table 2.3: WATCHDOG's Empirical Outburst Classification Criteria

Telescopes & Instruments	Hard Band (keV)	Soft Band (keV)	C_{soft}	C_{hard}
Swift BAT/MAXI GSC	15–50	4–10	0.2846	0.3204
Swift BAT/RXTE ASM	15–50	3–12	0.1646	0.2675
Swift BAT/RXTE PCA-scan	15–50	2.5–10	0.5597	0.8601
Swift BAT/INTEGRAL JEM-X	15–50	3–10	0.3884	0.5751
RXTE ASM	5–12	3–5	0.3843	0.4220
INTEGRAL ISGRI/JEM-X	18–40	3–10	0.3579	0.5449
RXTE HEXTE/ASM	15–30	3–12	0.3717	0.6890
RXTE HEXTE/PCA	15–30	4–9	0.2246	0.4938
RXTE PCA	9–20	4–9	0.4620	0.6433

NOTE. – C_{hard} and C_{soft} represent the X-ray hardness ratio limits, as determined by the calibration sources, for the hard and soft accretion states, respectively.

Table 2.4: Evolution of the Galactic BH-LMXB “Failed” to “Canonical” Outburst Ratio over Time

Time Segment	Time Period (MJD)	N_C	N_F	N_I	Failed Ratio	Total Rate (yr^{-1})
A: ASM ON–PCA ON	50088–51214	10	4	1	$0.29^{+0.17}_{-0.13}$	$4.86^{+1.61}_{-1.24}$
B: PCA ON–BAT/INTEGRAL ON	51214–53414	14	6	13	$0.30^{+0.14}_{-0.11}$	$5.48^{+1.13}_{-0.95}$
C: BAT/INTEGRAL ON–GSC ON	53414–55058	15	12	19	0.44 ± 0.11	$10.21^{+1.74}_{-1.50}$
D: GSC ON–ASM OFF	55058–55924	8	6	8	$0.43^{+0.17}_{-0.16}$	$9.28^{+2.43}_{-1.96}$
E: ASM OFF	55924–Present	5	4	6	$0.44^{+0.21}_{-0.20}$	$4.44^{+1.47}_{-1.13}$
F: Before BAT/INTEGRAL ON	50088–53414	24	10	13	$0.29^{+0.098}_{-0.084}$	$5.16^{+0.87}_{-0.75}$
G: After BAT/INTEGRAL ON	53414–Present	28	22	34	$0.44^{+0.081}_{-0.078}$	$8.19^{+0.99}_{-0.89}$
Total	50088–Present	52	32	47	$0.38^{+0.060}_{-0.056}$	$6.76^{+0.64}_{-0.59}$

NOTE.– N_C, N_F, and N_I refer to the number of outbursts detected, in a particular time-period, that were classified as “canonical”, “failed”, and “indeterminate”, respectively.

By splitting the WATCHDOG time period into logical segments defined by the addition/loss of each instrument used in this study, we have analyzed how the ratio of "failed" to "canonical" outbursts in the Galactic BH-LMXB population changes over time (see Table 2.4). We find that after *Swift* and *INTEGRAL* were turned on the rate of observed outbursts increased by ~ 1.5 and the "failed" ratio increased by $\sim 15\%$. While this suggests that the "failed" outburst ratio may have increased when the threshold for detection was lowered (i.e., since "failed" outbursts are faint, higher sensitivity instruments would detect more), the difference in "failed" ratios is only significant at the 1.7σ level. However, when we combine this finding with an extensive literature review (Tetarenko et al., 2016), which shows a near constant appearance of "failed" outbursts over the last ~ 50 years, it becomes clear that this "failed" behavior is neither a rare nor recent phenomenon.

2.2.2 Galactic Distribution of Outburst Properties

We have computed the distributions of outburst duration, recurrence rates, duty cycles, peak outburst luminosity, and total energy radiated during outburst, for the Galactic BH-LMXB population. These distributions include transient outbursts detected in 49 individual BH-LMXB sources by the WATCHDOG outburst tracker between 1996 January 6 – 2015 May 14. To do so, we make use of the WATCHDOG catalogue and outburst history, the results of WATCHDOG's outburst tracker, and WATCHDOG's spectral fitting tool, which has the ability to compute bolometric X-ray luminosity for a source on any given day during outburst.

Outburst Duration

For the time period, as defined above, we have calculated the duration of the 134 transient BH-LMXB outbursts detected by the WATCHDOG outburst tracker (see Figure 2.3). We find that the mean outburst duration for the Galactic transient BH-LMXB population is ≈ 250 days. When comparing the outburst durations of "canonical" (i.e., state transitions have occurred; "turtlehead" pattern observed) versus "failed" outbursts, we find mean outburst durations of ≈ 247 and ≈ 391 days, respectively. In addition, we test whether or not the durations of “canonical” and “failed” outbursts are systematically different by performing a two sample KS-test. We find a p-value of 3.9×10^{-4}, providing clear statistical evidence that the durations of “canonical” and “failed” outbursts do not arise from the same parent distribution.

Recurrence Time

In addition, we have also calculated the recurrence times between outbursts of this sample of 49 BH-LMXB sources. Figure 2.3 displays the distribution of outburst recurrence times, calculated by finding the time difference between the beginning of each outburst detected in a particular source. In the case where a source has only undergone one outburst in the time period, a lower limit is estimated by taking the time difference between (i) the beginning of our analysis (1996 January 6 – MJD = 50088) and the beginning of the outburst in the case where the outburst occurred closer to end of our analysis (2015 May 14 – MJD = 57156), or (ii) the end of our analysis and the beginning of the outburst in the case where the outburst occurred closer to the beginning of our analysis. Taking into account all detected recurrent events (i.e., not including lower limits) and ignoring the possibility that the WATCHDOG outburst tracker may have missed events between some of the recorded outbursts, we find the minimum, median, and maximum, recurrence time exhibited by the BH-LMXB population to be approximately 29, 414, and 6589 days, respectively.

We note that there is a possibility that our distribution is not the true distribution due to two contributing factors. First, there could be (and are) outbursts that the WATCHDOG outburst tracker has not detected (see the footnotes of Table 14 in Tetarenko et al. 2016 for thorough discussion). This would increase the count of short recurrence times. Second, the many sources that have only one recorded outburst (and in turn only a lower limit on recurrence time) may go into outburst in the future. This would effectively increase the count of long recurrence times.

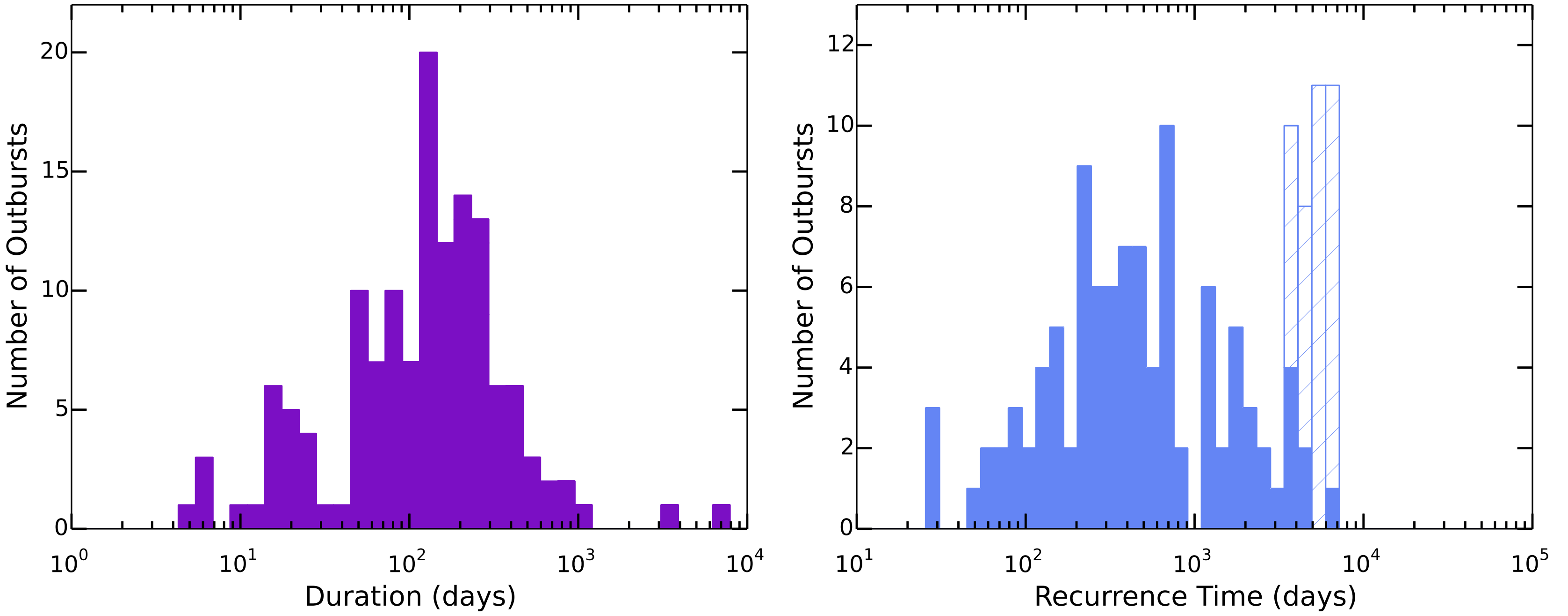

Figure 2.3: Distribution of (left) duration of transient outbursts, and (right) outburst recurrence times, for the Galactic BH-LMXB population between 1996 January 6 – 2015 May 14. Data is distributed into 50 equal size bins, between 1 and 10^4 days and 10 and 10^5 days for outburst duration and recurrence times, respectively. The mean outburst duration is 250 days. For sources that have undergone more than one outburst (solid blue), the median of the recurrence times between outbursts for the source is plotted. If a source has only one outburst detected in the time period (blue cross-hatch), a lower limit estimate on the recurrence time is plotted. Not including the lower limits, we find a median recurrence time for the transient population of ≈ 414 days.

Duty Cycles

Using the outburst durations and the number of outbursts detected by the WATCHDOG outburst tracker, we have estimated the duty cycle for the 49 BH-LMXB sources in the WATCHDOG sample. The duty cycle, defined as the fraction of total lifetime that a transient source has spent in outburst, is an important parameter needed to understand both the luminosity functions and binary evolution of these types of systems (e.g, Belczynski et al. 2004; Fragos et al. 2008, 2009). As such, being able to quantify the range of duty cycles exhibited by the BH-LMXB population is of crucial importance.

Figure 2.4 shows the Galactic distribution of duty cycles, calculated by taking the total time each source has spent in outburst and dividing by the total WATCHDOG observation time (1996 January 6 – 2015 May 14; 7068 days), for all 49 transient BH-LMXB sources. We find a wide distribution of duty cycles exhibited by the Galactic population, ranging from 0.20–100%, with an mean value of 10%, and a median value of 2.7%. Moreover, we find there is no observable systematic difference in duty cycle between those sources that have exclusively undergone "canonical" outbursts, exclusively undergone "failed" outbursts, or have undergone a combination of the two types of outbursts in the WATCHDOG time period.

Many of the sources in our sample have only undergone one outburst during the WATCHDOG observational time period, making the duty cycle we estimated only an upper limit on the true value. While the long term evolutionary history of these transient systems may not be fully represented by the 19 years of behavior WATCHDOG has cataloged, our analysis can at least provide order of magnitude estimates for their duty cycles, which are still exceedingly helpful input into the theoretical modelling of luminosity functions and binary evolution codes (Yan & Yu, 2015).

In making this argument we are assuming that the outburst recurrence times for these systems do not exceed ~ 200 years (an order of magnitude longer than our observation history). To determine if this assumption is valid we begin with an analytical relationship between orbital period and recurrence time. Using the DIM (see Section 1.2.1 for detailed discussion), a theory used to explain the outburst

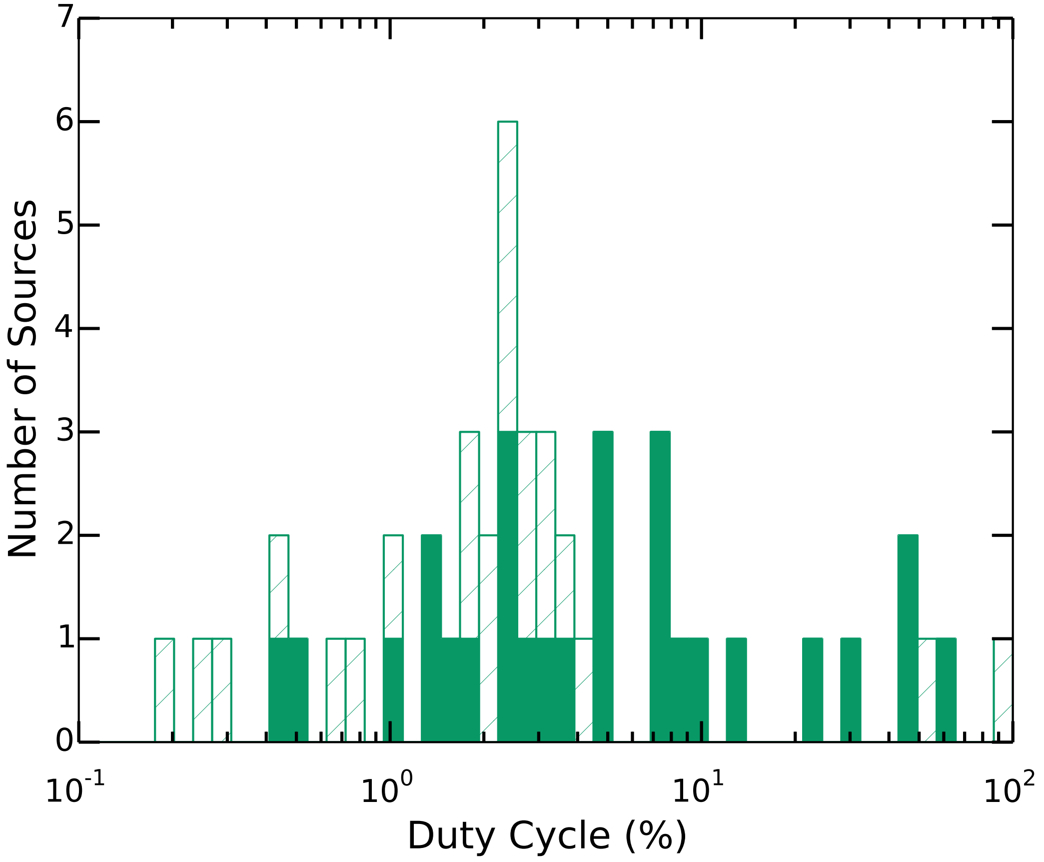

Figure 2.4: Distribution of the duty cycles for the Galactic BH-LMXB population between 1996 January 6 – 2015 May 14. Data is distributed into 50 equal size bins between 0.1% and 100% with a mean of 10% and median of 2.7% (including upper limits). Both sources that have undergone more than one outburst in the time period (solid green) and sources for which we only have upper limit estimates on the duty cycle due to only one outburst being detected in the time period (green cross-hatch) are displayed.

mechanism in LMXBs, and assuming recurrence time can be estimated as the time required to fill the disc to its maximum mass $M_{\rm max}$, Menou et al. (1999) find,

$$t_{\rm recur} \lesssim \frac{M_{\rm max}}{\dot{M}_{\rm BH}} = 2.64 \times 10^{21}\, \alpha^{-0.85}\, \dot{M}_{\rm BH}^{-1}\, M_1^{-0.37}\, R_{10}^{2.11} \tag{2.1}$$

where α is the α-viscosity parameter (a parameter describing the efficiency of angular-momentum and mass transport in an accretion disc; see Shakura & Sunyaev 1973 and Chapter 3), M_1 is the mass of the BH, $\dot{M}_{\rm BH}$ is the mass-transfer rate onto the BH, and R_{10} is the disc outer radius in units of 10^{10} cm. Following Menou et al. (1999), we assume R_{10} is approximately 70% of the Roche-lobe equivalent radius and use the formula for the Roche lobe equivalent radius given by Paczynski (1971) to approximate $R_{10} \sim 15\, M_{\rm BH}^{1/3}\, P_{\rm orb}^{2/3}$.

From Equation 2.1, it is clear that a large $P_{\rm orb}$ would be needed to give a long recurrence time. For a system with a $10\,M_\odot$ BH, and an $\dot{M}_{\rm BH}$ typical for longer period (> 10 hr) systems of $\sim 10^{-9}\,M_\odot{\rm yr}^{-1}$ (see Figure 2.7), a $P_{\rm orb} \sim 286$ hours would be required to give a $t_{\rm recur} \sim 200$ years. Using the typical radius-period relation (Frank et al., 2002), a system with $P_{\rm orb} \gtrsim 286$ hours (and therefore a $t_{\rm recur} \gtrsim 200$ years) would have to contain a giant companion of spectral type K7 or later. None of the known spectral types in the WATCHDOG BH-LMXB sample are red and large enough to give such a long recurrence time, with the exception of GRS 1915+105, which is thought to have a $t_{\rm recur} \sim 10^4$ years (Deegan et al., 2009).

While companion stars as large as the one in GRS 1915+105 can be ruled out in many of our systems with this argument, it cannot be used to rule out long recurrence times in systems where we have no serious limits on the companion. With this being said, one could also turn this argument around and say that a long recurrence time will also imply a long outburst time, so short outbursts will suggest short recurrence times. Examining the remainder of the transient population, for which we have no information on companion spectral type or orbital period, we find all outburst durations are $\lesssim 3$ years. We therefore believe that the assumption that $t_{\rm recur}$ does not exceed ~ 200 years for the systems in the WATCHDOG BH-LMXB sample is reasonable.

Peak Outburst Luminosities

By modelling each day's flux of a BH-LMXB as a combination of a soft disc-black body spectral component and hard Comptonized spectral component, assuming a Crab-like spectrum in each given energy band and a known distance (from the literature), WATCHDOG's spectral fitting tool can estimate bolometric X-ray luminosity L_{bol}. To accomplish this task, the WATCHDOG spectral fitting tool relies on the X-ray hardness ratio to determine the relative dominance of the disc and Comptonized spectral components in the spectrum and uses a Bayesian MCMC algorithm to fit for the flux of a BH-LMXB in a given energy band via,

$$f_X = a\,m_1 + b\,m_2, \tag{2.2}$$

where m_1 and m_2 are the flux of the disc and comptonized spectral component for the energy band in question, respectively.

Here, the standard two component spectral model in XSPEC, DISKBB+COMPTT, is used. This spectral model represents (i) the soft disc component of the spectrum with a $T_{\mathrm{in}} = 1$ keV multi-color disc-black body, typical of BH-LMXBs in the SDS (McClintock & Remillard, 2006), and (ii) the hard Componized component with the analytical COMPTT model corresponding to a plasma temperature of $T_{\mathrm{e}} = 50$ keV, a soft disc photon temperature of $T_{\mathrm{in}} = 1$ keV, and an optical depth $\tau = 1.26$, which has been calculated to roughly match a typical hard state photon index of 1.7 for the 3–20 keV range, as is often found in BH-LMXBs (McClintock & Remillard, 2006; Done, 2010).

Provided that there is one energy band available that can act as a hard band, one available energy band that can act as a soft band, and that at least one of these bands exhibits a detection of the source on the day in question, likelihood maximization can be performed by the MCMC method, resulting in posterior probability distributions (PDFs) of the normalization parameters a and b.

Once a and b are found for a given day, the algorithm can then estimate total bolometric flux (0.001–1000 keV), and the bolometric flux in each spectral component, by multiplying a and b by the derived bolometric correction from the XSPEC

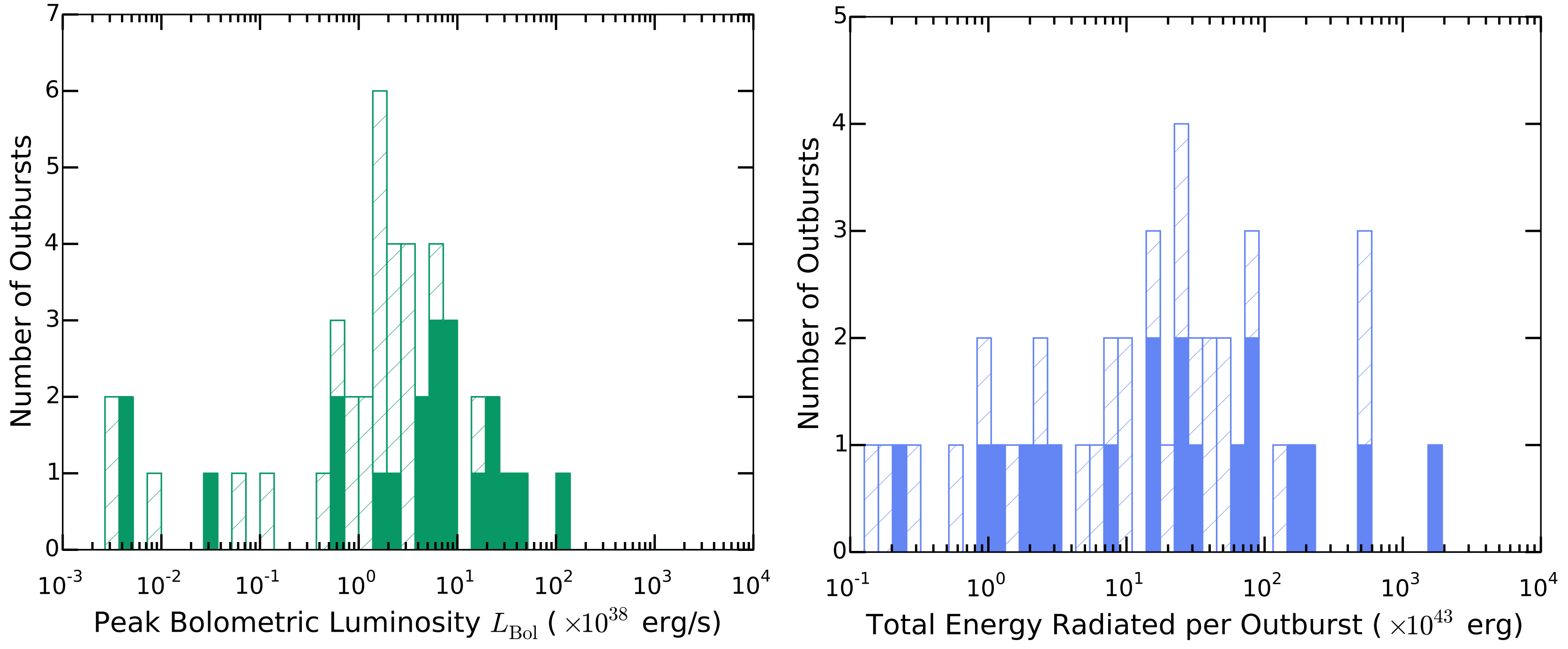

Figure 2.5: Distribution of the (left) peak bolometric outburst luminosity and (right) total X-ray energy released, for outbursts undergone by the Galactic BH-LMXB population between 1996 January 6 – 2015 May 14. Sources with (solid green and blue) and without (green and blue cross-hatch) known distance estimates are indicated in both histograms. Taking into account only outbursts undergone by sources with an available distance estimate, we find a mean peak bolometric luminosity of 1.40×10^{39} erg/s and the mean energy released during outburst to be 2.0×10^{46} erg.

models ($m_{1,\mathrm{bol}}$ and $m_{2,\mathrm{bol}}$) via,

$$f_{\mathrm{bol}} = a\, m_{1,\mathrm{bol}} + b\, m_{2,\mathrm{bol}} = f_{\mathrm{disc}} + f_{\mathrm{comp}}. \tag{2.3}$$

For a detailed description of the MCMC algorithm that WATCHDOG's spectral fitting tool is built on, see Tetarenko et al. 2016.

Using the bolometric fluxes obtained from WATCHDOG's spectral fitting tool, we computed and analyzed the peak luminosities for individual transient outbursts of the Galactic BH-LMXB population (see Figure 2.5).

If there are no available distance and/or BH mass estimates for a source, luminosity analysis is performed assuming a distance corresponding to a uniform distribution between 2 and 8 kpc and a BH mass that is sampled from the Ozel et al. (2010) mass distribution. Note that the BH mass estimates are only used for scaling the peak luminosity by the Eddington luminosity in our analysis.

This inferred distance of 2–8 kpc was chosen by taking the central 90% range of distances spanned by the 18 individual systems with known mass measurements (i.e., the dynamically confirmed BHs; Class A in Tetarenko et al. 2016), allowing us to sample from a range in distance in our analysis within which we would expect the majority of Galactic BH systems to lie. Using this criterion the closest and farthest systems, A 0620−00 at ∼1 kpc and GS 1354−64, which if the estimated distance (inferred from X-ray observations) is correct would make it the only known BH source in the Galactic halo, are excluded.

By choosing this uniform distribution in distance, we are implicitly assuming that whether or not follow-up observations have been performed on a source to determine distance/mass is more or less random. However, one could argue that the sources without distance/mass estimates are most likely to be those sources that are optically the faintest and behind the most reddening, which is more likely for sources on the far side of the Galaxy. In addition, if one were to look at a map of locations of LMXBs with distance estimates (e.g., Jonker & Nelemans 2004), they seem to be concentrated on the near side of the Galaxy.

On the other hand, (i) many large scale population studies like this work use similar assumptions for distance (e.g., Dunn et al. 2010), and (ii) we separate sources with and without known distances, and provide individual results, in all analyses involving luminosity in this work. As such, the reader should either (i) retain the caveat that, for our full sample, truncating uncertain distance distributions at 8 kpc may potentially cause inferred luminosity estimates to be skewed lower than the true luminosities for those sources, or (ii) focus only on the "known distance" parts of our analysis.

Eliminating outbursts undergone by sources with no available distance estimates yields a range in peak outburst luminosity of $4.0 \times 10^{35} - 1.0 \times 10^{40}$ $\mathrm{erg s^{-1}}$ and a mean peak outburst luminosity of 1.4×10^{39} $\mathrm{erg s^{-1}}$. Note that the one outburst peaking above 10^{40} $\mathrm{erg s^{-1}}$ is the 1997/1998 outburst of GS1354−64. However, the distance to this source is poorly constrained (25–61 kpc). If we were to place this system at our assumed standard Galactic value (i.e., a uniform distribution between 2 and 8 kpc) its peak luminosity would be on the order of 10^{38} $\mathrm{erg s^{-1}}$.

Total Energy Radiated During Outburst

Using the bolometric luminosities calculated with WATCHDOG's spectral fitting tool, we have also estimated the total X-ray energy released during outbursts of the Galactic BH-LMXB population. We define the total radiated energy as L_{bol} integrated over the duration of an outburst and calculate the quantity by first finding the weighted mean of L_{bol} during outburst, and then multiplying it by the total duration of the outburst. As there are asymmetric errors on our L_{bol} estimates, we calculate this weighted mean iteratively. Figure 2.5 shows the distribution of total radiated energy. Including only those sources that have a distance measurement available, we find a mean and range of total radiated energy during outburst for the BH-LMXB population to be 2.0×10^{46} erg and $8.8 \times 10^{41} - 3.8 \times 10^{47}$ erg, respectively.

2.2.3 Quantitative Properties of State Transitions

Using a combination of WATCHDOG's accretion state-by-day tool and spectral fitting tool, we have estimated the mean luminosity at which the forward (hard to soft) and reverse (soft to hard) accretion state transitions occur at during outbursts of the Galactic BH-LMXB population.

In Figure 2.6 we plot the probability distribution of transition luminosities in Eddington units ($L_{\rm bol}/L_{\rm edd}$). Using luminosities in Eddington units allows us to accurately compare across sources and take into account both uncertainties in distance to a source as well as BH mass. See the discussion of peak outburst luminosities above for details on how the distances are estimated for the sources without distance estimates in the literature. We are careful to include only those outbursts in which a source made a complete hard-soft or soft-hard transition. We do not include the erratic "jumps" between the intermediate states and the hard and soft states in this analysis.

The transition luminosity of a particular source during an outburst is estimated by finding the days in which the source was undergoing the specific state transition and calculating a weighted mean (and uncertainty) of the $L_{\rm bol}/L_{\rm Edd}$ estimates during this time period. To take into account the uncertainty in the estimated transition luminosities we make use of the Monte-Carlo method presented in Dunn et al. (2010), whereby we randomly select a value of $L_{\rm bol}/L_{\rm Edd}$ from a Gaussian distribution with 1σ values derived from the propagated error in the transition luminosity estimate for each state transition in our sample. We then use this to estimate the underlying probability distribution and display this in Figure 2.6.

Rather than fit a Gaussian distribution to the probability distribution (despite a large number of Monte-Carlo simulations, the precision of the distribution is relatively poor given the small number of total sources) as has been done in previous work, we have performed more distribution-agnostic characterizations of the hard-soft transition luminosities and the soft-hard transition luminosities. For each Monte-Carlo simulation we measure the mean and standard deviation of the log luminosities. The hard to soft transition is described by $\mu_{\rm logL_{Edd}} = -0.94^{+0.15}_{-0.16}$ and $\sigma_{\rm logL_{Edd}} = 0.41^{+0.09}_{-0.03}$, while the soft to hard transition is described by $\mu_{\rm logL_{Edd}} = -1.50^{+0.15}_{-0.14}$ and $\sigma_{\rm logL_{Edd}} = 0.37^{+0.03}_{-0.02}$. For illustrative purposes, we overplot Gaussian distributions given by the median $\mu_{\rm logL_{Edd}}$ and $\sigma_{\rm logL_{Edd}}$ (Shapiro-Wilk tests cannot reject the hypotheses that either population is drawn from a normal distribution;

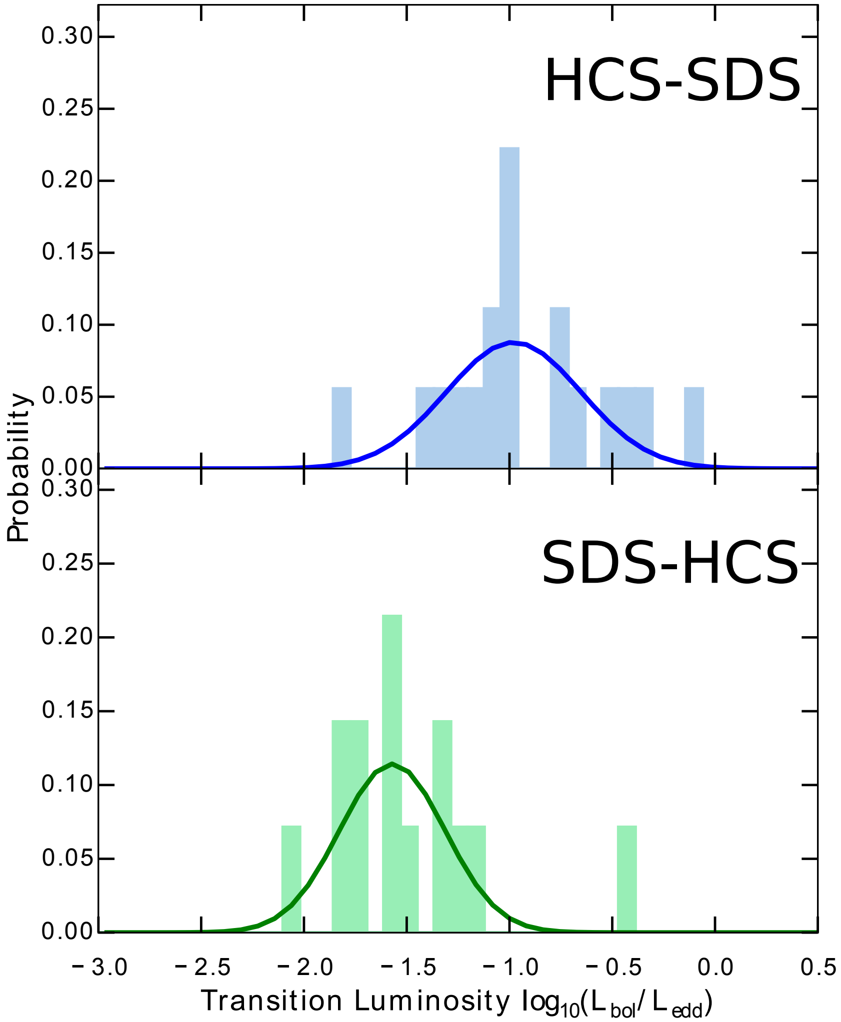

Figure 2.6: Probability distributions of the hard-soft (HCS-SDS; top) and soft-hard (SDS-HCS; bottom) transition luminosities in Eddington units, for outbursts undergone by the Galactic BH-LMXB population between 1996 January 6 – 2015 May 14. The histograms include only those outbursts with complete HCS-SDS and SDS-HCS state transitions. The mean and standard deviation of the log luminosities for the HCS-SDS and SDS-HCS transitions, found via a Monte-Carlo method (see text), are $(\mu, \sigma) = (-0.94, 0.409)$ and $(\mu, \sigma) = (-1.50, 0.369)$, respectively. Gaussian distributions (solid blue and green lines) are overplotted with these parameters for illustrative purposes.

$p_{\mathrm{H}\rightarrow\mathrm{S}} = 0.95$ and $p_{\mathrm{S}\rightarrow\mathrm{H}} = 0.086$). A non-parametric Wilcoxon rank-sum test of each simulation implies that the median (two-sided) probability that the hard-to-soft transition luminosities and the soft-to-hard transition luminosities are drawn from the same distribution is 5.5×10^{-4} (3.5σ).

A number of similar studies analyzing transition luminosities in BH-LMXBs exist. Dunn et al. (2010) used disc fraction luminosity diagrams[7] to determine transition luminosities for 25 BH-LMXB systems, and found a mean HCS-SDS transition luminosity ($\sim 0.3\,L_{\mathrm{edd}}$) that is significantly larger than our estimate; however, their range was comparable to our estimate (0.03–1 L_{edd}). Gierlinski & Newton (2006), using *RXTE*/ASM data and hardness-intensity diagrams, find a HCS-SDS transition luminosity comparable to our result, though they quote a range that is significantly narrower (0.01–0.28 L_{edd}).

In contrast, our mean SDS-HCS transition luminosity of $\sim 0.03\,L_{\mathrm{edd}}$ is consistent with both the estimates by Dunn et al. (2010) ($\sim 0.03\,L_{\mathrm{edd}}$) and Maccarone (2003) ($\sim 0.02\,L_{\mathrm{edd}}$), the latter who tabulated transition luminosities using available data of 6 BH-LMXBs from the literature. However, both Dunn et al. (2010) and Maccarone (2003) find a significantly narrower range (0.05–0.10 L_{edd} and 0.01–0.04 L_{edd}, respectively) for the SDS-HCS transition luminosity, when compared to our results.

Using our knowledge of the luminosity regimes in which hard-soft and soft-hard state transitions occour in BH-LMXBs, we have investigated possible causes of "failed" outbursts. The steady appearance of "failed" outbursts over the last ~ 50 years, indicates that there must be an underlying physical process, relatively common in BH-LMXBs, linked to this behaviour. Such a physical process would likely involve the mass-transfer rate onto the BH remaining at a low level rather than increasing as the outburst evolves, resulting in no state transition to the softer states occuring.

To test this theory we need to determine whether or not a "failed" outburst reaches the luminosity regime where the transition to the soft state tends to happen (i.e., are all "failed" outbursts faint, as the detection ratios presented in Section

---

[7] Disc fraction luminosity diagrams are sometimes used as an alternative to hardness-intensity diagrams. Here, disc fraction, the fraction of the total flux in the soft disc-blackbody spectral component, rather then hardness ratio is used as a tracer of X-ray spectral changes in a source.

2.2.1 tentatively suggest). We have therefore compared the peak Eddington scaled luminosities of all the "failed" outbursts in our sample, to our estimated mean hard-soft transition luminosity ($\sim 0.11\,L_{\rm edd}$; see above).

We find that all of these outbursts (with the exception of GS 1354−64) either have (i) upper limits on their Eddington scaled peak outburst luminosities that are $< 0.11\,L_{\rm edd}$, or (ii) have Eddington scaled peak luminosities consistent within error of the $< 0.11\,L_{\rm edd}$ regime. Overall, this suggests that "failed" behavior may indicate that a source did not reach the required mass-transfer rate needed to transition to the soft state. In the case of GS 1354−64, the distance is poorly constrained (25–61 kpc). If we were to place this system at our assumed standard Galactic value (i.e., a uniform distribution between 2 and 8 kpc), its Eddington scaled luminosity would be consistent within error of the $< 0.11\,L_{\rm edd}$ regime.

This being said, additional factors need to be addressed before such a strong claim against selection biases are made. These factors include: (i) the effect that distance could have on the outburst behaviors that we are able to observe, as an increase in sensitivity could largely increase the distance range within which we could observe the same outburst behaviors; (ii) the significance of individual instrument performance on outburst detection rates over time (e.g., *RXTE*/ASM detected significantly fewer outbursts towards the end of its life in 2011–2012 in comparison to during its earlier operation; Yan & Yu 2015); and (iii) the change in sensitivity of each instrument between soft and hard X-rays (i.e., while *RXTE* ASM and PCA included high sensitivity to soft state X-rays, *INTEGRAL*/ISGRI and *Swift*/BAT are only sensitive to hard X-rays, *INTEGRAL*/JEM-X has a relatively small field-of-view, and the only band in *MAXI* we found useful is not sensitive below 4 keV).

2.3 Fundamental Observational Tests of the DIM

2.3.1 The $\dot{M} - P_{\rm orb}$ Plane for BH-LMXBs

We have analyzed the relationship between long-term mass-transfer rate ($\dot{M}_{\rm BH}$) and orbital period ($P_{\rm orb}$) for the Galactic BH-LMXB population. To do so, we have derived the time-averaged bolometric luminosity and long-term mass-transfer rates, by making use of WATCHDOG's spectral fitting tool, for 17 transient BH-LMXB sources from the WATCHDOG catalogue that have a known $P_{\rm orb}$ and sufficient data available during WATCHDOG's observational time period (1996 January 6 – 2015 May 14). If a transient source has only undergone one outburst in this time period, only an upper limit estimate on the $\dot{M}_{\rm BH}$ for the source can be calculated.

Figure 2.7 presents the $\dot{M}_{\rm BH} - P_{\rm orb}$ plane for this Galactic BH-LMXB sample. This plot distinguishes between: (i) individual sources by colour; (ii) outburst behavior by shape — exclusively "failed" or incomplete state transitions exhibited (triangles), exclusively "canonical" (circles), or a combination "canoncial" and "failed" (squares); (iii) sources that have undergone multiple outbursts versus those with only lower limits on recurrence time (upper limit arrows); and (iv) sources with (closed shapes) and without (open shapes) known distance estimates.

Note that all our $\dot{M}_{\rm BH}$ estimates are in agreement with previous work done by Coriat et al. (2012), with the exception of XTE J1118+480 and GS 1354−64. In the case of XTE J1118+480, the discrepancy is most likely the result of Coriat et al. (2012) using a different accretion efficiency prescription when $L_X < 0.01\,L_{\rm edd}$, a luminosity regime in which this source remains in throughout outburst (i.e., $L_{\rm peak} \sim 0.004\,L_{\rm edd}$). In the case of GS 1354−64, the discrepancy is due to the use of a different distance estimate in our time-averaged bolometric luminosity calculation. While we use the full 25–61 kpc range, Coriat et al. (2012) use the lower limit of 25 kpc.

The inclusion of irradiation effects within the DIM (hereafter, the IDIM) has been shown to reproduce the global behaviour of many transient BH-LMXBs (e.g. Coriat et al., 2012). In particular, the IDIM can reproduce a significant portion of observed transient BH-LMXB X-ray outburst light-curves. See Chapters 3 and 4 for a detailed discussion on the Bayesian methodology I developed, which allows the use of outburst light-curves as a definitive test of the DIM in LMXBs.

However, this theory cannot adequately describe all features observed in the light-curves of the BH-LMXB population. Complex variability in the form of plateaus, rebrightening events, and flaring, can contaminate some of the X-ray outburst light-curves, making their use as a DIM diagnostic difficult. Further, the DIM works under

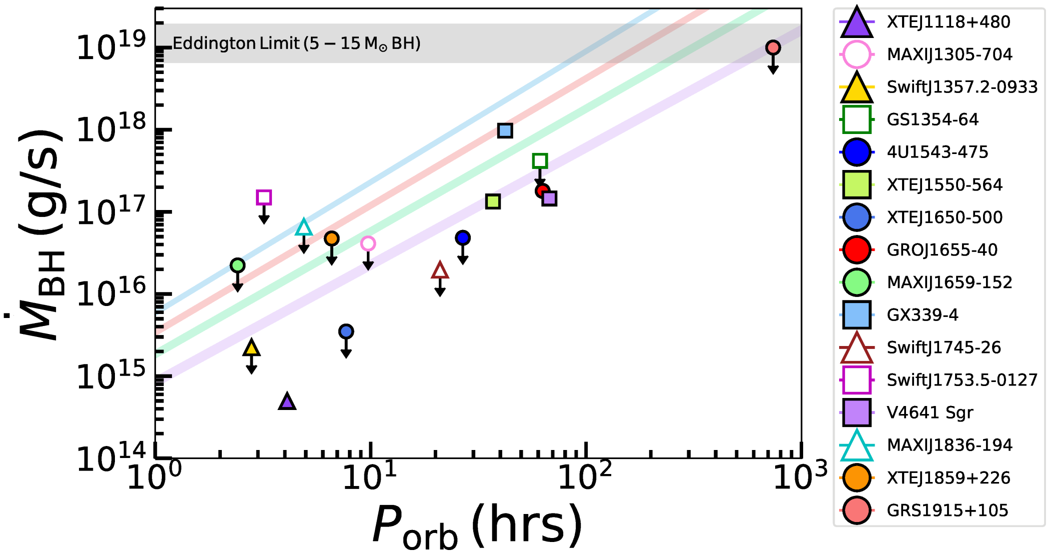

Figure 2.7: Long term mass-transfer rate onto the black hole ($\dot{M}_{\rm BH}$) vs. orbital period ($P_{\rm orb}$) for the Galactic BH-LMXB source sample. Colours represent individual sources (see legend). Shapes denote outburst behavior: exclusively "failed" outbursts or incomplete state transitions where the source only reaches as far as the intermediate states (triangles), exclusively "canonical" outbursts (circles), or a combination of these two options (squares). Filled and open shapes represent sources with and without reliable distance estimates, respectively. The mass-transfer rate estimates of sources that have only one detected outburst in the WATCHDOG time period are denoted as upper limits. The shaded grey region shows the Eddington limit for a $5-15\ M_{\odot}$ BH. The shaded blue ($C_{\rm irr} = 10^{-3}$), red ($C_{\rm irr} = 5 \times 10^{-3}$), green ($C_{\rm irr} = 3 \times 10^{-2}$) and purple ($C_{\rm irr} = 3 \times 10^{-1}$) regions plot the critical accretion rate for an irradiated disc around a 5–15 $M_{\odot}$ BH according to the DIM+irradiation (IDIM) for various strengths of irradiation heating $C_{\rm irr}$. Transient systems are expected to lie below the line. Note that all mass-transfer rates are calculated assuming a fixed accretion efficiency $\eta = 0.1$. Error bars, representing the 1σ confidence level, are too small to see.

simplifying assumptions as a means to deal with yet unknown physics, including the angular-momentum transport process (see Chapter 3), and the transition from efficient to inefficient accretion (see Chapter 4), in an accretion disc. See Chapters 3 and 4 for a discussion of the effect these two processes have on the X-ray outburst light-curves of LMXBs.

While there exist alternative methods, not limited by the complexity of light-curve morphology or tied directly to these simplifying assumptions (e.g., modelling the evolution of the observed UVOIR spectral energy distribution (SED) throughout outburst; see Chapter 5), a basic test of the validity of the theoretical predictions of DIM for LMXBs can be done by simply using source position in the $\dot{M} - P_{\mathrm{orb}}$ Plane (van Paradijs, 1996; Coriat et al., 2012). One of the key predictions of the IDIM is that there exists a critical mass-transfer rate, dependent on the size of the accretion disc in the system, dividing transient and persistently accreting systems into different regions of the parameter space.

According to the DIM, outbursts in transient systems are a result of the accretion disc cycling between a hot, ionized state and a cool, neutral state. The division between transient and persistent sources, predicted to occur in the $\dot{M}_{\mathrm{BH}} - P_{\mathrm{orb}}$ plane, is based on the condition of whether the discs are stable or unstable (Dubus et al., 1999).

An annulus R within the disc can remain in the hot state if the local accretion rate $\dot{M}(R)$ is greater then the critical accretion rate of the hot state $\dot{M_{\mathrm{crit}}}(R)$, which itself increases with radius. Thus, the condition required for the entire disc to remain in a stable hot equilibrium (i.e., a persistently accreting X-ray binary), is fulfilled when the mass-transfer rate from the companion star ($\dot{M_2}$) is larger than the critical mass-transfer rate in the outer disc, $\dot{M_{\mathrm{crit}}}(R_{\mathrm{out}})$. Alternatively, if $\dot{M_2} < \dot{M_{\mathrm{crit}}}(R_{\mathrm{out}})$, the disc will undergo outbursts, and thus, be transient. In our analyses here, we assume that there is no mass lost by the disc.

The critical accretion rate for an irradiated disc in a BH-LMXB is given by

(Lasota et al., 2008),

$$\dot{M}_{\rm crit} = 9.5 \times 10^{14} C_{\rm irr,3}^{-0.36} \alpha_{0.1}^{0.04+0.01\log C_{\rm irr,3}} R_{\rm disc,10}^{2.39-0.10\log C_{\rm irr,3}} M_1^{-0.64+0.08\log C_{\rm irr,3}} \ {\rm g/s}, \tag{2.4}$$

where M_1 is the BH mass in $M_\odot$, $R_{\rm disc,10}$ is the disc radius in units of 10^{10} cm, $\alpha_{0.1} = \alpha/0.1$ is the α-viscosity (a term parametrizing angular-momentum transport in the disc; see Chapter 3), and $C_{\rm irr,3} = C_{\rm irr}/10^{-3}$ is the irradiation constant[8] (a parameter used to describe the fraction of the central X-ray luminosity that is intercepted and reprocessed by the disc; see Chapter 4).

In Figure 2.7 we plot this critical accretion rate for an irradiated disc, parametrized with four different choices of $C_{\rm irr}$, around a $5-15M_\odot$ BH on the $\dot{M}-P_{\rm orb}$ plane. Using the Bayesian methodology I developed, allows derivation of the α-viscosity parameters directly from "well-behaved" X-ray outburst light-curves. Applying this methodology to the BH-LMXB population yields a range of $\alpha \sim 0.2-1$. However, whether our derived α-viscosity parameters are intrinsic to, or the result of strong mass-outflows from, these discs remains unclear (see Chapter 3 for details). Given the weak dependence of $\dot{M}_{\rm crit}$ on α-viscosity, we choose to set $\alpha = 0.2$ for this purpose and note that choosing $\alpha = 1$ has little effect on $\dot{M}_{\rm crit}$.

For this calculation, we assume the accretion disc radius $R_{\rm disc}$ is approximately 70% of the Roche-lobe equivalent radius (Menou et al., 1999), which itself can be written in terms of M_1, binary mass ratio q, and $P_{\rm orb}$ (Frank et al., 2002). We take $q = 0.1$, typical of BH-LMXBs in the Galaxy (Tetarenko et al., 2016).

Lastly, using the Bayesian methodology I developed, also allows derivation of the $C_{\rm irr}$ parameter directly from "well-behaved" X-ray outburst light-curves (See Chapter 4). Accordingly, we have chosen four different values of $C_{\rm irr} = 1 \times 10^{-3}$, $C_{\rm irr} = 5 \times 10^{-3}$, $C_{\rm irr} = 3 \times 10^{-2}$, and $C_{\rm irr} = 3 \times 10^{-1}$ to compute $\dot{M}_{\rm crit}$. These values correspond to the: (i) lowest $C_{\rm irr}$ we derive when applying my Bayesian methodology to BH-LMXB light-curves; (ii) the standard value assumed in theoretical work (Vrtilek et al., 1990; de Jong et al., 1996); and (iii) two values of $C_{\rm irr}$ considered to be very high, but still physically possible, respectively. See Chapter 4 for a thorough discussion on

---

[8] Note $C_{\rm irr}$ is not related to $C_{\rm soft}$ and $C_{\rm hard}$, used earlier to quantify accretion state.

the value $C_{\rm irr}$ takes in BH-LMXB discs.

From Figure 2.7, we can see that our representative sample of BH-LMXBs is in good agreement with the theoretical expectations of the IDIM, with one exception, SwiftJ1753.5-0127. See Chapter 5 for a detailed case study of the irradiated disc in this LMXB source and a thorough discussion on its position in the $\dot{M}_{\rm BH} - P_{\rm orb}$ plane.

Analyzing Figure 2.7, we also observe the appearance of numerous outliers and a great deal of scatter in the data, implying that the mass-transfer rates presented here may in fact be systematically under-estimating the true mass-transfer from the companion. Generally, theory predicts a correlation, where a larger $P_{\rm orb}$ should correspond to a larger $\dot{M}_{\rm BH}$ (Podsiadlowski et al., 2002). This expectation is based on the predictions of angular-momentum loss mechanisms, magnetic braking for relatively short-orbit systems (Verbunt & Zwaan, 1981), and nuclear evolution timescales for longer-orbit systems (Webbink et al., 1983). See King (1988) and King et al. (1996) for a review on the mechanisms driving mass-transfer in these binary systems.

We consider, in more detail, two possibilities to explain the scatter in the transient BH-LMXB sample. First, the scatter could imply a change in efficiency between the two regimes (e.g., more advection of energy during the hard state). However, given that (i) models that suggest this (e.g., ADAFs; Narayan & Yi 1994) show that the brightest hard states have only a minor reduction in luminosity due to advection ($\dot{M}_{\rm BH} \propto \eta$) and (ii) there is an observed absence of a clear luminosity change during spectral transitions in these types of systems (e.g., Maccarone 2005), the difference in accretion efficiencies between the hard and soft states (at the transition luminosity) is most likely minimal, ruling out the idea that radiative efficiency changes between the soft and hard states could effectively alter the observed mass-transfer rates.

Second, the scatter may also be a result of significant mass (and energy) loss via outflows present in BH-LMXB systems. Thus, we start by considering how significant a role the compact, steady jet could play during outburst. While some material will of course leave in the jet, the amount of material lost to this outflow is most likely not as much as has been found for accretion disc winds (see below). However, the jet may transport energy more effectively than mass.

It is thought that at lower Eddington luminosities a larger fraction of the energy released from the accreted material goes into the kinetic (and magnetic) energy of the jet rather than being radiated away (e.g., Fender et al. 2003), effectively resulting in a smaller contribution to accretion luminosity (and hence a lower $\dot{M}_{\rm BH}$) than would be the case if the jet was not present. Given that the jet is an outflow known to arise in the hard state (a regime associated with lower Eddington luminosities) and the jet is not seen in the soft state (Fender et al., 2004), the jet could be a possible means of explaining an underestimated mass-transfer rate in sources which exclusively undergo "failed" outbursts.

Next, we consider another type of outflow observed during outbursts of BH-LMXBs, an accretion disc wind. Originally predicted by the early works on accretion disc theory (Shakura & Sunyaev, 1973), the presence of winds from the outer accretion disc have been observed (mostly) in the soft/intermediate accretion states, and in a few cases at high flux levels ($> 10\%$ Eddington) in the hard accretion state, across the Galactic BH-LMXB population (Neilsen & Lee, 2009; Miller et al., 2006; Ponti et al., 2012; Neilsen, 2013b). For a recent review on accretion disc winds see Neilsen (2013a).

Accretion disc winds are thought to remove significant amounts of mass from the disc during outburst. Ponti et al. (2012) have estimated the wind outflow rate, in the majority of the sources in which a wind has been detected, to be at least twice the $\dot{M}$ onto the BH. In addition, a few exceptional cases at high Eddington ratio (e.g., the "heartbeat" states of GRS 1915+105 and IGR J17091−3624; Neilsen & Lee 2009 and King et al. 2012), show mass loss rates in excess of 10–20 $\dot{M}$ onto the BH.

Given that my recent study of the angular-momentum (and mass) transport process at work in BH-LMXBs (see Chapter 3) finds indirect evidence for the existence of accretion disc winds across all accretion states, and thus a wide range of luminosity regimes, it is plausible that an LMXB system may be losing a large fraction of the mass passing through its outer disc, and thus have an actual mass-transfer rate from its donor that is larger than our results here imply.

2.3.2 The $L_{\text{peak}} - P_{\text{orb}}$ Correlation in BH-LMXBs

A positive correlation between orbital period (P_{orb}) and peak outburst luminosity (L_{peak}) for LMXBs has been established in previous studies. (e.g., Shahbaz et al., 1998; Portegies Zwart et al., 2004; Wu et al., 2010).

Thus, we have analyzed the relationship between L_{peak} and P_{orb} for the Galactic BH-LMXB population (see Figure 2.8). To do so, we make use of WATCHDOG's spectral fitting tool, to derive peak bolometric luminosity of the outbursts in 17 transient BH-LMXB sources from the WATCHDOG catalogue that have a known P_{orb} and sufficient data available during WATCHDOG's observational time period (1996 January 6 – 2015 May 14).

We fit the data with a linear relation, to determine whether we observe the previously found positive correlation between L_{peak} and P_{orb} in our outburst sample. We perform a linear fit in log-space to the entire sample with a Bayesian MCMC algorithm. In doing so, we are able to estimate the slope (m) and intercept (b) for the correlation.

Initialization of m and b is accomplished by starting the "walkers" in a tight ball around the "best guess" found from a least-squares fit to the data (implemented using the `lmfit` PYTHON package). This is then followed by a 500 step "burn-in" phase. After likelihood maximization is performed, PDFs of m and b are obtained directly from the MCMC algorithm. The median and 1σ confidence intervals of the resulting distributions are taken to be the best-fit value of each parameter.

For the entire outburst sample, we find a best fit:

$$\log(L_{\text{peak}}/L_{\text{edd}}) = (0.16^{+0.03}_{-0.02})\log(P_{\text{orb}}) + (-1.13^{+0.07}_{-0.08}), \tag{2.5}$$

with a slope significantly smaller then the Wu et al. (2010) result. In addition, we have also performed a non-parametric (Kendall-Tau) test to determine whether there is statistical evidence for a positive correlation between P_{orb} and L_{peak} in our entire BH-LMXB outburst sample. To account for the uncertainty in L_{peak}, we have performed Monte-Carlo simulations in logarithmic space assuming a normal distribution and the errors the WATCHDOG spectral fitting tool measured for each outburst. For the entire outburst sample, we find a median Kendall-Tau correlation of $\tau = 0.03$ with an 80% chance that τ is consistent with 0. This tells us that, unlike previous studies, our outburst data shows no definitive evidence for a positive correlation existing between $L_{\rm peak}$ and $P_{\rm orb}$ in BH-LMXBs.

We have considered possible reasons for the large amount of scatter observed in our BH-LMXB outburst sample and whether the lack of statistical evidence for a correlation between $L_{\rm peak}$ and $P_{\rm orb}$ that we found is a result of this scatter.

Given (i) that outbursts from transient BH-LMXBs are far from phenomenologically identical (see Chen et al. 1997, Wu et al. 2010, this Chapter, Chapters 3 and 4), (ii) the fact that we have observed a stronger (then previously thought) prevalence towards BH-LMXBs undergoing under-luminous "failed" outbursts (see Section 2.2), and (iii) that it has been suggested that sources in the short-period regime ($P_{\rm orb} < 5$ hrs) may be more prone to "failed" outbursts than the longer-period systems (as there low $L_{\rm peak}$ drops near the limit for radiatively inefficient accretion, potentially causing them to remain in the low-luminosity hard state; Meyer-Hofmeister 2004; Maccarone & Patruno 2013; Knevitt et al. 2014), the question becomes whether or not "failed" outbursts have statistically different $L_{\rm peak}$ when compared to typical "canonical" outbursts (and thus are acting as outliers in our dataset).

From Figure 2.8, we observe that "failed" outbursts tend to have significantly lower (sub-Eddington) $L_{\rm peak}$ when compared to "canonical" outbursts from systems at the same $P_{\rm orb}$. This observation is expected as it is the inevitable result of these systems never reaching the high luminosity soft state associated with radiatively efficient accretion.

The one exception in our sample is GS 1354−64. In this particular case, the higher than expected $L_{\rm peak}$ is likely due to uncertainty in the poorly constrained distance estimate for this source ($25 - 61$ kpc). If we were to place GS 1354−64 at our assumed standard Galactic value (i.e., a uniform distribution between 2 and 8 kpc), $L_{\rm bol,peak} < 0.1\,L_{\rm edd}$, on par with the behavior we see from the other "failed" outbursts in our sample.

Performing a two sample KS-test, comparing $L_{\rm peak}$ for "failed" and "canonical" outbursts in the entire outburst sample, yields a p-value of 0.01. This provides clear statistical evidence that the $L_{\rm peak}$ of “failed” and “canonical” outbursts do not arise from the same parent distribution.

From a theoretical perspective, we expect any relation between $L_{\rm peak}$ and $P_{\rm orb}$ to break down for low-luminosity (i.e., a regime associated with “failed” outbursts) sources, as in these outbursts it is more likely that a much smaller fraction of the accretion disc has been accreted.

Accordingly, we predict that the brightest outburst of each source will tell us the most about the intrinsic properties of the binary itself. Thus, we also analyze the correlation between $L_{\rm peak}$ and $P_{\rm orb}$ for a sample including only the brightest outburst detected in each of these 17 sources. Repeating our fitting analysis, including only the brightest outburst of each source, we find a best fit:

$$\log(L_{\rm peak}/L_{\rm edd}) = (0.65^{+0.04}_{-0.19})\log(P_{\rm orb}) + (-1.02^{+0.09}_{-0.17}), \tag{2.6}$$

completely consistent with the Wu et al. (2010) result. Performing a non-parametric (Kendall-Tau) test, again including only the brightest outburst of each source, we find a median Kendall-Tau correlation of $\tau = 0.30$ with only a 15% chance that τ is consistent with 0. This is suggestive of a positive correlation between $L_{\rm peak}$ and $P_{\rm orb}$ (as has been found in previous studies of LMXBs) existing in this BH-LMXB outburst data.

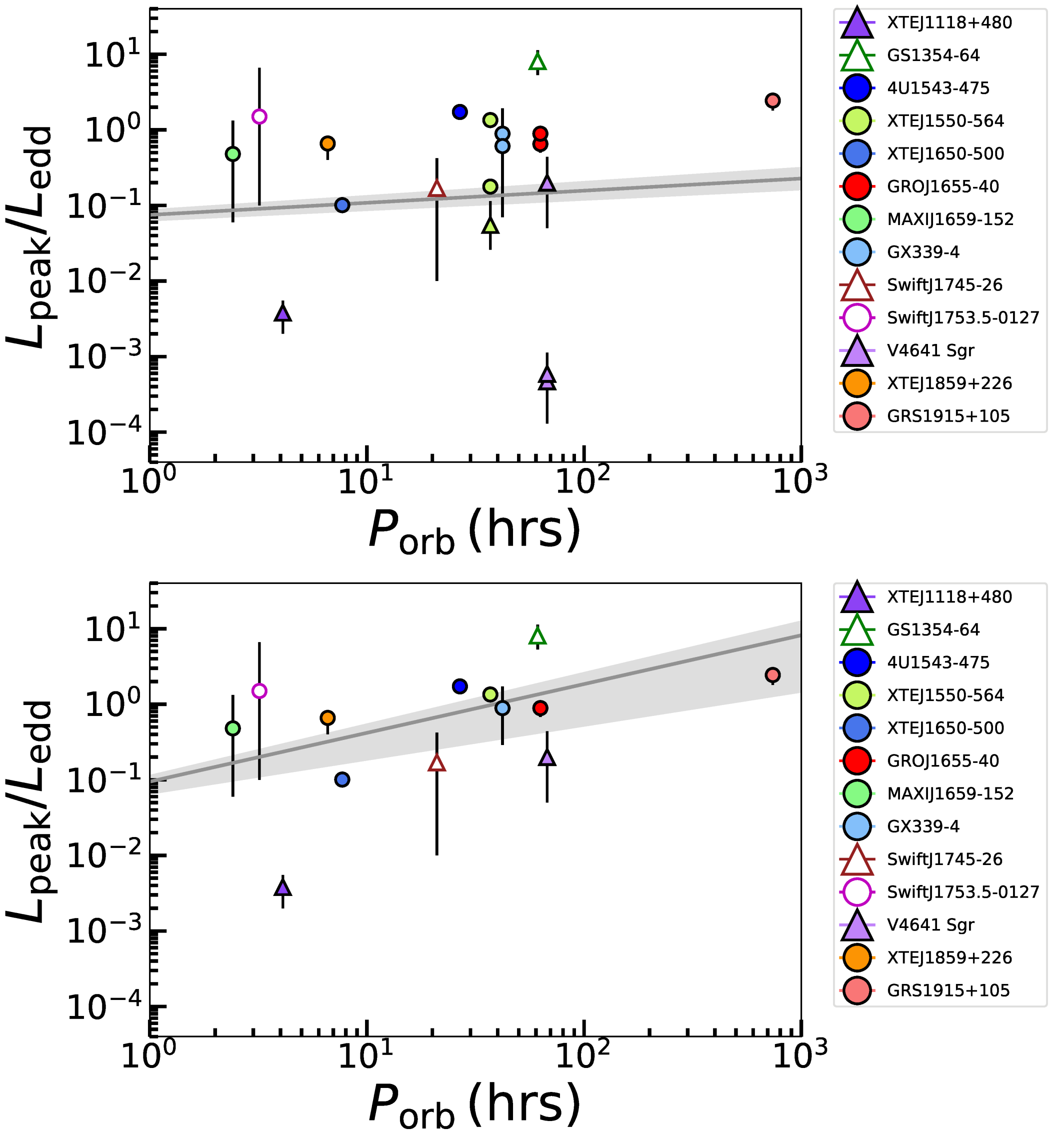

Figure 2.8: Peak bolometric outburst luminosity in Eddington units ($L_{\text{peak}}/L_{\text{edd}}$) vs. orbital period ($P_{\text{orb}}$) for the (top) entire Galactic BH-LMXB source sample and (bottom) brightest outburst of each source. Colours represent individual sources (see legend). Shapes denote outburst behavior: "failed" (triangles) or "canonical" (circles). Filled and open shapes represent sources with and without reliable distance estimates, respectively. Errors on luminosity represent the 1σ confidence level. The solid grey line and shaded region shows the best-fit, and 1σ confidence interval, for the linear function found by the MCMC algorithm.

Chapter 3

Quantifying the Mass Transport Process in X-ray Irradiated Accretion Discs of BH-LMXBs

Tetarenko, B.E., Lasota, J.-P., Heinke, C.O., Dubus, G., and Sivakoff, G.R.

Nature, 554, 69-72 (2018)

ABSTRACT

Recurring outbursts associated with matter flowing onto compact stellar remnants (black holes, neutron stars, white dwarfs) in close binary systems, provide strong test beds for constraining the poorly understood accretion process. The efficiency of angular-momentum (and thus mass) transport in accretion discs, which has traditionally been encoded in the α-viscosity parameter, shapes the light-curves of these outbursts. Numerical simulations of the magneto-rotational instability that is believed to be the physical mechanism behind this transport find values of $\alpha \sim 0.1-0.2$ (Hirose et al., 2014; Coleman et al., 2016; Scepi et al., 2017), as required from observations of accreting white dwarfs (Kotko & Lasota, 2012). Equivalent α-viscosity parameters have never been estimated in discs around neutron stars or black holes. Here we report the results of an analysis of archival X-ray light-curves of twenty-one black hole low-mass X-ray binary outbursts. Applying a Bayesian approach for a model of accretion allows us to determine corresponding α-viscosity parameters, directly from the light-curves, to be $\alpha \sim 0.2 - 1$. This result may be interpreted either as a strong intrinsic rate of angular-momentum transport in the disc, which can only be sustained by the magneto-rotational instability if a large-scale magnetic field threads the disc (Lesur et al., 2013; Bai & Stone, 2013; Salvesen et al., 2016), or as a direct indication that mass is being lost from the disc through substantial

mass outflows strongly shaping the X-ray binary outburst. Furthermore, the lack of correlation between our estimates of α-viscosity and accretion state implies that such outflows can remove a significant fraction of disc mass in all black hole X-ray binary accretion states, favouring magnetically-driven winds over thermally-driven winds that require specific radiative conditions (Higginbottom & Proga, 2015).

3.1 Introduction

The disc-instability model or DIM (Osaki, 1974; Meyer & Meyer-Hofmeister, 1981; Smak, 1984; Faulkner et al., 1983) was developed to explain outbursts in compact binaries where a white dwarf accretes from a low-mass companion. A cool (neutral) quiescent disc is built up through steady mass transfer from the companion star, causing the disc temperature to rise. Eventually at some radius (called the ignition radius) the disc temperature will reach the temperature where hydrogen ionizes. This triggers a thermal-viscous instability within the disc due to the steep temperature dependence of opacity in this temperature range. As a result, the disc will cycle between a hot, ionized, outburst state and a cold, neutral, quiescent state. The growth of the thermal-viscous instability at the ignition radius results in two heating fronts propagating inwards and outwards through the disc. This brings the disc into a hot state causing rapid in-fall of matter onto the compact object, and a bright optical and UV outburst.

As the disc is depleted over time (because mass falls onto the compact stellar remnant at a higher rate than it is being transferred from the companion star), the temperature and mass accretion rate in the outer radii will eventually be reduced to the point where hydrogen can recombine. This triggers the formation and propagation of a cooling front that returns the disc to its quiescent (neutral) state. While this predicted behaviour, characterized by alternating periods of disc-outbursts and quiescence, matches observations of accreting white dwarfs well, changes are needed for close binaries containing more compact stellar remnants (neutron stars and stellar-mass black holes) called low-mass X-ray binaries.

There are 18 confirmed black hole low-mass X-ray binaries (BH-LMXBs) in our Galaxy, identified through bright X-ray outbursts indicating rapid accretion episodes

(Tetarenko et al., 2016). These outbursts (Tetarenko et al., 2016) last considerably longer, and recur significantly less frequently, than in many types of accreting white dwarfs, due to heating of the outer disc by X-rays emitted in the inner regions of the accretion flow (van Paradijs, 1996).

X-ray irradiation will keep the accretion disc in its hot (ionized) state over the viscous timescale. This timescale, which is encoded in observed outburst light-curves, is directly related to the efficiency of angular-momentum transport, and thus, provides a means to measure this efficiency. See Section 3.2 and Figure 3.1 for a detailed discussion of the characteristic three-stage outburst decay profile present in a BH-LMXB light-curve.

The magneto-rotational instability (MRI) is thought to provide the physical mechanism behind angular-momentum (and mass) transport in accretion discs (Balbus & Hawley, 1998). The effective viscosity in these discs, commonly parametrized using the α-viscosity prescription (Shakura & Sunyaev, 1973), encapsulates the efficiency of this transport process. Physically, the α-viscosity parameter sets the viscous time of the accretion flow through the disc, and thus, according to the DIM, is encoded within the decay profile of an outburst light-curve. A disc with higher viscosity (higher α) in outburst will accrete mass more quickly, resulting in shorter decay times and shorter outburst durations (Dubus et al., 2001).

The α-viscosity has only ever been inferred in (non-irradiated) discs around accreting white dwarfs by comparing the outburst timescales from observed light-curves to synthetic model light-curves created by numerical disc codes for different α-viscosity inputs (Kotko & Lasota, 2012). α-viscosity parameters have never before been measured in irradiated accretion discs, such as those around stellar-mass BHs in LMXBs. The assertion (King et al., 2007) that $\alpha \simeq 0.2$–0.4 in such systems, was deduced from the calculations (Dubus et al., 2001) of “detailed models of complete light-curves”, but not from detailed comparison of models with observations. Note that we learned of the recent study of BH-LMXB 4U1543-475 (Lipunova & Malanchev, 2017) after acceptance of this manuscript.

Accordingly, we have built a novel Bayesian approach that characterizes the angular-momentum (and mass) transport occurring in the discs in LMXB systems.

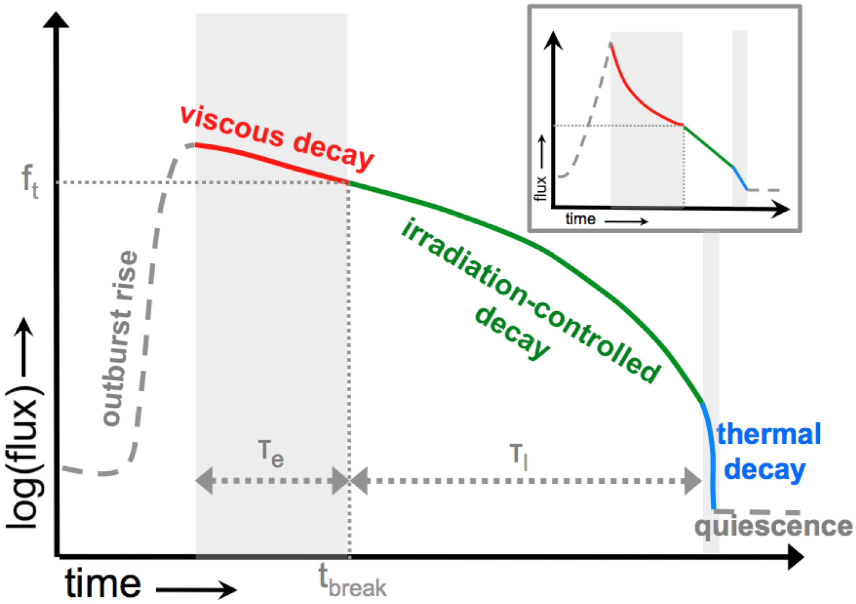

Figure 3.1: Schematic light-curve for an outburst of a LMXB system. The profile shown corresponds to the light-curve predicted by the DIM+irradiation (IDIM) picture for an outbursting irradiated disc. τ_e and τ_l represent the timescales of the exponential (viscous) and linear (irradiation-controlled) decay stages in the light-curve, respectively. The time (and flux) at which the transition between the viscous and exponential stages of the decay occurs (marking the point at which the temperature in the outer disc radii drops below the ionization temperature of hydrogen), are represented by t_{break} and f_t, respectively. The inset shows a representation of the light-curve profile on a linear scale.

The α-viscosity parameter in a hot, outbursting disc (α_h) sets the timescale on which matter moves through the hot (ionized) portion of the disc, and thus, controls the duration of the first stage of the decay profile observed in an X-ray light-curve (see Section 3.2 for details). This (viscous) timescale will vary depending upon the mass of the compact object and the size of the accretion disc, where the size of the disc itself is governed by the ratio of component masses in the system and the binary orbital period.

To reconcile the multi-level, interconnected relationships existing between these parameters defining the properties of the accretion flow, we use a powerful statistical data analysis technique referred to as Bayesian hierarchical modelling. This allows us to derive: (i) timescales associated with individual stages of the outburst decay, (ii) the rate of mass-accretion through the disc during, and the time of occurrence of, the transitions between the individual decay stages.

Ultimately, this Bayesian technique allows us to effectively take into account our prior knowledge of the orbital parameters that define a LMXB system (BH mass, companion mass, and orbital period), to sample the α-viscosity parameter in a hot, outbursting disc (α_h) directly from its observed X-ray light-curve. For details of this Bayesian methodology, see Section 3.2.

3.2 Methods

3.2.1 Archival X-ray Data Collection and Reduction

We have collected all outburst data available since 1996, for each of the 12 systems in our source sample, from the (i) Proportional Counter Array (PCA) aboard the Rossi X-ray Timing Explorer (RXTE), (ii) X-ray Telescope (XRT) aboard the Swift Observatory, (iii) Gas-Slit Camera (GSC) aboard the Monitor of All-sky Image (MAXI) Telescope, (iv) Advanced CCD Imaging Spectrometer (ACIS-S) and High Resolution Camera (HRC-S) aboard the Chandra X-ray Observatory, and (v) European Photon Imaging Camera (EPIC) aboard XMM-Newton.

All X-ray light-curve data from *RXTE*/PCA were collected from the WATCH-

DOG project (see Chapter 2; Tetarenko et al. 2016). These authors compiled all available good pointed PCA observations (i.e., no scans or slews) from the HEASARC archive, for 77 BH X-ray binary sources in the Galaxy, over the entire 16-year *RXTE* mission. For each individual source in our sample, we use scripts from the WATCHDOG project, involving the *rex* script within the Heasoft Software Package[1], to reduce and extract (mission-long) daily time-binned, background-subtracted light-curves in the 2–10 keV band, from the PCA Std2 data available on that source in the WATCHDOG database.

We have also compiled all available *MAXI*/GSC data using the WATCHDOG project's online light-curve tool[2] (see Chapter 2; Tetarenko et al. 2016). This tool compiles all the publicly available data from the *MAXI* archive[3] in three standard bands ($2-4$, $4-10$, $10-20$ keV), and runs it through the WATCHDOG processing pipeline (Tetarenko et al., 2016). Using this tool, we have extracted (mission-long) daily time-binned, background-subtracted light-curves in the 2–10 keV band, for each individual source (where available).

In addition, we use the *Swift*/XRT online product builder[4] (Evans et al., 2009) to compile (mission-long) daily time-binned, background-subtracted light-curves in the 2–10 keV band, using all available windowed timing and photon counting mode XRT pointed observations. Lastly, we have collected all available *Chandra*/ACIS-S, *Chandra*/HRC-S, and *XMM-Newton*/EPIC pointed observations from the literature for individual outbursts, where available. We then convert individual count-rates to fluxes in the 2–10 keV band using PIMMS v4.8c[5] and the spectral information available in the literature.

3.2.2 Conversion from Count-rate to Bolometric Flux

We use millicrabs as a baseline unit of flux to calculate approximate count rate equivalences in the 2–10 keV band data from *RXTE*/PCA, *Swift*/XRT, and *MAXI*/GSC.

---

[1] http://heasarc.nasa.gov/lheasoft/

[2] http://astro.physics.ualberta.ca/WATCHDOG/download_data

[3] http://maxi.riken.jp/top/

[4] http://www.swift.ac.uk/user_objects/index.php

[5] http://cxc.harvard.edu/toolkit/pimms.jsp

Integration of the now accepted "canonical" simple power-law spectrum of the Crab Nebula (Toor & Seward, 1974), over the 2–10 keV band, gives us a straightforward method for converting between count rate and flux in this band.

Assuming that a source spectrum is Crab-like in nature will cause uncertainty in the computed source flux. However, as it has been found that assuming a Crab-like spectral shape in narrow X-ray energy bands (such as the 2–10 keV band we make use of here), will produce no more than a 20% (and typically $< 10\%$) error in the source flux for a flat power-law versus a blackbody (Tetarenko et al., 2016), this approach is justified.

To convert flux in the 2–10 keV band to bolometric flux, we make use of the following bolometric corrections (BCs), estimated for each individual accretion state (Migliari & Fender, 2006) occurring during outbursts of black hole low-mass X-ray binaries; $BC = 5$ (hard state) and $BC = 1.25$ (soft & intermediate states). By combining the above discussed bolometric corrections with the daily accretion state information, obtained from the WATCHDOG project (Tetarenko et al., 2016) online Accretion-State-By-Day tool[6] (see Chapter 2; Tetarenko et al. 2016), for each outburst, we are able to compute daily time-binned bolometric light-curves.

3.2.3 Markov-Chain Monte Carlo (MCMC) Fitting Algorithm

We make use of a Bayesian approach to estimate the five parameters that describe the shape of an observed light-curve decay profile: the (i) exponential (viscous) decay timescale (τ_e), (ii) linear (irradiation-controlled) decay timescale (τ_l), (iii) X-ray flux of the system at the transition between exponential and linear decay stages (f_t), (iv) time after the outburst peak when the transition between exponential and linear decay stages occurs ($t_{\rm break}$), and (v) X-ray flux limit of the exponential decay stage (f_2) (see Figure 3.1). Using the `emcee` PYTHON package (Foreman-Mackey et al., 2013), an implementation of Goodman & Weare's Affine Invariant MCMC Ensemble Sampler (Goodman & Weare, 2010), we apply a MCMC algorithm to simultaneously

---

[6] http://astro.physics.ualberta.ca/WATCHDOG

fit the exponential (viscous) and linear (irradiation-controlled) stages of each decay (as described in the main text and Figure 3.1) where applicable.

Before fitting occurs, secondary maxima and other rebrightening events (King & Ritter, 1998; Menou et al., 2000; Dubus et al., 2001) contaminating the decays are removed by hand. These data are not included in the fits; analysis of these rebrightening events will be presented in a later paper. The removal of these rebrightening events has no effect on the determination of α-viscosity from the X-ray light-curves. The remaining data is then fit in logarithmic (bolometric) flux space with our five-parameter analytical model (for details see below).

The `emcee` PYTHON package runs a modified version of the Metropolis-Hastings Algorithm, in which an ensemble of "walkers" simultaneously move through and explore the parameter space. To fit each light-curve, we make use of 50 "walkers", 10 times our model dimensions. For the `emcee` to run optimally, we first appropriately set the initial positions of our ensemble of "walkers" in the parameter space. To do so, we make use of `pyHarmonySearch` (Geem et al., 2001), an implementation of the harmony search global optimization algorithm, to perform an initial survey of our parameter space. `pyHarmonySearch` essentially acts as a less time-consuming version of a brute force grid search method, allowing us to place our ensemble of "walkers" in a tight ball around the best guess it finds. This "best guess" provides a starting point for the MCMC algorithm.

Prior distributions for each of the five parameters are also set from the results of the `pyHarmonySearch` of the parameter space. In the case of a well-sampled light-curve (i.e., near-continuous daily data throughout the outburst), a Gaussian prior for each parameter with a mean set by the results of the `pyHarmonySearch` is used. In the case where only scattered data is available on only a portion of the full decay, wide flat priors (based on expectations from other outbursts of the same source, or outbursts from sources with similar orbital periods) are used for each parameter.

After initialization, we begin running the MCMC on each light-curve with a 500 step "burn-in" phase. Here the ensemble of "walkers" are evolved over a series of steps, with the sole purpose of making sure that the initial configuration we have set allows the "walkers" to sufficiently explore the parameter space. At the end of the “burn-in” phase, if the initial configuration is appropriate for the problem, the “walkers” will have ended up in a high probability region, a place in the parameter space where the states of the Markov-chain are more representative of the distribution being sampled. After this phase, the MCMC is restarted, with the “walkers” starting at the final position they acquired during the “burn-in” phase, and run until convergence. The number of steps required for convergence is dependent upon the amount of data available and the complexity of the outburst decay profile.

After likelihood maximization is performed, the MCMC algorithm will output the converged solution in the form of posterior distributions of each parameter. We take the best fit result (i.e., the best-fit value along with the upper and lower limits on this value) as the median and 1σ (68%) confidence interval of each posterior distribution, respectively.

3.2.4 The Analytical Outburst Decay Model

Figure 3.1 shows the predicted characteristic three-stage decay profile shape present in a BH-LMXB light-curve (King & Ritter, 1998; Dubus et al., 1999, 2001).

In the first stage (viscous decay), X-ray irradiation keeps the whole disc in a hot (ionized) state, preventing the formation of a cooling front. As more mass is accreted onto the BH than is transferred from the companion at this time, the disc is drained by viscous accretion of matter only, resulting in an exponential-shaped decay profile on the viscous timescale. Eventually, as the mass in the disc, and mass-transfer rate, decreases, the dimming X-ray irradiation can no longer keep the outer regions of the disc in the hot (ionized) state and a cooling front forms, behind which the cold matter drastically slows its inward flow. At this point, the system enters the second stage (irradiation-controlled decay), during which the propagation of the cooling front is controlled by the decay of the irradiating X-ray flux. The hot (ionized) portion of the disc continues to flow and accrete but gradually shrinks in size, causing a linear-shaped decay profile. Eventually, the mass-accretion rate onto the BH becomes small enough that X-ray irradiation no longer plays a role. In this third and final stage (thermal decay), the cooling front propagates inward freely on a thermal-viscous timescale, resulting in a steeper linear decay in the light-curve down to the quiescent accretion level.

The analytical model we use to describe the outburst decay profiles, predicted by the (irradiated) DIM picture, in BH-LMXB light-curves is rooted in the "classic" King & Ritter (1998) formalism. This formalism combines knowledge of the peak X-ray flux and outer radius of the irradiated disc to predict the shape that the decay of an X-ray light-curve of a transient LMXB system would follow.

The temperature of most of the accretion disc in transient LMXBs during outburst is dominated by X-ray heating from the inner accretion region. The X-ray light-curve will show an exponential decline if irradiation by the central X-ray source is able to ionize the entire disc, keeping it in the hot (ionized) state and preventing the formation of the cooling front (Lasota, 2001). The X-ray light-curve will show a linear decline if irradiation by the central X-ray source is only able to keep a portion of the entire disc in the hot (ionized) state. Then, the central X-ray flux can no longer keep the outer regions of the disc above the hydrogen ionization temperature ($\sim 10^4$ K), and a cooling front will appear and propagate down the disc. As the cooling front cannot move inward on a viscous timescale (i.e., the farthest it can move inward is set by the radius at which $T = 10^4$ K), a linear shaped decline is observed in the light-curve.

By assuming, like many studies of X-ray irradiated discs in close binary systems, an isothermal disc model (i.e., the disc is assumed to be vertically isothermal because it is irradiated, where the central mid-plane temperature is equal to the effective temperature set by the X-ray irradiation flux at the disc surface; de Jong et al. 1996), King & Ritter were able to derive the critical X-ray luminosity for a given disc radius R_{11} (in units of 10^{11} cm),

$$L_{\rm crit}({\rm BH}) = 1.7 \times 10^{37}\, R_{11}^2\, {\rm erg\, s^{-1}}, \tag{3.1}$$

above which the light-curve should display an exponential decay shape, and below which the light-curve should display a linear decay shape.

In this formalism, a well sampled light-curve (in both time and amplitude) should show a combination of exponential and linear shaped stages in the decay profile. The exponential decay is replaced with a linear decay when the X-ray flux has decreased sufficiently, resulting in a distinct brink (e.g., a break in slope) in the light-curve shape. By deriving analytical expressions for the shape that light-curve decays of transient LMXB systems take, King & Ritter predicted the timescales of the exponential and linear stages of a decay, the peak mass-accretion rate (and in-turn X-ray luminosity for a given accretion efficiency), and the time at which the exponential decay was replaced by the linear decay.

This approach has since been supported by smooth-particle-hydrodynamics accretion simulations (Truss et al., 2002) and applied to observations of various classes of X-ray binaries (Shahbaz et al., 1998; Powell et al., 2007; Heinke et al., 2015; Campana et al., 2013; Simon et al., 2006; Torres et al., 2008) with varied success. However, while the King & Ritter formalism has, rather coincidentally, been found to agree relatively well with observations, it oversimplifies the physics of the X-ray-irradiated discs to which it is applied (Lasota, 2001). Thus, instead, we make use of a modified version of the King & Ritter formalism.

In this modified version we (i) include the effects of continuing mass-transfer from the donor star (Powell et al., 2007; Heinke et al., 2015), and (ii) use the disc structure established by Dubus et al. (1999,2000), where X-ray irradiation affecting BH-LMXB discs is modelled using a general irradiation law,

$$T_{\mathrm{irr}}^4 = \frac{C_{\mathrm{irr}} L_X}{4\pi\sigma R^2}. \tag{3.2}$$

Here, the irradiation parameter C_{irr} is defined as the fraction of the central X-ray luminosity ($L_X = \eta c^2 \dot{M}_c$ for accretion efficiency η) that heats up the disc. As C_{irr} contains information on the illumination and disc geometry, and the temperature profile of the X-ray irradiation, it effectively parameterizes our ignorance of how these discs are actually irradiated. Physically, C_{irr} controls the timescale of the linear decay stage (and the overall outburst duration), when the transition between decay stages occur, and sets a limit on the amount of mass that can be accreted during the outburst. Stronger irradiation (larger C_{irr}) increases the duration of the outburst and thus, the relative amount of matter able to be accreted during an outburst. Consequently, if more matter is accreted during outburst, the following time in quiescence will lengthen, as the disc will require more time to build up again.

Following the procedure outlined in previous work (Powell et al., 2007; Heinke et al., 2015), and instead making use of the general irradiation law defined above, yields the following analytical form for the flux of a BH-LMXB as a function of time during the exponential (viscous),

$$f_X = (f_t - f_2) \exp\left(\frac{-(t - t_{\text{break}})}{\tau_e} \right) + f_2, \tag{3.3}$$

and linear (irradiation-controlled),

$$f_X = f_t \left(1 - \frac{(t - t_{\text{break}})}{\tau_l} \right), \tag{3.4}$$

stages of the decay. Here τ_e and τ_l are defined as the viscous (exponential) decay timescale in the hot (ionized) zone of the disc and the linear decay timescale, respectively. $f_2 = \eta c^2(-\dot{M}_2)/4\pi d^2$, is the flux limit of the exponential decay, dependent upon the mass-transfer rate from the companion $(-\dot{M}_2)$ and source distance (d). t_{break} is defined as the time when the temperature of the outer edge of the disc is just sufficient enough to remain in a hot (ionized) state, and f_t is the corresponding X-ray flux of the system at time t_{break}. We perform fits to the flux space, as opposed to the luminosity space, to avoid the correlated errors (due to an uncertain distance) that would arise if we were to fit the latter; the uncertain distance (and other parameters) are incorporated below.

By fitting this model to our sample of observed X-ray light-curves we are able to derive the viscous decay timescales in BH-LMXBs to range between $\sim 50 - 190$ days, consistent with conclusions of previous works (Yan & Yu, 2015). See Table 3.2 for fit results.

3.2.5 The Bayesian Hierarchical Methodology

We quantify angular-momentum (and mass) transport occurring in the irradiated accretion discs present in LMXB systems using the α-viscosity parameter. In the current form of the DIM, the use of this simple α-viscosity parameter results from the inability of current numerical simulations to follow *ab initio* turbulent transport driven by the MRI on viscous timescales in a global model of the accretion disc.

This parameter is encoded within the viscous (exponential) stage of the light-curve decay profile. During this first stage of the decay, irradiation of the disc traps it in a hot (ionized) state that only allows a decay of central mass-accretion rate on a viscous timescale,

$$\tau_e = \frac{R_{\rm disc}^2}{3\nu_{\rm KR}} \tag{3.5}$$

where $\nu_{\rm KR}$ is the Shakura-Sunyaev viscosity (Shakura & Sunyaev, 1973), the average value of the kinematic viscosity coefficient near the outer edge of the disc (King & Ritter, 1998), and $R_{\rm disc}$ is the radius of the hot (ionized) zone of the disc. For Keplerian discs, the Shakura-Sunyaev viscosity is related to the dimensionless viscosity parameter in the hot disc α_h by,

$$\nu_{\rm KR} = \alpha_h \frac{c_s^2}{\Omega_k}, \tag{3.6}$$

where Ω_k is the Keplarian angular velocity and c_s is the sound speed in a disc (i.e., $c_s \propto T_c^{0.5}$). Thus, using $\Omega_k = (GM_1/R^3)^{1/2}$, the viscous timescale in the disc can be written as a function of the α-viscosity parameter in the hot disc α_h, compact object mass M_1 and accretion disc radius $R_{\rm disc}$ such that,

$$\left(\frac{\tau_e}{s}\right) = \left(\frac{G^{0.5} m_H M_\odot^{0.5} (10^6)}{3\gamma k_b T_c}\right) \left(\frac{\alpha_h}{0.1}\right)^{-1} \left(\frac{M_1}{M_\odot}\right)^{0.5} \left(\frac{R_{\rm disc}}{10^{10}{\rm cm}}\right)^{0.5}, \tag{3.7}$$

Because the central midplane temperature of the disc (T_c) is only weakly dependent on viscosity and X-ray irradiation in irradiated discs, we can approximate its value as a constant 16300 K (Lasota et al., 2015).

Solving for α_h yields,

$$\left(\frac{\alpha_h}{0.1}\right) = \left(\frac{G^{0.5} m_H M_\odot^{0.5} (10^6)}{3\gamma k_b T_c}\right) \left(\frac{\tau_e}{s}\right)^{-1} \left(\frac{M_1}{M_\odot}\right)^{0.5} \left(\frac{R_{\rm disc}}{10^{10}{\rm cm}}\right)^{0.5}. \tag{3.8}$$

As the α-viscosity parameter in the hot disc (α_h) is dependent on parameters characterizing the outburst decay profile of a LMXB (i.e., observed data), as well as the orbital parameters defining the binary system (i.e., parameters that we have prior knowledge of), namely compact object mass and accretion disc radius (which in itself is dependent on the masses of the compact object and companion star in the system and the orbital period), we require a multi-level Bayesian statistical sampling technique to effectively sample α_h.

Thus, we have built a Bayesian hierarchical model. A Bayesian hierarchical model is a multi-level statistical model that allows one to estimate a posterior distribution of some quantity by integrating a combination of known prior distributions with observed data. In our case, the (i) established binary orbital parameters (M_1, q, and $P_{\rm orb}$) for a system act as the known priors, and (ii) quantitative outburst decay properties derived from fitting the light-curves of a LMXB system with our developed analytical version of the irradiated DIM (τ_e), act as the observed data.

Making use of the `emcee` PYTHON package (Foreman-Mackey et al., 2013) (see above for details), our hierarchical model simultaneously samples α_h for all outbursts of each of the 12 sources in our sample using 240 walkers, 10 times our model dimensions. Of these dimensions, 12 correspond to 6 established BH mass measurements, 4 known binary mass ratios, and 2 observationally-based Galactic statistical population distributions, the Ozel BH mass distribution (Ozel et al., 2010) and distribution of binary mass ratios for the dynamically-confirmed stellar-mass BHs in the Galaxy (Tetarenko et al., 2016). The remaining 12 dimensions correspond to the accretion disc radii for each system.

Initialization is accomplished by placing our ensemble of “walkers” in a tight ball around a “best guess”. This “best guess” corresponds to the best known estimates of the binary parameters (M_1, q, and $P_{\rm orb}$) for each system. If a reliable estimate of BH mass is not known for a system, the mean of the Ozel mass distribution (Ozel et al., 2010) is used. Similarly, if the binary mass ratio is not known for a system, the median of the uniform distribution between the minimum and maximum of the known values of mass ratio for all dynamically confirmed BHs in the Galaxy (Tetarenko et al., 2016) is used.

Our hierarchical model samples accretion disc radii from a uniform distribution between the circularization radius[7] (R_{circ}), and the radius of the compact object's Roche lobe (R_1) in the system, both of which depend only on the BH mass (M_1), binary mass ratio (q) and orbital period (P_{orb}). Initial values of accretion disc radii are set as the median of the uniform distribution between R_{circ} and R_1 for each system, calculated using the "best guess" for BH mass and binary mass ratio (discussed above), and the known orbital period.

The prior distributions for each of the 24 parameters are also set using the "best guess" binary orbital parameters for each system. If there exists a constrained measurement of the parameter (i.e., value with uncertainty), a Gaussian prior based on this measurement and its uncertainty is used. If only a range is quoted in the literature for a parameter, a uniform prior is used. The prior distributions for accretion disc radii are taken as the uniform distribution between R_{circ} and R_1 for each system.

After initialization, we begin running the `emcee` sampler on the observed data (τ_e) with a 500 step "burn in" phase. After this phase, the `emcee` sampler is restarted, with the "walkers" starting at the final position they ended at in the "burn-in" phase, and run until convergence. Ultimately, the `emcee` sampler outputs the converged solution in the form of posterior distributions of the α-viscosity parameter in the hot disc for each outburst/system. The converged value along with the upper and lower limits on this value is taken as the median and 1σ confidence interval of each posterior distribution, respectively (see Table 3.2).

---

[7] In the Roche-lobe overflow process in LMXBs, we can approximate the trajectory of the mass-transfer stream as the orbit of a test particle released from rest at $\mathscr{L}_1$, with a given angular-momentum, falling into the gravitational field of the compact object. The gas following this trajectory will tend towards the orbit of lowest energy for a given angular-momentum (i.e. a circular orbit). The radius at which the gas initially orbits the compact object in the binary plane, called the circularization radii or R_{circ}, is the radius such that the Keplerian orbit has the same specific angular-momentum as the transferring gas had as it passed through $\mathscr{L}_1$. See Frank et al. (2002) for a thorough discussion.

Table 3.1: The binary orbital parameters used for our Galactic BH-LMXB source sample

Source Name	distance (kpc)	M_1 ($M_\odot$)	q (M_2/M_1)	$P_{\rm orb}$ (hrs)
XTE J1118+480	1.72 ± 0.1	7.2 ± 0.72	0.024 ± 0.009	4.1
MAXI J1305−704	-	-	-	9.74
Swift J1357.2−0933	1.5–6.3	12.4 ± 3.6	-	2.8
GS 1354−64	-	-	0.12±0.04	61.1
4U 1543−475	7.5±0.5	9.4±2.0	0.25–0.31	26.8
XTE J1550−564	4.4±0.5	10.39±2.3	0.031–0.037	37.0
XTE J1650−500	2.6±0.7	4.7±2.2	-	7.7
GRO J1655−40	3.2±0.5	5.4±0.3	0.38±0.05	62.9
MAXI J1659−152	1.6–8.0	-	-	2.414
GX 339−4	8.0±2.0	-	-	42.1
Swift J1745−26	-	-	-	$\leq$21
MAXI J1836−194	-	-	-	<4.9
XTE J1859+226	8±3	10.83±4.67	-	6.6

NOTE. – When no acceptable estimates of distance, BH mass M_1, or binary mass ratio q are available, known Galactic distributions (Tetarenko et al., 2016; Ozel et al., 2010) are used.

3.3 Analysis and Discussion

We analyzed a representative sample of X-ray light-curves of 21 individual outbursts of 12 BH-LMXB systems, from the WATCHDOG project (see Chapter 2; Tetarenko et al. 2016). See Table 3.1. Figure 3.2 shows examples of the analytical irradiated DIM model fit to observed data. In this figure, we overlay predicted decay profiles that illustrate how varying the α-viscosity parameter in a hot, outbursting disc changes the predicted light-curve decay profile.

For these 21 outbursts, we derive $0.19 < \alpha < 0.99$ (see Figure 3.3 and Table 3.2). These results represent the first-ever derivation of α-viscosity parameters in LMXB accretion discs from a fit to the observed outburst light-curves of such systems.

There are two probable explanations for the high values of α-viscosity we measure in BH-LMXB discs. The first is that we are actually measuring the intrinsic α-viscosity parameters of these discs. The only way to reproduce such high intrinsic α-viscosity parameters in accretion disc simulations is for a net magnetic field to thread the disc, with concurrent mass outflows strongly shaping the outburst as a whole.

Simulations of angular-momentum transport driven by the MRI, carried out in vertically-stratified boxes representing a local patch of the disc (shearing box), typically yield $\alpha \approx 0.02$ without a net magnetic flux (Davis et al., 2010; Simon et al., 2012). Convection enhances transport to $\alpha \approx 0.2$ in the conditions appropriate to accreting white dwarfs (Hirose et al., 2014; Coleman et al., 2016; Scepi et al., 2017).

This is consistent with the values deduced from observations of outbursts of the non-irradiated discs around these objects (Kotko & Lasota, 2012), but is insufficient to explain the higher values of $\alpha \gtrsim 0.2$ that we measure from BH-LMXB outbursts. However, when the shearing box is threaded by a net magnetic flux, simulations show that α scales as $\beta^{-1/2}$, where β is the ratio of the thermal pressure to the imposed magnetic pressure, reaching values as high as $\alpha \approx 1$ when $1 \lesssim \beta \lesssim 10^3$, with $\beta = 1$ the lower limit for the MRI to operate in a thin disc (Lesur et al., 2013; Bai & Stone, 2013; Salvesen et al., 2016).

Table 3.2: Derived quantities describing the mass transport process in outbursting LMXB accretion discs

Source Name	Outburst ID	τ_e (days)	R_{disc} ($\times 10^{10}$ cm)	α_h	Accretion State(s) Reached	Max Eddington Fraction
4U1543−475	2002	58.94 ± 0.42	$27.91^{+12.2}_{-10.1}$	$0.66^{+0.16}_{-0.14}$	H,I,S	0.16
GS1354−64	2015	$139.69^{+0.63}_{-0.65}$	$52.10^{+18.1}_{-15.3}$	0.36 ± 0.07	H	$0.085^{a,b}$
GX339−4	1996-1999	$167.17^{+2.12}_{-2.31}$	$37.30^{+15.6}_{-14.2}$	0.25 ± 0.06	H,I,S	0.011^{a}
	2008	$168.24^{+5.89}_{-5.81}$	$37.24^{+15.5}_{-14.1}$	0.25 ± 0.06	H	0.0059^{a}
	2009	$166.88^{+4.96}_{-4.48}$	$37.33^{+15.4}_{-14.1}$	0.25 ± 0.06	H	0.0088^{a}
	2013	$172.37^{+3.14}_{-3.51}$	$37.29^{+15.2}_{-14.0}$	$0.24^{+0.06}_{-0.05}$	H	0.014^{a}
	2014/2015	$188.90^{+0.25}_{-0.23}$	$37.20^{+15.4}_{-14.0}$	0.22 ± 0.05	H,I,S	0.15^{a}
MAXIJ1305−704	2012	$52.90^{+0.11}_{-0.12}$	$12.72^{+5.70}_{-4.65}$	0.49 ± 0.11	H,I,S	$0.051^{a,b}$
MAXIJ1659−152	2010/2011	$60.69^{+1.19}_{-1.23}$	$5.49^{+2.31}_{-2.07}$	0.27 ± 0.06	H,I,S	0.15^{a}
MAXIJ1836−194	2011/2012	$93.09^{+1.81}_{-2.00}$	$8.84^{+3.61}_{-3.34}$	0.22 ± 0.05	H	$0.11^{a,b}$
SwiftJ1357.2−0933	2011	$68.31^{+2.16}_{-2.05}$	$6.85^{+3.00}_{-2.46}$	$0.35^{+0.07}_{-0.06}$	H	0.0019
	2017	$64.89^{+3.47}_{-3.68}$	$6.73^{+2.95}_{-2.42}$	0.37 ± 0.07	H	0.00038
SwiftJ174510.8−262411	2012/2013	$81.49^{+1.92}_{-1.86}$	$23.49^{+9.71}_{-8.92}$	$0.41^{+0.10}_{-0.09}$	H	$1.2^{a,b}$
XTEJ1118+480	1999/2000	$85.96^{+0.55}_{-0.56}$	$12.94^{+1.80}_{-2.10}$	$0.28^{\pm}0.02$	H	0.0017
	2005	$79.01^{+1.29}_{-1.04}$	$12.95^{+1.78}_{-2.10}$	0.30 ± 0.02	H	0.00047
XTEJ1550−564	2000	$61.78^{+0.38}_{-0.37}$	$55.97^{+10.7}_{-9.53}$	$0.96^{+0.15}_{-0.16}$	H,I,S	0.043
	2001	$61.92^{+5.04}_{-5.79}$	$56.14^{+10.7}_{-9.68}$	$0.96^{+0.10}_{-0.09}$	H,I	0.0068
	2001/2002	$60.38^{+0.64}_{-0.63}$	$56.06^{+10.8}_{-9.60}$	$0.99^{+0.15}_{-0.15}$	H	0.013
	2003	$61.89^{+0.55}_{-0.52}$	$55.99^{+10.7}_{-9.52}$	$0.96^{+0.15}_{-0.14}$	H	0.015
XTEJ1650−500	2001/2002	93.12 ± 1.26	$9.80^{+4.36}_{-3.56}$	$0.19^{+0.03}_{-0.05}$	H,I,S	0.016
XTEJ1859+226	1999/2000	$56.61^{+0.07}_{-0.08}$	$11.62^{+5.23}_{-4.27}$	$0.50^{+0.14}_{-0.09}$	H,I,S	0.18

NOTE. – The efficiency of angular-momentum (mass) transport (α-viscosity parameter), assuming no mass loss in the hot disc, and related quantities, sampled using our Bayesian Hierarchical Methodology, are presented. The accretion state(s) reached in each outburst are indicated by: hard (H), intermediate (I), soft (S). For the maximum fraction of the Eddington luminosity, we assume $M_1 = 10M_{\odot}$ ^{a} or $d = 8$ kpc^{b} when one or both of these are unconstrained.

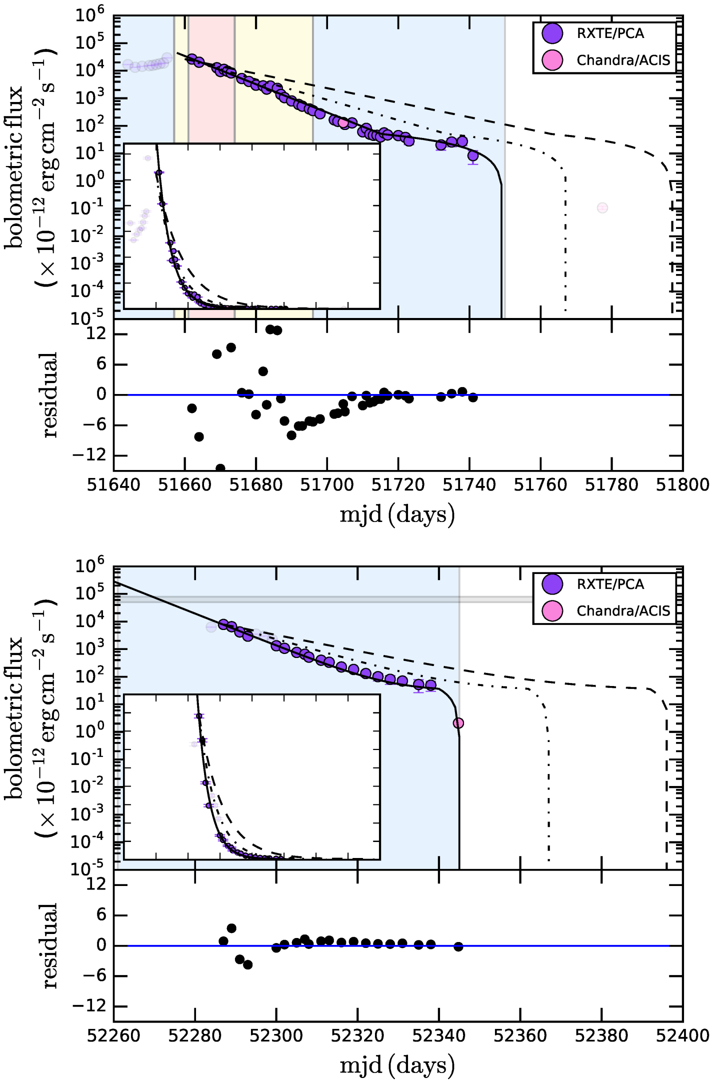

Figure 3.2: Example LMXB outburst light-curves. The figure displays the observed X-ray light-curves for the (top panel) 2000 and (bottom panel) 2001/2002 outbursts of LMXB XTE J1550−564, which harbours a $10.4 \pm 2.3 M_{\odot}$ BH (Tetarenko et al., 2016). In this source, which has undergone multiple outbursts in the past two decades, we measure an extremely high α-viscosity. Error bars show the instruments' statistical uncertainties. Shaded colours show the accretion state(s) of the source during the outbursts: blue = hard, yellow = intermediate, red = soft. Although XTE J1550−564 transitions from the soft to hard accretion states during the decay of the 2000 outburst, the light-curve shows no signature of that transition. Disc outflows have only been observed in the soft/intermediate states or at high flux levels (> 10% Eddington) (Neilsen, 2013b); above the grey region (right panel) in the hard state. Coloured circles represent data from different X-ray instruments; translucent data indicate the rise of the outburst, which was not included in the fits. The inset axes shows the outburst on a linear scale. The best fit analytical model (solid black line) and residuals (lower panels) are displayed in both figures. We measure $\alpha = 0.96 \pm 0.15$ and $\alpha = 0.99^{+0.15}_{-0.14}$ from the 2000 and 2001/2002 outburst light-curves, respectively. We over-plot the resulting decay profiles corresponding to $\alpha = 0.7$ (dot-dashed line) and $\alpha = 0.5$ (dashed line), demonstrating how the light-curve shape changes with different values of the α-viscosity parameter.

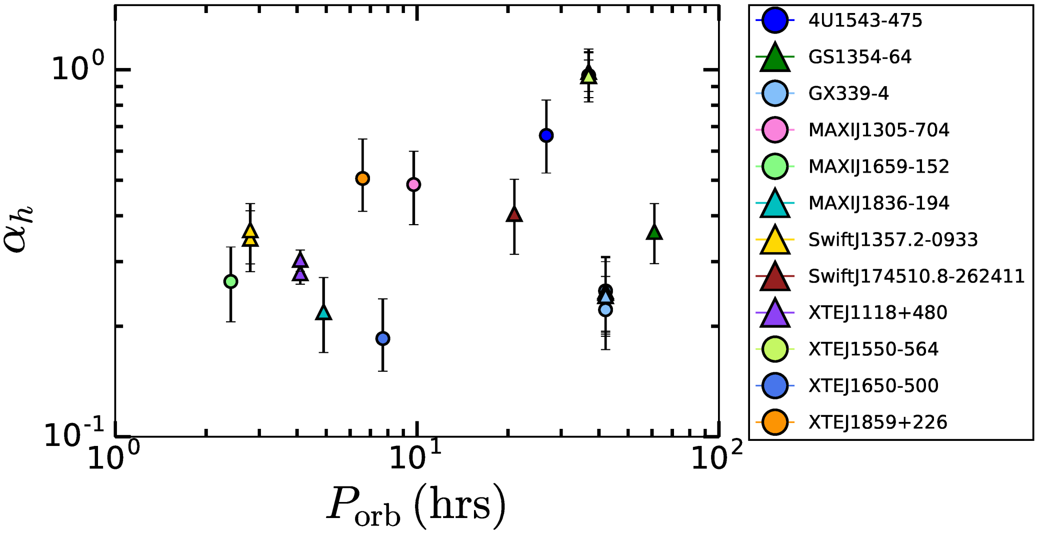

Figure 3.3: Characterization of the mass transport process at work in accretion discs. α-viscosity, the parameter which encompasses the efficiency of angular-momentum (and mass) transport in accretion discs, as derived by our Bayesian methodology, is plotted vs. binary system orbital period ($P_{\rm orb}$), for the 21 individual outbursts occurring in our sample of 12 Galactic BH-LMXBs with measured orbital periods. The different colours represent individual sources. The shapes indicate accretion state(s) reached by the source during outburst: (circles) hard/intermediate/soft states reached and (triangles) only hard state reached. Error bars represent the 68% confidence interval. α-viscosity parameters are derived in both outbursts where the source cycles through all the accretion states and those where the source remains only in the hard state.

Hence, strong intrinsic angular-momentum transport indicates the presence of a large-scale field in the accretion disc, whose origin and evolution have yet to be determined in BH-LMXB transients. Moreover, simulations reproducing high intrinsic α-viscosity also display strong outflows, which actually do not remove much angular-momentum, thus angular-momentum transport is still primarily driven by the MRI.

The second possibility is that the intrinsic α-viscosity parameters in BH-LMXB accretion discs are smaller than we measure (e.g., comparable to $\alpha \sim 0.2$), and unspecified strong mass outflows are significantly shaping the overall observed light-curve profiles. Figure 3.4 illustrates how including a mass (and angular-momentum) loss term within the irradiated DIM mimics the effect that a high α-viscosity has on the light-curve decay profile.

In both cases, significant outflows appear to play a key role in regulating the disc-accretion process. Strong mass outflows have been observed in outbursting LMXBs in the soft/intermediate states or at high flux levels ($>10\%$ Eddington) in the hard state (Miller et al., 2006; Ponti et al., 2012; Neilsen, 2013b) in the form of accretion disc winds. These outflows have been attributed to thermal winds driven by X-ray irradiation or to magnetic winds driven by centrifugal acceleration along magnetic field lines anchored in the disc (Ohsuga & Mineshige, 2011; Higginbottom & Proga, 2015).

It has recently been shown that thermally-driven winds (e.g., Compton-heated winds; Ponti et al. 2012), can only be produced in the soft accretion state, as the ionization state of the wind becomes unstable in the hard state (e.g. Chakravorty et al. 2013; Bianchi et al. 2017). The absence of correlation between the values of α-viscosity and the X-ray flux or accretion state in our outburst sample, suggests that the outflow mechanism is generic, and favours magnetically-driven over thermally-driven outflows.

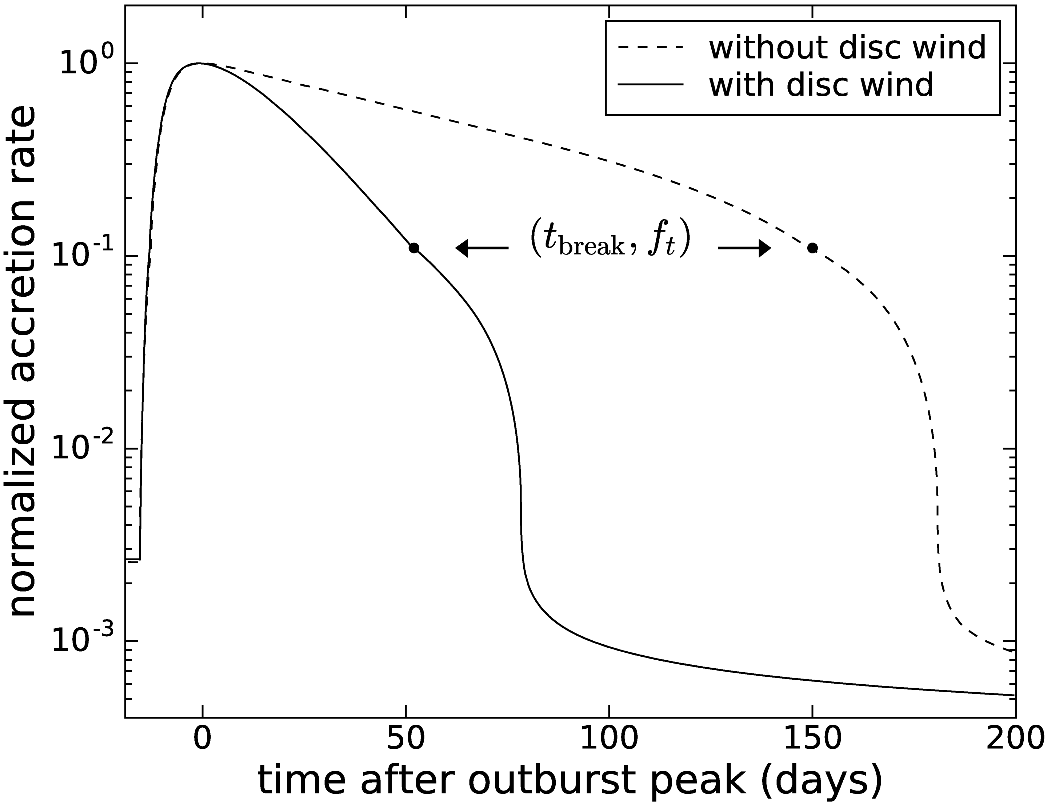

Figure 3.4: The "disc wind" toy model. Two model light-curves for an irradiated disc around a $6M_\odot$ BH and an $\alpha = 0.2$ accretion disc are shown: (dashed line) no mass loss present, and (solid line) including a mass loss term during outburst. The latter is computed assuming mass loss is proportional to central mass-transfer rate onto the BH ($\dot{M}_w = \epsilon_w \dot{M}_c$) during the decay (meant to be representative of a disc "wind" type outflow). While the profile shape remains the same, the effective timescale (τ_e) is reduced to $(1-\epsilon_w)\tau_e$. Thus, as fraction of mass lost increases, τ_e decreases, mimicking the effect an arbitrary large α-viscosity parameter has on the light-curve profile (i.e., a high α-viscosity parameter corresponds to a fast decay). A measurement of $\alpha = 1$ would correspond to a disc with $\alpha = 0.2$, $\epsilon_w = 0.8$ in the toy model, indicative of a significant outflow. Note that, while this model assumes the local outflow rate is related to the local accretion rate in the disc, this need not be the case. Further, this simplifying assumption, used purely to numerically solve the light-curve, will limit what we can say on how much mass is lost in the outflow. While this model requires $\dot{M}_w/\dot{M}_c < 1$, it is certainly possible that the outflow rate is larger than the central mass-transfer rate onto the BH.

Chapter 4

Understanding X-ray Irradiation in BH-LMXBs directly from their Light-Curves

Tetarenko, B.E., Dubus, G., Lasota, J.-P., Heinke, C.O., and Sivakoff, G.R.

Monthly Notices of the Royal Astronomical Society, 480, 2-16 (2018)

ABSTRACT

The X-ray light-curves of the recurring outbursts observed in low-mass X-ray binaries provide strong test beds for constraining (still) poorly understood disc-accretion processes. These light-curves act as a powerful diagnostic to probe the physics behind the mechanisms driving mass inflow and outflow in these binary systems. We have thus developed an innovative methodology, combining a foundation of Bayesian statistics, observed X-ray light-curves, and accretion disc theory. With this methodology, we characterize the angular-momentum (and mass) transport processes in an accretion disc, as well as the properties of the X-ray irradiation-heating that regulates the decay from outburst maximum in low-mass X-ray transients. We recently applied our methodology to the Galactic black hole low-mass X-ray binary population, deriving from their light-curves the first-ever quantitative measurements of the α-viscosity parameter in these systems (Tetarenko et al., 2018b). In this paper, we continue the study of these binaries, using Bayesian methods to investigate the X-ray irradiation of their discs during outbursts of strong accretion. We find that the predictions of the disc-instability model, assuming a source of X-ray irradiation proportional to the central accretion rate throughout outburst, do not adequately describe the later stages of BH-LMXB outburst light-curves. We postulate that the complex and varied light-curve morphology observed across the population is evidence for irradiation

that varies in time and space within the disc, throughout individual transient outbursts. Lastly, we demonstrate the robustness of our methodology, by accurately reproducing the synthetic model light-curves computed from numerical codes built to simulate accretion flows in binary systems.

4.1 Introduction

Throughout their lifetimes, many astrophysical objects (e.g. newborn stars, planets, black holes) grow and evolve by accumulating mass through a disc. For these objects to grow, matter must lose angular-momentum to flow inward, and avoid being removed from the system via outflows. Among accreting astrophysical systems, low-mass X-ray binaries (LMXBs), in which compact objects (neutron stars and black holes) accrete from their low-mass ($M_2 \lesssim 1\, M_\odot$) companion stars, provide us with strong test beds for constraining this poorly understood process of accretion.

So far, 18 confirmed (and $\sim$ 46 candidate) LMXBs harbouring stellar-mass black holes (BHs) have been identified through their bright X-ray outbursts, indicative of rapid accretion episodes, in our Galaxy (McClintock & Remillard, 2006; Tetarenko et al., 2016; Negoro et al., 2017; Kawamuro et al., 2018; Kawase et al., 2018; Barthelmy et al., 2018, and references therein). All these systems are transient. They display long-term behaviour characterized by extended periods of time (typically years to decades) spent in a quiescent state, where the system is faint ($L_X \sim 10^{30} - 10^{33}\, \mathrm{erg\, s^{-1}}$) as a result of very little accretion occurring onto the compact object (e.g. Garcia et al., 2001).

These prolonged quiescent periods are interrupted by occasional bright disc-outbursts, typically lasting hundreds of days, during which the X-ray luminosity will increase by multiple orders of magnitude ($L_{\mathrm{X,peak}} \sim 10^{36} - 10^{39}\, \mathrm{erg\, s^{-1}}$; Chen et al. 1997; Tetarenko et al. 2016).

Although less frequent, the recurring nature of outbursts observed in transient BH-LMXBs is reminiscent of the behaviour observed in dwarf novae (i.e. compact binary systems consisting of a white dwarf accreting from a low-mass companion; Warner 1995). In dwarf novae, the mechanism behind such outbursts is well understood using the disc-instability model (DIM; Osaki 1974; Meyer & Meyer-Hofmeister 1981; Smak 1983, 1984; Cannizzo et al. 1985; Cannizzo 1993; Huang & Wheeler 1989), which predicts alternating periods of bright disc-outbursts, lasting days, and faint quiescence, lasting weeks.

According to the DIM, this behaviour results from a thermal-viscous instability developing within the disc, causing it to cycle between a hot, ionized outburst state and a cool, neutral, quiescent state. The instability, triggered by the continuous accumulation of matter from the companion star eventually heating and subsequently ionizing the disc, causes a dramatic increase in the viscosity (i.e. the ability of the disc to move angular-momentum outwards) of the disc. This increased viscosity results in a rapid in-fall of matter onto the compact object and a bright outburst in the optical and ultraviolet (UV) bands.

X-ray irradiation of the disc must be taken into account when describing transient outbursts of LMXBs. LMXBs have deeper potential wells and thus undergo brighter X-ray, optical, and UV outbursts that last longer and recur less frequently (Tetarenko et al., 2016), than most dwarf novae[1]. The majority of the UV, optical and infrared (IR) light emitted by the accretion discs in LMXBs comes from reprocessed X-rays. Here the inner regions of the accretion flow heat the outer disc (van Paradijs, 1983; van Paradijs & McClintock, 1994; van Paradijs, 1996).

A major contributor to the thermal balance in the accretion flow, this X-ray irradiation keeps the disc in a hot, ionized state controlling most of the outburst decay towards quiescence. Consequently, the light-curve profile for an outburst of an irradiated disc will differ from that of a non-irradiated disc (see Figures 3.1 and 3.2 in Chapter 3; King & Ritter 1998; Dubus et al. 2001).

Taken as a whole, the multi-wavelength light-curves of the recurring outbursts in LMXBs encode within them key physical parameters describing how (and on what timescale) matter moves through, and is removed from, the discs in these systems. Thus, LMXB outburst light-curves offer a means in which to understand the mech-

---

[1] The notable exceptions here are WZ Sge type dwarf novae, where outbursts typically last months and recur after tens of years, similar to those of BH-LMXBs. See Kato 2015 for a review of WZ Sge dwarf novae.

anism behind the X-ray irradiation affecting these discs which still remains poorly understood (see Dubus et al. 1999 and references therein). Accordingly, we have developed an innovative methodology, combining a foundation of Bayesian statistics, the observed X-ray light-curves, and accretion disc theory. With this methodology, we characterize the angular-momentum (and mass) transport processes in an accretion disc, as well as the properties of the X-ray irradiation-heating that the discs are subject to.

In Tetarenko et al. (2018b) (hereafter Paper I) and Chapter 3, we presented the details of this methodology. By applying this approach to the BH-LMXB population, we were able to derive the first-ever measurements of the efficiency of the angular-momentum (and mass) transport process (parametrized via α-viscosity; Shakura & Sunyaev 1973) in the X-ray irradiated discs of LMXBs, directly from observations. In this paper, we continue our analysis of Galactic BH-LMXB discs with our methodology, studying the physical properties of the X-ray irradiation heating these discs.

The outline of this chapter is as follows. In Section 4.2 we describe how we model the X-ray irradiation that affects the accretion discs in LMXB systems and the Bayesian methodology we employ. Section 4.3 describes the application of our methodology to the BH-LMXB population of the Galaxy, including details behind the selection of our BH-LMXB source and outburst sample, and X-ray data collection, reduction, and analysis procedures. In Section 4.4, we present the results of fitting the X-ray light-curve profiles of our BH-LMXB outburst sample and the observational constraints that can be derived using these characterized light-curve profiles. In Section 4.5 we discuss what LMXB light-curve profiles can tell us about the structure and geometry of the irradiation source heating LMXB discs and how our observationally based methodology compares to the output of numerical disc codes. Lastly, Section 4.6 provides a summary of this work.

4.2 Modelling the X-ray Irradiation affecting LMXB discs

4.2.1 The Irradiation Prescription

X-ray irradiation from the inner accretion region is the dominant factor that determines the temperature over most of the accretion disc during outbursts of BH-LMXBs. The fraction of the X-ray flux that is intercepted and reprocessed in the outer disc is not well understood. Simple prescriptions based on the radial profile of the disc height lead to shadowing of the outer disc, suggesting part of the irradiation process may occur via a larger-sized scattering corona (Kim et al., 1999; Dubus et al., 1999). We make use of the prescription used by Dubus et al. (2001) to model the light-curves of X-ray irradiated BH-LMXB accretion discs,

$$T_{\mathrm{irr}}^4 = \frac{C_{\mathrm{irr}} L_{\mathrm{bol}}}{4\pi\sigma_{\mathrm{SB}} R^2}. \tag{4.1}$$

Here, C_{irr} is a constant encapsulating the information about the fraction of the bolometric accretion (mostly X-ray) luminosity ($L_{\mathrm{bol}} = \eta c^2 \dot{M}_c$ for radiative efficiency η) that is intercepted and reprocessed by the disc (i.e. it encapsulates the irradiation geometry, the X-ray albedo, the X-ray spectrum, etc.). Since the effective temperature of the disc is defined through

$$T_{\mathrm{eff}}^4 = \frac{3GM\dot{M}}{8\pi\sigma_{\mathrm{SB}} R^3}, \tag{4.2}$$

the ratio of the irradiation to effective temperatures is

$$\frac{T_{\mathrm{irr}}^4}{T_{\mathrm{eff}}^4} = \frac{4}{3} C_{\mathrm{irr}} \eta \frac{R}{R_S}, \tag{4.3}$$

where $R_S = 2GM/c^2$ is the Schwarzschild radius, disc irradiation is important only in the outer disc regions ($R > 10^3\, R_S$ for $\eta = 0.1$ and $C_{\mathrm{irr}} \sim 5 \times 10^{-3}$, see below).

Physically, C_{irr} controls the overall outburst duration and sets a limit on the amount of mass that the black hole can accrete during the outburst. A larger value of

$C_{\rm irr}$, corresponding to stronger irradiation in the outer disc, will increase the duration of the outburst and thus, the relative amount of matter that can be accreted during a given outburst. A larger $C_{\rm irr}$ during outburst will also result in a more lengthy quiescent period following the outburst, as the disc will require more time to build up again.

The actual value $C_{\rm irr}$ takes in accretion discs has been a matter of debate for decades. $C_{\rm irr}$ (in the outer disc) has been previously measured in five BH-LMXBs (by modelling a combination of X-ray and optical data) and two persistently accreting (non-transient) neutron star LMXBs. In these cases, the authors assumed a vertically-isothermal disc and derived a disc opening angle and albedo from optical observations.

For the BHs: Hynes et al. (2002a) found $C_{\rm irr} \sim 7.4 \times 10^{-3}$ for XTE J1859+226; Suleimanov et al. (2008) estimated $\sim 7 \times 10^{-4}$ and 3×10^{-4} for A0620−00 and GRS 1124−68, respectively; for XTE J1817−330, Gierliński et al. (2009) found $C_{\rm irr} \sim 1 \times 10^{-3}$ in the soft state and $\sim 6 \times 10^{-3}$ in the hard state (consistent with predictions of increased absorption of hard X-ray photons); and finally Lipunova & Malanchev (2017) constrain $C_{\rm irr} < 6 \times 10^{-4}$ for 4U 1543−47.

Vrtilek et al. (1990) and de Jong et al. (1996) model two persistent neutron star LMXBs, leading to the so-called "standard" value of $C_{\rm irr} \sim 5 \times 10^{-3}$ typically assumed in theoretical work. This value of $C_{\rm irr}$ has also been shown to be consistent with the amount of X-ray heating required to stabilize persistent neutron star and transient BH-LMXB systems against the thermal-viscous instability (van Paradijs, 1996; Coriat et al., 2012).

However, as we only have this limited sample of BH-LMXBs where $C_{\rm irr}$ has actually been estimated, it remains unclear whether the same value would describe the outburst properties of discs across the Galactic BH-LMXB population. Moreover, it is also unknown how (or if) the value of $C_{\rm irr}$ varies from source to source (e.g., with changing $P_{\rm orb}$ or component masses; Esin et al. 2000) or even between outbursts of the same source (e.g. with changing peak outburst luminosity or outburst duration; Esin et al. 2000).

4.2.2 The Light-Curve Model

The outburst light-curve of an LMXB, as predicted by DIM+irradiation (IDIM), involves a characteristic three-stage decay profile after the outburst peak (see Figure 3.1 in Chapter 3; King & Ritter 1998; Dubus et al. 2001). The outburst decay begins with a viscous phase during which the X-ray irradiation from the inner accretion flow can keep the whole disc in a hot (ionized) state, preventing the onset and propagation of a cooling front. Since the accretion rate is larger than the mass-transfer rate, and the mass of the hot disc can only change through central accretion onto the black hole, the light-curve will show an exponential-shaped decline on the viscous timescale.

Over time, the mass in the disc and central mass-accretion rate will decrease. When the dimming X-ray irradiation can no longer keep the outer regions of the disc in the hot (ionized) state (i.e. above the hydrogen ionization temperature $T_{\rm irr}(R_{\rm disc}) > 10^4$ K), a cooling front forms and propagates down the disc, bringing the disc to a cold state.

At this point, the second phase of the decay begins, during which the speed of the propagation of this cooling front, and thus the timescale of the phase itself, is controlled by the temperature of the decaying irradiating X-ray flux. Here, the cooling-front inward propagation is hindered by irradiation. The farthest it can move inward is set by the radius at which $T = 10^4$ K. While the hot (ionized) zone of the disc will continue to flow and accrete, it must now gradually shrink in size as the central mass-accretion rate decreases ($R_{\rm hot} \sim \dot{M}_1^{1/2}$), leading to a linear-shaped decline in the light-curve.

Eventually, the central mass-accretion rate will become small enough that X-ray irradiation will no longer play a role and the system will enter the final (thermal) decay stage. X-ray irradiation may also decline faster than the mass-accretion rate when the inner disc switches to a radiatively-inefficient accretion flow with a smaller radiative efficiency η. At this point the cooling front will be allowed to propagate inward through the thin disc on a thermal-viscous timescale (where the speed of the front can be written as $v_f \sim \alpha c_S$), where c_S is the sound speed for $T_{\rm eff} \sim 10^4$K, ultimately resulting in a steeper final dwarf-nova type decline in the light-curve down to the quiescent accretion level.

As detailed in Paper I and Chapter 3, we have built an improved analytical version of this "classic" irradiated disc-instability model. Our version builds on the simple model of irradiated discs by King & Ritter (1998), using the irradiation flux as set by Equation 4.1. This analytical model effectively characterizes the light-curve profile of a transient LMXB using five parameters as follows,

$$f_X = \begin{cases} (f_t - f_2)\exp\left(-(t - t_{\mathrm{break}})/\tau_e\right) + f_2 & t \le t_{\mathrm{break}} \\ f_t\left(1 - (t - t_{\mathrm{break}})/\tau_l\right) & t > t_{\mathrm{break}} \end{cases}$$

where τ_e is the viscous timescale in the hot (ionized) zone of the disc, τ_l is the timescale of the irradiation-controlled stage of the decay, t_{break} defines the transition time between viscous and irradiation-controlled stages, f_t is the corresponding bolometric X-ray flux of the system at time t_{break}, and f_2 represents the bolometric flux limit of the viscous stage of the decay, dependent upon the mass-transfer rate from the companion ($-\dot{M}_2$) and source distance (d). See Powell et al. (2007) and Heinke et al. (2015) for full derivation of this analytical form and Paper I and Chapter 3 for a more detailed discussion on the development of this model.

While the formalism developed by King & Ritter (1998) is simplified compared to other formalisms (e.g., Lipunova & Shakura, 2000, where the kinematic viscosity is allowed to vary with surface density and time), it remains unclear if the additional layers of complexity in a more detailed semi-analytical model provide a correspondingly clearer physical insight. In addition, we continue using the King & Ritter (1998) formalism for continuity with Paper I and Chapter 3.

4.2.3 The Bayesian Hierarchical Methodology

As detailed in Paper I and Chapter 3, the viscous timescale τ_e in the disc can be written in terms of the α-viscosity parameter (α_h), which describes the efficiency of angular-momentum and mass transport through the hot zone of the disc, compact object mass (M_1) and accretion disc radius (R_{disc}) such that,

$$\left(\frac{\tau_e}{1s}\right) = (1 \times 10^6)\left(\frac{G^{0.5} m_H M_\odot^{0.5}}{3\gamma k_b T_c}\right)\left(\frac{\alpha_h}{0.1}\right)^{-1}\left(\frac{M_1}{M_\odot}\right)^{0.5}\left(\frac{R_{\mathrm{disc}}}{10^{10}\mathrm{cm}}\right)^{0.5}. \tag{4.4}$$

This expression was used to constrain α in Paper I. Note that, as discussed in Paper I and shown in Dubus et al. (2001, see their Figure 6), the central midplane temperature of the disc (T_c) is only weakly dependent on viscosity and X-ray irradiation in irradiated discs, thus we can approximate its value as a constant.

The transition from the viscous to the irradiation-controlled (linear) phase of the outburst's decay occurs when the irradiation temperature at the outer radius is $T_{\rm irr} \approx 10^4$ K, the temperature at which hydrogen starts to recombine, since it is the outermost region of the disc that starts the transition to the quasi-neutral, cold state. Therefore we make use of the irradiation law of Equation 4.1 to obtain the value of $C_{\rm irr}$ by assuming $T_{\rm irr} = 10^4$ K in

$$\left(\frac{C_{\rm irr}}{T_{\rm irr}^4}\right) = (5.4 \times 10^6)\left(\frac{f_t}{10^{-12}{\rm erg s^{-1} cm^{-2}}}\right)^{-1}\left(\frac{d}{\rm kpc}\right)^{-2}\left(\frac{R_{\rm disc}}{10^{10}{\rm cm}}\right)^2. \tag{4.5}$$

Here $C_{\rm irr}$ depends only on the transition luminosity between these two stages of the outburst decay and the known measurements of compact object mass (M_1), binary mass ratio (q), and orbital period ($P_{\rm orb}$).

As these quantities are readily obtained from a combination of fitting X-ray outburst light-curves with the analytical decay model (described in Paper I, Chapter 3, and Section 4.2.2) and a literature search (see Table 4.1), it is possible to derive observational constraints on the strength of the X-ray irradiation heating the outer regions of LMXB discs using a multi-level Bayesian statistical sampling technique.

Paper I (and Chapter 3) describes in detail the development and (PYTHON) implementation of the Bayesian methodology we use to sample $C_{\rm irr}$ effectively. In short, we have built a hierarchical model, a multi-level statistical model that makes use of a combination of known prior distributions and observational data to estimate a posterior distribution of a physical quantity effectively. Together with Equation 4.5, we sample $C_{\rm irr}$ using only the established binary orbital parameters (M_1, q, $P_{\rm orb}$) for a system as known priors and the observed X-ray light-curve data. From the light-curves we are able to measure the posterior distribution of the observed flux of the system at the transition between viscous and irradiation-controlled decay stages (f_t). This quantity acts as the observational data in our hierarchical model.

4.3 Application to the BH-LMXB Population of the Galaxy

4.3.1 Source and Outburst Selection

We have used the WATCHDOG catalogue (Chapter 2; Tetarenko et al. 2016) to compile a representative sample of BH (and BH candidate) LMXBs in our Galaxy. This sample, consisting of 13 BH-LMXBs and 30 individual outbursts undergone by these sources, includes only those systems with a known $P_{\rm orb}$ that have undergone at least one outburst since 1996. Tables 4.1 and 4.2 display binary parameter information, outburst information, and data availability for our source/outburst sample.

4.3.2 Mining X-ray Light-curves of the Galactic Population

We have collected X-ray data available during outbursts occurring in our source sample from the following instruments: (i) Proportional Counter Array (PCA) aboard the Rossi X-ray Timing Explorer (RXTE), (ii) X-ray Telescope (XRT) aboard the Neil Gehrels Swift Observatory, (iii) Gas-Slit Camera (GSC) aboard the Monitor of All-sky Image (MAXI) Telescope, (iv) Advanced CCD Imaging Spectrometer (ACIS-S) and High Resolution Camera (HRC-S) aboard the Chandra X-ray Observatory, and (v) European Photon Imaging Camera (EPIC) aboard XMM-Newton.

We used the *RXTE*/PCA and *MAXI*/GSC data obtained with the WATCHDOG project (Chapter 2; Tetarenko et al. 2016). This compilation includes all (i) good pointed PCA observations (i.e. no scans or slews) available (over the 16-year *RXTE* mission) in the HEASARC archive and (ii) publicly available *MAXI*/GSC data from the *MAXI* archive[2]. We obtained *Swift*/XRT data, including all available windowed-timing and photon-counting mode pointed observations, from the *Swift*/XRT online product builder[3](Evans et al., 2009). Finally, we collected select pointed observations

---

[2] http://maxi.riken.jp/top/

[3] http://www.swift.ac.uk/user_objects/index.php

Table 4.1: The Binary Orbital Parameters of our Galactic BH-LMXB Sample

Source Name	distance (kpc)	M_1 ($M_\odot$)	q (M_2/M_1)	$P_{\rm orb}$ (hrs)
XTE J1118+480	1.72 ± 0.1	7.2 ± 0.72	0.024 ± 0.009	4.1
MAXI J1305−704	$\cdots$	-	$\cdots$	9.74
Swift J1357.2−0933	2.3–6.3	12.4 ± 3.6	$0.04^{+0.005}_{-0.003}$	2.8
GS 1354−64	$\cdots$	-	0.12 ± 0.04	61.1
4U 1543−475	7.5 ± 0.5	9.4 ± 2.0	0.25–0.31	26.8
XTE J1550−564	4.4 ± 0.5	10.39 ± 2.3	0.031–0.037	37.0
XTE J1650−500	2.6 ± 0.7	4.7 ± 2.2	$\cdots$	7.7
GRO J1655−40	3.2 ± 0.5	5.4 ± 0.3	0.38 ± 0.05	62.9
MAXI J1659−152	1.6–8.0	$\cdots$	-	2.414
GX 339−4	8.0 ± 2.0	$\cdots$	-	42.1
Swift J1745−26	$\cdots$	-	$\cdots$	$\leq$21
MAXI J1836−194	$\cdots$	-	$\cdots$	$<$4.9
XTE J1859+226	8 ± 3	10.83 ± 4.67	$\cdots$	6.6

NOTE. – All binary parameters taken from the WATCHDOG catalogue (Chapter 2; Tetarenko et al. 2016), with the exception of SwiftJ1357.2−0933 (Casares, 2016). The observed Galactic BH distributions from Tetarenko et al. (2016) and Ozel et al. (2010) are used when no acceptable estimates of BH mass M_1 or binary mass ratio q are available in the literature. A distance of 8kpc is assumed when no distance estimates exist in the literature.

with *Chandra*/ACIS-S and HRC-S, and *XMM-Newton*/EPIC, occurring during the decay phase of outbursts in our sample, from the literature. See Table 4.2 for details.

All *RXTE*/PCA, *Swift*/XRT, and *MAXI*/GSC light-curves were extracted in the 2–10 keV band. Following Tetarenko et al. (2016), individual instrument count-rates were then converted to flux by using crabs as a baseline unit and calculating approximate count rate equivalences. Count-rates from *Chandra* ACIS-S and HRC-S, and *XMM-Newton*/EPIC were converted to flux in the 2–10 keV band using PIMMS v4.8c[4] and spectral information available in the literature.

Lastly, all 2–10 keV band flux light-curves were converted to bolometric flux light-curves using a combination of the bolometric corrections estimated for each BH-LMXB accretion state by Migliari & Fender (2006) and WATCHDOG project's online Accretion-State-By-Day tool[5] (see Chapter 2), the latter of which provides accretion state information on daily timescales during outbursts of BH-LMXBs. For a detailed account of the complete data reduction and analysis procedures used refer to Chapter 3 and Paper I.

4.4 Results

4.4.1 X-ray Light-curve Fitting

By fitting the decay profiles found in our sample of BH-LMXB X-ray light-curves with the analytical irradiated DIM described in Paper I, Chapter 3, and Section 4.2.2, we can derive the flux level at which the transition occurs between the viscous and irradiation-controlled decay stages in a light-curve. We find this transition flux found in BH-LMXB light-curves to occur between $\sim 3.6 \times 10^{-11} - 1.3 \times 10^{-8}\,\mathrm{erg\,cm^{-2}\,s^{-1}}$ (for models whose fits we classified as trusted – Class A; see Table 4.3 and Section 4.4.2).

All fitting was performed in logarithmic bolometric flux space, as opposed to luminosity space, to avoid the possibility of correlated errors resulting from uncertain

---

[4] http://cxc.harvard.edu/toolkit/pimms.jsp

[5] http://astro.physics.ualberta.ca/WATCHDOG

distance estimates. Uncertainties in the distance (as well as other binary parameters) are incorporated within the Bayesian Hierarchical model itself. Secondary maxima and other re-brightening events that can contaminate BH-LMXB decay profiles are removed by hand before fitting occurs. Removing such events has been found to have no effect on either of the characteristic timescales derived from the X-ray light-curves.

All 23 fitted X-ray light-curves are presented in panels of Figures 4.6–4.9. Each light-curve has been plotted in logarithmic space on the main axis. In addition, a small zoomed-in inset, displaying the outburst in linear space, is also included. Data in each figure has been colour-coded by instrument: *RXTE*/PCA (purple), *Swift*/XRT (blue), *MAXI*/GSC (green), *Chandra* ACIS-S and HRC-S (pink), and *XMM-Newton*/EPIC (orange).

All data not included in the fits (including the outburst rise and rebrightening events) are displayed in translucent versions of these colors. Shaded background colours show accretion state information of the source, computed with the WATCHDOG project's Accretion State-by-Day tool (Chapter 2; Tetarenko et al. 2016), throughout the outburst on a daily timescale.

A sizeable fraction of BH-LMXB outburst light-curves in our sample do not display simple "clean" decays. In fact, of the 30 outbursts in our sample, 23% (7/30) exhibit complex variability, in the form of multiple intermediate flares and decays, throughout the individual outbursts themselves. While 50% (15/30) show a combination of exponential plus linear decays, 20% (6/30) show pure exponential decays and 7% (2/30) show pure linear decays.

We reiterate that one should by no means assume that the standard disc-instability picture governs the complex variability observed in the form of intermediate flares and decays. As our analytical decay model is too simple to draw any conclusions about the cause of this complex variability, we do not fit or include these outbursts that exhibit "complex variability" (marked by a "*" in Table 4.2) in any further analysis presented in this chapter. Instead, we review possible causes of this behaviour in the discussion.

Table 4.2: Outburst History for our Galactic BH-LMXB Source Sample

Source Name	Outburst Year	t_b (MJD)	t_e (MJD)	Data Available	Refs.
XTE J1118+480	1999/2000	51538.0	51770.0	PCA	-
	2005	53380.0	53420.0	PCA	-
MAXI J1305−704	2012	56009.5	56190.0	GSC,XRT	-
Swift J1357.2−0933	2011	55576.5	55653.0	EPIC,PCA,XRT	1
	2017	57874.0	57977.0	XRT	-
GS 1354−64	1997/1998	50714.0	50870.0	PCA	-
	2015	57153.0	57315.0	GSC,XRT	-
4U 1543−475	2002	52435.0	52503.0	EPIC,PCA	2
XTE J1550−564	1998/1999*	51062.0	51316.0	PCA	-
	2000	51597.0	51719.0	ACIS-S,PCA	3–5
	2001	51934.0	51986.0	PCA	-
	2001/2002	52261.0	52312.0	ACIS-S,PCA	5
	2003	52725.0	52775.0	PCA	-
XTE J1650−500	2001/2002	52149.0	52366.0	ACIS-S,PCA	7
GRO J1655−40	1996/1997*	50184.0	50690.0	PCA	-
	2005*	53415.0	53654.0	PCA	-
MAXI J1659−152	2010/2011	55456.5	55685.0	ACIS-S,GSC,PCA,XRT	8
GX 339−4	1996-1999	50259.0	51298.0	PCA	-
	2002/2003*	52350.0	52750.0	PCA	-
	2004/2005*	53054.0	53515.0	PCA	-
	2006	53751.0	53876.0	PCA	-
	2006/2007*	54053.0	54391.0	PCA,XRT	-
	2008	54624.0	54748.0	PCA,XRT	-
	2009	54875.0	55024.0	EPIC,PCA,XRT	9,10
	2009-2011*	55182.5	55665.0	ACIS-S,GSC,PCA,XRT	11
	2013	56505.5	56608.0	GSC,XRT	-
	2014/2015	56936.0	57311.0	GSC,XRT	-
Swift J1745−26	2012/2013	56178.0	56463.0	XRT	-
MAXI J1836−194	2011/2012	55793.5	56154.5	GSC,PCA,XRT	-
XTE J1859+226	1999/2000	51437.0	51661.0	PCA	-

NOTE. – The outburst year and start (t_b) and end (t_e) times of the outburst are taken from the WATCHDOG catalogue (Chapter 2; Tetarenko et al. 2016). A “*” in the outburst year indicates that the outburst in question displays complex variability, and thus is not included in the analysis of this paper. References for *Chandra* and *XMM-Newton* data used – [1] Armas Padilla et al. (2014), [2] La Palombara & Mereghetti (2005), [3] Tomsick et al. (2001a), [4] Tomsick et al. (2003), [5] Corbel et al. (2006), [7] Tomsick et al. (2004), [8] Jonker et al. (2012), [9] Basak & Zdziarski (2016), [10] Plant et al. (2014), and [11] Corbel et al. (2013).

Table 4.3: Results of our Bayesian Methodology Applied to Outbursts of BH-LMXBs

Source Name	Outburst Year	Function Type	Outburst Class[a]	$f_{\rm t}$ ($\times 10^{-12}$) (ergs^{-1}cm^{-2}s^{-1})	$t_{\rm break}$ (mjd)	τ_l (days)	f_2 ($\times 10^{-12}$) (ergs^{-1}cm^{-2}s^{-1})	τ_e (days)	α_h[b]	$C_{\rm irr}$[c]
XTEJ1118+480	1999/2000	exp+lin	A	2843^{+15}_{-16}	$51726.23^{+0.36}_{-0.37}$	$34.18^{+0.47}_{-0.45}$	2831^{+16}_{-17}	$85.96^{+0.55}_{-0.56}$	0.28 ± 0.02	$\left(1.20^{+0.44}_{-0.40}\right) \times 10^{-1}$
	2005	exp	C	$0.00002^{+0.005}_{-0.0000004}$	$53465.37^{+3.37}_{-0.02}$	$\cdots$	$0.00001^{+0.002}_{-0.000001}$	$79.0^{+1.3}_{-1.0}$	0.30 ± 0.02	$> 4.9 \times 10^{0}$
MAXIJ1305-704	2012	exp+lin	A	896^{+10}_{-12}	$56128.28^{+0.19}_{-0.10}$	$97.7^{+4.2}_{-4.0}$	$0.78^{+0.21}_{-0.20}$	$52.90^{+0.11}_{-0.12}$	0.49 ± 0.11	$\left(2.31^{+1.96}_{-1.40}\right) \times 10^{-2}$
SWIFTJ1357.2-0933	2011	exp+lin	A	425^{+32}_{-33}	$55647.0^{+3.3}_{-2.8}$	$57.6^{+2.4}_{-2.8}$	173^{+28}_{-30}	$68.3^{+2.2}_{-2.0}$	0.35 ± 0.07	$\left(4.5^{+6.8}_{-2.8}\right) \times 10^{-2}$
	2017	exp+lin	A	142^{+20}_{-18}	$57909.9^{+5.2}_{-4.9}$	$63.4^{+3.6}_{-3.7}$	$7.0^{+1.0}_{-1.0}$	$64.9^{+3.5}_{-3.7}$	0.37 ± 0.07	$\left(1.31^{+2.05}_{-0.81}\right) \times 10^{-1}$
GS1354-64	1997/1998	lin	C	7266^{+77}_{-77}	$50774.25^{+0.86}_{-0.88}$	$90.6^{+1.5}_{-1.5}$	$\cdots$	$\cdots$	$\cdots$	$< 2.8 \times 10^{-3}$
	2015	exp	B	$57.8^{+2.8}_{-2.7}$	$57358.49^{+0.94}_{-0.91}$	$\cdots$	0.01 ± 0.001	$139.69^{+0.63}_{-0.65}$	0.36 ± 0.07	$> 3.7 \times 10^{-3}$
4U1543-475	2002	exp+lin	A	$79.0^{+6.1}_{-5.6}$	$52501.36^{+0.60}_{-0.59}$	$3.43^{+0.69}_{-0.72}$	$5.6^{+1.0}_{-1.0}$	$58.94^{+0.42}_{-0.42}$	$0.66^{+0.16}_{-0.14}$	$\left(1.16^{+0.99}_{-0.69}\right) \times 10^{0}$
XTEJ1550-564	2000	exp+lin	A	$50.9^{+2.9}_{-3.3}$	$51715.25^{+0.57}_{-0.48}$	$34.2^{+3.0}_{-2.6}$	$0.37^{+0.10}_{-0.10}$	$61.78^{+0.38}_{-0.37}$	$0.96^{+0.15}_{-0.16}$	$\left(19.8^{+8.3}_{-6.7}\right) \times 10^{0}$
	2001	exp	B	$52.4^{+6.0}_{-3.9}$	$52014.5^{+9.5}_{-6.5}$	$\cdots$	$47.4^{+2.0}_{-2.0}$	$61.9^{+5.0}_{-5.8}$	$0.96^{+0.10}_{-0.09}$	$> 9.8 \times 10^{0}$
	2001/2002	exp+lin	A	$37.0^{+3.4}_{-3.4}$	$52339.91^{+0.94}_{-0.94}$	$5.18^{+0.96}_{-0.99}$	$30.6^{+3.6}_{-3.6}$	$60.38^{+0.64}_{-0.63}$	$0.99^{+0.15}_{-0.15}$	$\left(27.2^{+12.1}_{-9.5}\right) \times 10^{0}$
	2003	exp+lin	A	1000^{+10}_{-10}	$52776.93^{+0.74}_{-0.73}$	$4.61^{+0.83}_{-0.84}$	$4.5^{+2.1}_{-2.0}$	$61.89^{+0.55}_{-0.52}$	$0.96^{+0.15}_{-0.14}$	$\left(1.00^{+0.39}_{-0.32}\right) \times 10^{0}$
XTEJ1650-500	2001/2002	exp+lin	B	1267^{+47}_{-59}	$52230.90^{+2.1}_{-1.5}$	$45.8^{+1.7}_{-2.1}$	533^{+16}_{-16}	$93.1^{+1.3}_{-1.3}$	$0.19^{+0.03}_{-0.05}$	$\left(7.3^{+7.8}_{-4.6}\right) \times 10^{-2}$
MAXIJ1659-152	2010/2011	exp+lin	A	3000^{+350}_{-380}	$55522.6^{+1.9}_{-1.6}$	$30.0^{+3.2}_{-2.8}$	$5.8^{+2.1}_{-2.1}$	$60.7^{+1.2}_{-1.2}$	0.27 ± 0.06	$\left(2.9^{+8.2}_{-2.0}\right) \times 10^{-3}$
GX339-4	1996–1999	exp+lin	B	2700^{+10}_{-10}	$51254.8^{+1.3}_{-1.3}$	$75.6^{+1.7}_{-1.6}$	$10.0^{+2.1}_{-2.1}$	$167.2^{+2.1}_{-2.3}$	0.25 ± 0.06	$\left(4.7^{+7.0}_{-3.1}\right) \times 10^{-2}$
	2006	lin	A	2456^{+10}_{-10}	$53742.7^{+1.1}_{-1.1}$	$160.0^{+1.0}_{-1.0}$	$\cdots$	$\cdots$	$\cdots$	$< 1.2 \times 10^{-1}$
	2008	exp	B	$16.7^{+3.2}_{-2.9}$	$54802.3^{+8.5}_{-8.2}$	$\cdots$	$6.9^{+2.0}_{-2.0}$	$168.2^{+5.9}_{-5.8}$	0.25 ± 0.06	$> 6.8 \times 10^{-1}$
	2009	exp	B	$22.8^{+6.0}_{-3.5}$	$55048.3^{+5.6}_{-7.6}$	$\cdots$	$1.31^{+0.49}_{-0.52}$	$166.9^{+5.0}_{-4.5}$	0.25 ± 0.06	$> 6.9 \times 10^{-1}$
	2013	exp	B	0.03 ± 0.01	$56716.0^{+4.8}_{-4.5}$	$\cdots$	0.01 ± 0.005	$172.4^{+3.1}_{-3.5}$	$0.24^{+0.06}_{-0.05}$	$> 3.3 \times 10^{-1}$
	2014/2015	exp+lin	B	2218^{+16}_{-15}	$57233.70^{+0.34}_{-0.34}$	$56.77^{+0.34}_{-0.33}$	$0.14^{+0.23}_{-0.11}$	$188.90^{+0.25}_{-0.23}$	0.22 ± 0.05	$\left(5.7^{+8.5}_{-3.7}\right) \times 10^{-2}$
SWIFTJ1745-26	2012/2013	exp+lin	B	13280^{+100}_{-100}	$56266.5^{+2.8}_{-2.6}$	$104.0^{+4.2}_{-4.4}$	3070^{+100}_{-100}	$81.5^{+1.9}_{-1.9}$	$0.41^{+0.10}_{-0.09}$	$\left(4.4^{+3.7}_{-2.7}\right) \times 10^{-3}$
MAXIJ1836-194	2011/2012	exp+lin	B	1132^{+25}_{-22}	$55894.4^{+2.7}_{-2.6}$	$212.8^{+2.6}_{-2.7}$	1027^{+16}_{-15}	$93.1^{+1.8}_{-2.0}$	0.22 ± 0.05	$\left(7.3^{+6.3}_{-4.5}\right) \times 10^{-3}$
XTEJ1859+226	1999/2000	exp+lin	A	2648^{+13}_{-13}	$51507.12^{+0.12}_{-0.11}$	$111.55^{+0.52}_{-0.50}$	152^{+10}_{-10}	$56.61^{+0.066}_{-0.084}$	$0.51^{+0.14}_{-0.09}$	$\left(5.0^{+6.8}_{-3.2}\right) \times 10^{-3}$

[a] Class of the outburst describing how confident we are in the fit given the available data. See Section 4.4.2 for a detailed explanation for each individual outburst.

[b] from Chapter 3 and Paper I.

[c] Upper and lower limits on $C_{\rm irr}$ are calculated in the cases of pure linear decays by assuming f_t is the maximum observed flux and pure exponential decays by using the minimum observed flux, respectively.

4.4.2 The Outburst Light-Curve Sample

In Table 4.3, each outburst in our sample has been assigned a class (A, B, or C) to indicate how confident we are that the best fit preferred by our algorithm accurately describes and constrains the outburst light-curve behaviour.

We define these three classes as follows: (A) the data clearly constrain the shape of both the viscous (exponential) and irradiation-controlled (linear) stages of the decay, as well as the transition point between these two stages; (B) while the data clearly indicate an exponential or linear decay type, missing data in the early (near the outburst peak) or late (in the irradiation-controlled decay) stages of the outburst introduce uncertainty in the fitted transition flux or irradiation-controlled decay timescale; (C) due to insufficient data available, we cannot be confident in our identification of the decay type, or other fit parameters.

In the following paragraphs, we explain our reasoning behind our classifying individual outbursts as Class B or C.

> *GS1354-64 (1997/1998): (Class C)* While the algorithm prefers a pure linear fit, the limited data for this outburst does not clearly discriminate between a linear or exponential fit. The 2015 outburst of this source (for which we have relatively complete coverage of both the rise and viscous decay stage) peaks at a similar flux level to the first available data of the 1997/1998 outburst. Stochastic variability in an exponential decay may have led our algorithm to select a pure linear decay instead.
>
> *GS1354-64 (2015), GX339-4 (2013), and XTEJ1550-564 (2001): (Class B)* We have good coverage of the rise and viscous portion of the decay in these outbursts. While this is sufficient to derive a viscous timescale (see Paper I and Chapter 3), we do not observe the transition to the irradiation-controlled decay. Thus, our transition flux estimates cannot be considered reliable.
>
> *GX339-4 (1996-1999): (Class B)* While we have no coverage of the outburst peak, sufficient data is available from the later stages of the viscous decay through to quiescence. Thus, we are confident in the fitted transition flux

and irradiation-controlled decay timescale. We note that even though we are missing the outburst peak, comparison to other outbursts of the same source with more complete data coverage validates the fitted viscous timescale and value of α-viscosity derived from it (see Paper I and Chapter 3).

GX339-4 (2008 and 2009): (Class B) In both of these outbursts we have good data coverage of both the rise and a significant portion of the viscous decay, allowing for an accurate fitted viscous timescale. However, both light-curves display a significant data gap later in the viscous decay stage. It is possible that the source could have decayed to quiescence and exhibited a reflare during these gaps, bringing the validity of the fitted transition flux calculated by our algorithm into question.

GX339-4 (2014/2015): (Class B) We have good coverage of the rise and viscous portion of the decay in this outburst, and thus an accurate fitted viscous timescale. However, stochastic variability (e.g. secondary maxima) occurring around the transition between viscous and irradiation-controlled decay stages introduces uncertainty in the transition flux found by our algorithm. Further, clear structure is seen in the residuals during the late stages of the decay. Fitting synthetic model light-curves, which include the effects of disc evaporation (see Section 4.5.2), with our analytical algorithm, we encounter similar residual behavior. We postulate that the steeper decline seen in the data may be the result of the inner disc transitioning to a radiatively inefficient accretion flow, an effect not taken into account in our analytical algorithm.

MAXIJ1836-194 (2011/2012): (Class B) We have good coverage of the rise and viscous decay, then a data gap, after which the source is brighter than before the gap. It is unclear whether the transition to quiescence at the end of our data can be associated with the initial viscous decay, or whether the source would have transitioned to quiescence during the data gap, in the absence of the rebrightening episode.

SWIFTJ1745-26 (2012/2013) and XTEJ1650-500 (2001/2002): (Class B) We have sufficient data coverage during the rise and initial portion of the viscous decay stage, allowing for our algorithm to determine a viscous timescale from these light-curves. However, the irregular flaring behaviour seen in these outbursts (e.g. Yan & Yu 2017) requires the removal of much of the later data to fit an appropriate decay curve. The choice of which data to include is subjective and affects the final fitted parameters (transition flux and irradiation-controlled decay timescales) of these outbursts.

XTEJ1118+480 (2005): (Class C) We have only 11 data points in this decay. Although these are best-fit by an exponential decay, this conclusion is very uncertain. Furthermore, the best-fit decay from our algorithm generates an extremely low transition flux. These lead us to suggest that this decay is actually an irradiation-controlled decay and that this outburst completely lacks a viscous decay.

4.4.3 The Irradiation Constant ($C_{\rm irr}$)

Using our Bayesian hierarchical methodology (as described in Paper I, Chapter 3, and Section 4.2.3), we have sampled the strength of the X-ray irradiation heating the outer regions of BH-LMXB discs, parametrized with the irradiation constant $C_{\rm irr}$. For the 15 outbursts in our sample that display the full exp+lin decay profile, we derive $3 \times 10^{-3} < C_{\rm irr} < 30$. See Figures 4.1 and 4.2, and Table 4.3.

In Figure 4.1, we see that most, but not all of the systems with $C_{\rm irr} > 1$ (i.e., the most unphysically high $C_{\rm irr}$) are associated with long-period systems. Similarly, most, but not all, systems with $C_{\rm irr} > 1$ underwent “failed” outbursts. However, there are at least two long-period, “failed” outburst systems that do not have unphysical $C_{\rm irr}$. On the other hand, in Figure 4.2, we see that systems with $C_{\rm irr} > 1$ can occur in systems that are more strongly ($\alpha \sim 1$) and less strongly ($\alpha \sim 0.2$) transferring angular-momentum, regardless of the accretion state transitions made during the outburst. Future work on larger samples will be needed to test if long-period, “failed” outburst systems continue to dominate the systems where our Bayesian methodology predicts unphysically high $C_{\rm irr}$.

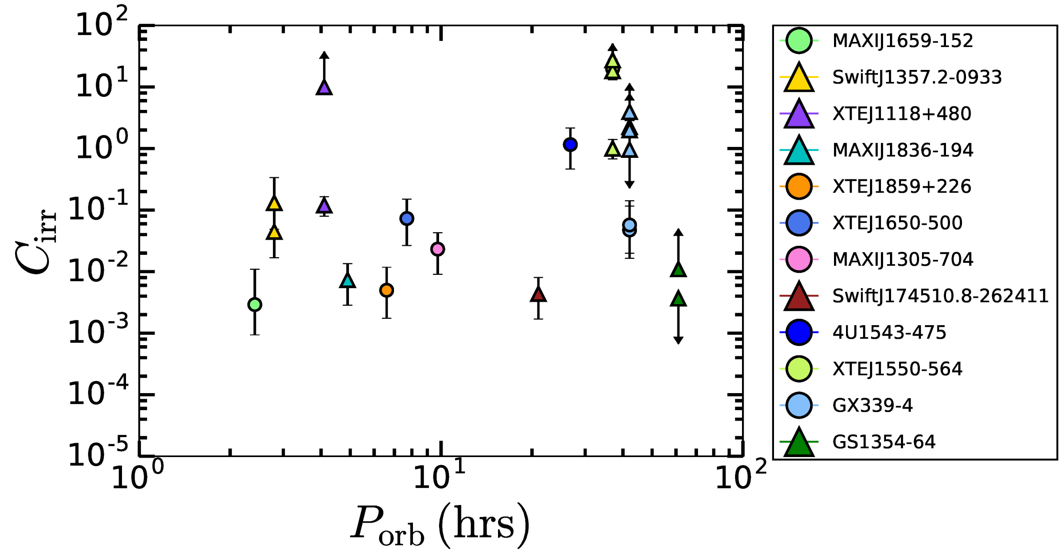

Figure 4.1: $C_{\rm irr}$, the parameter that encompasses the strength of the X-ray irradiation heating the surface of the outer regions of BH-LMXB accretion discs (derived by our Bayesian methodology) is plotted vs. binary orbital period ($P_{\rm orb}$). We include the 23 individual outbursts in our sample of 12 Galactic BH-LMXBs with measured orbital periods. Marker colours represent individual sources and marker shape indicates accretion state(s) reached during outburst: (circles) hard/intermediate/soft states and (triangles) only hard state. The error bars show the 68% confidence interval on $C_{\rm irr}$. $C_{\rm irr}$ is derived during both outbursts where the source cycles through all the accretion states (canonical) and those where the source remains only in the hard state (failed).

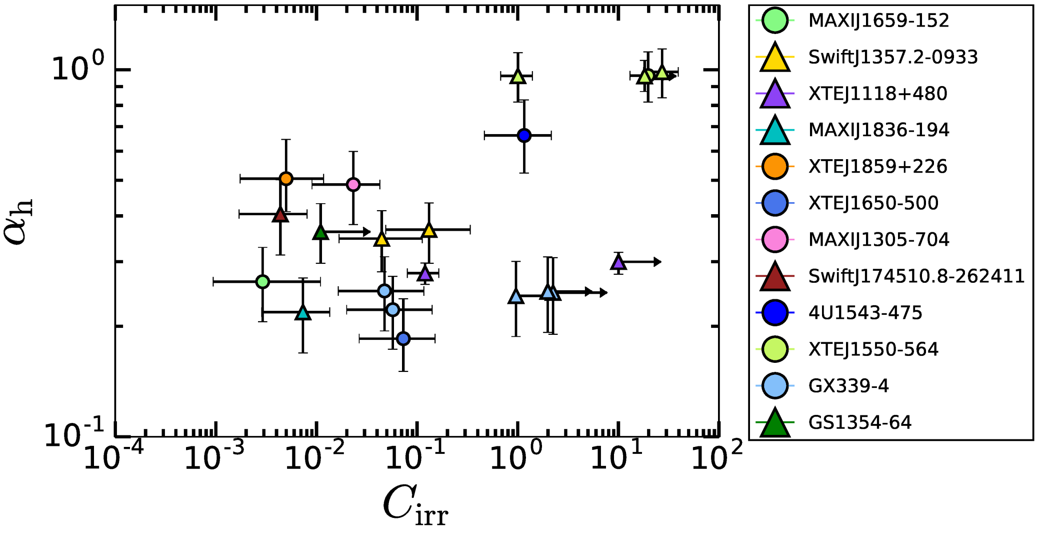

Figure 4.2: α-viscosity (α_h) plotted vs. $C_{\rm irr}$, derived from our Bayesian methodology. We include the 21 individual outbursts that exhibit exp+lin or pure exp decays. For the pure exp decays, only lower limits on $C_{\rm irr}$ are available. Marker colours represent individual sources and marker shape indicates accretion state(s) reached during outburst: (circles) hard/intermediate/soft states and (triangles) only hard state. The error bars show the 68% confidence intervals on $C_{\rm irr}$ and α_h.

4.5 Discussion

4.5.1 The Light-curve Profiles of BH-LMXB Systems

We have found 15 outbursts that display the full exponential+linear shaped decay profile and thus allow us to determine $C_{\rm irr}$ from the transition luminosity. We find values that are typically a factor ~ 5 higher than the expected value, $C_{\rm irr,expected} \sim 5 \times 10^{-3}$. Such values can arise if the albedo of the disc is low and if the intercepted fraction is high, both of which might result from an irradiation source that is large and causes X-rays to impinge on the disc vertically (e.g. via a corona). A value of $C_{\rm irr} \sim 3 \times 10^{-2}$ would still be compatible with the stability limits between transient and persistent LMXBs (Coriat et al., 2012).

However, we also find unphysical values of $C_{\rm irr} > 1$ in 4 outbursts and values >0.1 in 2 outbursts. The latter stretch credibility as they require an unrealistically high fraction of the X-ray flux to be reprocessed. In three cases (panels b, e, f of Figure 4.7) the transition luminosity is essentially set by the last flux measurement in the light-curve. At worst, we have an upper limit on the transition luminosity, hence a lower limit on $C_{\rm irr}$. This issue is not the case for the others, where the transition can be traced very well in the data. It is interesting to note that the most physically unrealistic values of $C_{\rm irr}$ occour in the largest-orbital-period systems.

We could overestimate $C_{\rm irr}$ for a variety of reasons in the context of the model that we applied to the data: because we underestimate the distance (hence L_X); because we underestimate the irradiation flux (e.g. if there is a large FUV contribution that is not accounted for); and because we overestimate the disc radius. We consider that these issues may lead to corrections of $O(1)$ but are unlikely to explain values of $C_{\rm irr}$ reaching 20, more than 1000 times the expected value.

We also find that the linear decay timescale τ_l and the exponential decay timescale τ_e differ significantly in some cases, whereas both should be comparable according to the model of King & Ritter (1998). This model implicitly assumes that the viscosity does not depend on the radius within the hot region of the disc. This assumption is unlikely to be realized since the disc is close to a steady-state Shakura & Sunyaev (1973) disc in this region, for which $\nu \propto R^{3/4}$ (see e.g., the physical model for nonstationary viscous α-discs from Lipunova & Shakura (2000) and its application to observations in Suleimanov et al. 2008 and Lipunova & Malanchev 2017).

In addition, α_h might be a function of radius (Coleman et al., 2016). In this case, τ_l will change slightly compared to τ_e and lead to a more complex relationship of $\dot{M}$ with time. The effect of mass loss via a wind in the hot region is also likely to change τ_l. However, in these cases, toy-model calculations (i.e., see Figure 3.4 Chapter 3) lead us to expect differences of O(1) between τ_e and τ_l, whereas differences of O(10) are found in Table 4.3, notably when $C_{\rm irr}$ is high.

The standard DIM interpretation of the linear-shaped portion of the decay profile is the result of a cooling front propagating inward through the disc at a speed controlled purely by the decaying X-ray irradiating flux. This model is most likely an oversimplification. Realistically, the ways in which these discs are irradiated are complicated by a number of factors. Some possible explanations to explain the light-curve profiles we observe are as follows:

> At some point in the outburst decay, the inner disc switches from a radiatively efficient thin disc to a radiatively inefficient corona (i.e. an advection dominated accretion flow; ADAF). The radiative efficiency η will decrease with time, whereas it is assumed constant in the model. The transition radius (between these accretion flows) will also move outward as the inner thin disc evaporates (Liu et al., 1999; Menou et al., 2000), on a timescale that may be comparable to the cooling front propagation timescale. This change differs from the model we use where the inner radius of the thin disc is assumed constant. A transition radius that propagates outward will terminate the decay prematurely and result in a small τ_l (Dubus et al., 2001).
>
> The irradiation geometry may not be constant during outbursts, due to changes in a disc warp or to properties of the X-ray corona (leading to $C_{\rm irr}$ changing during outburst; Esin et al. 2000). A major change would be if the source of irradiating X-rays is not at a distance R but is much closer to the reprocessing site (for instance if the X-rays are produced in the corona directly above the disc), leading to a measured $C_{\rm irr} > 1$ given our definition. This implies the

size of the X-ray emitting region would have to be comparable to the size of the optical emission region. We consider this unlikely since most of the energy dissipation in the accretion flow naturally occurs close to the compact object. Furthermore, the irradiation flux would not be decoupled from the local conditions, contrary to what is assumed in the model of the linear decay.

Spectral state transitions observed during outbursts (e.g. McClintock & Remillard, 2006) may change the amount of X-rays absorbed by the outer disc, either because the geometry changes (for instance, because the inner thin disc gives way to a geometrically thick disc, or the size of the corona changes, or an X-ray emitting jet structure appears) or because harder X-rays deposit heat deeper in the disc, thus leading to a temporally varying C_{irr}. However, there is no clear relation between the X-ray state and the value of C_{irr} in the systems investigated here (§4.3).

Heating of the outer disc by tidal heating of the expanding disc or by the stream impact of incoming material may keep the disc hot longer (Buat-Ménard et al., 2001a), especially if the mass-transfer rate from the companion is enhanced during outburst (Augusteijn et al., 1993; Esin et al., 2000).

A disc wind with the ability to remove a significant portion of disc mass throughout the outburst decay could affect how $\dot{M}$ changes with disc radius and, therefore, how L_X evolves with time (see e.g. Cannizzo, 2000). In our model here, we assumed $\dot{M}$ was constant with radius in the hot region. In Paper I and Chapter 3, we found strong evidence for disc winds throughout the outbursts, due to the unusually short viscous timescales (high α) we observe in the light-curves. There is some evidence that high values of C_{irr} are correlated with high values of α (Figure 4.2).

More generically, the transition luminosity that we are fitting might not be produced by a transition between an exponential and a linear (irradiation-controlled) decay. Instead, the transition luminosity may be produced by some other physical process going on in the disc or X-ray emission region, unrelated to the DIM (e.g. a change in how large-scale magnetic fields diffuse, or in rotational energy-extraction from the black hole, etc). In (at least) a quarter of our systems, some other physics must be altering the later parts of the light-curves. However, the observed exponential decay is a robust feature of a fully-irradiated disc accreting on a viscous timescale. Hence the results presented in Paper I (and Chapter 3) are unaffected by the issues raised above.

The 2002 outburst of 4U 1543−564 is the only outburst (of the 15 in this paper) where $C_{\rm irr}$ has been estimated previously. Comparing the optical/near-infrared and X-ray light-curves, Lipunova & Malanchev (2017) find $C_{\rm irr} < 6 \times 10^{-4}$, which is in conflict with our measurement of $C_{\rm irr} = 1.16^{+0.99}_{-0.69}$. This is one of the sources where we find a linear decay timescale τ_l and the exponential decay timescale τ_e that differ significantly. While this may point to an issue with the simplifying assumptions in King & Ritter (1998), this outburst remains difficult to fit when the formalism of Lipunova & Shakura (2000) and Lipunova & Malanchev (2017) is adopted.

Lipunova & Malanchev (2017) attempted to fit theoretical light-curves to the outburst: either $L_{\rm bol} \propto t^{-10/3}$ for a viscous decay (our "exponential" decay) or $L_{\rm bol} \propto (t - t_{\rm end})^{-40/13}$ for an irradiation-controlled decay (our "linear" decay), where $t_{\rm end}$ is the time the source returns to quiescence. Although they found an acceptable solution for the latter, they only fit to X-ray data taken within ~ 30 days of the peak X-ray flux. The X-ray data continue another ~ 30 days. While we can reproduce their fit when only ~ 30 days of X-ray data are included, a pure irradiation-controlled decay cannot fit the entire light-curve decay. This demonstrates the need for a more-detailed comparison (which is beyond the scope of this paper) of how different formalisms fit existing data, as well as how different formalisms can or cannot constrain α and $C_{\rm irr}$ based on X-ray light-curves alone.

4.5.2 Comparison of our Bayesian Methodology with Numerical Disc Codes

Given the occasional high values of $C_{\rm irr}$ that we measured in Section 4.4.3 and the potential issues regarding the simplifying assumptions that we discussed in Section 4.5.1, we investigate here how our Bayesian statistical methodology compares to numerical disc codes that were built to simulate accretion flows in binary systems. We have applied our method to a set of synthetic light-curves computed with the code described in Dubus et al. (2001), which uses the same description of the irradiation flux that we used. This code is developed from the numerical scheme of Hameury et al. (1998), adapted to include irradiation heating from Dubus et al. (1999) and inner disc evaporation (Menou et al., 2000). Using this code we have run 46 individual disc models that cover the large BH-LMXB parameter space well. These models vary from $4\,M_\odot < M_1 < 15\,M_\odot$, $3 \times 10^{10} < R_{\rm disc} < 1 \times 10^{12}$ cm, $0.1 < \alpha_h < 1.0$, and $0.005 < C_{\rm irr} < 0.1$.

By reversing the direction of our Bayesian hierarchical methodology, we gain the ability to predict a light-curve profile. In this case, the known priors used are M_1 and $R_{\rm circ}$ (specified for each code run) and q, taken as a uniform distribution between the minimum and maximum of the known values of q for all dynamically confirmed BHs in the Galaxy. The "backwards" Bayesian hierarchical methodology then uses these known priors in combination with known disc/system properties (α_h, $C_{\rm irr}$, $-\dot{M}_2$) specified for each code run, to sample the remaining parameters (τ_e, τ_l, and L_t) that our analytical irradiated DIM needs to describe a LMXB light-curve profile. For a detailed description of the implementation and use of our Bayesian hierarchical model, see Paper I and Chapter 3.

In 34 of the 46 runs, the heating fronts reach the outer edge of the discs. At the peak of each outburst in these runs, the entire disc is in the hot, ionized state (i.e. $R_h = R_{\rm disc}$). Thus, (as expected) we observe the characteristic exp+lin shaped decay profile. In the remaining 12 runs the heating fronts do not reach the outer edges of the discs due to weaker irradiation. As $R_h < R_{\rm disc}$ in these cases, the synthetic light-curves exhibit only a pure linear-shaped decay. Unfortunately, in these cases, where the heating front does not reach the outer edge of the disc, we are not able to predict the light-curve profile with the "backwards" Bayesian hierarchical methodology.

Taking into account only the runs in which the characteristic exp+lin shaped decay profile is observed, we find that the 1σ confidence intervals for the light-curves generated by the"backwards" Bayesian methodology include the synthetic model light-curve output by the numerical code in 74% (25/34) of the runs.

Figures 4.10–4.15 display light-curve comparison plots for a representative sample of disc models we have run, demonstrating how our Bayesian hierarchical methodology matches the light-curve profile predicted by the numerical code.

For each model, the "backwards" hierarchical methodology samples τ_e, τ_l, and L_t. These parameters can then be used to estimate α, and $C_{\rm irr}$ using the same method we used on the observed data. In Figures 4.3–4.5, we display correlation plots, comparing the three light-curve parameters (τ_e, τ_l, and L_t, where the latter corresponds to f_t at a known distance) derived from our Bayesian methodology to the same set of parameters predicted by the disc code. Here, each disc model run has been colour coded, with green and red representing those runs in which we effectively match and cannot match the model light-curves to within 1σ confidence intervals, respectively. For the well-matched light-curves, individual values of L_t are within 1 (9/25) – 2 (24/25) σ of the model values; we typically underpredict L_t by a factor of ~ 2. Similarly, individual values of τ_e are within 1 (12/25) – 2 (24/25) σ of the model values; we typically overpredict τ_e by a factor of ~ 1.2. We have more difficulties reproducing values of τ_l: 8, 12, and 16 out of 25 models are within 1, 2, and 3 σ of the model τ_l values, respectively. Here, if we correct for our underpredicting τ_l by a factor of ~ 1.5, we get much stronger agreement: 10 and 24 models are within 1 and 2 σ of the model τ_l, respectively.

Our slight overprediction of τ_e might suggest that the intrinisic α may be slightly higher than that we measured in Paper I and Chapter 3. This highlights that we were conservative there, even when claiming high values of α. We also note that the values of the α-viscosity in the hot disc (α_h) used to create the synthetic light-curves in each of the well-matched code runs are enclosed within the one-sigma confidence interval of the value of these parameters implied by the "backwards" Bayesian methodology in 24/25 cases (the other is within the 2 σ confidence interval).

While we underpredict L_t by a factor of ~ 2, this does not strictly transfer to our having overpredicted $C_{\rm irr}$ by a factor of ~ 2, as might be implied from Equation 4.5. In our Bayesian approach, we do not have a strong constraint on $R_{\rm disc}$. And in fact, our Bayesian values of $C_{\rm irr}$ are a factor of ~ 2 lower than the model's input value. Since $R_{\rm disc}$ is sampled from a uniform distribution between the circularization radius

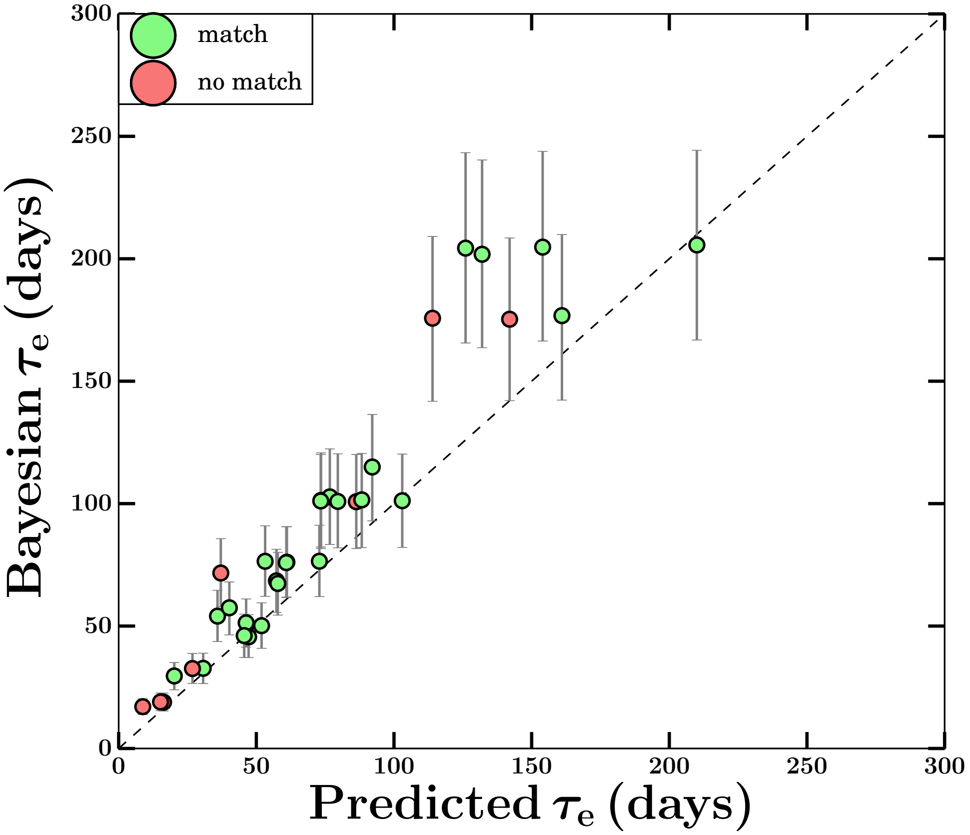

Figure 4.3: Correlation plot for the viscous timescale in the hot disc (τ_e), comparing the predicted value (from the numerical code) to the Bayesian value (from our methodology). Error bars show the 1σ confidence interval from our Bayesian methodology. Data is colour coded to show whether or not we can reproduce the entire model light-curve decay with our Bayesian method. The black dotted line represents the 1-to-1 line on the plot.

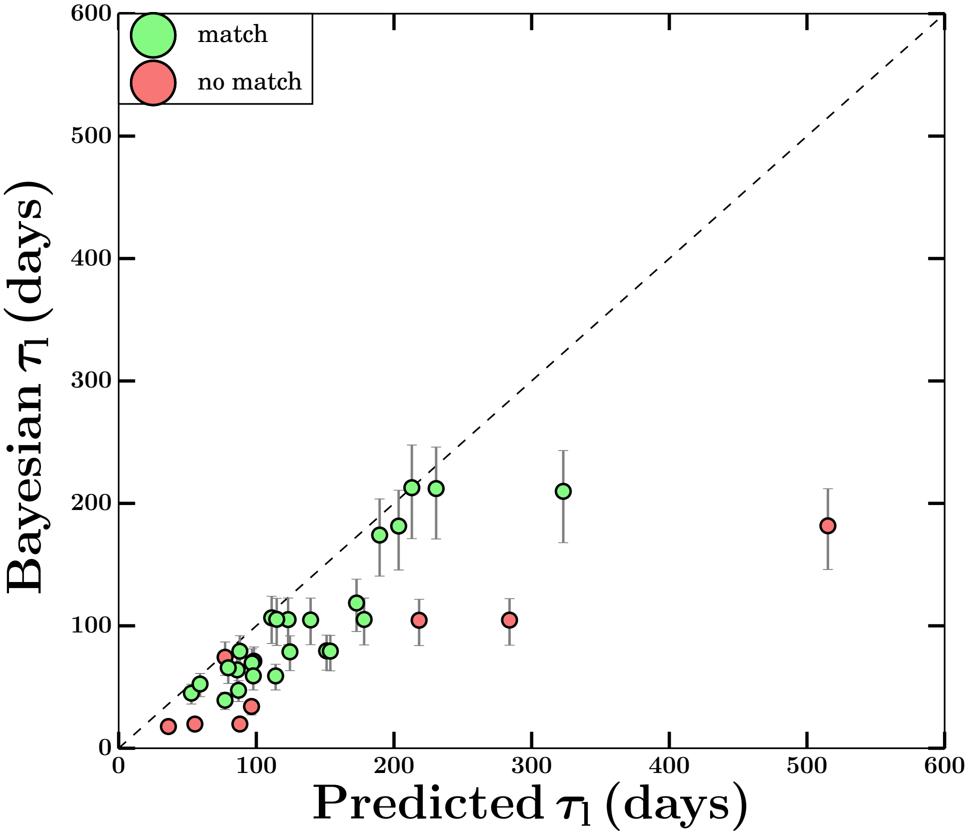

Figure 4.4: Correlation plot for the linear decay timescale in the disc (τ_l), comparing the predicted value (from the numerical code) to the Bayesian value (from our methodology). Error bars show the 1σ confidence interval from our Bayesian methodology. Colours are the same as in Figure 4.3. The black dotted line represents the 1-to-1 line on the plot.

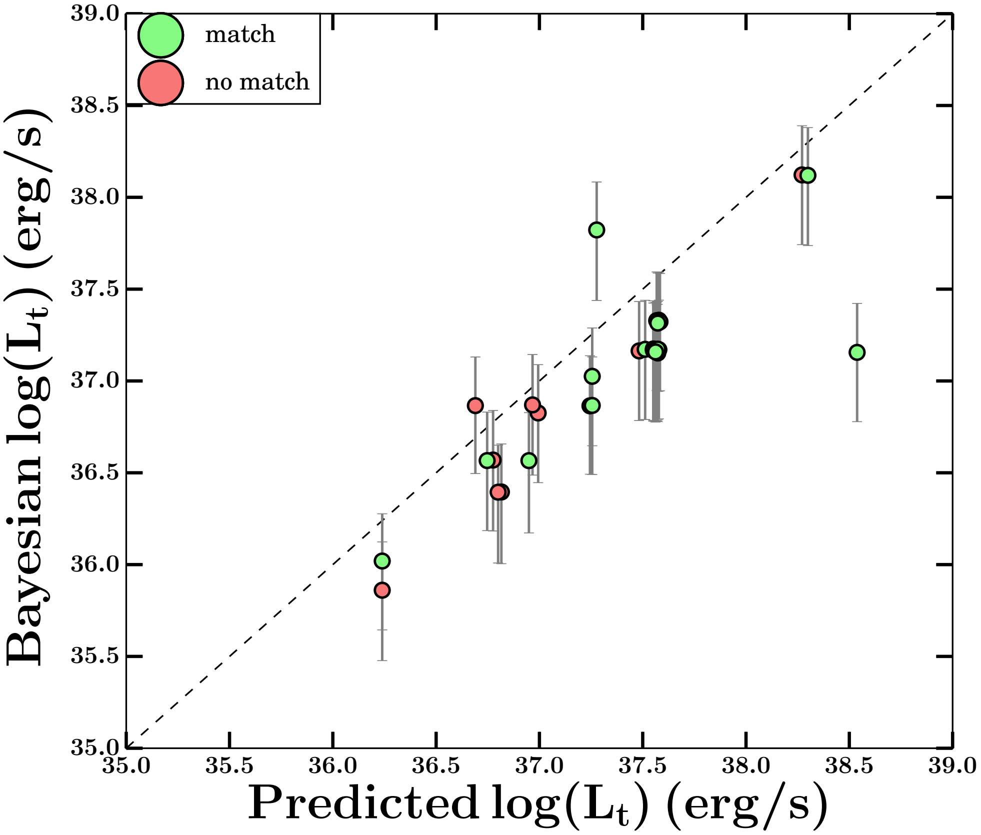

Figure 4.5: Correlation plot for the transition luminosity in the disc (L_t), comparing the predicted value (from the numerical code) to the Bayesian value (from our methodology). Error bars show the 1σ confidence interval from our Bayesian methodology. Colours are the same as in Figure 4.3. The black dotted line represents the 1-to-1 line on the plot.

$R_{\rm circ}$ and outer disc radius $R_{\rm max}$, $R_{\rm disc,median} \approx R_{\rm max}/2$). Given Equation 4.5, this explains how we can both underpredict L_t and $C_{\rm irr}$. Because of the large range in the $R_{\rm disc}$ prior, all but one of the 1 σ confidence intervals for $C_{\rm irr}$ from the Bayesian approach include the model value of $C_{\rm irr}$.

We note that correcting for our underprediction of $C_{\rm irr}$ exacerbates the issue of too-high $C_{\rm irr}$ values we report on in this Chapter. The large (and sometimes unphysical) values of $C_{\rm irr}$ that we are deriving via our Bayesian methodology are likely caused by a physical mechanism in the binary systems themselves.

Analyzing the 26% (9/34) of the runs that are unable to reproduce the model light-curves from the code, we find that our Bayesian methodology has trouble dealing with strong irradiation ($0.01 < C_{\rm irr} < 0.1$), when combined with large discs ($R_{\rm circ} > 1\times10^{11}$ cm) and large viscosities ($\alpha_h > 0.7$). We postulate that a possible explanation for this could stem from the fact that our Bayesian method is underestimating the increase in outburst duration that should happen, as a result of the delay in cooling-front propagation allowing more mass to be accreted, when irradiation is stronger. It remains unclear why our Bayesian method underestimates the timescale of the linear-shaped portion of the decay in these cases.

4.6 Summary

The X-ray light-curves of the recurring transient outbursts occurring in LMXBs encode within them the physics behind the mechanisms driving mass inflow and outflow in these binary systems. We have developed an algorithm that effectively links the disc-instability picture (including irradiation) to observations of real accretion discs. This algorithm characterizes a light-curve profile into definitive stages based on observable properties (i.e. timescales, flux) describing how matter moves through LMXB discs throughout an outburst.

We have tested this method against model light-curves calculated under the assumptions of the DIM, including irradiation and evaporation. We reproduce (to within 1σ confidence) the model light-curves derived from the numerical code for 74% of the disc models we ran, only having trouble reproducing specific models involving a combination of very strong irradiation, large discs, and large values of the α-viscosity parameter. We note that, with only the knowledge of the peak outburst flux/luminosity required, our Bayesian methodology can predict the outburst decay profile, and thus, may prove a tool to aid ongoing observational monitoring campaigns of X-ray binaries at optical through X-ray wavelengths.

Applying this Bayesian methodology to a representative sample of X-ray light-curves from outbursts occurring in BH-LMXBs, we have derived observational constraints on the efficiency of the angular-momentum transport process (α-viscosity; presented in Paper I and Chapter 3), and the strength of the X-ray irradiation heating (parametrized by $C_{\rm irr}$) , in the outbursts of LMXBs according to the DIM (this chapter).

We find that the strength of the X-ray irradiation parameter, describing the heating of the outer regions of the discs in these systems, lies in the range $3 \times 10^{-3} < C_{\rm irr} < 30$. Values of $C_{\rm irr} \geq 1$ are clearly unphysical. The outburst decay profile is predicted to show a final, linear-shaped stage, due to a cooling front propagating inward through the disc, at a rate controlled by the amount of irradiation heating. We conclude that our modeling of this stage inadequately describes part of our sample of BH-LMXB outburst light-curves.

We suggest that the varied light-curve morphology we observe proves that the late-time evolution of the disc is more complex than linear (a dependence that has been obtained using strong simplifying assumptions). It also provides indirect evidence for the existence of a temporal and spatially varying X-ray irradiation source heating the discs in these systems.

More likely, given the high values of $C_{\rm irr}$, it suggests that the light-curve morphology, beyond the exponential decays that are well-accounted for by a viscously-accreting fully-irradiated disc, involve a variety of physical mechanisms of which irradiation is only one. In particular, mass loss through inner disc evaporation to a radiatively-inefficient structure or through a magnetized disc wind may play a prominent role in shaping the outburst light-curves, a significant change in paradigm.

To begin to understand the evolution of accretion disc structure and the geometry of the X-ray irradiating source heating the discs through the course of a LMXB outburst, it is clear that we require a method that is (i) not limited by the complexity of light-curve morphology observed (e.g. can deal with variability on a range of timescales), or is (ii) tied directly to the simplifying assumptions of the DIM. Possible future avenues of investigation to effectively tackle this complex, multi-scale problem include: making use of simultaneous, multi-wavelength, time-series data sets and phase-resolved spectroscopic data.

For example, one could use the observed UVOIR spectral energy distribution (SED), at different times during an outburst, to model the irradiated disc in the binary system, with the goal of trying to understand the time-series evolution of the X-ray irradiation heating the disc in the system (e.g. Hynes 2005, Russell et al. 2006, Gierliński et al. 2009, Meshcheryakov et al. 2018). Also see Chapter 5 for implementation of this method to BH-LMXB SwiftJ1753.5-0127.

Another possibility is to make use of a combination of optical and X-ray light-curves of these systems. Here, constraints on $C_{\rm irr}$ can be derived by computing the fraction of X-ray emission needed to be reprocessed to explain the observed optical luminosity (e.g., see Suleimanov et al. 2008; Lipunova & Malanchev 2017).

A third possibility involves using the correlation between X-ray and optical variability often observed in LMXBs to understand physical properties of the different components (i.e. disc vs. corona) that make up the accretion flow in LMXBs. These properties include the size of the emitting regions, and the characteristic timescales at which matter moves through different regions of the accretion flow (e.g. Malzac et al. 2003; Hynes et al. 2004; Veledina et al. 2017; Gandhi et al. 2017).

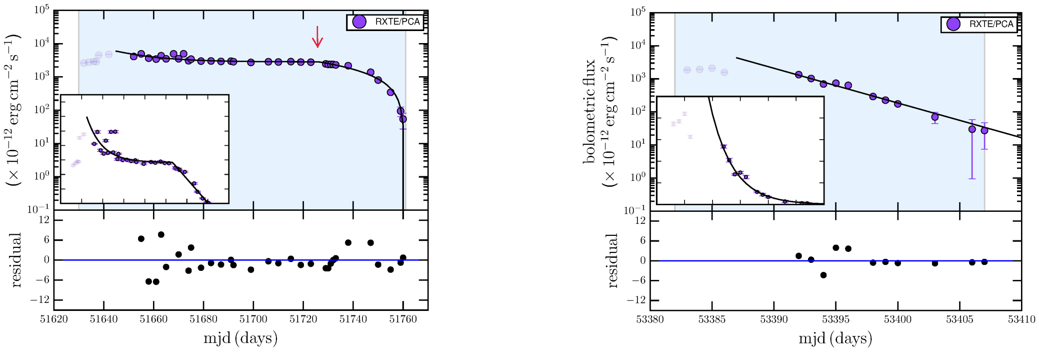

(a) 1999/2000 - XTEJ1118+480

(b) 2005 - XTEJ1118+480

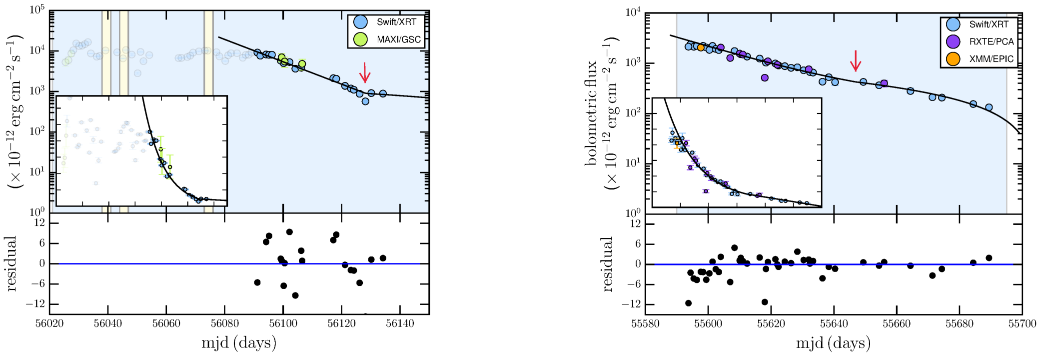

(c) 2012 - MAXIJ1305−704

(d) 2011 - SwiftJ1357.2−0933

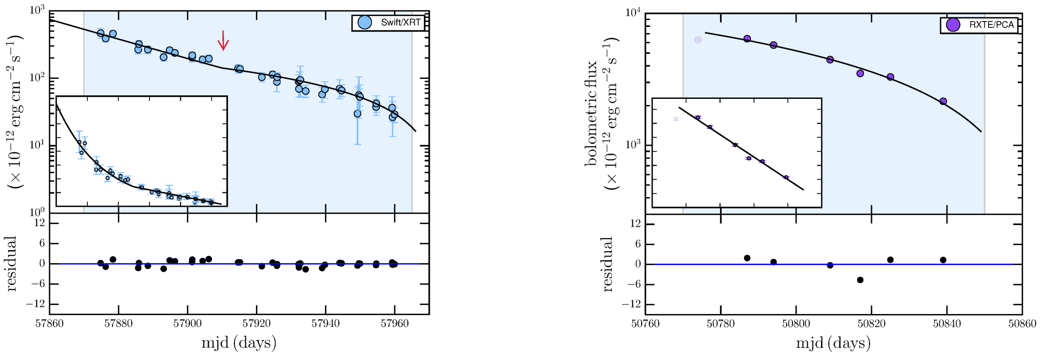

(e) 2017 - SwiftJ1357.2−0933

(f) 1997/1998 - GS1354−64

Figure 4.6: X-ray outburst light-curves for our BH-LMXB sample. Error bars are individual instrument uncertainties only. Inset axes show data on a linear scale. Red arrows indicate the transition between viscous and irradiation-controlled decay stages occurs (where applicable). Background shaded colours show accretion state(s) of the source, computed from the WATCHDOG project (Chapter 2; Tetarenko et al. 2016), throughout the outburst: blue = hard, yellow = intermediate, red = soft. The best fit analytical model is represented by the solid black line and residuals are presented in the lower panel of each figure. Coloured markers represent data from individual X-ray instruments: *RXTE*/PCA (purple), *Swift*/XRT (blue), *MAXI*/GSC (green), *Chandra*/ACIS-S and *Chandra*/HRC-S (pink), and *XMM-Newton*/EPIC (orange). Translucent data markers indicate portions of the outburst not included in the fit (e.g. outburst rise, flares and re-brightening events).

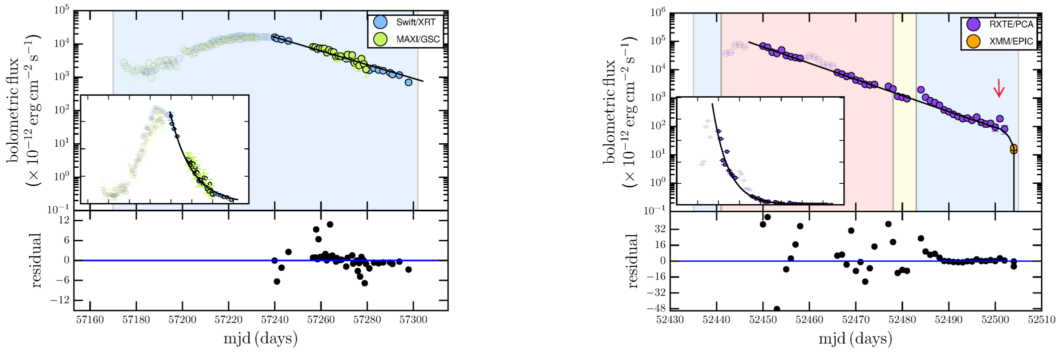

(a) 2015 - GS1354−64

(b) 2002 - 4U1543−475

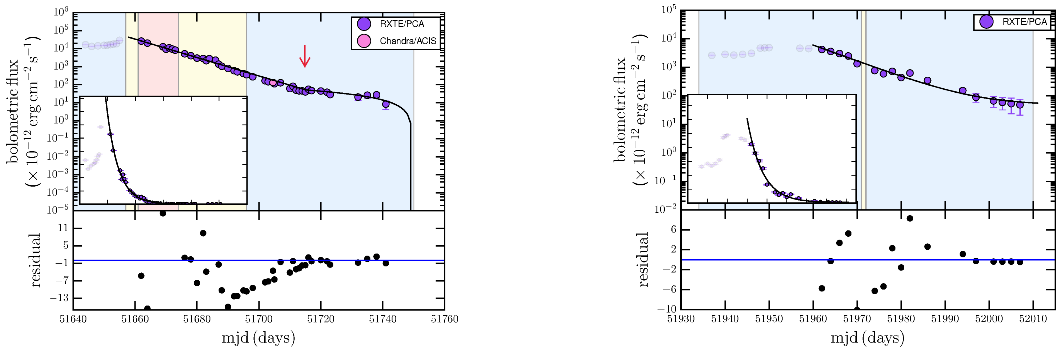

(c) 2000 - XTEJ1550−564

(d) 2001 - XTEJ1550−564

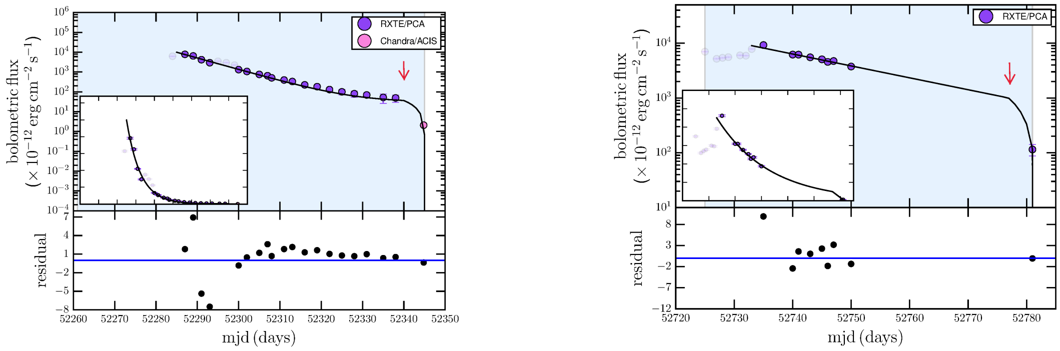

(e) 2001/2002 - XTEJ1550−564

(f) 2003 - XTEJ1550−564

Figure 4.7: X-ray outburst light-curves for our BH-LMXB sample - Part 2. See Figure 4.6 for details.

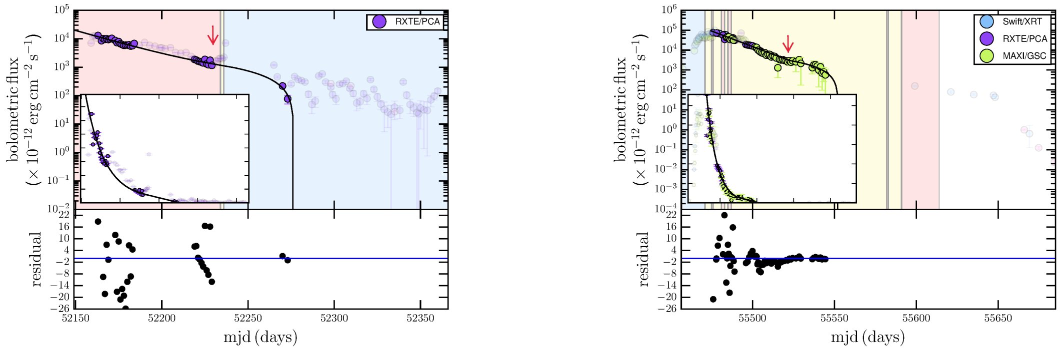

(a) 2001/2002 - XTEJ1650−500

(b) 2010/2011 - MAXIJ1659−152

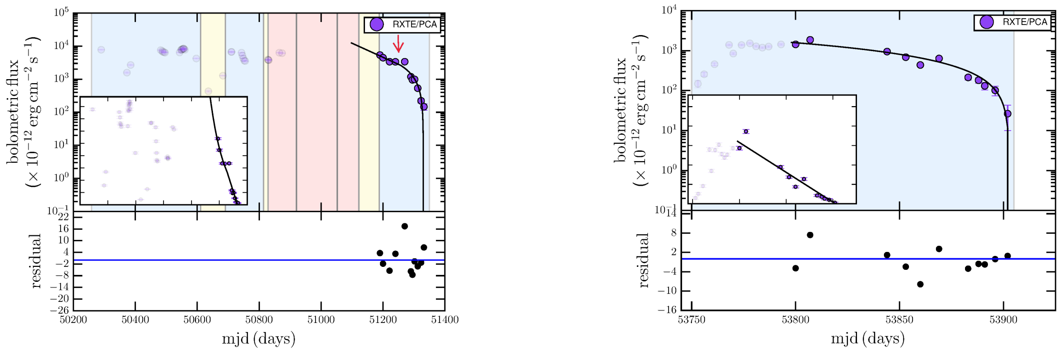

(c) 1996-1999 - GX339−4

(d) 2006 - GX339−4

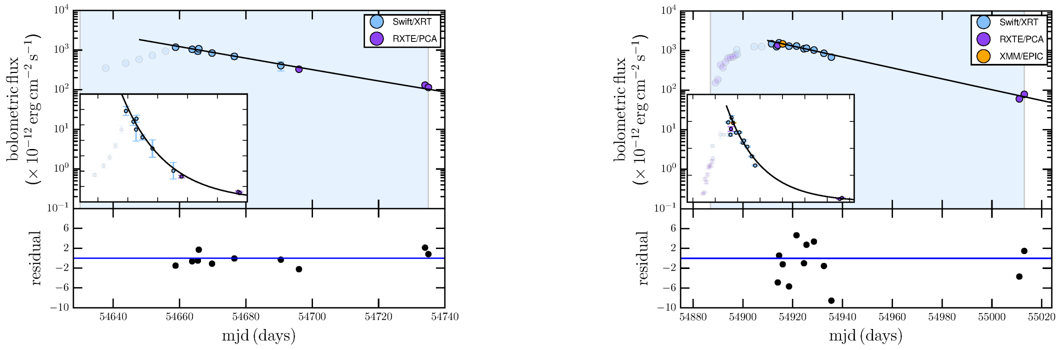

(e) 2008 - GX339−4

(f) 2009 - GX339−4

Figure 4.8: X-ray outburst light-curves for our BH-LMXB sample - Part 3. See Figure 4.6 for details.

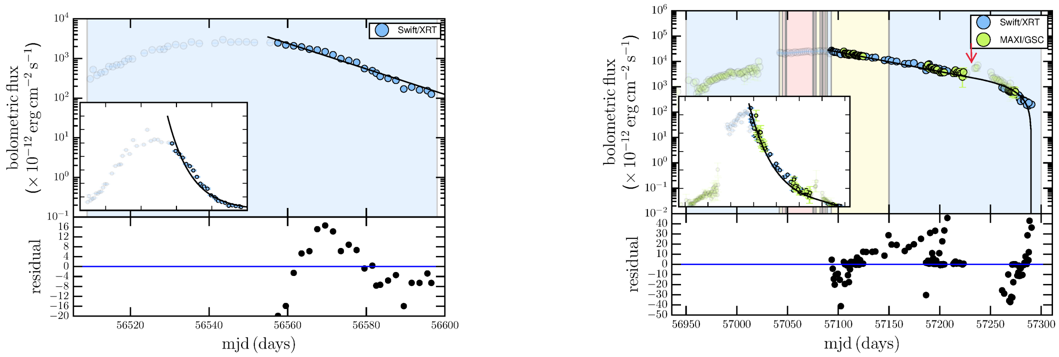

(a) 2013 - GX339−4

(b) 2014/2015 - GX339−4

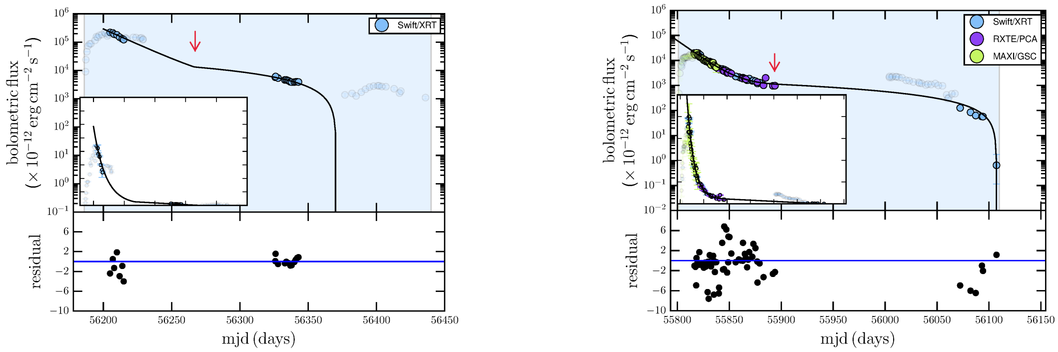

(c) 2012/2013 - SWIFTJ1745−26

(d) 2011/2012 - MAXIJ1836−194

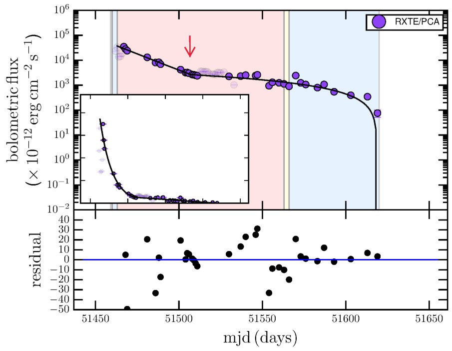

(e) 1999/2000 - XTEJ1859+226

Figure 4.9: X-ray outburst light-curves for our BH-LMXB sample - Part 4. See Figure 4.6 for details.

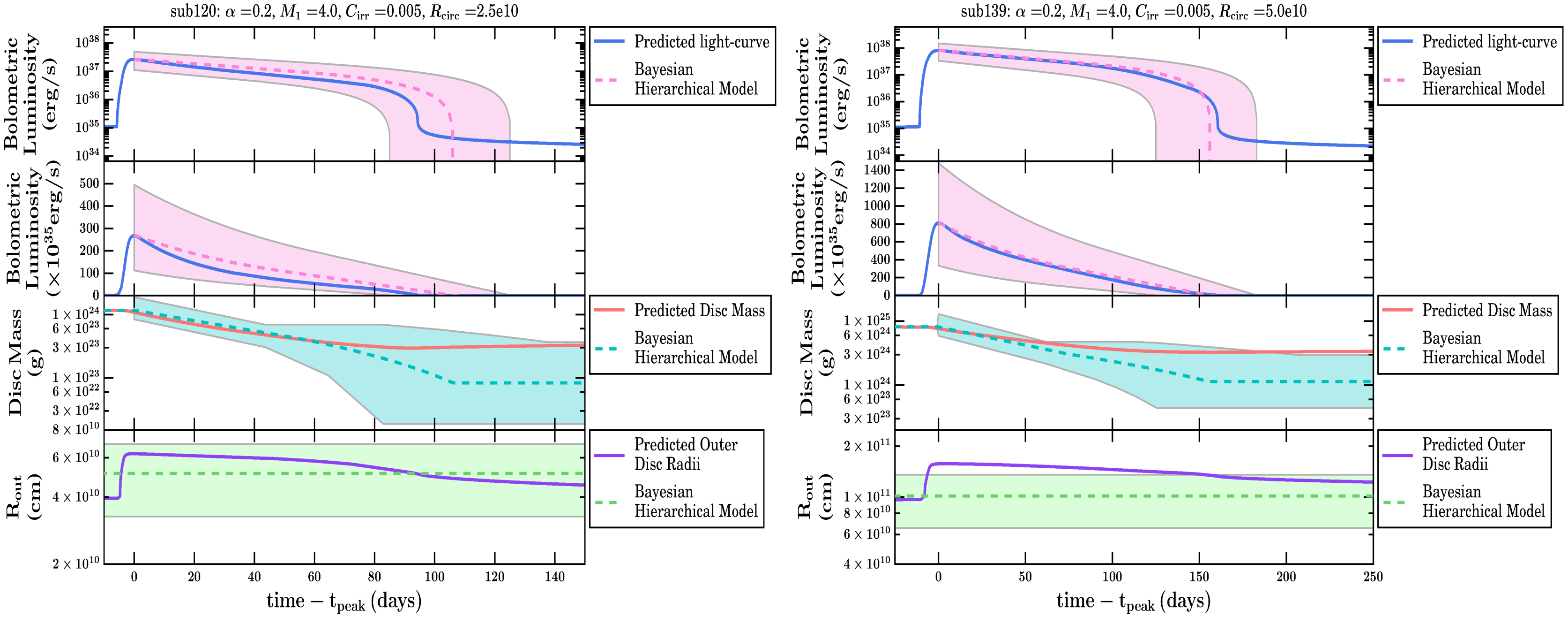

Figure 4.10: Example outburst correlation plots comparing the predicted (from the numerical code) and Bayesian estimates (from our methodology) of the: light-curve decay profiles in log (top panel) and (second panel) linear space, (third panel) mass in the hot disc over time, and (bottom panel) outer disc radius, for varying M_1, α_h, C_{irr}, and R_{circ}. The solid lines represent the output of the numerical code. The dotted lines and shaded regions represent the best-fit value and 1σ confidence intervals from our Bayesian methodology, respectively.

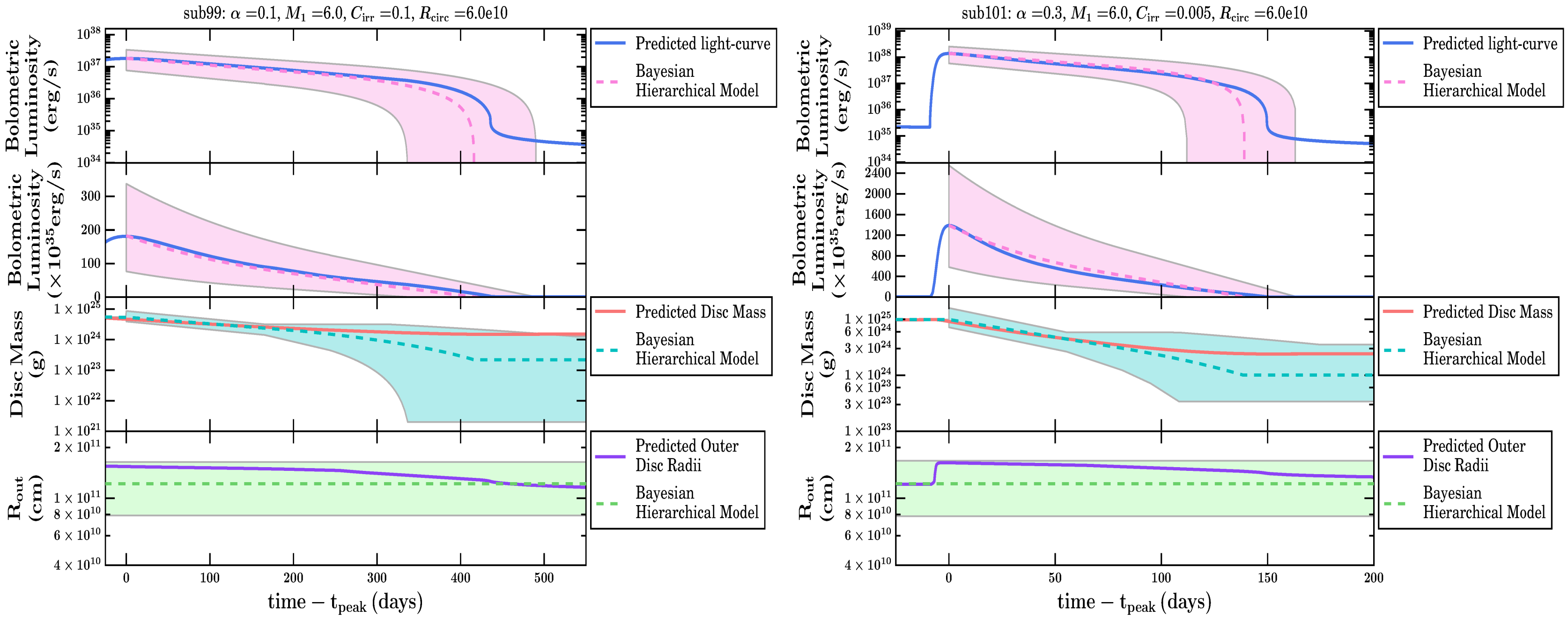

Figure 4.11: Example Outburst Correlation Plots - Part 2. See Figure 4.10 for details.

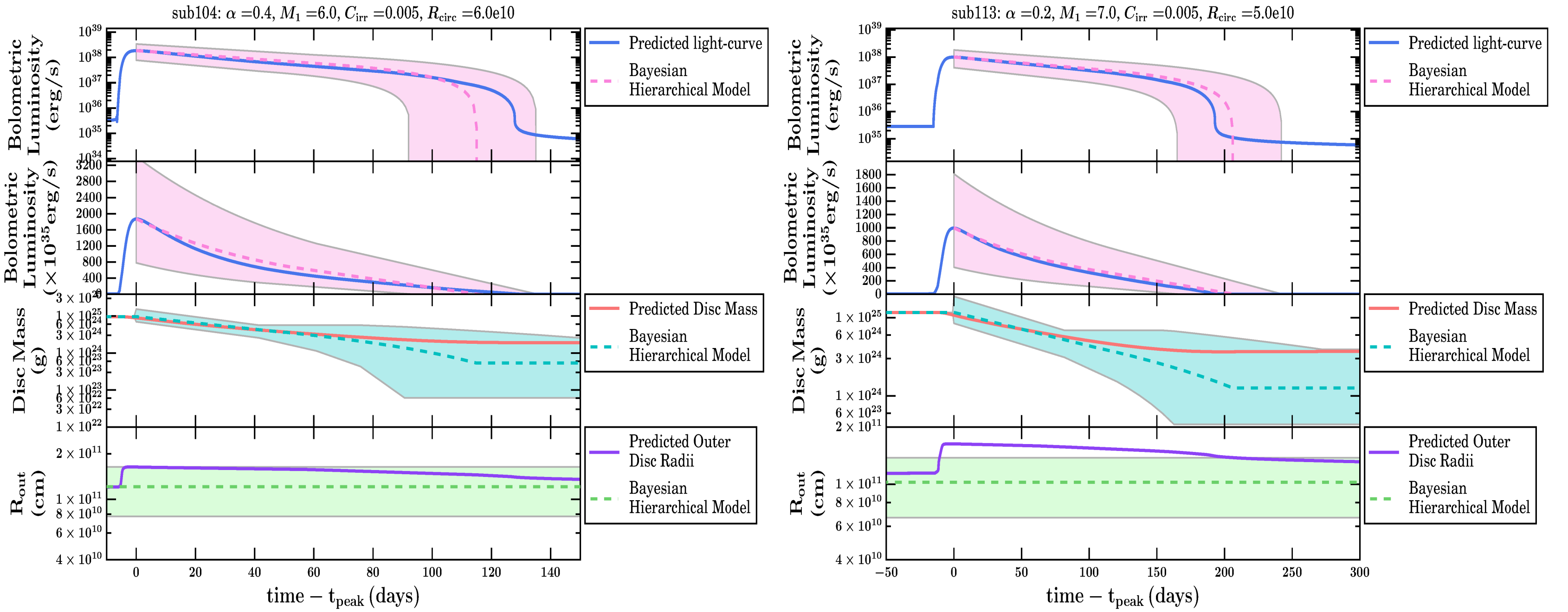

Figure 4.12: Example Outburst Correlation Plots - Part 3. See Figure 4.10 for details.

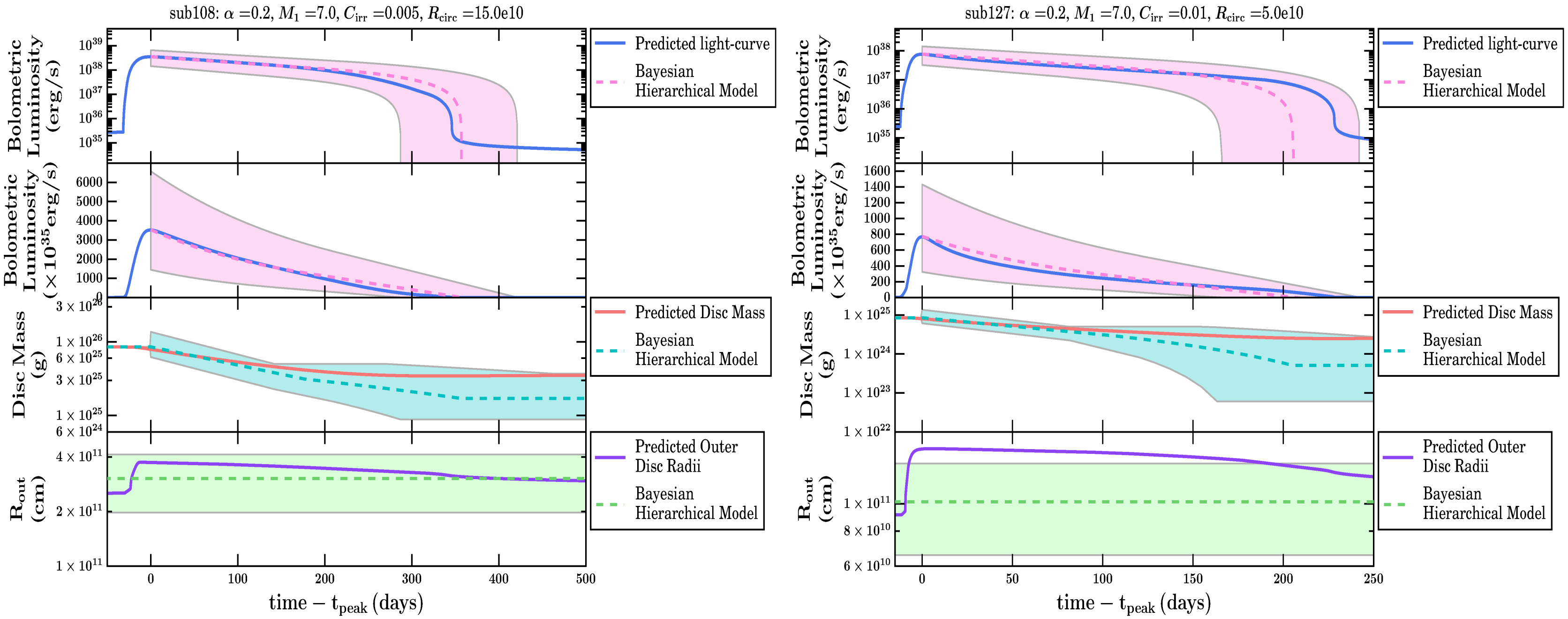

Figure 4.13: Example Outburst Correlation Plots - Part 4. See Figure 4.10 for details.

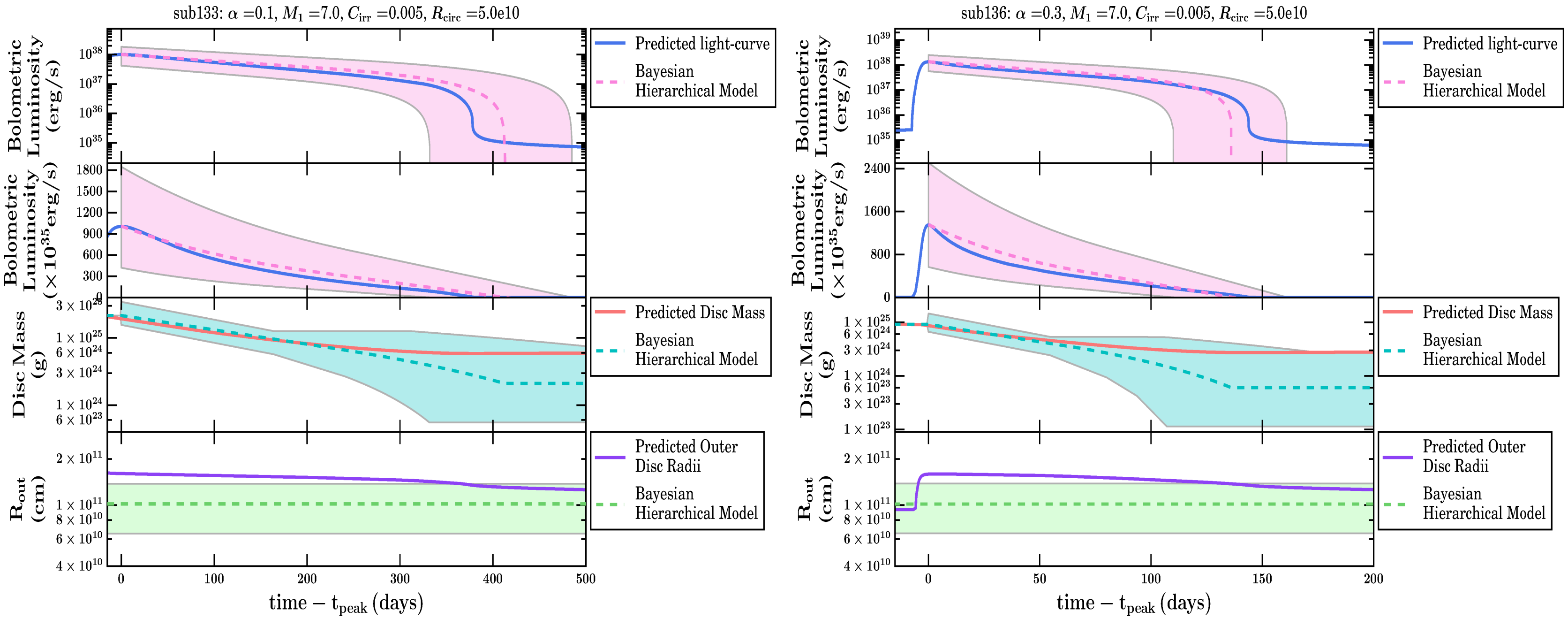

Figure 4.14: Example Outburst Correlation Plots - Part 5. See Figure 4.10 for details.

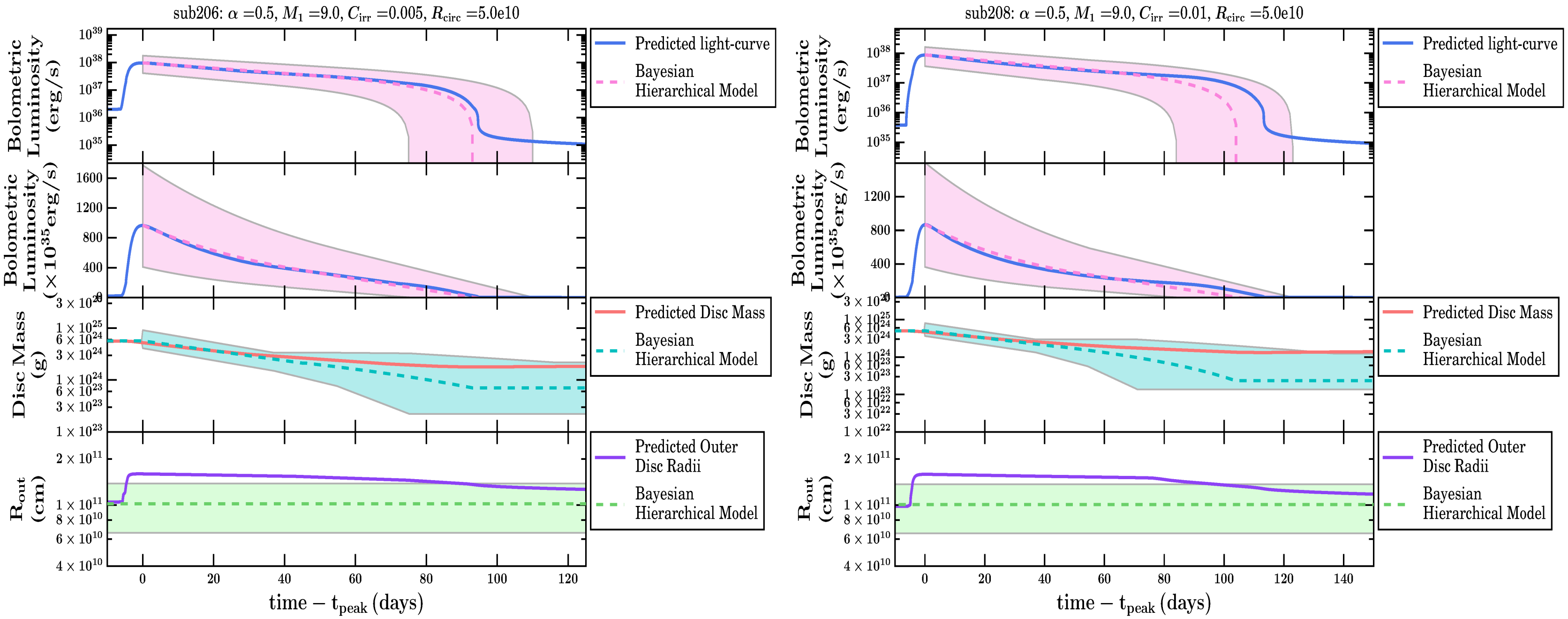
sub206: α =0.5, M_1 =9.0, $C_{\rm irr}$ =0.005, $R_{\rm circ}$ =5.0e10

sub208: α =0.5, M_1 =9.0, $C_{\rm irr}$ =0.01, $R_{\rm circ}$ =5.0e10

Figure 4.15: Example Outburst Correlation Plots - Part 6. See Figure 4.10 for details.

Chapter 5

The Curious Case of Swift J1753.5-0127: A BH-LMXB Analogue to Z Cam Type Dwarf Novae

Shaw, A.W., Tetarenko, B.E., Dubus, G., Dincer, T., Tomsick, J.A.,
Gandhi, P., Plotkin, R.M., and Russell, D.M.,

Monthly Notices of the Royal Astronomical Society, submitted (2018)

ABSTRACT

Swift J1753.5-0127 (J1753) is a candidate black hole low-mass X-ray binary (BH-LMXB) that was discovered in outburst in May 2005. It remained in outburst for ~ 12 years, exhibiting a wide range of variability on various timescales, before entering quiescence after two short-lived, low-luminosity "mini-outbursts" in April 2017. The unusually long outburst duration in such a short-period ($P_{\mathrm{orb}} \approx 3.24$ hrs) source and complex variability observed during this outburst period, challenges the predictions of the widely accepted disc-instability model, which has been shown to broadly reproduce the behaviour of LMXB systems well. The long-term behaviour observed in J1753 bears a striking resemblance to the Z Cam class of dwarf novae, whereby variable mass-transfer from the companion star drives unusual outbursts, characterized by stalled decays and abrupt changes in luminosity. Using sophisticated modelling of the multi-wavelength light-curves and spectra of J1753 during the ~ 12 years the source was active, we investigate the hypothesis that periods of enhanced

mass-transfer from the companion star may have driven this unusually long outburst. Our modelling suggests that J1753 is in fact a BH-LMXB analogue to Z Cam systems, where the variable mass-transfer from the companion star is driven by the changing irradiation properties of the system, affecting both the disc and companion star.

5.1 Introduction

Low-mass X-ray binaries (LMXBs) are binary systems consisting of a compact object (black hole or neutron star) accreting matter from a low-mass ($\lesssim 1M_{\odot}$) main sequence companion. Most LMXBs exhibit transient behaviour, characterized by long periods of quiescence (years to decades), followed by bright outbursts in which the X-ray and optical luminosity increases by several orders of magnitude (Chen et al., 1997; Tetarenko et al., 2016).

The mechanism behind LMXB outbursts can broadly be explained with the disc-instability model (DIM; Osaki, 1974; Meyer & Meyer-Hofmeister, 1981; Smak, 1983, 1984; Cannizzo et al., 1985; Cannizzo, 1993; Huang & Wheeler, 1989). Originally developed to explain outbursts in dwarf novae, the DIM explains transient behaviour in the context of the accretion disc cycling between a hot, ionized outburst state and a cool, neutral, quiescent state. This limit-cycle is triggered by the accumulation of matter in the disc, eventually heating the disc until a substantial portion is ionized. In this hot, ionized state, the viscosity (i.e., ability to move angular momentum outwards) of the disc dramatically increases, ultimately resulting in matter rapidly falling onto the compact object, triggering a bright outburst.

The DIM has been shown to reproduce the global behaviour of a number of transient and persistent LMXBs (e.g. Coriat et al., 2012; Tetarenko et al., 2016). However, to do so it must be modified to include irradiation heating from the inner accretion disc (hereafter the IDIM; Dubus et al., 1999, 2001). Most of the ultraviolet, optical and infrared light emitted by LMXB accretion discs is the result of reprocessed X-rays from the inner regions of the accretion flow heating the outer disc[1] (van

---

[1] Note that there exists alternative models attributing the dominant source of optical/UV emission (during LMXB outbursts) to self-produced synchrotron emission from a hot corona flow, rather then the irradiated disc itself. See Veledina et al. (2017) and references therein.

Paradijs, 1983; van Paradijs & McClintock, 1994; van Paradijs, 1996). This X-ray irradiation is the dominant factor determining the temperature over the majority of the accretion disc during outburst. However, despite decades of theoretical work, the actual fraction of the central X-ray flux that is intercepted and reprocessed in the outer disc regions of LMXBs remains largely uncertain.

Outburst durations in LMXBs harbouring stellar-mass black holes (BH-LMXBs) are typically consistent with the viscous timescale of accretion discs (∼months, see Chapters 2 and 3, as well as Tetarenko et al., 2016, 2018b). Therefore, studying these binary systems during outburst allows us to probe the fundamental physics of accreting X-ray irradiated discs on accessible timescales. Recently, Tetarenko et al. (2018b) developed an analytical methodology to describe the outburst light-curves of the Galactic BH-LMXB population in the context of the irradiated DIM (see Chapter 3 and 4). With this methodology, Tetarenko et al. (2018b) were able to quantify both angular-momentum and mass transport (via the α-viscosity parameter; Shakura & Sunyaev 1973) within these discs, and the physical properties of their X-ray irradiation heating.

In another recent study (see Chapter 4), Tetarenko et al. (2018a) demonstrated how the extremely diverse light-curve morphology observed across the BH-LMXB population suggest there likely is a temporally and spatially varying irradiation source heating the discs in these systems. In this Chapter, we build on their progress, presenting an alternative method to tackle this complex, multi-scale problem using the unusual BH-LMXB Swift J1753.5-0127 as a case study.

Swift J1753.5-0127 (hereafter J1753) was discovered by the Burst Alert Telescope (BAT; Barthelmy et al., 2005) on board the *Neil Gehrels Swift Observatory* (*Swift*) in 2005 (Palmer et al., 2005). The source luminosity peaked within a week, at a flux of ∼200 mCrab, as observed by the *Rossi X-Ray Timing Explorer*'s (*RXTE*) All-Sky Monitor (Cadolle Bel et al., 2007). Identification of an $R \sim 16$ optical counterpart (Halpern, 2005), ~ 5 magnitudes brighter than the limit of the Digitized Sky Survey, established J1753 as a new LMXB.

Although the mass of the primary has not yet been dynamically measured, J1753 is classified as a BH candidate (BHC). *RXTE* observations revealed a 0.6 Hz quasi-periodic oscillation (QPO) with characteristics typical of BHCs (Morgan et al., 2005). In addition, the hard X-ray spectrum was found to exhibit a hard power-law tail up to $\sim$ 600 keV, very typical of a BHC in the hard accretion state (Cadolle Bel et al., 2007). By investigating the double-peaked hydrogen recombination lines in the optical spectrum, Shaw et al. (2016a) calculated a conservative lower limit to the mass of the primary, $M_1 > 7.4 \pm 1.2\mathrm{M}_{\odot}$, strongly favouring a BH nature for the compact object in J1753. The orbital period of J1753 is known to be $P_{\rm orb} \approx 3.24\mathrm{h}$[2] from periodic variability in its optical light-curves observed during outburst (Zurita et al., 2008). The high amplitude variations in the R-band orbital light-curve suggest that the inclination, i, is high. However, the source is neither dipping[3] nor eclipsing, and a measurement of i remains elusive (see Shaw et al., 2016a); previous studies have adopted values of $i \gtrsim 40°$ (e.g. Neustroev et al., 2014; Tomsick et al., 2015). The distance, D, to J1753 is also an unknown. There is no measurement of a radio parallax, and optical parallax from *Gaia* in only poorly constrained (Gandhi et al., 2018). However, Zurita et al. (2008) estimate $D > 7.2$ kpc based on the relationship between $P_{\rm orb}$ and the observed peak V-band magnitude (Shahbaz & Kuulkers, 1998). Froning et al. (2014), on the other hand, derive $D < 7.7$ kpc from modelling the UV spectrum. In this Chapter, we assume the standard Galactocentric distance of $D = 8$ kpc.

Almost immediately after its peak, the flux of J1753 began to decline exponentially, as is typical with similar BH-LMXBs. However, instead of returning to quiescence the decay stalled, remaining at roughly constant flux at approximately $\sim$ 20 mCrab for over 6 months (Cadolle Bel et al., 2007), before appearing to increase in flux once more (see e.g. Shaw et al., 2013). For the following $\sim$ 11 years,

---

[2] This photometric period is likely a superhump period, slightly larger than the orbital period, due to an extreme mass ratio between the primary and the secondary. "Superhumps" are variations in the optical light-curve at a period close to that of the orbital period of the system, effectively distorting its shape. They are caused by the precession, within the binary, of an eccentric accretion disc, resulting in intrinsic variations in light observed from the disc (Charles & Coe, 2006). For discussion of superhumps in LMXBs, see Haswell et al. (2001).

[3] Periodic dips in X-ray flux, which repeat with orbital period, are observed in some LMXBs. This behaviour is caused by periodic shadowing of the X-ray emitting region by a structure (thought to be the impact region of the mass-transfer stream from the companion star) located in the outer disc.

the source continued to actively accrete, exhibiting significant long term variability (see e.g. Soleri et al., 2013; Shaw et al., 2013). J1753 remained a persistent LMXB in the hard accretion state for the majority of this prolonged period of activity, aside from a brief excursion to a low-luminosity soft, disc-dominated accretion state in 2015 (Shaw et al., 2016c; Rushton et al., 2016).

In November 2016, observations of J1753 with the Faulkes Telescope North indicated a fading optical flux (Russell et al., 2016; Al Qasim et al., 2016). Shaw et al. (2016b) confirmed the decay with a non-detection by both the *Swift* X-ray Telescope (XRT; Burrows et al., 2005) and Ultra-Violet/Optical Telescope (UVOT; Roming et al., 2005). Unfortunately due to the source becoming Sun constrained soon after the decay to quiescence was noted, follow-up opportunities were limited (Neustroev et al., 2016; Plotkin et al., 2016). Upon emerging from the Sun constraint, J1753 was found to be active once more, having undergone a mini-outburst[4] (Al Qasim et al., 2017; Bright et al., 2017; Tomsick et al., 2017) that lasted from late January 2017 until April 2017, when the flux appeared to return to quiescent levels (Shaw et al., 2017). However, in late April 2017, J1753 underwent another, shorter duration mini-outburst (Bernardini et al., 2017), before finally entering a seemingly more permanent quiescent state in July of the same year (Zhang et al., 2017).

In this Chapter, we initially focus on the first mini-outburst of J1753 during its descent into quiescence. We utilize near-simultaneous near-infrared (NIR), optical, ultraviolet (UV) and X-ray data in an attempt to model and constrain how the physical properties of the X-ray irradiation source heating an accretion disc varies over time during outburst. To achieve this we have developed a Bayesian algorithm to fit the observed UV, optical and NIR (UVOIR) spectral energy distribution (SEDs) with an irradiated disc model. We then compare the mini-outburst with the main outburst of J1753 in an attempt to investigate the nature of its long-term behaviour.

The Chapter format is as follows: Section 5.2 describes in detail the irradiated disc model and the Bayesian algorithm used to fit such a model to observed SEDs.

---

[4] We choose the nomenclature 'mini-outburst' to remain consistent with Plotkin et al. (2017), who note that the flux during this period was at similar levels prior to quiescence. Following Chen et al. (1997), such behaviour is referred to as a 'mini-outburst.' See discussion in Zhang et al. (2018, submitted).

Section 5.3 describes the observations that we have utilized in this work. Section 5.4 presents the results from fitting the X-ray spectra, UVOIR SEDs, X-ray light-curves, and UVOIR-X-ray correlations during the 12 yrs that J1753 was active. Section 5.5 discusses the nature of the unusual long-term behaviour displayed by J1753 over the past 12 years, drawing a parallel with Z Cam type dwarf novae. Lastly, Section 5.6 provides a summary of this work.

5.2 Modelling X-ray Irradiated Accretion Discs

5.2.1 The Irradiated Disc Model

Simultaneous, multi-wavelength data sets can constrain the evolution and X-ray irradiation and heating of the accretion disc through LMXB outbursts. By modelling the observed UVOIR SED of a LMXB system at different times throughout an outburst, one can effectively track the evolution of the physical properties of the X-ray irradiation source heating the disc in the system (e.g. Hynes 2005, Russell et al. 2006, Meshcheryakov et al. 2018).

Starting with a power-law temperature distribution of the form,

$$T(R) = T_{\rm in} \left(\frac{R}{R_{\rm in}} \right)^{-n}, \tag{5.1}$$

and assuming a local blackbody spectrum in a particular disc annulus at radius R, we can describe the integrated SED of the disc in terms of 3 parameters: the inner disc temperature ($T_{\rm in}$), temperature of the outer disc ($T_{\rm out}$), and the disc normalization ($N_{\rm disc}$). The resulting SED takes the form,

$$F_\nu = N_{\rm disc}^2 T_{\rm in,K}^{\frac{2}{n}} \nu^{3-\frac{2}{n}} I(x), \tag{5.2}$$

where $I(x)$ is Planck's law integrated over the disc, using the general substitution

$x = h\nu/k_bT$, and must be evaluated numerically. The normalization takes the form

$$N_{\rm disc} = \left(\frac{4\pi h^{1-\frac{2}{n}} k_b^{\frac{2}{n}} \cos(i)}{nc^2}\right)^{1/2} \left(\frac{R_{\rm in}}{\rm cm}\right) \left(\frac{D}{\rm cm}\right)^{-1}. \tag{5.3}$$

To model the X-ray irradiation heating LMXB accretion discs, we use the prescription presented in Dubus et al. (2001),

$$T_{\rm out}^4 = \frac{C_{\rm irr} L_X}{4\pi\sigma_{\rm SB} R^2}, \tag{5.4}$$

where the irradiating flux drops off with the inverse square of the disc radius. Here $C_{\rm irr}$ is a constant representing the fraction of the X-ray luminosity that is intercepted and reprocessed by the disc.

We consider temperature profiles (Eq. 5.1) with the power law index n equal to 1/2 (i.e., standard irradiated disc) or 3/7 (i.e., a maximally-irradiated, isothermal disc). In addition to these irradiated cases, we also consider the $n = 3/4$ model, appropriate for an non-irradiated disc. See Hynes et al. (2002b) and Hynes (2005) for detailed discussions of the various temperature profile options to fit UVOIR SEDs of LMXBs.

In addition to reprocessed X-rays, OIR emission may also be produced by relativistic jets, as seen to dominate during the hard accretion states of some BH-LMXBs (e.g., see Homan et al. 2005; Russell et al. 2006). These jets produce a flat optically thick spectrum that can extend from the radio to OIR wavelengths (Fender, 2001; Corbel & Fender, 2002; Homan et al., 2005; Russell et al., 2006; Chaty et al., 2011; Rahoui et al., 2015). To account for jet emission in the OIR regime, a two-parameter power-law component can be added to the disc models described above, as $F_\nu = N_{\rm pl}\nu^{-\beta}$, where $N_{\rm pl}$ is the power-law normalization and β is the power-law index.

5.2.2 Markov-Chain Monte Carlo (MCMC) Algorithm

We use a Bayesian algorithm to estimate the three to five parameters required to describe the observed UVOIR SEDs of a BH-LMXB in outburst: the (i) inner disc temperature ($T_{\rm in}$); (ii) temperature of the outer disc ($T_{\rm out}$); (iii) disc normalization ($N_{\rm disc}$); (iv) power-law normalization ($N_{\rm pl}$); and (v) power-law index (β). Specifically, we make use of the `emcee` PYTHON package (Foreman-Mackey et al., 2013), an implementation of Goodman & Weare's Affine Invariant MCMC Ensemble Sampler (Goodman & Weare, 2010) to fit the observed UVOIR SEDs with the models described in Section 5.2.1.

`emcee` employs a modified version of the Metropolis-Hastings Algorithm, where an ensemble of "walkers" simultaneously explores the parameter space. We use a number of walkers equal to 10 times the model dimensions to fit our SEDs. For the initial inspection of our parameter space, we use a harmony search global optimization algorithm called `pyHarmonySearch` (Geem et al., 2001) for all parameters except for $T_{\rm in}$. The "best guess" provided by `pyHarmonySearch` acts as a starting point for the MCMC walkers.

The prior distribution and initialization for $T_{\rm in}$ is set using the constraints from the X-ray spectral fits. As no disc component is observed in the $0.6 - 10$ keV band XRT spectra, we use a uniform distribution ($0.0 < T_{\rm in}(\mathrm{keV}) < 0.6$) as the prior for $T_{\rm in}$. The prior distributions for the remaining four parameters ($T_{\rm out}$, $N_{\rm disc}$, $N_{\rm pl}$, β) are chosen to be Gaussians, with means set using the `pyHarmonySearch` harmony search global optimization algorithm.

After initialization, the MCMC is run on each SED, starting with a "burn-in" phase where an ensemble of "walkers" are evolved over a series of 500 steps. Following the "burn-in" phase, the MCMC is run again, until convergence. The MCMC algorithm outputs the converged solution in the form of posterior distributions of each parameter. We take the median and 1σ (68%) confidence interval of each posterior distribution as the best-fit result for each parameter.

5.3 Observations and Data Reduction

5.3.1 X-ray

Swift/XRT

We utilized 17 *Swift*/XRT observations of J1753 during the two observed mini-outbursts (ObsIDs 00030090116 – 00030090137), from 2017 Feb 16 to May 15. XRT observed in auto exposure mode for the majority of this time, adjusting the CCD readout mode between windowed timing (WT) and photon counting (PC) modes depending on the source count rate.

Data were reprocessed using the HEASOFT v6.23 task XRTPIPELINE. WT mode observations were extracted from a 20 pixel ($\approx 47''$) radius circular aperture centered on the source. Background spectra in WT mode were extracted from an annulus centered on the source with inner and outer radii of 80 and 120 pixels, respectively[5]. PC mode observations are more susceptible to photon pile-up than WT mode observations. Thus, PC mode source spectra were initially extracted from a circular region of the same radius as in WT mode, and the average count rate was then calculated to determine if photon pile-up was significant. Observations with count rates higher than 0.5 count s^{-1} were re-extracted using an annular region with an outer radius of 20 pixels and the central portion of the point spread function excluded. The radius of the excluded region was determined by NASA's XIMAGE package[6] and ranged from $\sim 2-4$ pixels. PC mode background spectra were extracted from an annulus centered on the source with inner and outer radii of 50 and 70 pixels, respectively.

Source and background spectra were extracted using the HEASOFT tool XRTPRODUCTS and were grouped such that each energy bin contained a minimum of one count. Ancillary response files were generated with XRTMKARF and the relevant canned response matrix files were obtained from the High Energy Astrophysics Science Archive Research Center (HEASARC) calibration database (CALDB). All X-ray spectral fits were performed in XSPEC v.12.10.0 (Arnaud, 1996), using Cash

---

[5] http://www.swift.ac.uk/analysis/xrt/backscal.php

[6] http://www.swift.ac.uk/analysis/xrt/pileup.php

statistics for background subtracted spectra (W-statistic; Cash, 1979). Interstellar absorption was accounted for with the `tbabs` model with Wilms et al. (2000) abundances and Verner et al. (1996) photoionisation cross-sections. Unabsorbed 2–10 keV fluxes were calculated using the `cflux` model. All uncertainties on parameters derived from the X-ray spectral fits are at the 90% confidence level, unless otherwise stated.

For observations where the source was not detected by *Swift*/XRT, we derived 90% confidence upper limits on the 2–10 keV flux using the methods described by Gehrels (1986). We assumed a power law model with index $\Gamma = 1.7$ (e.g. Shaw et al., 2016d) and a hydrogen column density $N_{\rm H} = 2 \times 10^{21}$ cm^{-2} (Froning et al., 2014). For observations where a source was clearly detected (at $> 99\%$ confidence), but at a low count rate such that X-ray spectral fitting was not possible, we followed the procedure of Plotkin et al. (2017). Fluxes in this case were derived assuming the same model as above and we derived uncertainties using 90% confidence intervals from Kraft et al. (1991), factoring in a photon index that was allowed to vary from $1 < \Gamma < 2.5$.

Long-term X-ray light-curves

We built a long-term X-ray light-curve for J1753 using data from the *RXTE* /Proportional Counter Array (PCA), *Swift*/XRT, and *Monitor of All-sky X-ray Image*/Gas-Slit Camera (*MAXI*/GSC).

We collected all the *RXTE*/PCA and *MAXI*/GSC data from the WATCHDOG project (Chapter 2; Tetarenko et al. 2016). These datasets include good pointed PCA observations (i.e. no scans or slews) available in the HEASARC archive over the entire *RXTE* mission and *MAXI*/GSC data from the public online archive[7]. We collected all available *Swift*/XRT data (including WT and PC mode pointed observations) between May 2005 and April 2017 using the *Swift*/XRT online product builder[8](Evans et al., 2009).

All light-curves were collected in the 2–10 keV band. Individual instrument count

---

[7] http://maxi.riken.jp/top/

[8] http://www.swift.ac.uk/user_objects/index.php

rates were converted into flux using milliCrabs as a baseline unit and calculating approximate count rate equivalences. See Tetarenko et al. (2016) for details on this method.

5.3.2 UVOIR

For constructing and fitting the SEDs, the UVOIR photometry described in the following sections is corrected for interstellar extinction according to Fitzpatrick & Massa (1999). To deredden the data we use the `specutils` package in PYTHON, and $E(B-V)=0.45$ (Froning et al., 2014).

Swift/UVOT

Swift/UVOT is a 30cm diameter telescope that operates simultaneously with the XRT. When possible, we obtained observations in each of the six filters available for UVOT, from the UV ($UVW2, UVM2, UVW1$) to optical (U, B, V). As a result, we have 17 UVOT observations simultaneous with the XRT exposures described in Section 5.3.1.

Aperture photometry was performed on the images with the HEASOFT tool UVOTSOURCE, using a $5''$ radius circular region centered on the source. The background was measured using a $20''$ radius circular aperture centred on a source-free region. All reported magnitudes are in the Vega system and have been converted into flux densities using the known flux zero-points for each filter. Uncertainties include the statistical 1σ error and a systematic uncertainty that accounts for the uncertainty in the shape of the UVOT point spread function (PSF).

SMARTS

Upon the discovery of the first mini-outburst, we commenced optical and NIR monitoring of J1753 with A Novel Dual Imaging CAMera (ANDICAM; DePoy et al., 2003) on the 1.3m *Small & Moderate Aperture Research Telescope System* (*SMARTS*; Subasavage et al., 2010) at Cerro Tololo, Chile. An observing sequence consisted of observations in V, R, I, J, H and K bands[9] with exposure times of 360 s in the optical filters and 30 s in each of 8 to 10 dithered images in the NIR filters. Images were reduced using the Image Reduction and Analysis Facility (IRAF; Tody, 1986, 1993), following the standard procedures described by Buxton et al. (2012). Point-spread function photometry was performed on all images. The magnitudes were calibrated to the Vega system with respect to nearby stars in the field, with absolute calibration performed on clear nights using Landolt (1992) standards and the 2 Micron All-Sky Survey (2MASS) catalogue (Skrutskie et al., 2006) in the optical and NIR, respectively.

5.3.3 Other 2014 observations

We also utilize multi-wavelength data from 2014 Apr 2 – 5 observations of J1753, taken with an array of instruments. In UVOIR, we utilize observations performed in all six *Swift*/UVOT filters, in the g', r', i' and z' bands using the Lulin 41cm *Super-Light Telescope* (*SLT*), located in Taiwan and in the B, V, J and K_s bands using the HONIR instrument on the 1.5m *Kanata* telescope at the Higashi-Hiroshima Observatory, Japan. We also utilize a single 2.4ks *Swift*/XRT observation performed on 2014 Apr 5 (ObsID 00080730001). The data reduction of all of the 2014 data is described by Tomsick et al. (2015).

5.3.4 The Bolometric Correction

To convert the 2–10 keV unabsorbed flux from *Swift*/XRT, *MAXI*/GSC, and *RXTE*/PCA, to a bolometric flux, we use a combination of the: (i) bolometric corrections estimated for each accretion state by Migliari & Fender (2006); (ii) WATCHDOG project's online Accretion-State-By-Day tool[10] (see Chapter 2), which provides accretion state information on daily timescales during outbursts of BH-LMXBs; and (iii) Shaw et al. (2016c), who quantify J1753's brief excursion to the soft state in 2015.

---

[9] The K-band images were of poor quality due to the rapidly changing sky background at longer wavelengths, so we choose not to include them in this work.

[10] http://astro.physics.ualberta.ca/WATCHDOG

We note that using this method assumes that the bolometric conversion factor remains constant when the source is in each individual accretion state. This may not always be the case. Specifically for J1753, the high-energy cutoff in the X-ray spectrum has been observed to vary between $\sim 100-600$ keV throughout its 12 years of activity, where it mostly remained in the hard accretion state (see e.g., Cadolle Bel et al. 2007; Kajava et al. 2016). Without any continuous X-ray monitoring at $>$100 keV we have no way of quantifying whether (or how) this correction may change throughout the main outburst, standstill period, or mini-outbursts. Thus, we assume that the bolometric correction remains constant and acknowledge that if this is not the case, some uncertainty will be introduced into our calculation of bolometric flux.

5.4 Results

5.4.1 X-ray Spectral Fitting

All X-ray spectra are adequately fit with an absorbed power-law model (`tbabs*power law` in XSPEC syntax), with no model fit improved by the addition of a `diskbb` model at a significant level. The best-fit power law indices (Γ) and unabsorbed 2–10 keV fluxes at each *Swift* epoch are plotted in Figure 5.1. For the duration of the two mini-outbursts shown in Figure 5.1, Γ remains roughly constant at ~ 1.6, a value consistent with that typically expected of an LMXB in a hard accretion state. However, while Γ remains roughly constant, the flux does not, first rising and then decaying as the first mini-outburst progresses. We also note the onset of the second mini-outburst at MJD ~ 57880, which was investigated by Plotkin et al. (2017), in our data.

5.4.2 UVOIR SED Fitting

We fit the UVOIR SEDs from six individual epochs during the J1753 mini-outburst (see Figure 5.1 and Table 5.1) with the disc+power-law model described in Section 5.2.1. Each epoch has strictly simultaneous or quasi-simultaneous (within 1 day) UV through IR data from *Swift*/UVOT and *SMARTS* (see Sections 5.3.2 and 5.3.2).

All broadband SEDs during each of our six epochs are presented in Figures 5.12–

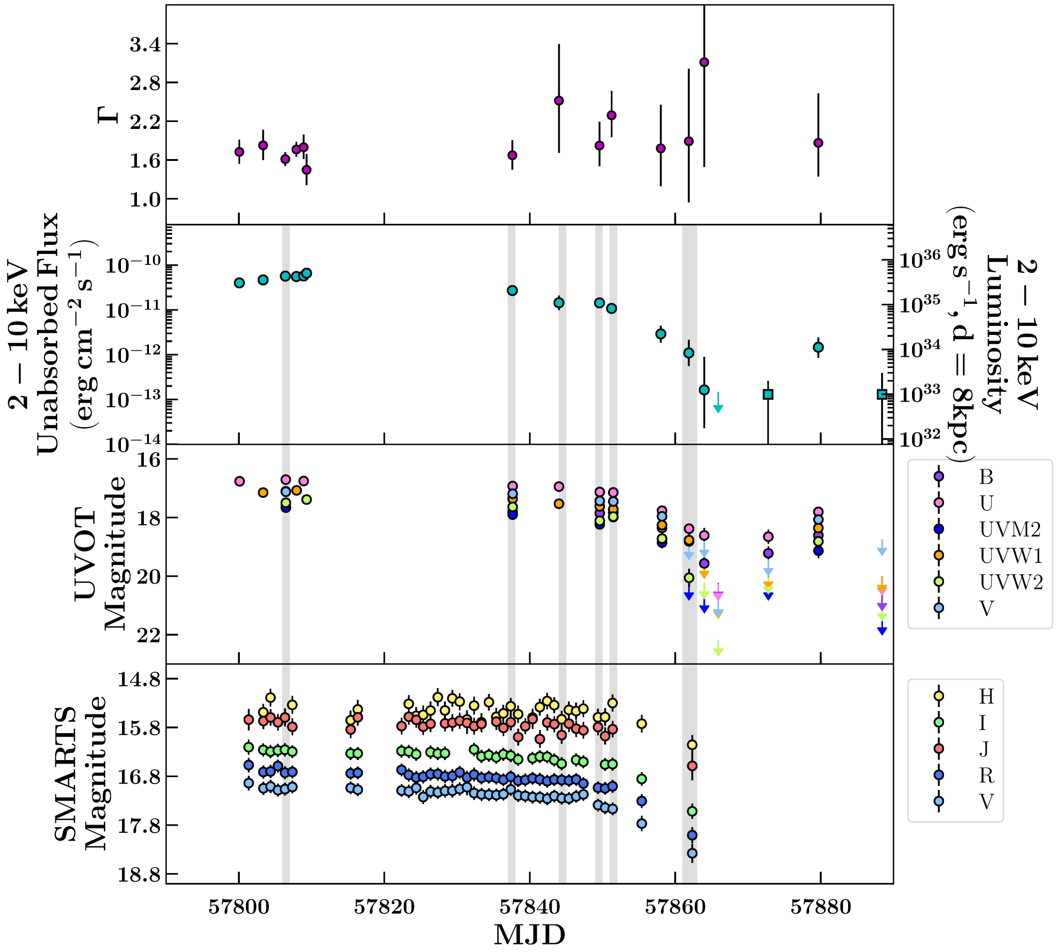

Figure 5.1: Multi-wavelength view of the J1753 mini-outbursts. Our six individual epochs with simultaneous/quasi-simultaneous UVOIR data are indicated with grey vertical bars. The panels give the photon index from X-ray spectral fits (top panel), and the *Swift*/XRT (second panel), *Swift*/UVOT (third panel), and *SMARTS* (bottom panel) light-curves. Upper limits are displayed with coloured arrows and low count rate flux estimates are represented by square markers (see Section 5.3.1 for details). Note that the UVOT and *SMARTS* data displayed here are not dereddened.

5.14. Each SED has been plotted in frequency space with the (dereddened) data colour-coded by wavelength: UVOIR (UVOT and *SMARTS*; red), X-ray (XRT: $2-10$ keV; purple), and radio (VLA: 9.8 GHz and AMI: 15.5 GHz from Plotkin et al. 2017; yellow). Note that only the UVOIR data are fit with our MCMC algorithm. X-ray and radio data show the multi-wavelength behaviour of the source[11]. All X-ray and radio data plotted are either simultaneous or quasi-simultaneous (within 1 day) with the UVOIR data, with the exception of Epoch 1, in which the closest available radio data were taken three days prior to the UVOIR data. Epochs 1, 2, 5, and 6 required the addition of a power-law component (indicative of the presence of emission from a jet) to the disc component to sufficiently match the UVOIR behaviour, while Epochs 3 and 4 were well fit with a pure disc model.

From our SED fitting, we are able to derive the time-series evolution of $T_{\rm in}$, $T_{\rm out}$, and $N_{\rm disc}$ over the course of the mini-outburst, for the irradiated disc model with two different temperature distributions (Figure 5.2) and the non-irradiated disc model (Figure 5.3). We find our six SEDs are well fit with an inner disc temperature that varies between $T_{\rm in} \sim 0.03 - 0.2$ keV and $T_{\rm in} \sim 0.01 - 0.1$ keV, for the irradiated $n = 1/2$ and $n = 3/7$ models, respectively. This is consistent with the range of $T_{\rm in} \sim 0.1 - 0.4$ keV, found in previous X-ray spectral studies during the 12 yr long outburst of J1753, when the source was in the hard spectral state (Miller et al., 2006; Hiemstra et al., 2009; Chiang et al., 2010; Reynolds et al., 2010; Cassatella et al., 2012; Kolehmainen et al., 2014; Tomsick et al., 2015). However, we note that the $T_{\rm in}$ is not well constrained by our data in the irradiated models (see Section 5.5.3). For the non-irradiated ($n = 3/4$) case, we find that the six SEDs are fit with an inner disc temperature that varies between $T_{\rm in} \sim 0.002 - 0.005$ keV ($\sim 2.3 - 5.8 \times 10^4$ K), significantly smaller than the irradiated cases.

For the irradiated cases, our SED fits show the temperature in the outer disc decreases from $T_{\rm out} \sim 1.1 \times 10^4 - 6.2 \times 10^3$ K and $T_{\rm out} \sim 1.2 \times 10^4 - 6.2 \times 10^3$ K for the $n = 1/2$ and $n = 3/7$ models, respectively, as the source evolves from outburst

---

[11] To derive the X-ray fluxes plotted in Figures 5.12–5.14, we fit the X-ray data with the `pegpwrlw` model. where the model normalization is the flux density in μJy at a specified energy. We derive this normalization at discrete energies in the range 1–10 keV and plot them in Figures 5.12–5.14.

Table 5.1: MCMC SED Fitting Results

Epoch	Date (MJD)	Function Type	$T_{\rm in}^{a}$ (keV)	$T_{\rm out}$ ($\times 10^3$ K)	$N_{\rm disc}$ ^{b}	$N_{\rm pl}$ ^{c}	β	$\log_{10}(R_{\rm out}/R_{\rm in})$	$F_{\rm disc} \times 10^{-10}$ ($\rm erg\,cm^{-2}\,s^{-1}$)	$R_{\rm in}$ ^{d} ($\times R_g$)
Standard Irradiated Disc ($n = 1/2$)										
1	57806-57807	disc+pl	$0.19^{+0.03}_{-0.02}$	11.0 ± 0.5	$5.0^{+1.1}_{-1.0}$	$3.6^{+0.9}_{-1.1}$	$1.18^{+0.02}_{-0.01}$	4.6 ± 0.1	$1.9^{+3.8}_{-1.2}$	$2.1^{+2.5}_{-1.7}$
2	57837-57838	disc+pl	$0.16^{+0.04}_{-0.02}$	9.7 ± 0.5	$5.9^{+1.2}_{-1.1}$	$9.3^{+2.9}_{-3.1}$	$1.21^{+0.03}_{-0.02}$	$4.56^{+0.13}_{-0.04}$	$1.4^{+3.4}_{-0.9}$	$2.4^{+3.0}_{-1.9}$
3	57844	disc	$0.10^{+0.05}_{-0.01}$	$6.2^{+0.4}_{-0.3}$	12 ± 1	< 11	$\cdots$	$4.50^{+0.30}_{-0.02}$	$0.8^{+4.2}_{-0.3}$	$5.0^{+5.5}_{-4.6}$
4	57849	disc	$0.090^{+0.055}_{-0.004}$	$6.2^{+0.3}_{-0.4}$	14 ± 1	< 3.1	$\cdots$	$4.48^{+0.32}_{-0.03}$	$0.7^{+4.8}_{-0.2}$	$5.7^{+6.1}_{-5.2}$
5	57851	disc+pl	$0.04^{+0.02}_{-0.01}$	$8.1^{+1.2}_{-0.9}$	62^{+15}_{-27}	$4.7^{+3.5}_{-2.8}$	$1.17^{+0.02}_{-0.03}$	$3.58^{+0.21}_{-0.04}$	$0.6^{+4.5}_{-0.6}$	26^{+32}_{-14}
6	57861-57862	disc+pl	0.03 ± 0.01	$6.1^{+0.6}_{-0.8}$	61 ± 2	132 ± 3	$1.31^{+0.05}_{-0.07}$	3.5 ± 0.1	$0.2^{+0.2}_{-0.1}$	25^{+26}_{-25}
*	56752	disc	0.06 ± 0.01	6.8 ± 0.4	46 ± 15	$\cdots$	$\cdots$	4.0 ± 0.1	$1.1^{+3.5}_{-0.8}$	19^{+26}_{-13}
Fully Irradiated Disc ($n = 3/7$)										
1	57806-57807	disc+pl	$0.09^{+0.02}_{-0.01}$	12.5 ± 0.6	$1.6^{+0.6}_{-0.5}$	1.9 ± 1.0	$1.15^{+0.01}_{-0.02}$	4.5 ± 0.1	$0.8^{+2.4}_{-0.6}$	$2.3^{+3.2}_{-1.5}$
2	57837-57838	disc+pl	0.09 ± 0.01	11.8 ± 0.6	$1.7^{+0.4}_{-0.3}$	1.2 ± 0.5	$1.15^{+0.01}_{-0.02}$	$4.50^{+0.04}_{-0.03}$	$0.7^{+0.7}_{-0.4}$	$2.3^{+2.8}_{-1.9}$
3	57844	disc	$0.04^{+0.02}_{-0.01}$	$7.9^{+0.6}_{-0.7}$	$6.7^{+1.3}_{-2.1}$	< 6.5	$\cdots$	$4.17^{+0.26}_{-0.05}$	$0.5^{+2.7}_{-0.3}$	$9.4^{+11.3}_{-6.5}$
4	57849	disc	$0.035^{+0.004}_{-0.003}$	6.6 ± 0.1	$7.8^{+1.8}_{-1.6}$	< 2.4	$\cdots$	4.2 ± 0.1	$0.3^{+0.5}_{-0.2}$	11^{+13}_{-9}
5	57851	disc+pl	$0.034^{+0.003}_{-0.002}$	$11.3^{+0.6}_{-0.7}$	13 ± 2	0.8 ± 0.3	$1.12^{+0.01}_{-0.02}$	$3.590^{+0.040}_{-0.003}$	$0.5^{+0.4}_{-0.2}$	18^{+20}_{-15}
6	57861-57862	disc+pl	$0.016^{+0.001}_{-0.002}$	6.2 ± 0.4	24 ± 4	$6.5^{+2.9}_{-2.4}$	$1.20^{+0.08}_{-0.09}$	$3.420^{+0.002}_{-0.004}$	$0.07^{+0.05}_{-0.03}$	34^{+40}_{-29}
*	56752	disc	0.04 ± 0.01	7.3 ± 0.4	$9.0^{+3.4}_{-3.8}$	$\cdots$	$\cdots$	$4.2^{+0.2}_{-0.1}$	$0.6^{+2.7}_{-0.5}$	13^{+18}_{-7}
Non-Irradiated Disc ($n = 3/4$)										
1	57806-57807	disc+pl	$(5.2^{+0.2}_{-0.1}) \times 10^{-3}$	6.1 ± 0.7	1.6 ± 0.1	$3.5^{+0.7}_{-0.3}$	$1.54^{+0.04}_{-0.06}$	1.3 ± 0.1	0.9 ± 0.2	$(6.2^{+6.4}_{-5.9}) \times 10^3$
2	57837-57838	disc+pl	$(4.3 \pm 0.1) \times 10^{-3}$	$6.1^{+1.0}_{-0.9}$	1.9 ± 0.1	0.030 ± 0.001	$1.40^{+0.02}_{-0.01}$	1.2 ± 0.1	$0.6^{+0.2}_{-0.1}$	$(7.3^{+7.6}_{-7.0}) \times 10^3$
3	57844	disc	$(2.9 \pm 0.1) \times 10^{-3}$	4.4 ± 0.6	3.3 ± 0.1	< 0.06	$\cdots$	1.2 ± 0.1	$0.34^{+0.04}_{-0.05}$	$(1.3^{+1.3}_{-1.2}) \times 10^4$
4	57849	disc	$(2.60 \pm 0.05) \times 10^{-3}$	4.1 ± 0.6	3.8 ± 0.1	< 464	$\cdots$	1.2 ± 0.1	$0.30^{+0.04}_{-0.03}$	$(1.5^{+1.5}_{-1.4}) \times 10^4$
5	57851	disc+pl	$(2.10 \pm 0.04) \times 10^{-3}$	8.0 ± 0.8	5.7 ± 0.1	400 ± 10	1.67 ± 0.01	$0.66^{+0.05}_{-0.04}$	$0.26^{+0.02}_{-0.02}$	$(2.2 \pm 2.2) \times 10^4$
6	57861-57862	disc+pl	$(1.3 \pm 0.1) \times 10^{-3}$	$5.7^{+0.8}_{-0.9}$	7.8 ± 0.7	5505^{+99}_{-107}	$1.82^{+0.13}_{-0.04}$	$0.57^{+0.06}_{-0.05}$	$0.06^{+0.02}_{-0.06}$	$(3.0^{+3.2}_{-2.7}) \times 10^4$
*	56752	disc	$(2.3 \pm 0.2) \times 10^{-3}$	5.9 ± 0.4	$6.4^{+0.6}_{-0.7}$	$\cdots$	$\cdots$	0.88 ± 0.01	$0.5^{+0.4}_{-0.2}$	$(2.4^{+2.7}_{-2.2}) \times 10^4$

[a] 1keV $\approx 1.2 \times 10^7$K

[b] The disc normalization $N_{\rm disc}$: $\times 10^{-19}$ ($n = 1/2$), $\times 10^{-15}$ ($n = 3/7$), and $\times 10^{-16}$ ($n = 3/4$).

[c] The PL normalization $N_{\rm pl}$: $\times 10^{19}$ ($n = 1/2$ and $n = 3/7$) and $\times 10^{24}$ ($n = 3/4$). Upper limits on $N_{\rm pl}$ are found using the disc flux in the H-band and assuming the β of the closest available observation.

[d] Calculated for an assumed distance of $D = 8$ kpc and inclination $i = 40°$.

[*] Best fit to data taken during the main outburst (Tomsick et al., 2015). See Sections 5.3.3 and 5.5 for details.

maximum towards quiescence, with the exception of Epoch 5. Interestingly, we observe an increase in $T_{\rm out}$ during Epoch 5 for both irradiated disc models, the same epoch that shows the largest excess emission in the UV bands. The decrease in $T_{\rm out}$ as the X-ray flux decreases during outburst decay is consistent with the predictions of the DIM+irradiation (IDIM; Dubus et al. 1999, 2001).

5.4.3 The X-ray light-curve

The X-ray light-curves of recurring transient outbursts in LMXBs can be used as a powerful diagnostic to probe the physical mechanisms driving mass inflow/outflow in these systems (Chapter 3 and 4; Tetarenko et al. 2018a,b). To this end, we have applied the Bayesian methodology developed by Tetarenko et al. (2018b) (see Chapter 3) to the X-ray light-curve of the J1753 mini-outburst, fitting their analytical irradiated disc-instability model to our data (see Figure 5.9). The IDIM predicts a multi-stage decay profile, starting with an exponential-shaped portion attributed to a viscously-accreting fully-irradiated disc, followed by a linear-shaped portion, occuring as a result of a cooling front propagating inward through the disc, at a rate set by the amount of irradiation heating (see King & Ritter 1998; Dubus et al. 2001).

We find that the J1753 mini-outburst can be well fit by a pure linear-shaped decay on a timescale of $\tau_l = 71 \pm 7$ days, and does not require the exponential+linear decay profile as in many Galactic BH-LMXB outbursts (see Chapter 4; Tetarenko et al. 2018a). A pure linear profile allows us to calculate an upper limit on $C_{\rm irr}$ by assuming f_t, the flux level at which the transition occurs between the viscous (exponential-shaped) and irradiation-controlled (linear-shaped) decay stages in the light-curve, is the maximum observed flux (Tetarenko et al., 2018a). We find $C_{\rm irr} < 2.8 \times 10^{-2}$ (for an assumed $D = 8\,{\rm kpc}$).

Since an exponential decay stage could have occurred in the gap in our data around MJD $\sim 57810 - 57838$, we also tested an exponential+linear decay profile. The best fit gives an exponential (viscous) timescale of $\tau_e = 52^{+8}_{-9}$ days, a linear decay timescale of $\tau_l = 48 \pm 9$ days, and a transition (between exponential and linear stages) occurring at time $t_{\rm break} = 57814 \pm 9$ and flux level $f_t = (2.3 \pm 0.5) \times 10^{-10}\,{\rm erg\,cm^{-2}\,s^{-1}}$. This exponential+linear profile allows us to calculate a $C_{\rm irr}$ from f_t, the flux level

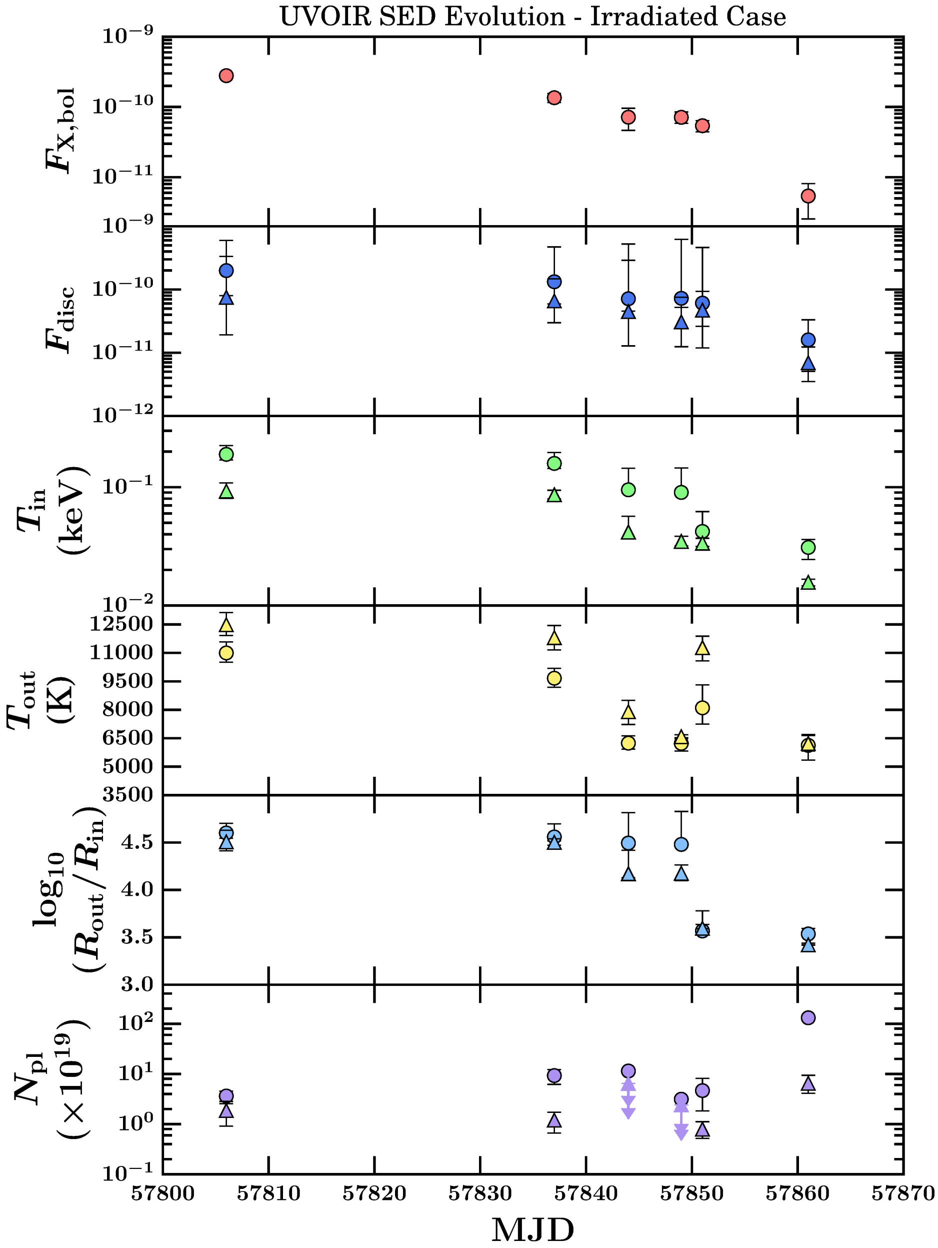

Figure 5.2: Irradiated disc model fits to the J1753 mini-outburst. For each of our six epochs, we plot: bolometric X-ray flux (top panel), integrated irradiated disc flux (second panel), and the parameters derived from the MCMC algorithm: inner disc temperature T_{in} (third panel); outer disc temperature T_{out} (fourth panel); log of the ratio of outer to inner disc radius $\log_{10}(R_{\text{out}}/R_{\text{in}})$ (fifth panel); and power-law normalization N_{pl} (bottom panel). Filled circles ($n = 1/2$) and triangles ($n = 3/7$) are the results from fitting the SEDs with our irradiated disc model with two different temperature profiles, $T \propto R^{-n}$. The errors on bolometric flux include (90% confidence) statistical instrument uncertainty only. Errors on fit parameters are 1σ confidence. Upper limits on N_{pl} are displayed as purple arrows.

Table 5.2: MCMC UVOIR/X-ray Correlation Fitting Results

Wave Band	Central λ (μm)	m_ν	b_ν
$UVW2$	0.1928	$0.52^{+0.14}_{-0.10}$	$-0.25^{+0.25}_{-0.56}$
$UVM2$	0.2246	$0.29^{+0.08}_{-0.07}$	$-0.59^{+0.12}_{-0.16}$
$UVW1$	0.2600	$0.31^{+0.05}_{-0.06}$	$-0.68^{+0.11}_{-0.14}$
U	0.3465	$0.25^{+0.03}_{-0.04}$	$-0.35^{+0.03}_{-0.04}$
B	0.4392	$0.20^{+0.04}_{-0.03}$	$-0.18^{+0.04}_{-0.03}$
V	0.5468	$0.22^{+0.03}_{-0.04}$	$-0.10^{+0.13}_{-0.04}$
R	0.641	$0.08^{+0.07}_{-0.08}$	$-0.24^{+0.17}_{-0.15}$
I	0.798	$0.08^{+0.08}_{-0.07}$	$-0.29^{+0.18}_{-0.17}$
J	1.22	$0.05^{+0.05}_{-0.06}$	$-0.45^{+0.15}_{-0.12}$
H	1.63	$0.04^{+0.07}_{-0.08}$	$-0.48^{+0.20}_{-0.16}$

NOTE. – A linear fit was performed in log-space, where m_ν and b_ν are the slope and intercept, respectively.

at which the transition occurs between the viscous (exponential) and irradiation-controlled (linear) decay stages in the light-curve, of $C_{\rm irr} = (2.2^{+0.8}_{-0.5}) \times 10^{-2}$ (for an assumed $D = 8$ kpc).

5.4.4 UVOIR–X-ray Correlations

In addition to light-curves and spectra, another way to quantify the contributions of different emission processes during an LMXB outburst is through the power-law correlations that exist between the flux at UVOIR wavelengths and the X-ray flux (Russell et al. 2006 and references therein). In Figures 5.4 and 5.5, we plot $F_{\rm UV}$ and $F_{\rm opt/IR}$ versus F_X for all simultaneous UV through X-ray data taken during the J1753 mini-outburst. We fit the correlations between the 10 individual UVOIR bands during the mini-outburst and the $2-10$ keV X-ray flux (see Table 5.2) to determine the dominant emission processes in each waveband. All individual correlation fits are presented in Figures 5.6 and 5.7.

We performed a linear fit in log-space to each dataset with our Bayesian MCMC algorithm (see Section 5.2.2), and estimated the slope (m_ν) and intercept (b_ν) for each individual correlation. As the standard linear formulation (i.e., $y_\nu = m_\nu x + b_\nu$)

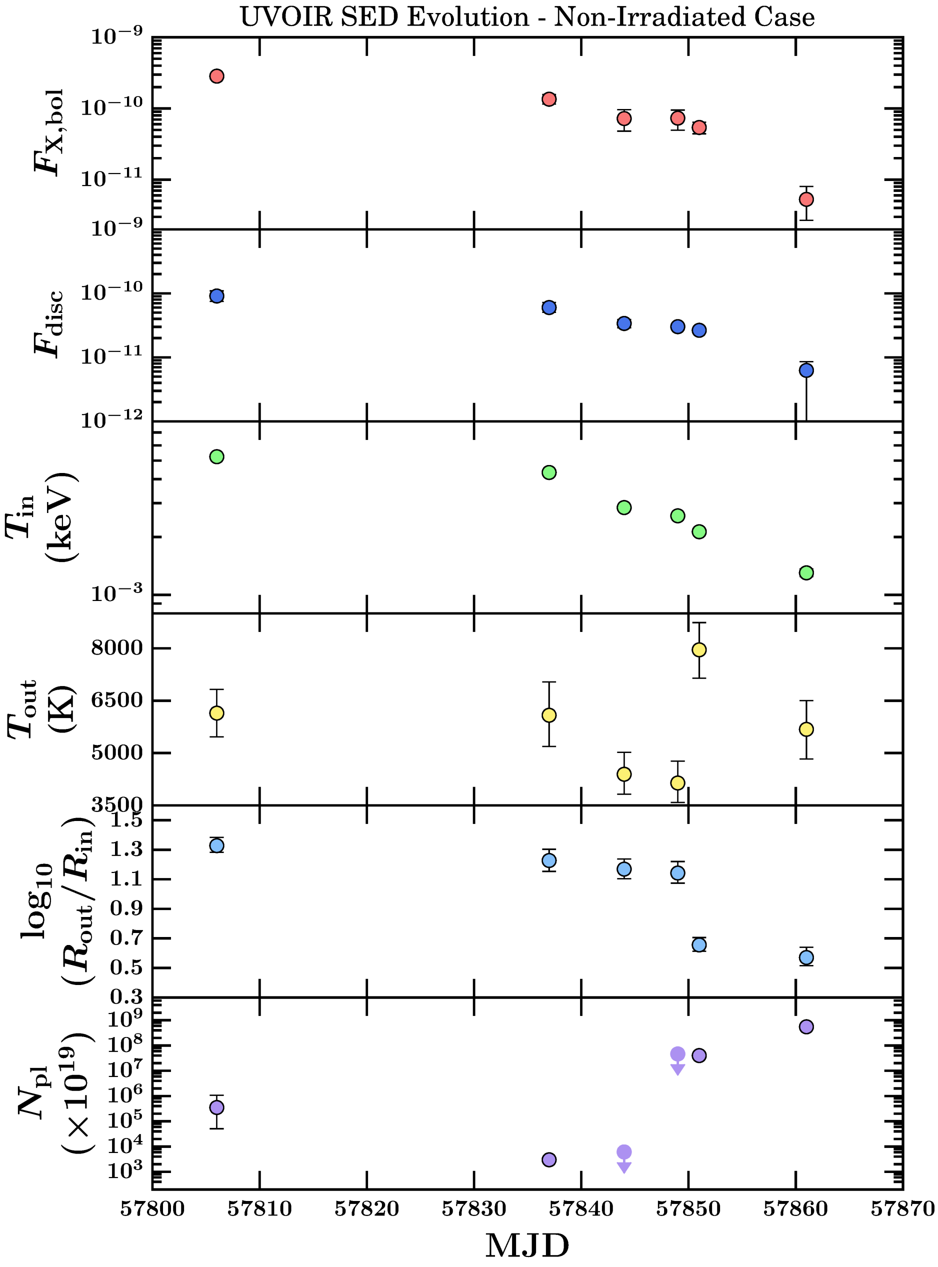

Figure 5.3: Non-irradiated disc model fits to the J1753 mini-outburst. For each of our six epochs, we plot: bolometric X-ray flux (top panel); integrated disc flux (second panel), and the parameters derived from the MCMC algorithm fit with the non-irradiated disc model with temperature profile $T \propto R^{-3/4}$; inner disc temperature T_{in} (third panel); outer disc temperature T_{out} (fourth panel); log of the ratio of outer to inner disc radius $\log_{10}(R_{\mathrm{out}}/R_{\mathrm{in}})$ (fifth panel); and power-law normalization N_{pl} (bottom panel). The errors on bolometric flux include (90% confidence) statistical instrument uncertainty only. Errors on fit parameters are 1σ confidence. Upper limits on N_{pl} are displayed as purple arrows.

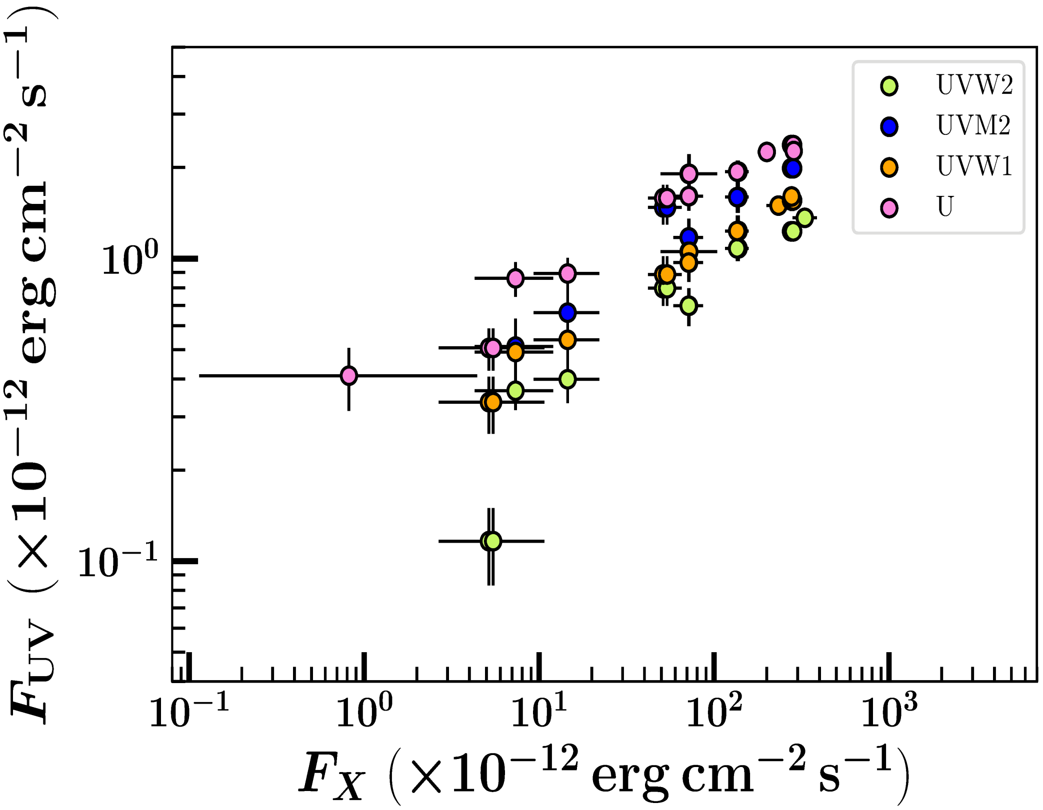

Figure 5.4: UV–X-ray correlation during the J1753 mini-outburst. Dereddened flux in the available UV bands from *Swift*/UVOT is plotted vs. unabsorbed 2$-$10 keV flux from *Swift*/XRT. Individual bands are colour-coded (see legend). Error bars include instrumental uncertainty only.

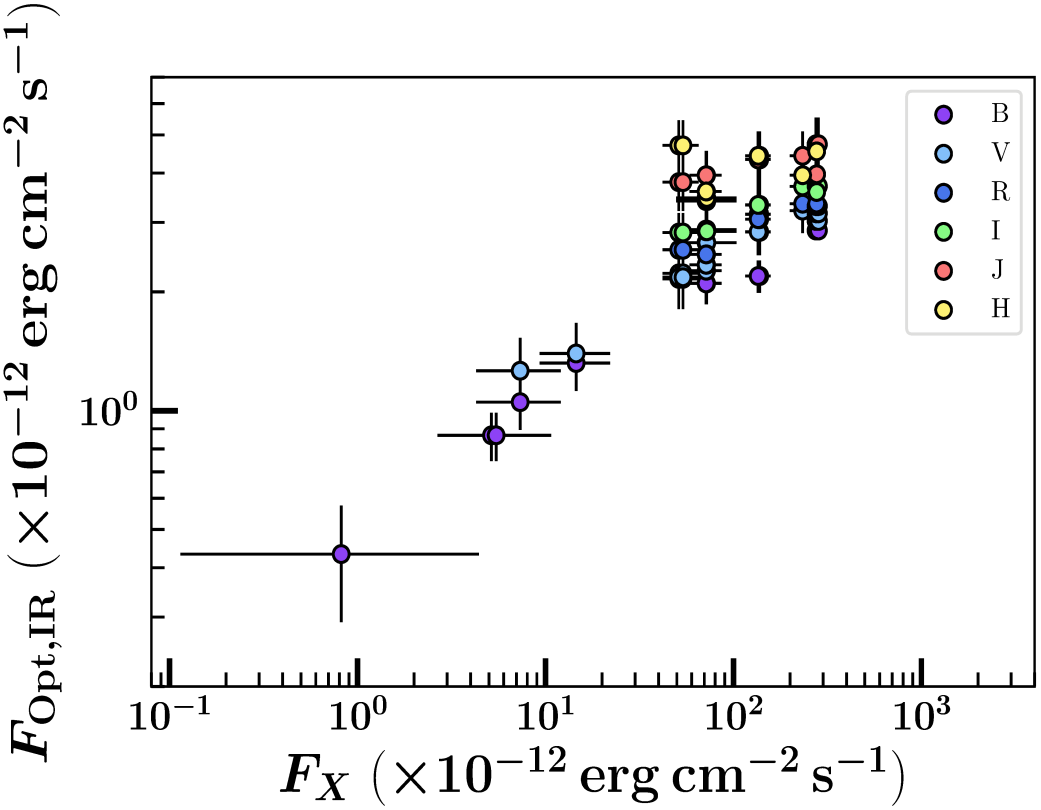

Figure 5.5: Optical/IR–X-ray correlation during the J1753 mini-outburst. Dereddened flux in the available OIR bands from *Swift*/UVOT and *SMARTS* is plotted vs. unabsorbed $2-10$ keV flux from *Swift*/XRT. Individual bands are colour-coded (see legend). Error bars include instrumental uncertainty only.

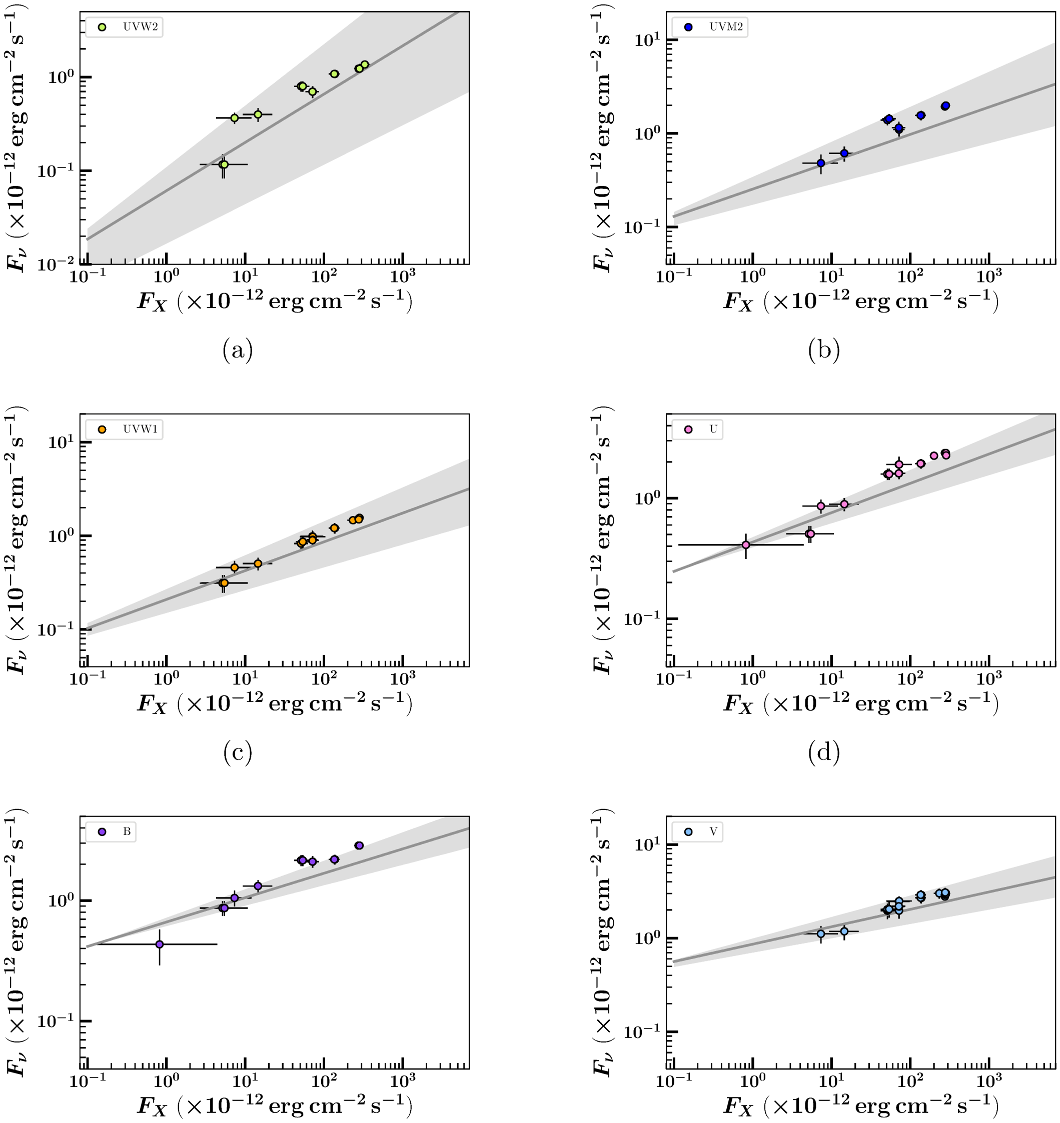

(a) (b)

(c) (d)

(e) (f)

Figure 5.6: Correlations between the dereddened flux in 10 individual UVOIR bands (*Swift*/UVOT and *SMARTS*) and the unabsorbed X-ray flux (2-10 keV; *Swift*/XRT) during the J1753 mini-outburst. The solid grey line and shaded regions represent the best-fit and 1σ confidence intervals from the MCMC fitting algorithm, respectively. Error bars represent instrumental uncertainty only.

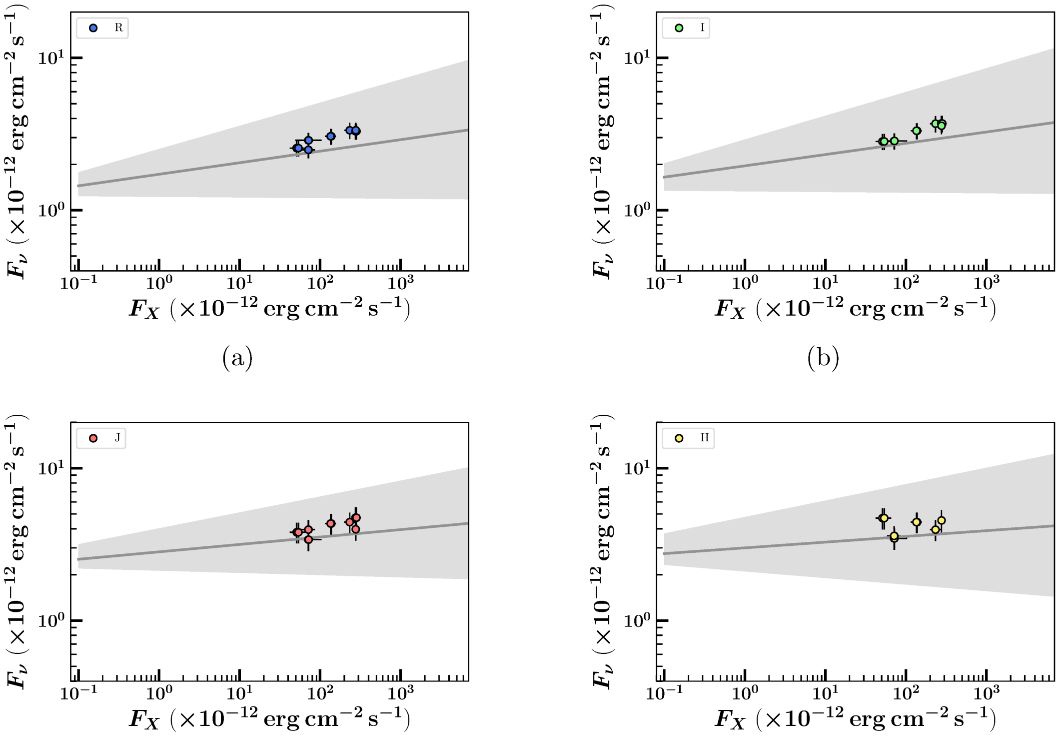

(a) (b) (c) (d)

Figure 5.7: Correlations between the dereddened flux in 10 individual UVOIR bands (*Swift*/UVOT and *SMARTS*) and the unabsorbed X-ray flux (2-10 keV; *Swift*/XRT) during the J1753 mini-outburst. The solid grey line and shaded regions represent the best-fit and 1σ confidence intervals from the MCMC fitting algorithm, respectively. Error bars represent instrumental uncertainty only.

is ill-suited for problems involving two-dimensional uncertainties, we use an alternative method, which parametrizes the slope in terms of the parameter θ, defined as the angle that the linear function makes with the x-axis (Hog et al., 2010). After likelihood maximization is performed for θ and the y-intercept y_b, PDFs of m_ν and b_ν are obtained by taking the tangent of the resulting PDFs for θ and y_b.

We find that as the selected wavelength decreases, the slope of the correlation, m_ν, increases. This trend has been found in outbursts of other short-period LMXBs containing both BHs and neutron stars (e.g., Swift J1357.2-0933, SAX J1808.4-3658; Armas Padilla et al. 2013; Beri, A. et al. 2018, submitted; Patruno et al. 2016). This trend is expected for thermal emission.

5.5 Discussion - The Nature of the Long-term Behaviour in J1753

The standard IDIM model cannot adequately describe the abnormal behaviour, characterized by outbursts of varying amplitude and duration, observed in the short-period BH-LMXB J1753. The division between transient and persistently accreting sources, predicted to occur by the IDIM in the $\dot{M}_{\rm BH} - P_{\rm orb}$ plane, is based on whether an accretion disc is in the stable or unstable regime (Dubus et al., 1999). An annulus R within the disc can remain in the hot, stable state if the local accretion rate $\dot{M}(R)$ is greater than the critical accretion rate of the hot state $\dot{M}_{\rm crit}(R)$, which increases with radius. Thus, for the entire disc to remain in a stable hot equilibrium (i.e., present as a persistent source), the mass-transfer rate from the companion star ($\dot{M}_2$) must be larger than the critical mass-transfer rate in the outer disc, $\dot{M}_{\rm crit}(R_{\rm out})$. If $\dot{M}_2 < \dot{M}_{\rm crit}(R_{\rm out})$, the disc will be in an unstable regime, undergo outbursts, and thus, be transient.

The critical accretion rate for an irradiated disc is parameterized as (Lasota et al., 2008),

$$\dot{M}_{\rm crit} = 9.5 \times 10^{14} C_{\rm irr,3}^{-0.36} \alpha_{0.1}^{0.04+0.01\log C_{\rm irr,3}} R_{\rm disc,10}^{2.39-0.10\log C_{\rm irr,3}} \cdot M_1^{-0.64+0.08\log C_{\rm irr,3}} \text{ g/s}, \tag{5.5}$$

where M_1 is the compact object mass in $M_\odot$, $R_{\rm disc,10}$ is the disc radius in units of 10^{10} cm, $\alpha_{0.1} = \alpha/0.1$ is the α-viscosity (a term parametrizing the efficiency of angular-momentum transport in the disc; see Chapter 3 and Shakura & Sunyaev 1973), and $C_{\rm irr,3} = C_{\rm irr}/10^{-3}$ is the irradiation constant (a parameter used to describe the fraction of the central X-ray luminosity that is intercepted and reprocessed by the disc; see Chapter 4 and Dubus et al. 1999, 2001).

In Figure 5.8, we plot the long-term mass-transfer rate ($\dot{M}_{\rm BH}$) as a function of $P_{\rm orb}$ for the Galactic BH-LMXB source sample, computed in the time-period 1996 January 6 – 2015 May 14, from the WATCHDOG project (Chapter 2; Tetarenko et al. 2016). Overlaid on the $\dot{M} - P_{\rm orb}$ plane, we plot the (i) critical accretion rate for an irradiated disc, parametrized with four different choices of $C_{\rm irr}$, around a $5 - 15 M_\odot$ BH, and (ii) the average mass-transfer rate of J1753 during each of the three accretion regimes it traversed between May 2005 and April 2017 (dotted horizontal lines; see below for details).

The $\dot{M}_{\rm BH}$ of J1753, averaged over a $\sim$ 20 year period, places it in the stable (persistent) region of the diagram. The nature of J1753's position in the plot has been discussed by multiple authors (see e.g., Coriat et al. 2012; Tetarenko et al. 2016). As suggested by Coriat et al. (2012), for such a small disc ($P_{\rm orb} = 3.2$ hrs or $R_{\rm disc} \sim 7.4 \times 10^{10}$ cm) one of the most feasible ways to explain how J1753 stayed bright for so long, and in turn the sheer amount of material accreted during such an outburst, is via a variable $\dot{M}_2$. An increase in $\dot{M}_2$ from its average value can keep the disc in a hot, stable state. We note that, there have been alternative explanations put forth to explain J1753, using the addition of tidal effects to the DIM (the tidal instability; Zurita et al. 2008; Maccarone & Patruno 2013), similar to what has been used to explain SU UMa stars (Osaki & Kato, 2013). However, we do not focus on these alternative explanations in this chapter.

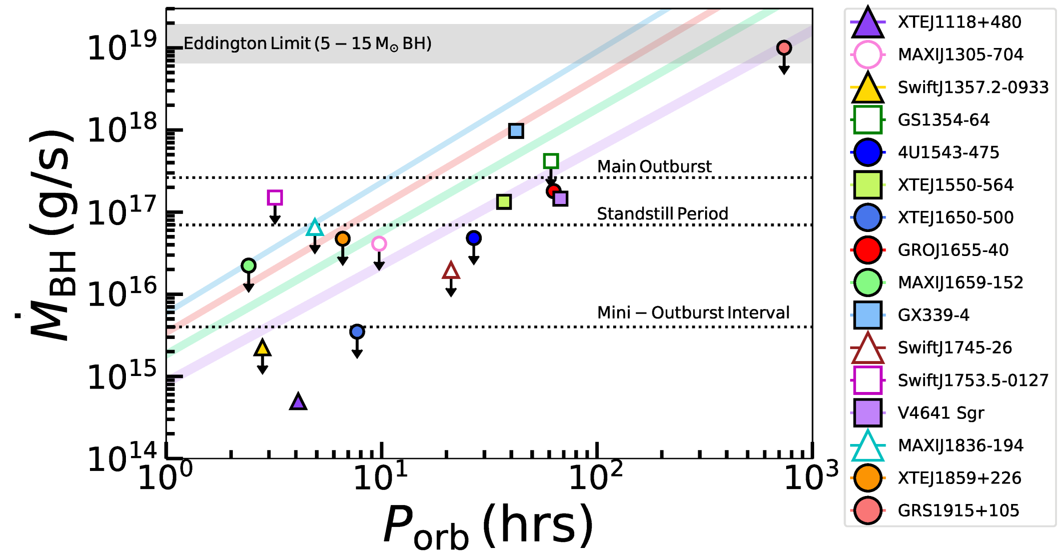

Figure 5.8: Long term mass-transfer rate ($\dot{M}$) vs. orbital period ($P_{\rm orb}$) for the transient Galactic BH-LMXB source sample, computed in the time-period 1996 January 6 – 2015 May 14, from the WATCHDOG project (see Chapter 2; Tetarenko et al. 2016). Mass-transfer rates calculated assuming an accretion efficiency $\eta = 0.1$. 1σ error bars are too small to see. Colours represent individual sources (see legend). Shapes denote accretion state(s) reached during outburst as determined by the WATCHDOG project: exclusively hard state or incomplete state transitions (source only reaches as far as the intermediate states) observed during all outbursts of the source (triangles), state transitions observed during all outbursts of the source (circles), or a combination of these two options (squares). Filled and open shapes represent sources with and without reliable distance estimates, respectively. The mass-transfer rate estimates of sources that have only one detected outburst in the WATCHDOG time period are denoted as upper limits. The shaded grey region shows the Eddington limit for a $5-15\ M_\odot$ BH. The shaded blue ($C_{\rm irr} = 10^{-3}$), red ($C_{\rm irr} = 5 \times 10^{-3}$), green ($C_{\rm irr} = 3 \times 10^{-2}$) and purple ($C_{\rm irr} = 3 \times 10^{-1}$) regions plot the critical accretion rate for an irradiated disc around a 5–15 $M_\odot$ BH according to the IDIM for various strengths of irradiation heating $C_{\rm irr}$. The dotted black lines show the average mass-transfer rate of J1753 calculated during each of the three accretion regimes. See Section 5.5 for details.

This behaviour is reminiscent of what is observed in Z Cam stars[12] (Simonsen, 2011; Szkody et al., 2013). A subclass of dwarf novae, Z Cam stars are characterized by the "standstill" phenomenon (see e.g., Buat-Ménard et al. 2001b). In these systems, the decay from outburst maximum to quiescence is interrupted. Following the interruption, the luminosity of the system increases and then settles at an intermediate level, corresponding to some fraction of the original peak outburst luminosity.

This standstill, which can last anywhere from days to years at a time, ends when the system finally declines to the typical quiescent state once again. In the framework of the DIM, the standstill behaviour was originally interpreted as a stable phase of accretion (Osaki, 1974), as a result of a mass-transfer rate from the companion star that fluctuates (either intrinsically or due to irradiation) about the critical mass-transfer rate above which the disc is stable (Meyer & Meyer-Hofmeister, 1983; Lin et al., 1985). This conclusion was confirmed by various authors (see Buat-Ménard et al. 2001b; Hameury & Lasota 2014), who were able to successfully model and reproduce the observed light-curves of Z Cam systems by including a variable mass-transfer rate in their numerical DIM codes.

We test the hypothesis that J1753 is the BH-LMXB analog to Z Cam systems using the: (i) available long-term X-ray light-curves from *RXTE*/PCA, *Swift*/XRT and *MAXI*/GSC (see Figures 5.9 and 5.10, and Section 5.3.1); and (ii) (quasi) simultaneous UVOIR and X-ray data from discrete intervals, during the time period of May 2005 to April 2017. To do so, we split the $\sim$ 12 years of outburst activity into three accretion regimes: the main outburst (A); standstill period (B); and mini-outburst interval (C).

5.5.1 Regime A: The Main Outburst

Regime A can be attributed to a typical transient outburst, predicted by the irradiated DIM, in which the accumulation of matter in the disc triggers the thermal-viscous instability and subsequent cycling of the disc into a hot, ionized outburst

---

[12] Neutron star LMXBs have also been shown to exhibit Z Cam type behaviour. See Haswell & King 2001.

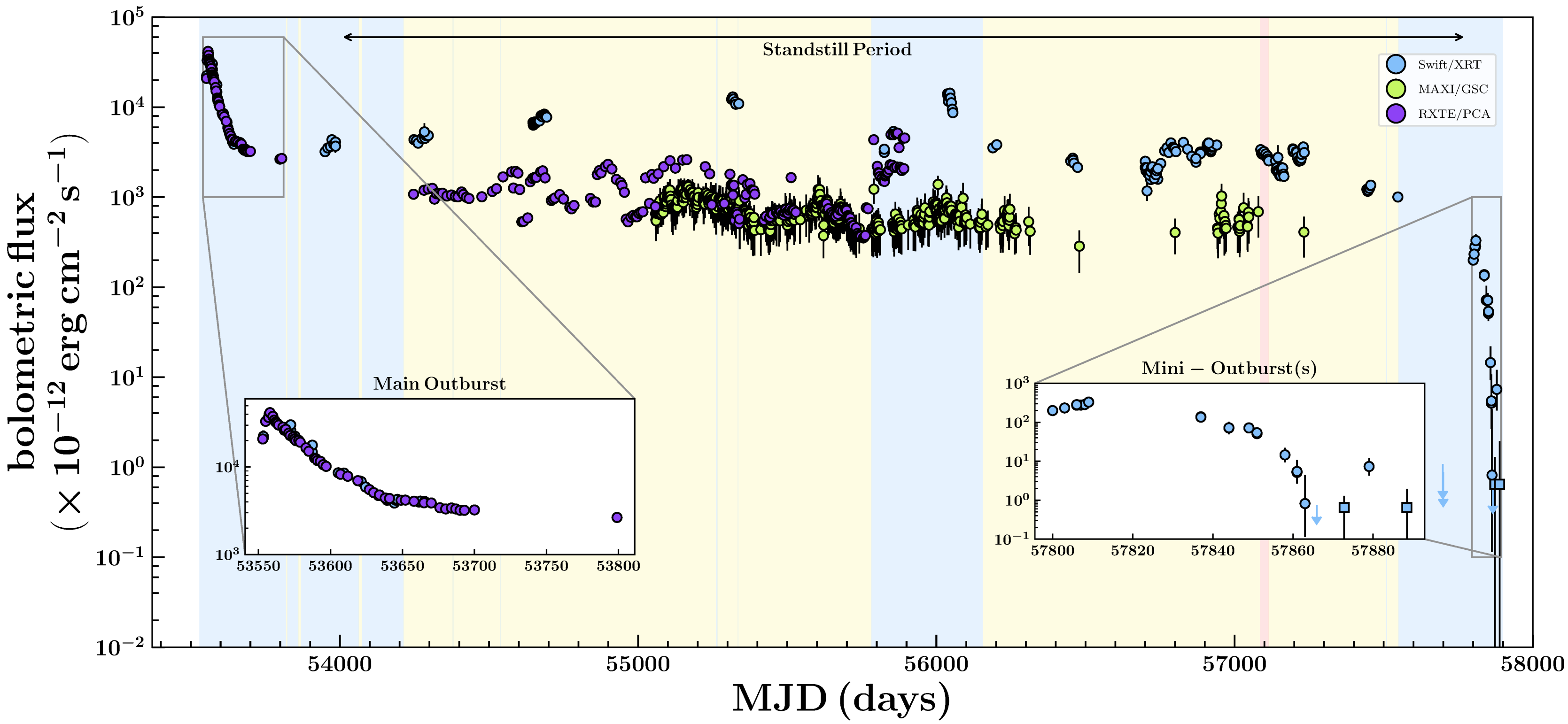

Figure 5.9: Bolometric X-ray light-curve of the J1753 spanning May 2005 to April 2017. Data from individual instruments are colour coded (see legends). Error bars represent individual (90% confidence) instrumental uncertainties. Upper limits are displayed with coloured arrows and low count rate flux estimates are represented by square markers (see Section 5.3.1 for details). Background shaded colours show the accretion state of J1753 as determined by the WATCHDOG project (see Chapter 2; Tetarenko et al. 2016) and Shaw et al. (2016c): hard (blue), soft (red), and intermediate (yellow). See Section 5.3.1 for details. Labelled on this figure are the three accretion regimes we have split the ∼ 12 yr time period into: the main outburst; “standstill” period; and mini outburst interval. The inset axes display zoomed in versions of the main outburst and mini-outburst regimes.

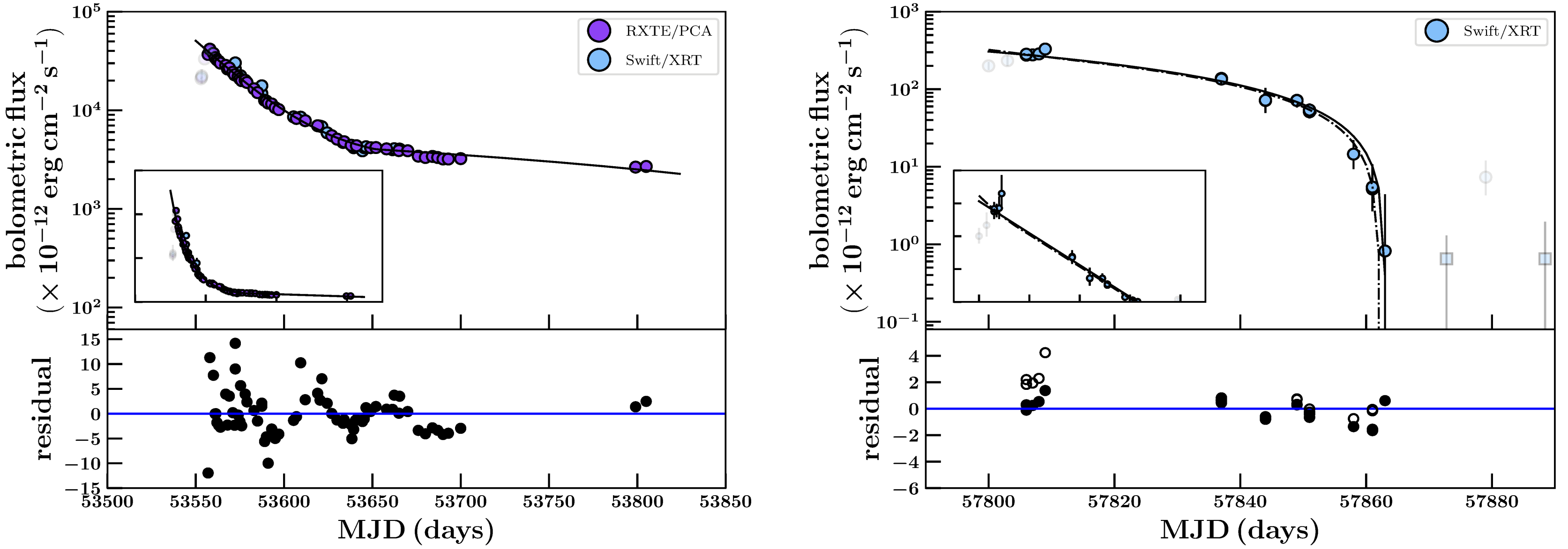

(a) Main Outburst

(b) Mini-Outburst(s)

Figure 5.10: Bolometric X-ray light-curves of the J1753: main outburst (left) and mini-outbursts (right). Data from individual instruments are colour coded (see legends). Error bars represent individual (90% confidence) instrumental uncertainties. Upper limits are displayed with coloured arrows and low count rate flux estimates are represented by square markers (see Section 5.3.1 for details). The black lines and lower panels represent the best fit analytical model and residuals, respectively. For the mini-outbursts (right), we show the best fit pure linear (solid black, filled circle residuals) and exp+lin (dot-dashed line and open circle residuals) decay models. Translucent markers on both figures indicate the rise of the outburst, and second mini-outburst, not included in the fits. The inset axes display the light-curves on a linear scale.

state over a viscous timescale.

X-ray light-curve Fitting

As the disc is drained by viscous accretion of matter at this point, we expect to see an exponential-shaped decay profile in the X-ray light-curve. As described in Section 5.4.3 for the mini-outbursts, we model the observed bolometric X-ray light-curve of the main outburst using the analytical version of the IDIM (Dubus et al., 2001) built by Tetarenko et al. (2018b) (see Chapters 3 and 4). The light-curve (Figure 5.9) is well fit with an exponential+linear shaped decay profile. The exponential timescale is $\tau_e = 117 \pm 1$ days[13], and the estimated mass-transfer rate from the companion is $\dot{M}_2 = (2.63^{+0.04}_{-0.04}) \times 10^{17}$ g/s, significantly higher than the critical mass-transfer rate in the outer disc of J1753, $\dot{M}_{\rm crit} = (1.6^{+0.4}_{-0.2}) \times 10^{16}$ g/s (calculated for a standard $C_{\rm irr} = 5 \times 10^{-3}$).

The standard IDIM interpretation (Dubus et al., 2001) attributes the linear-shaped (irradiation-controlled) portion of the decay profile to a cooling front propagating inward through the disc, where the speed at which this front propagates is controlled by the decaying X-ray irradiating flux. In this interpretation, the transition from the exponential (viscous) to the linear (irradiation-controlled) stage of the decay occurs when the irradiation temperature at the outer radius drops below $T_{\rm out} \approx 10^4$ K, the temperature at which hydrogen starts to recombine. Tetarenko et al. (2018b) (also see Chapter 4) find the flux level of this transition in short-period ($P_{\rm orb} < 5$ hr) BH-LMXB systems to vary between $f_t \sim 1 \times 10^{-10} - 3 \times 10^{-9}\,{\rm erg\,cm^{-2}\,s^{-1}}$. From our light-curve modelling, we find (i) that this transition occurs at time $t_{\rm break} = 53652^{+2}_{-1}$ (MJD) and flux level $f_t = (4.03 \pm 0.04) \times 10^{-9}\,{\rm erg\,cm^{-2}\,s^{-1}}$, and (ii) a subsequent linear decay timescale of 394^{+18}_{-17} days.

Here, we postulate a scenario, similar to what is described in Hameury & Lasota (2014) for Z Cam stars, whereby the $\dot{M}_2$ decreases, allowing $T_{\rm out}$ to drop below 10^4 K, triggering the development of an inward propagating cooling front in the outer

---

[13] Using the methodology developed by Tetarenko et al. 2018b (see Chapter 3) and this viscous timescale, we find the light-curve profile corresponds to an α-viscosity parameter of $\alpha = 0.16 \pm 0.03$. Interestingly, this is consistent with the $\alpha \sim 0.1 - 0.2$ inferred in dwarf novae (Kotko & Lasota, 2012).

disc. If $\dot{M}_2$ remained low, and the inward movement of the cooling front (and thus observed X-ray decline) was purely controlled by the decaying X-ray irradiating flux, we would expect the source to drop into quiescence at MJD $\sim$ 54046. However, J1753 did not follow this predicted pattern.

5.5.2 Regime B: The Standstill Period

After several months spent in a linear decay stage (at a nearly constant flux level), the flux began gradually increasing, until MJD $\sim$ 54500, where a sudden increase in flux was observed (see Soleri et al. 2013; Shaw et al. 2013). J1753 then spent $\sim$ 9 years at an intermediate flux level, before dropping into quiescence at MJD $\sim$ 57698 (Shaw et al., 2016b). We connect this standstill period, regime B, to the standstill phenomenon observed in Z Cam stars (see Hameury & Lasota 2014). We postulate that, at some point, $\dot{M}_2$ increased, before the cooling front had a chance to reach the inner edge of the disc. At this point, an outburst beginning in the outer disc (an "outside-in" outburst) began, as a result of the enhanced mass-transfer, before the disc had a chance to reach quiescence.

Quantifying Mass-transfer

To determine if this scenario is plausible, we have first computed an average mass-transfer rate onto the black hole during the standstill period (which we approximate as MJD = 54000–57698). Using the algorithm presented in Tetarenko et al. (2016) (also see Chapter 2), we estimate an average mass-transfer rate by computing the time-averaged bolometric luminosity using the X-ray light-curve data for this time period available from RXTE/PCA, Swift/XRT, and MAXI/GSC (see Figure 5.9 and Section 5.3.1 for details), assuming $D = 8$ kpc and a fixed accretion efficiency $\eta = 0.1$. We find $\dot{M}_2 = 6.7^{+0.2}_{-0.1} \times 10^{16}$ g/s, which is greater then $\dot{M}_{\rm crit}$ in the outer disc, supporting the standstill phenomenon scenario.

UVOIR SED Fitting

In addition, we have also fit the UVOIR SED, made up of simultaneous data obtained during one epoch of this standstill period (April 4-5 2014; Tomsick et al. 2015), with our disc models. See Table 5.1 for best-fit results and Figure 5.11.

Overall, we find that the 2014 SED is consistent with a cool disc, as reported by Tomsick et al. (2015), with no evidence of a jet in the NIR. Despite the much higher bolometric flux in comparison to the mini-outburst period, $T_{\rm out}$, in the irradiated cases, is consistent with values during the decay of the first mini-outburst (see Section 5.5.3 below). In addition, we find a similar pattern for $T_{\rm in}$ and $N_{\rm disc}$ in the 2014 observations, compared to the mini-outbursts, in both irradiated cases.

From the SED fit, we also derive an integrated disc flux of $F_{\rm disc} = (0.3 - 4.6) \times 10^{-10}\,{\rm erg\,cm^{-2}\,s^{-1}}$ and $F_{\rm disc} = (0.1 - 3.3) \times 10^{-10}\,{\rm erg\,cm^{-2}\,s^{-1}}$ for the irradiated $n = 1/2$ and $n = 3/7$ models, respectively. Combining knowledge of $F_{\rm disc}$ with the simultaneous X-ray data allows for an estimate of the irradiation constant $C_{\rm irr}$, defined as the fraction of the X-ray luminosity intercepted and reprocessed by the disc. We find $C_{\rm irr} \sim 8.8 \times 10^{-2}$ and $C_{\rm irr} \sim 4.6 \times 10^{-2}$ for the $n = 1/2$ and $n = 3/7$ models, respectively. Both estimates are significantly larger[14] than the standard value typically assumed in LMXBs (5×10^{-3}; Dubus et al. 2001), suggesting it is possible that strong X-ray irradiation of the companion star could be the cause of this period of enhanced $\dot{M}_2$ in the system.

The changes in observed spectral properties of J1753, from the main outburst regime through the standstill phase, are also consistent with the scenario implied by our UVOIR SED fitting, whereby the disc truncates and recedes from the BH as the outburst evolves. Kajava et al. (2016) find that the evolution of spectral changes, observed in J1753 from the main outburst through the standstill phase, is consistent with being driven by the truncation of the disc and subsequent formation of a large hot inner corona inside it. This causes the dominant source of X-ray emission (i.e., seed photons for Comptonization) to switch from the disc (via up-scattering) to self-

---

[14] It is worth noting that a large fraction of intercepted X-rays ($C_{\rm irr}$) has been found to be consistent with observations in multiple other BH-LMXBs as well (e.g. Gandhi et al., 2010; Tetarenko et al., 2018a). Also see Chapter 4.

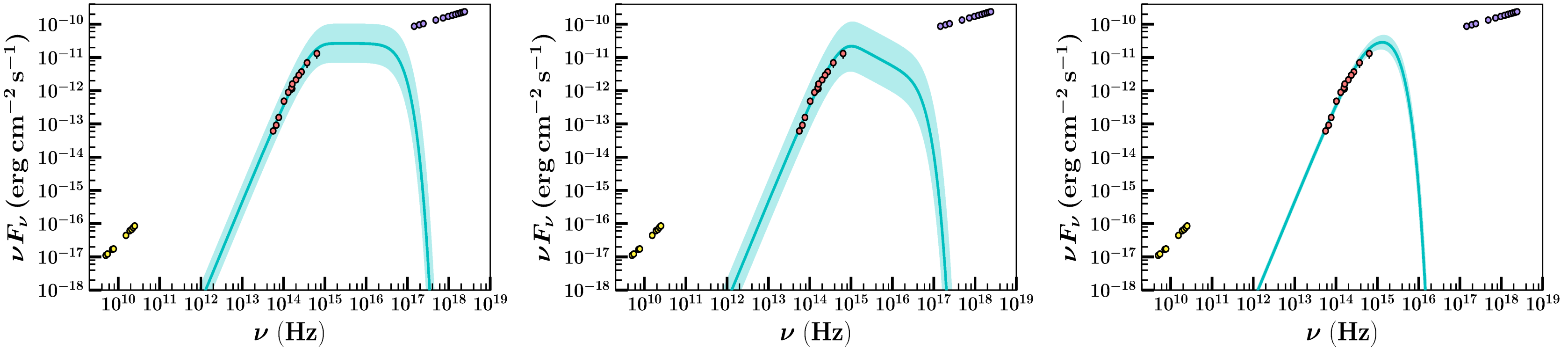

Figure 5.11: Broadband SED, during one epoch of the standstill period of J1753 (April 4-5, 2014; 56751-56752), fit with the irradiated disc model with a temperature distribution $T \propto R^{-n}$ characterized by $n = 1/2$ (left), $n = 3/7$ (middle), and a non-irradiated disc model with a temperature distribution characterized by $n = 3/4$ (right). All data are simultaneous or quasi-simultaneous (within 1 day) with the exception of K-band which was taken two days prior. All data have been dereddened. The solid cyan line and shaded regions represent the best-fit and 1σ confidence intervals from the MCMC fitting algorithm, respectively. Only the UVOIR data (red) are fit. X-ray (*Swift*/XRT; purple) and radio (VLA and AMI; yellow) are also plotted to show the multi-wavelength behaviour of the source.

produced synchrotron emission (via syncrotron self-Compton) in the hot corona.

Finally, we note that the 2014 data can also be fit well with a non-irradiated disc model. In this case, the scenario would be a thin viscous disc, truncated at a high inner radius, with presumably a hot radiatively inefficient flow inside producing the hard X-ray emission. However, from the SED fit with the $n = 3/4$ model, the derived integrated disc flux of $F_{\rm disc} = 0.5^{+0.4}_{-0.2} \times 10^{-10} {\rm erg\,cm^{-2}\,s^{-1}}$, corresponds to a mass-accretion rate $> 10^{19}$ g/s (for an assumed $D = 8$ kpc and an inclination $i < 80$ degrees). This mass-accretion rate is far too large to be consistent with the truncated thin disc scenario. Thus, we consider the non-irradiated disc model to be unphysical.

5.5.3 Regime C: The Mini-Outburst Interval

Finally, after a standstill period, J1753 returned to a quiescent state on 2016 November 6 (MJD = 57698). However, it would not remain in quiescence for long. ~ 102 days later (MJD ~ 57800), J1753 was observed to undergo two low-luminosity mini-outbursts before returning to a quiescent state for the second time. We attribute the mini-outburst interval, regime C, to $\dot{M}_2$ remaining low enough (i.e., below $\dot{M}_{\rm crit}$) that the disc is in the instability zone, allowing for a series of transient outbursts to occur.

Quantifying Mass-transfer

To determine if this scenario is plausible, we have first computed an average mass-transfer rate (with the same method described in Section 5.5.2 above), during the period ranging from when J1753 first returned to a quiescent state (MJD ~ 57698) until the end of the two mini-outbursts (MJD ~ 57885). We find $\dot{M}_2 = 4.0^{+2.7}_{-3.0} \times 10^{15}$ g/s, which is well below $\dot{M}_{\rm crit}$ in the outer disc of J1753. Thus, transient outbursts are expected.

X-ray light-curve Fitting

As described in Section 5.4.3, we model the observed bolometric X-ray light-curve of the first-mini-outburst using the analytical version of the IDIM built by Tetarenko et al. (2018b) (see Chapters 3 and 4). As there is a gap in the data between MJD $\sim$ 57810–57838, during which time an exponential (viscous) decay may have taken place prior to the linear decay, we attempt to fit the data (see Figure 5.10) with both a pure linear-shaped decay profile and an exponential+linear shaped decay profile.

In the context of the IDIM, if the decay is truly only linear, this would imply that the heating front never reached the outer disc. In the standard DIM, an "inside-out" heating front can stall somewhat easily (Dubus et al., 2001), leading to short, low-amplitude outbursts that take place in the innermost regions of the disc. This is because the critical density needed to raise a ring of accreting matter to the hot, ionized state increases with radius. So, if the outward moving heating front is unable to raise the density above this critical value, the outburst stalls and a cooling front will develop. In the IDIM, irradiation heating will reduce the critical density, allowing the heating front to reach larger radii. However, this assumes that the irradiating flux is seen by the entire disc, i.e., there is no self-screening of the central X-ray source by the inner disc (Dubus et al., 2001).

This assumption is unlikely to be true in J1753. The estimates of $C_{\rm irr} < 2.8\times10^{-2}$ (pure linear decay) and $C_{\rm irr} = (2.2^{+0.8}_{-0.5}) \times 10^{-2}$ (exponential+linear decay), from the X-ray light-curves fitting, are a factor $\sim$ 5 higher than the standard value of $C_{\rm irr,expected} \sim 5 \times 10^{-3}$. However this value of $C_{\rm irr}$ is still compatible with the stability limits between transient and persistent LMXBs (Coriat et al., 2012). If the irradiation source in J1753 is large, causing X-rays to encroach on the disc vertically (e.g. via a hot, inner corona flow), then the intercepted fraction could be high. This, combined with the low peak flux and short duration of the mini-outburst, leads us to favour the exponential+linear shaped decay in the X-ray light-curve, which supports the scenario implied by the UVOIR SED behaviour (see Section 5.5.3 below), of a fully-irradiated, truncated disc, heated by a source of irradiating X-rays produced in a corona above the disc.

UVOIR SED Fitting

We have also fit the UVOIR SEDs, made up of simultaneous/quasi-simultaneous data obtained during six individual epochs of the first mini-outburst. See Figures 5.12–5.14 and Table 5.1. Figures 5.2 and 5.3 show the evolution of $T_{\rm out}$ in the outer disc throughout the course of the mini-outburst for the irradiated and non-irradiated cases, respectively.

In the irradiated cases, our UVOIR SED fits imply that, overall, the outer disc cools as the source heads toward quiescence (prior to the second mini-outburst). According to the predictions of the IDIM, when $T_{\rm out} < 10^4$ K, the temperature at which hydrogen ionizes, a cooling front propagates through the disc, resulting in the source flux declining towards quiescence. This behaviour is echoed in Figure 5.2. In conjunction with this cooling, we also note an upward trend in $N_{\rm disc}$ (and by extension $R_{\rm in}$; Table 5.1), indicating that the inner disc recedes from the BH as the mini-outburst progresses. The simultaneous decrease of $T_{\rm in}$ is consistent with this recession, indicating that the inner edge of the disc cools as it moves further away from the BH.

Interestingly, we observe a strong increase in $N_{\rm disc}$ in the last two epochs, indicating that there must also be a strong increase in $R_{\rm in}$ (see Table 5.1). Working under the assumption that $R_{\rm out}$ does not change much over the mini-outburst, this observation is compatible with the decrease observed in $\log_{10}(R_{\rm out}/R_{\rm in})$. This decrease suggests that $R_{\rm in}$ increased by a factor 4–8 (depending upon the choice of n, see Table 5.1) in ~ 2 days. This large change seems to coincide with the drop in optical magnitude prior to the second mini outburst (see Figure 5.1).

Although the overall trend is one of a cooling disc as J1753 heads toward quiescence, in Epoch 5 there is an apparent increase in $T_{\rm out}$ with respect to Epoch 4. In Epoch 6, $T_{\rm out}$ returns to a level consistent with Epoch 4, as the cooling continues. Interestingly, the SED of J1753 at Epoch 5 (Figures 5.12–5.14) shows evidence of a significant excess (with respect to the best-fit model) in the UV bands. In various dwarf novae, a similar UV excess is observed (see e.g., Smak 1999, 2000; Hameury et al. 2000). This excess is attributed to brightening of the hot spot, where the mass-transfer stream interacts with the outer disc, as a result of mass-transfer variations from the companion. This is unlikely to be the case in J1753, as the irradiated disc would likely dominate over hot spot emission in the UV bands.

From the SED fits, we derive an integrated irradiated disc flux of $F_{\rm disc} \gtrsim F_{\rm X,bol}$ in all epochs, implying an unphysical $C_{\rm irr} > 1$. While this suggests that the data are not consistent with an irradiated disc, it is more likely that we are just overestimating $F_{\rm disc}$, as we discuss below.

In the irradiated disc fits, the $T_{\rm in}$ parameter is not well constrained. The break between the flat power-law and the Wien exponential cutoff in the spectrum is set by $T_{\rm in}(R_{\rm in})$. Looking at the fitted irradiated disc SEDs (see Figures 5.12–5.13), it is clear that a disc truncated at a larger $R_{\rm in}$, which would effectively change the higher end of the spectrum without changing the lower end, could also fit the data. A smaller $T_{\rm in}$ parameter (and thus a disc truncated at a larger $R_{\rm in}$) would lead to a lower $F_{\rm disc}$. The (i) X-ray spectrum throughout the mini-outburst, fit well with a power-law and no viscous disc-blackbody needed and (ii) the large $C_{\rm irr}$ parameter estimated from the X-ray light-curve fitting, implying an irradiation source in a hot, inner corona flow, both support this truncated irradiated disc scenario.

The other possibility to explain the large $F_{\rm disc}$ estimates is that only a part of the disc was hot during the mini-outbursts. The SED model explicitly assumes that $T_{\rm out}$ is measured at the outer radius of the full disc, $R_{\rm out}$. If the heating front never reached the outer edge of the disc during the mini-outburst, the temperature $T_{\rm out}$ we measure would refer to the maximum radius of the hot disc $R_{\rm hot} < R_{\rm out}$. Thus, the true value of $F_{\rm disc}$ would be smaller. However, we note that this scenario is at odds with the large $C_{\rm irr}$ that we estimate from the light-curves.

Similar to the 2014 data, we note that the mini-outburst can also be fit well with a non-irradiated disc model. However, the derived integrated disc fluxes in all epochs correspond to mass-accretion rates $> 5 \times 10^{18}$ g/s (for an assumed $D = 8$ kpc and an inclination $i < 80$ degrees). As discussed in 5.5.2 regarding the 2014 data, these mass-accretion rates are far too large to be consistent with the truncated thin disc scenario. Thus, we do not consider the non-irradiated disc model to be a viable option to describe the mini-outburst data.

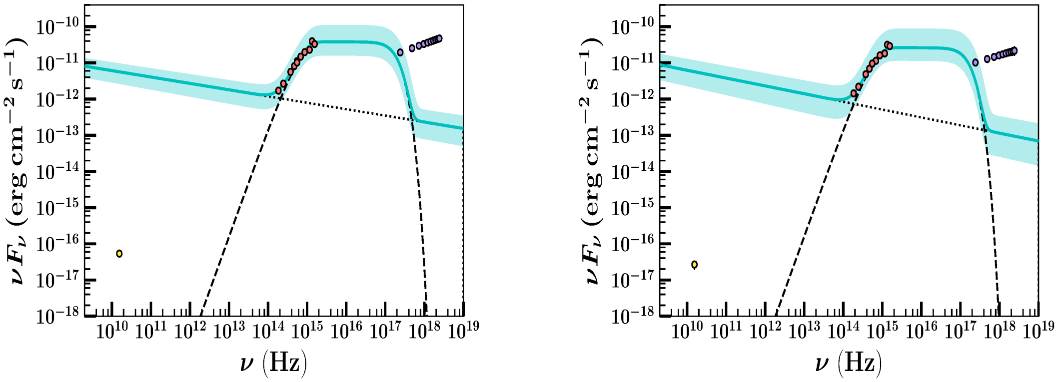

(a) Epoch 1: Feb. 22-23 (57806-57807)

(b) Epoch 2: Mar. 25-26 (57837-57838)

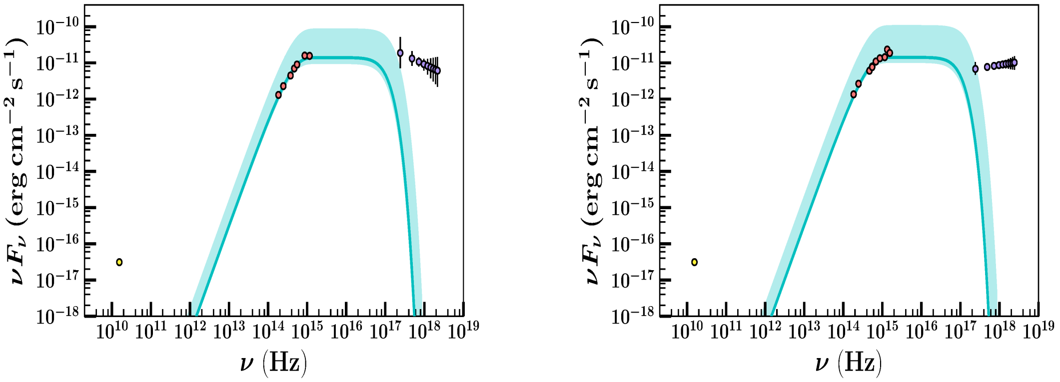

(c) Epoch 3: Apr. 1 (57844)

(d) Epoch 4: Apr. 6 (57849)

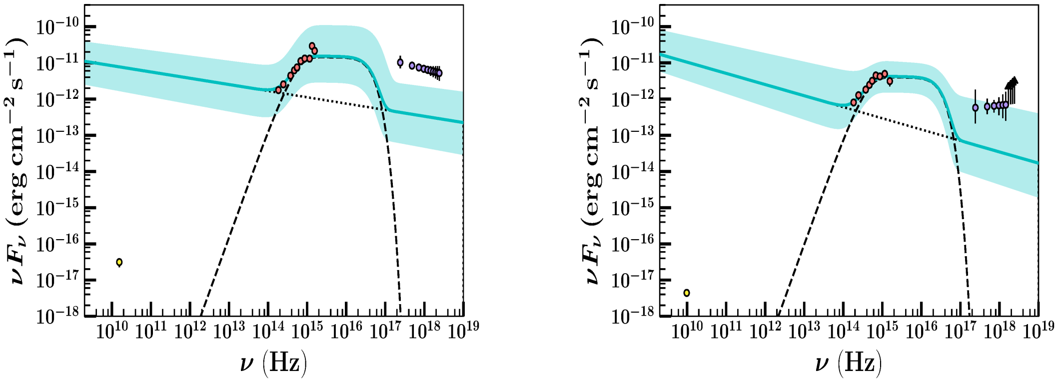

(e) Epoch 5: Apr. 8 (57851)

(f) Epoch 6: Apr. 18-19 (57861-57862)

Figure 5.12: Broadband SEDs for 6 individual epochs during the J1753 mini-outburst fit with the irradiated disc model with a temperature distribution $T \propto R^{-1/2}$. All data is simultaneous or quasi-simultaneous (within 1 day) and has been dereddened. The solid cyan line and shaded regions represent the best-fit and 1σ confidence intervals from the MCMC fitting algorithm, respectively. The dotted lines show the individual contributions from the irradiated disc (dashed) and jet (dotted), where applicable. Only the UVOIR data (*Swift*/UVOT and *SMARTS*; red) are fit. X-ray (*Swift*/XRT: $2-10$ keV; purple) and radio (VLA: 9.8 GHz and AMI: 15.5 GHz from Plotkin et al. 2017; yellow) are also plotted to show the multi-wavelength behaviour of the source.

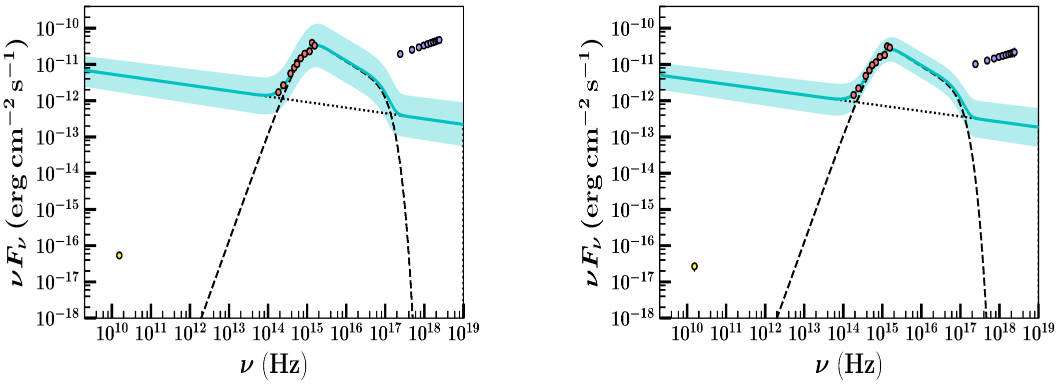

(a) Epoch 1: Feb. 22-23 (57806-57807)

(b) Epoch 2: Mar. 25-26 (57837-57838)

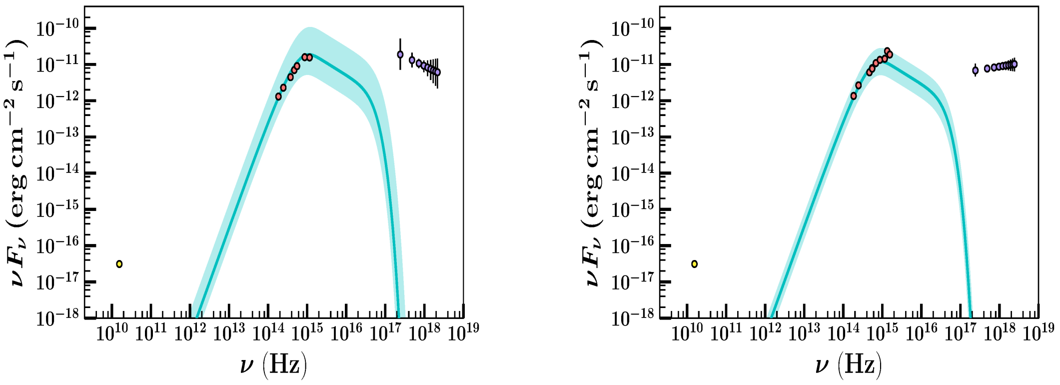

(c) Epoch 3: Apr. 1 (57844)

(d) Epoch 4: Apr. 6 (57849)

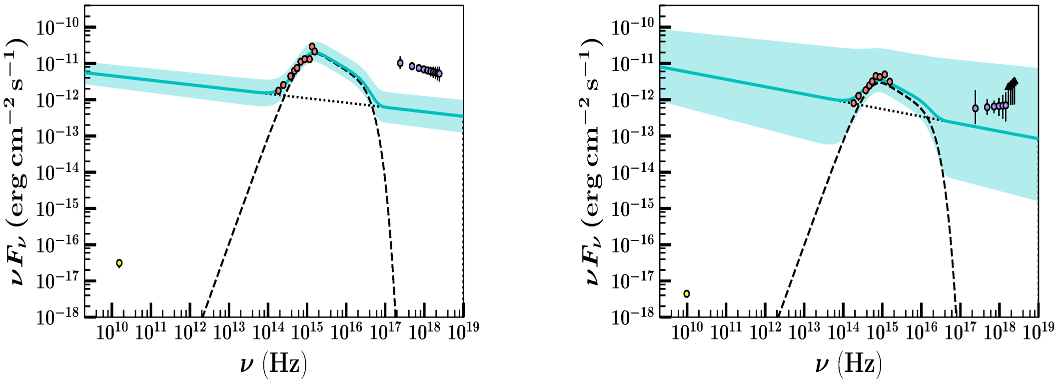

(e) Epoch 5: Apr. 8 (57851)

(f) Epoch 6: Apr. 18-19 (57861-57862)

Figure 5.13: Broadband SEDs for 6 individual epochs during the J1753 mini-outburst fit with the irradiated disc model with a temperature distribution $T \propto R^{-3/7}$. All data is simultaneous or quasi-simultaneous (within 1 day) and has been dereddened. The solid cyan line and shaded regions represent the best-fit and 1σ confidence intervals from the MCMC fitting algorithm, respectively. The dotted lines show the individual contributions from the irradiated disc (dashed) and jet (dotted), where applicable. Only the UVOIR data (*Swift*/UVOT and *SMARTS*; red) are fit. X-ray (*Swift*/XRT: $2-10$ keV; purple) and radio (VLA: 9.8 GHz and AMI: 15.5 GHz from Plotkin et al. 2017; yellow) are also plotted to show the multi-wavelength behaviour of the source.

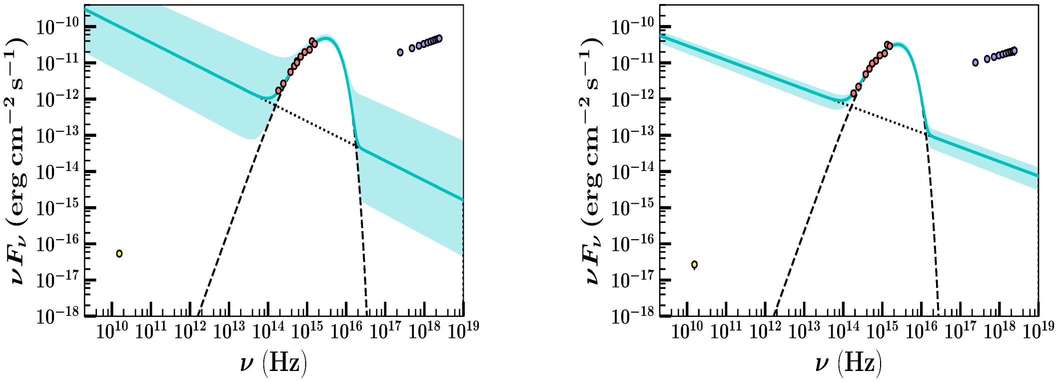

(a) Epoch 1: Feb. 22-23 (57806-57807)

(b) Epoch 2: Mar. 25-26 (57837-57838)

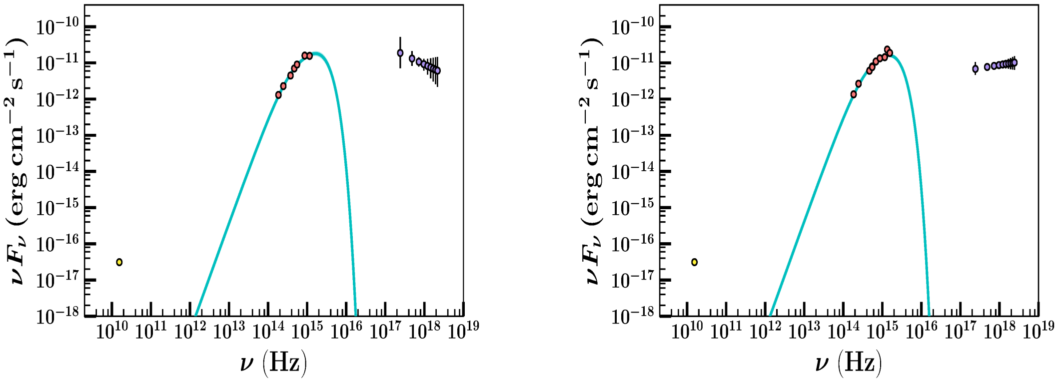

(c) Epoch 3: Apr. 1 (57844)

(d) Epoch 4: Apr. 6 (57849)

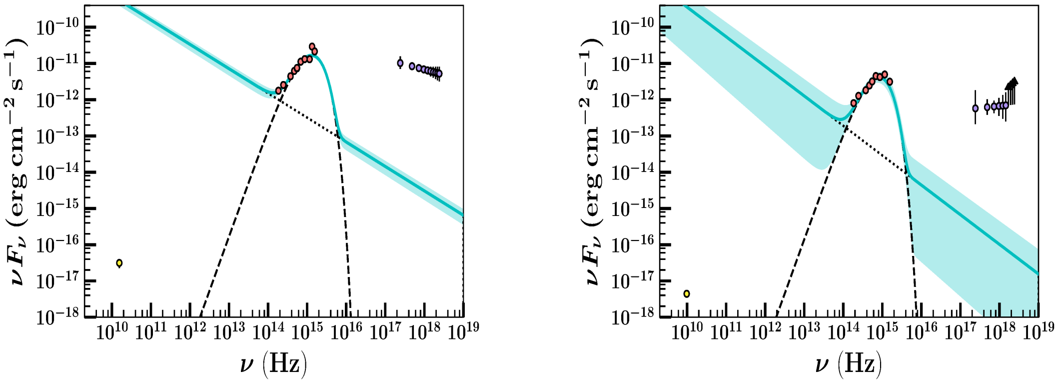

(e) Epoch 5: Apr. 8 (57851)

(f) Epoch 6: Apr. 18-19 (57861-57862)

Figure 5.14: Broadband SEDs for 6 individual epochs during the J1753 mini-outburst fit with the non-irradiated disc model with a temperature distribution $T \propto R^{-3/4}$. All data is simultaneous or quasi-simultaneous (within 1 day) and has been dereddened. The solid cyan line and shaded regions represent the best-fit and 1σ confidence intervals from the MCMC fitting algorithm, respectively. The dotted lines show the individual contributions from the irradiated disc (dashed) and jet (dotted), where applicable. Only the UVOIR data (*Swift*/UVOT and *SMARTS*; red) are fit. X-ray (*Swift*/XRT: $2-10$ keV; purple) and radio (VLA: 9.8 GHz and AMI: 15.5 GHz from Plotkin et al. 2017; yellow) are also plotted to show the multi-wavelength behaviour of the source.

UVOIR–X-ray correlation

In a study of 33 LMXBs, Russell et al. (2006) found a global correlation with a slope $m_\nu = 0.6 \pm 0.1$ for $F_{\mathrm{opt/IR}} \propto F_X^{m_\nu}$ for BH-LMXBs in the hard accretion state. This correlation, which extends to the UV regime (e.g. Rykoff et al., 2007), is instrumental in our understanding of the emission processes in the accretion disc. The value of m_ν can vary significantly, depending on the dominant emission mechanism. van Paradijs & McClintock (1994) find that $m_\nu = 0.5$ is expected for emission dominated by X-ray reprocessing in the disc, whereas $m_\nu = 0.7$ implies the presence of an optically thick synchrotron jet (Russell et al., 2006). For a viscously heated disc, we expect m_ν in the range $0.15 - 0.3$ in the NIR to UV bands (Russell et al., 2006).

Figures 5.4 and 5.5 show the UVOIR fluxes plotted against their corresponding X-ray flux (in the 2–10 keV band) during the first mini-outburst. The results of a linear fit (in log-space) to the data in each UVOIR band are presented in Table 5.2 and Figures 5.6 and 5.7. As discussed in Section 5.4.4 we find a decreasing slope as we move to redder filters. A dependency of m_ν on wavelength is predicted by theory (Frank et al., 2002) and has been observed in the short period BH-LMXB Swift J1357.2-0933 (Armas Padilla et al., 2013). However, unlike Swift J1357.2-0933, in which the slope was consistent with a viscous disc in all *Swift*/UVOT filters, we see an apparent switch from a viscous disc to reprocessed emission in the $UVW2$ band.

The fact that only the $UVW2$ flux is consistent with reprocessing in the UVOIR-X-ray correlations could suggest that the entire disc is not being irradiated and thus, there is a screening process preventing the irradiating flux from reaching the outer radii of the disc. In this case, irradiation alone would not bring the entire disc into a hot, ionized state. As a result, the heating front would never reach the outer edge of the disc during the mini-outburst, resulting in an outburst from only a portion of the disc.

However, this scenario is inconsistent with the large C_{irr} estimates from the X-ray light-curve fits, which imply a large source of X-ray irradiation (possibly via the hot, inner corona flow). We also note that the best-fit value for m_ν in the $UVW2$ band appears to be driven by one data point at a low flux, highlighted by the relatively large uncertainties compared to those in the other filters. If the low-flux point is removed, then the $UVW2$-X-ray correlation would be consistent with the viscous disc scenario implied by other filters. We therefore are cautious to interpret the $UVW2$ emission as being a result of X-ray reprocessing alone.

The likely reality is that there are a number of emission processes contributing to the optical and UV flux of J1753 during the mini-outburst. In addition to supporting the scenario where both the disc geometry and the source of X-ray emission change as J1753 evolves from the main outburst through the standstill phase, the evolution of the timing properties of the source have also been shown to be consistent with the existence of multiple sources of optical/UV emission. Recently, Veledina et al. (2017) attributed the dramatic changes in the shape of the optical/X-ray cross-correlation functions (CCFs), as J1753 evolved from the main outburst to the standstill phase, as the source of optical/UV emission switching from purely reprocessed X-ray photons in the outer regions of the disc (during the initial stages of the main outburst), to a combination of emission from the irradiated disc and synchrotron emission from the hot inner corona (following the drop in X-ray flux and the subsequent change in the source of seed photons producing the comptonized X-ray emission in the standstill phase).

The shallower (than expected for emission from a pure irradiated disc) optical/UV-X-ray correlations we observe during the mini-outburst are consistent with this scenario, whereby the optical/UV emission is a combination of X-ray reprocessing in the outer disc and a (likely significant) contribution of (optical/UV) synchrotron emission from the corona, effectively reducing the slope we observe and fit.

In the NIR J and H bands, the slope is consistent with 0, implying that there is no NIR response to the changing X-ray flux. We find that a jet component is required to describe the NIR emission in four of the six SEDs (Figures 5.12–5.14), indicating that the jet may be contaminating the NIR-X-ray correlations. This is similar to the BH-LMXB XTE J1550-564, which underwent a mini-outburst in 2003 and exhibited evidence of a compact jet in the NIR portion of the SED (Chaty et al., 2011), and has also been seen in J1753 previously (Rahoui et al., 2015).

The $\beta \sim 1.2$ spectral index of the PL component found to fit the NIR emission in our SEDs is steeper than typically seen in optically thin radio jets ($\beta \sim 0.6$ e.g. Russell et al., 2010) but not unphysical (see e.g., discussion in Tetarenko et al. 2017). We must note that the best-fit value of β is only driven by one or two NIR data points, so this value is likely less well-constrained than the MCMC derived uncertainties suggest. Therefore we suggest that the contribution from the jet is likely contaminating the NIR-X-ray correlation.

5.6 Summary and Conclusions

We have presented here a comprehensive study of the BH-LMXB Swift J1753.5-0127, focusing in particular on multi-wavelength data obtained during a mini-outburst toward the end of its ~ 12 year long outburst. By modelling the observed UVOIR SED at six epochs during the mini-outburst with an irradiated accretion disc we were able to track the evolution of important physical properties of the disc. Additionally, we modelled the profile of the X-ray light-curve during the mini-outburst, enabling us to probe the mechanisms of mass transport in the disc and the properties of X-ray irradiation. Finally, we utilized our wealth of (near-) simultaneous multi-wavelength data to investigate the correlation between the observed X-ray and UVOIR fluxes. These correlations allowed us to investigate the emission mechanisms present during the mini-outburst.

Ultimately, we conclude that the evolution of the mini-outburst is consistent with a scenario involving a fully irradiated disc, truncated at a large radius, with a hot, radiatively inefficient, accretion flow inside it, within which the source of irradiating X-rays (likely produced mainly by the synchrotron self-Compton process), and a significant portion of the optical/UV (via synchrotron photons) emission, are produced.

This scenario is supported by the observed:

- light-curve profile, displaying the classic exponential+linear shape predicted by the IDIM (Dubus et al., 1999, 2001) for the outburst of an irradiated disc,
- high fraction of reprocessed X-rays (C_{irr}) derived from the X-ray light-curve,

implying the presence of a large source of irradiating X-rays impinging on the disc,

- evolution of the UVOIR SEDs throughout the mini-outburst, consistent with a truncated irradiated disc cooling and receding further from the BH, and
- power-law correlations between optical/UV and X-ray emission, showing only the far-UV emission to be consistent with pure reprocessed X-ray irradiation and evidence for multiple sources of optical and (near and middle) UV emission present.

We have also presented an investigation of the long-term behaviour of J1753, which, prior to the mini-outbursts, had remained in outburst since its discovery in 2005 (see e.g. Soleri et al., 2013; Shaw et al., 2013; Tomsick et al., 2015). Fitting the X-ray light-curve of the initial outburst, we find the classic BH-LMXB outburst decay profile (i.e. an exponential followed by a linear decay). However, instead of returning to quiescence the source underwent a standstill phase. We attribute this to a variable mass-transfer rate from the companion star (see also Coriat et al., 2012), in which, during this phase, $\dot{M}_2 > \dot{M}_{\rm crit}$ allowing the disc to remain in a hot, ionized stable state.

From the long-term X-ray light-curve (Figure 5.9), we calculated the time-averaged $\dot{M}_2$ to be greater than the critical value during the standstill phase, supporting our hypothesis. The UVOIR SED (obtained during this phase) is well fit with an irradiated disc truncated at large radii, and implies a large fraction of X-rays being reprocessed in the outer disc ($C_{\rm irr} \sim 8.8 \times 10^{-2}$), consistent with the source of irradiating X-rays being produced in a corona existing inside and above the disc. Previous spectral (e.g., Kajava et al. 2016) and timing (e.g., Veledina et al. 2017) studies during the standstill phase of this source have been found to also support this scenario. Given the available evidence, we suggest that a period of strong X-ray irradiation may have driven the enhanced mass-transfer of the standstill phase.

The long-term behaviour observed in J1753 bears a striking resemblance to Z Cam stars, whereby variable mass-transfer from the companion drives unusual outbursts, characterized by stalled decays and abrupt changes in luminosity (Buat-

Ménard et al., 2001b; Hameury & Lasota, 2014). Thus, we suggest that J1753 is in fact a BH-LMXB analogue to Z Cam type dwarf novae.

Chapter 6

Conclusion

6.1 Summary

In this thesis, I have presented a methodology that effectively links accretion theory to observations of real accretion discs. Temporal and spectral data taken during the recurring transient outbursts occurring in LMXBs encode within them the physics behind the mechanisms driving mass inflow and outflow in these binary systems. My method characterizes: (i) a light-curve profile into definitive stages based on observable properties (i.e. timescales, flux) describing how matter moves through, and is removed from, LMXB discs throughout an outburst; and (ii) the broadband spectral energy distribution (SED) of an outbursting LMXB based upon physical properties of the irradiated disc in the system. In doing so, this methodology allows one to place observational constraints on both the angular momentum (and mass) transport process occurring in, and X-ray irradiation heating and regulating outbursts of, LMXB discs.

Established the accretion history of Galactic BH-LMXBs

In Chapter 2, I presented a study of the population of BH-LMXBs in our Galaxy using the Whole-sky Alberta Time-resolved Comprehensive black-Hole Database of the Galaxy (WATCHDOG) project that I developed. This unique resource collates observable properties from the literature with long-term X-ray light-curves from a combination of wide-field (all-sky), scanning survey, and narrow-field pointed X-ray instruments, to detect, track, monitor, and analyze LMXB outburst behaviour over decades of energy and time. WATCHDOG includes: (i) a comprehensive catalogue and outburst history of the Galactic BH-LMXB population; and (ii) an interactive suite of tools, built to analyze the long-term temporal and spectral evolution observed in BH-LMXBs during there recurrent outbursts.

Using WATCHDOG's suite of tools, I have been able to:

1. Characterize nearly two decades of outburst behaviour exhibited by the BH-LMXB population of our Galaxy, including 134 detected transient events in 49 individual sources.
2. Perform a statistical study on the distributions of a number of outburst properties across the Galactic population, including outburst detection rates, duration, recurrence timescales, duty cycles, total energy radiated during outburst, and peak outburst luminosity.
3. Study the luminosity regimes of accretion state transitions.
4. Derive and analyze the long-term mass-transfer history of the population.
5. Study the relationship between LMXB outburst properties and the orbital parameters that define the size and mass scales of these binary systems.

In doing so, I have found that our current suite of more sensitive X-ray instruments in space detecting a greater number of sources, an estimated ∼4–12 transient outbursts per year, more than a factor of three larger than in the pre-RXTE era (Chen et al., 1997) alone. This rate peaked when there was both a sensitive low-energy X-ray all-sky monitor/bulge survey program (RXTE ASM/PCA) and high-energy X-ray all-sky monitor (*Swift* BAT). I also find that $38^{+6.0}_{-5.6}$ % of the outbursts detected, do not undergo state transitions. This "failed" outburst behavior is neither a rare nor recent phenomena; there is a near constant appearance of "failed" outbursts in the Galactic BH-LMXB population over the last ~ 50 years. I postulate that this finding, paired with the fact that "failed" outbursts tend to have peak Eddington scaled luminosities that are $\lesssim 0.11\, L_{\rm edd}$ (a regime at or below that where we expect the transition from the hard to the soft state to happen), may be indicative of "failed" behavior being a result of the mass-transfer rate onto the BH remaining at a low level throughout the outburst, below the (yet unknown) instability that triggers the change to the soft state.

Given that I find a substantial fraction of the total transient BH-LMXB outburst sample over the past two decades is represented by "failed" outbursts, I have considered the ramifications that the larger number of these so-called "failed" outbursts (and the entire population of observed BH-LMXB outbursts) have on the correlations between observable outburst properties and binary orbital parameters of the system (which is predicted to exist by accretion theory).

While I find that the long-term mass-transfer history of my representative sample of BH-LMXBs are in good agreement with the theoretical expectations of the DIM, I also observe numerous outliers from the theoretically expected correlation for LMXBs in the $\dot{M} - P_{\rm orb}$ plane (Podsiadlowski et al., 2002). There exist a number of explanations for these outliers, including, but not limited to: different binary evolution paths (i.e., not all objects at one $P_{\rm orb}$ have the same history); differing local conditions at the first Lagrangian point (e.g., star spots); irradiation-induced mass-transfer cycles (e.g., see Podsiadlowski 1991; Harpaz & Rappaport 1991; Buning & Ritter 2004); uncertainties in distance and inclination (and thus beaming); a significant change in accretion efficiency existing between accretion states (e.g., more advection of energy during the hard state; see Knevitt et al. 2014); or the possibility that a significant amount of accreted matter (or energy from this matter) may be removed from a system via a substantial outflow (i.e., a relativistic jet or accretion disc wind) before it has a chance to fall through the disc and contribute to the accretion luminosity.

In Chapter 2, I considered the last two options. Given that previous studies (e.g., Maccarone 2005) have ruled out the possibility that the bright hard states of BH-LMXBs have a significantly different radiative efficiency than the soft states at similar luminosities, I favor the outflow scenario to explain the scatter in the observed mass-transfer rates from the expected correlation. I conclude that our inferred $\dot{M}$ estimates may in fact only be lower limits on the true mass-transfer rates from the companions in these systems.

In addition, I find that the expected correlation between peak outburst luminosity ($L_{\rm peak}$) and orbital period ($P_{\rm orb}$) in LMXBs breaks down for low-luminosity (sub-Eddington) outburst behaviour. Contrary to previous studies (Shahbaz et al., 1998; Portegies Zwart et al., 2004; Wu et al., 2010), I only find evidence for a positive correlation between $L_{\rm peak}$ and $P_{\rm orb}$ in a sample that includes the brightest outburst detected in each source. No such correlation was found for the entire BH-LMXB outburst sample. I postulate that the breakdown of this correlation in the low-luminosity (sub-Eddington) sources is likely the result of a much smaller fraction of the accretion disc being accreted during their transient outbursts. Accordingly, I predict that it is the brightest outburst of each source that will tell us the most about the intrinsic properties of the binary itself.

Overall, this all-sky study has allowed us to probe the wide and varying array of outburst behavior exhibited by Galactic BH-LMXBs, its impact on the physical observables of individual systems alone, and thus the universal properties of the Galactic population as a whole. With my results I have demonstrated that enumerating the frequency at which outbursts occur, tracking outburst properties across the population and quantitatively classifying the wide range of behavior exhibited during outburst is critical to furthering our understanding of the physical mechanisms driving mass-transfer in binary BH systems. The continuation of this work is a key step toward filling in the many gaps in our knowledge of how BH-LMXBs form, accrete and evolve.

Extensively applied a new methodology to study disc-accretion across a sample of BH-LMXBs

The work in Chapter 2 provides the critical accretion history of BH-LMXBs in our Galaxy. However, that history is merely the input for the more important studies of accretion-disc properties presented in the rest of this thesis.

In Chapter 3, I present a new methodology I developed to study the process of disc-accretion in LMXBs. This methodology combines advanced Bayesian statistical techniques and the principles of the disc-instability model to derive observational constraints on the angular-momentum (and mass) transport process at work in the irradiated accretion discs of LMXBs directly from their observed X-ray outburst light-curves. By applying this Bayesian methodology to the BH-LMXB population of the Galaxy I was able to derive the first-ever measurements of the efficiency of the angular-momentum (and mass) transport process (parametrized via α-viscosity) in LMXBs, directly from observations.

Overall, I have found that, during outburst, the depletion of mass in the accretion discs in these LMXB systems occurs at an unusually rapid rate. This is indicative of either:

- strong angular-momentum transport (i.e., rapid accretion), which according to numerical accretion disc simulations can only be sustained when a large-scale magnetic field threads the disc (whose origin and evolution is still unclear in accretion flows around stellar-mass BHs), ;
- strong accretion disc winds, with the ability to remove a substantial fraction of the disc mass, must exist during all stages of the outburst decay (in all accretion states and across different luminosity regimes) throughout outbursts of BH-LMXBs; or
- a combination of both exist during the vast majority of BH-LMXB outbursts.

Overall, these results open up a new chapter in the study of accretion physics, where global models of accretion discs must be able to explain fast depletion of mass in the accretion disc during outburst. Moreover, they also motivate in-depth searches for outflow signatures across all X-ray accretion states and luminosity levels throughout an outburst.

These changes to our understanding of the disc-accretion process, one of the most fundamental building blocks responsible for the growth and evolution of objects across astrophysical scales, may also have applications to astronomical objects ranging from newborn stars to supermassive black-holes at the center of galaxies. For instance, the presence of magnetically-driven outflows at low accretion levels in supermassive black holes would change our evolving understanding of the role that accretion-induced feedback (potentially from outflows) appears to play between supermassive black-holes and the evolution of entire galaxies (Di Matteo et al., 2005; Croton et al., 2006; Page et al., 2012; King & Pounds, 2015).

In Chapter 4, I continue our analysis of Galactic BH-LMXBs with my Bayesian methodology, studying the physical properties of the X-ray irradiation heating their accretion discs. Applying this methodology to a representative sample of BH-LMXB X-ray outburst light-curves, I derived observational constraints on the strength of the X-ray irradiation heating in the outbursts of BH-LMXBs according to the DIM.

I find a large range for the parameter describing the strength of the X-ray irradiation heating of the outer regions of the discs in these systems, $3 \times 10^{-3} < C_{\mathrm{irr}} < 30$. I find values of $C_{\mathrm{irr}} \geq 1$, which are clearly unphysical. This tells us that the late-time evolution of the accretion disc is more complex than the linear form predicted by the DIM (i.e., attributed to a cooling front propagating inward through the disc at a rate controlled by the amount of irradiation heating).

While the first stages of outburst decays (i.e., the exponential-shaped decays discussed in Chapter 3) were well-accounted for by a viscously-accreting fully-irradiated disc, the later stages show a more varied light-curve morphology. This diversity provides indirect evidence for the existence of a temporal and spatially varying X-ray irradiation source heating the discs in these systems. It also suggests that the later-stage light-curve morphology involves a variety of physical mechanisms of which irradiation is only one (e.g., mass loss through inner disc evaporation to a radiatively-inefficient structure or through a magnetized disc wind may play a more prominent role in shaping the outburst light-curves than originally thought). This is a significant change in paradigm from what is typically assumed in these types of systems.

Lastly, I have investigated how our Bayesian statistical methodology compares to numerical DIM codes that were built to simulate accretion flows in binary systems. I find that we are able to reproduce the model light-curves 74% of the time, only having trouble reproducing specific models involving a combination of very strong irradiation, large discs, and large values of the α-viscosity parameter. This demonstrates the robustness and usefulness of our methodology.

Applied a new methodology to establish a new class of BH-LMXBs

In Chapter 5, I performed a comprehensive study of the unusual BH-LMXB Swift J1753.5-0127 (J1753), during its ~ 12 years of outburst activity.

First, I have presented an investigation of the long-term behaviour of J1753 using X-ray light-curves from three different telescopes covering a time period ranging from J1753's discovery in 2005 to present day. While I find the light-curve of the main outburst is well described by the classic LMXB outburst decay profile (i.e. an exponential followed by a linear decay), the system never fully decayed to a quiescent level, as is typical of these systems. Instead, J1753 underwent a standstill phase, following the main outburst, in which it remained at an intermediate flux level (below the peak outburst flux of the main outburst), exhibiting variability on various timescales, before finally returning to a true quiescent level.

Through sophisticated modelling of both the X-ray light-curve and UVOIR SED obtained during this phase, I was able to attribute this observed standstill to a variable mass-transfer rate from the companion star (see also Coriat et al., 2012), $\dot{M}_2 > \dot{M}_{\rm crit}$, allowing the disc to remain in a hot,ionized stable state for an ~ 9 year period. This hypothesis is supported by (i) a calculated time-averaged $\dot{M}_2$ (over the standstill phase), which was greater than the critical value in the outer disc, and (ii) the UVOIR SED behaviour (obtained during this phase). The latter was consistent with a scenario involving an irradiated disc truncated at large radii, and an inner corona flow (existing inside and above the disc) acting as the source of irradiating X-rays, of which a large fraction are reprocessed in the outer disc ($C_{\rm irr} \sim 8.8 \times 10^{-2}$). Moreover, this scenario is also supported by previous spectral (e.g., Kajava et al. 2016) and timing (e.g., Veledina et al. 2017) studies during the standstill phase of this source. Given the available evidence, I suggest that a period of strong X-ray irradiation may have driven the enhanced mass-transfer of the standstill phase.

Contrary to what we expect from BH-LMXBs (typical recurrence timescales are $\sim$ years – decades), J1753 would not remain in quiescence for very long. Approximately 102 days after J1753 returned to quiescence, it was observed to undergo two low-luminosity mini-outbursts, before returning to a quiescent state for the second time in its history. I attribute the mini-outburst interval to $\dot{M}_2$ remaining low enough (i.e., below $\dot{M}_{\rm crit}$), that the disc remained in the instability zone, allowing for a series of transient outbursts to occur. Through sophisticated modelling of the X-ray light-curves and spectra, UVOIR SEDs, and UVOIR/X-ray correlations, I am able to conclude that the evolution of the first mini-outburst is consistent with a scenario involving a fully irradiated disc, truncated at a large radius, with a hot, radiatively inefficient, accretion flow inside it, within which the source of irradiating X-rays (likely produced mainly by the synchrotron self-Compton process), and a significant portion of the optical/UV (via synchrotron photons) emission, are produced.

This scenario is supported by the observed: (i) light-curve profile, displaying the classic exponential+linear shape predicted by the DIM+irradiation (IDIM; Dubus et al. 1999, 2001) for the outburst of an irradiated disc; (ii) high fraction of reprocessed X-rays ($C_{\rm irr}$) derived from the X-ray light-curve, implying the presence of a large source of irradiating X-rays impinging on the disc; (iii) evolution of the UVOIR SEDs throughout the mini-outburst, consistent with a truncated irradiated disc cooling and receding further from the BH; and (iv) power-law correlations between optical/UV and X-ray emission, showing only the far-UV emission to be consistent with pure reprocessed X-ray irradiation and evidence for multiple sources of optical and (near and middle) UV emission present.

Overall, I have found that the long-term behaviour observed in J1753 bears a striking resemblance to Z Cam stars, whereby variable mass-transfer from the companion drives unusual outbursts, characterized by stalled decays and abrupt changes in luminosity. Thus, I suggest that J1753 is in fact a BH-LMXB analogue to Z Cam type dwarf novae, where the enhanced mass-transfer from the companion is driven by the changing irradiation properties of the system, affecting both the accretion disc and companion star.

Most broadly, this work demonstrates the greater amount of physics that can be revealed when combining broad-band SED studies with my Bayesian methodology of the X-ray light curves. This combined method can:

- probe, and track the evolution of, the mechanisms of mass transport in the disc, as well as the properties of the X-ray irradiation heating the disc;

- investigate the dominant emission mechanisms present throughout each accretion regime; and
- quantitatively build a mass-transfer history for any given BH-LMXB.

6.2 Future Work

To begin to understand the evolution of accretion disc structure through the course of a LMXB outburst, we need to: (i) quantify the significant role mass loss, through a strong disc wind, plays in the disc-accretion process; (ii) probe how the strength and geometry of the X-ray irradiating source heating the discs in these systems evolves over time and spatially within the disc itself; (iii) investigate how outburst properties of discs vary across the Galactic LMXB population; and (iv) understand what governs the rate, and evolution over time, of mass-transfer from the companion star to discs in accretion binary systems.

High resolution X-ray spectral data that are taken throughout an outburst decay, and thus across all accretion states and a wide range of luminosity regimes, can be used to search for the signature of an accretion disc wind. In this way, one can quantify both the mass loss rate, and outflow mechanism responsible, whether it be magnetically-driven or thermally-driven in nature, for the accretion disc wind outflow in LMXBs. I am a co-investigator on an approved *Chandra* program that will target the relatively uncharted cooling of a disc wind. Moreover, I am also working on adding mass loss prescriptions, more advanced then the basic toy model presented in Chapter 3, to my Bayesian methodology. The goal here being to develop an algorithm to derive disc wind mass loss rates (which have traditionally only ever been measured using X-ray spectroscopy) directly from observed X-ray light-curves.

Simultaneous, multi-wavelength, time-series data sets and phase-resolved spectroscopic data could be used to probe the temporally and spatially variable effects of X-ray irradiation. One possibility is to make use of a combination of optical and X-ray light-curves to quantify, the currently poorly understood, fraction of bolometric accretion luminosity that is intercepted and reprocessed by the disc in an LMXB system. By computing the fraction of X-ray emission needed to be reprocessed to explain the observed optical luminosity (e.g., see Suleimanov et al. 2008; Lipunova & Malanchev 2017), one can put observational constraints on the irradiation constant $C_{\rm irr}$, a parameter which encapsulates information on many unknown properties of LMXB discs such as the irradiation geometry and the X-ray albedo in the disc. A second possibility involves using a combination of X-ray and optical light-curves to understand physical properties of the different components that make up the accretion flow in LMXBs. Using the correlation between X-ray and optical variability often observed in LMXBs one could potentially put constraints on properties such as the size of, and the characteristic timescales at which matter moves through, different emitting regions of the accretion flow (e.g. Malzac et al. 2003; Hynes et al. 2004; Veledina et al. 2017; Gandhi et al. 2017).

Combining data from historical (e.g., Ariel-V, BeppoSAX, Ginga) and recently launched (e.g., NICER) X-ray missions, and telescopes operating at UVOIR wavelengths — such as Swift/UVOT, SMARTS, and AAVSO — would help expand the limited sample of LMXBs where we have disc properties, such as α-viscosity and the irradiation constant $C_{\rm irr}$, derived. Obtaining a larger sample would further our understanding of how (or if) the value of physical properties such as these vary from source to source (e.g., with changing $P_{\rm orb}$ or component masses; Esin et al. 2000) or even between outbursts of the same source (e.g. with changing peak outburst luminosity or outburst duration; Esin et al. 2000).

Studying various classes of X-ray binaries that are known to exhibit Z Cam type behaviour, and comparing them to systems with similar binary parameters that do not exhibit this behaviour, may further our understanding of the mechanisms driving mass-transfer in accreting binary systems. Mass-transfer rates in various classes of X-ray binaries (e.g., CVs and LMXBs) show huge variations, from system to system, on various timescales. In fact, Z Cam-like behaviour in particular, characterized by standstill phases where mass-transfer varies close to the critical rate for the accretion disc in the system, is not uncommon, having been observed in multiple BH and neutron star LMXBs (e.g., Esin et al. 2000; Haswell & King 2001; Kotze & Charles

2012). Through a combination of theoretical modelling and multi-wavelength observational analysis, it may be possible to determine why some systems are Z Cam analogues and others are not.

Appendix A

A New Bayesian Hierarchical Methodology for BH-LMXB Outbursts

In this appendix I provide a visual representation (Figure A.1) and detailed step-by-step description (see below) of the process involved in my Bayesian hierarchical methodology. This methodology, developed as part of this thesis and used in Chapters 3–5, allows one to derive observation constraints on the α-viscosity parameter (α_h), and fraction of X-ray reprocessed ($C_{\rm irr}$), in the irradiated accretion discs of an ensemble of LMXB systems directly from observational data. This is done by sampling from the posterior distribution of each quantity.

A.1 Detailed Work-flow of the Bayesian Hierarchical Methodology

1. Data Preparation: The purpose of this phase is to build bolometric light-curves of individual outbursts using band-limited light-curves from multiple X-ray instruments. This phase can be run sequentially for data from multiple outbursts occurring in the user specified sample of LMXBs. The steps involved for an

individual outburst are as follows:

   (a) *Convert Instrument Count-rate to Flux:* One can use mCrabs as a baseline unit of flux to calculate approximate count rate equivalences in a given energy band. This is accomplished by integrating the now accepted canonical simple power-law spectrum of the Crab Nebula (Toor & Seward, 1974),

   $$I(E) = 9.7E^{-1.10}\mathrm{keV\,cm^{-2}\,s^{-1}\,keV^{-1}}, \tag{A.1}$$

   over the given band. This methodology uses this algorithm because it is a useful approximation for data-sets, covering long periods of time, for which detailed spectral information is not always available.

   (b) *Determine and Apply Bolometric Correction:* The bolometric correction (BC) factor during outburst depends on the spectral shape of a source. One option is to assume a BC that remains constant when a source transverses through each accretion state during outburst. To convert the band-limited flux light-curve derived in the previous step into a bolometric flux light-curve under this assumption, this methodology first parses through an outburst on a daily timescale, using the WATCHDOG online Accretion-State-By-Day tool[1] (see Chapter 2) to determine the accretion state of the source on each day. Then it applies the appropriate BC (derived by Migliari & Fender (2006): BC= 5 and BC= 1.25 for the hard and soft/intermediate states, respectively) to the daily-averaged flux on each day of available data. This results in a times-series data-set of bolometric flux over an individual outburst. The user also has the option of using custom BCs per accretion state.

2. Characterize Outburst Light-curve Profiles: The purpose of this phase is to characterize the shape of an outburst light-curve profile based on parameters that govern the timescales at which matter moves through, and the emitted

---

[1] http://astro.physics.ualberta.ca/WATCHDOG

flux of, an accretion disc throughout outburst.

(a) *The Model:* To characterize an outburst light-curve profile, this methodology fits an analytical version of the irradiated DIM (as developed in Chapters 3 and 4), to the bolometric flux light-curve(s) created in the previous step. This analytical model, defined as,

$$f_X = \begin{cases} (f_t - f_2)\exp\left(-(t - t_{\text{break}})/\tau_e\right) + f_2 & t \leq t_{\text{break}} \\ f_t\left(1 - (t - t_{\text{break}})/\tau_l\right) & t > t_{\text{break}}, \end{cases}$$

describes the flux of a LMXB during the decay phase of an outburst in terms of five parameters:

  i. exponential (viscous) decay timescale (τ_e);
  ii. linear (irradiation-controlled) decay timescale (τ_l);
  iii. X-ray flux of the system at the transition between exponential and linear decay stages (f_t);
  iv. time after the outburst peak when the transition between exponential and linear decay stages occurs (t_{break}); and
  v. X-ray flux limit of the exponential decay stage (f_2).

(b) *The Fitting Algorithm:* This methodology uses the `emcee` PYTHON package (Foreman-Mackey et al., 2013), an implementation of Goodman & Weare's Affine Invariant MCMC Ensemble Sampler (Goodman & Weare, 2010), to fit the analytical irradiated DIM to a bolometric flux light-curve. This MCMC algorithm works by using an ensemble of "walkers" to simultaneously move through and explore the parameter space. The steps involved in this algorithm are as follows:

  i. *Choose Ensemble of "Walkers":* One has the option of choosing the number of "walkers" used for this task. The input variable is N times the model dimensions. The default value is $N = 10$, corresponding to 10 "walkers" per model dimension.
  ii. *Determine a Starting Point:* For the algorithm to run optimally, one

needs to set the initial positions of the chosen ensemble of “walkers” in the parameter space. This methodology does so by feeding the light-curve model and bolometric flux light-curve created earlier into `pyHarmonySearch` (Geem et al., 2001), a global optimization algorithm that acts as a less time-consuming version of a brute force grid search. The user must input a “by-eye” estimate for the parameter set before `pyHarmonySearch` can run. Ultimately, `pyHarmonySearch` provides an initial survey of the parameter space, and in-turn a “best guess” for the set of model parameters, that is used as starting point for the MCMC sampler.

iii. *Set Priors on Model Parameters:* Before running the MCMC sampler, prior distributions for each of the five parameters must also be set. For a well-sampled light-curve, the methodology assumes a Gaussian prior for each parameter, with a mean set by the results of the `pyHarmonySearch`. If the light-curve is not well-sampled, the methodology defaults to a wide flat prior (based on expectations from other outbursts of the same source, or outbursts from sources with similar orbital periods) for each parameter. The user has the option of overriding these default priors, and setting a custom prior for each parameter.

iv. *Run MCMC Sampler For an Initial “Burn-in” Phase:* Before fully running the MCMC Sampler, the methodology first checks if the initial configuration chosen in the above steps allows the “walkers” to sufficiently explore the parameter space by running the sampler through a “burn-in” phase. To accomplish this task, the methodology: (i) builds the specified ensemble of “walkers and places them in the determined initial positions in the parameter space; (ii) feeds the light-curve model, bolometric flux light-curve data, and estimated priors on the model parameters into the MCMC Sampler; and then (iii) evolves the ensemble of “walkers” over a series of 500 steps.

v. *Start MCMC Sampler Again:* After “burn-in”, the MCMC algorithm is restarted, with the "walkers" starting at the final position they acquired during the "burn-in" phase, and run until convergence. When an acceptance fraction (i.e., the ratio of accepted to proposed steps) reaches the range between 0.2–0.5, the methodology marks the fit as converged and the likelihood maximization as complete.

(c) *Posterior Distributions of Light-curve Parameters:* After the likelihood maximization is complete, the methodology will prompt the user to perform visual inspection of the trace plots (i.e., path of the ensemble of "walkers" through the parameter space), to confirm convergence. If the user accepts that the fit has converged, the methodology will output the converged solution found from the MCMC algorithm in the form of posterior distributions of each parameter (τ_e, τ_l, f_t, $t_{\rm break}$, and f_2). The steps for the fitting algorithm presented are repeated for all individual outbursts occurring in a set of LMXB systems specified by the user. Accordingly, at the end of this process, the methodology will output a data file containing the best-fit light-curve parameters for each individual outburst in the user specified sample.

3. Set Disc Structure and Composition: The purpose of this phase is to choose the disc structure that the methodology will use to describe the user-specified LMXB sample.

   (a) *Choose Disc Temperature Profile:* One has the option of defining how temperature varies with radius in the disc. In this methodology, a power-law temperature distribution of the form,

   $$T(R) = T_{\rm in}\left(\frac{R}{R_{\rm in}}\right)^{-n}, \tag{A.2}$$

   is assumed. The power-law index, n, can be set between $0.4 - 0.5$, appropriate for modelling an irradiated disc. The default is set at $n = 0.5$.

   (b) *Choose Disc Midplane Temperature:* As the central midplane temperature of the disc (T_c) is only weakly dependent on viscosity and X-ray irradiation in LMXBs, this methodology approximates its value as a constant, which can be chosen by the user. The default value is set at 16300 K (Lasota et al., 2015).

(c) *Choose Disc Composition:* The user has the option of choosing a disc composed of hydrogen or helium. This is accomplished by inputting the appropriate adiabatic gas constant (γ) and gas particle mass (m_i). The default is set for a disc composed of hydrogen ($\gamma = 7/5$ and $m_i = m_H$).

4. Constrain Accretion Disc Properties: The purpose of this phase is to characterize the angular-momentum (and mass) transport process, and the X-ray irradiation heating, in the accretion discs of LMXB systems by deriving observational constraints on the α-viscosity parameter (α_h) and the irradiation constant ($C_{\rm irr}$), which represents the fraction of X-rays reprocessed in the outer disc.

(a) *The Model:* Both α-viscosity and $C_{\rm irr}$ are related to the shape of the outburst light-curve profile, as well as the orbital parameters defining the size and mass scales of the binary system (namely the compact object mass and accretion disc radius, which in itself is dependent on the masses of the compact object and companion star in the system and the orbital period), via,

$$\left(\frac{\alpha_h}{0.1}\right) = \left(\frac{G^{0.5} m_H M_\odot^{0.5}(10^6)}{3\gamma k_b T_c}\right)\left(\frac{\tau_e}{s}\right)^{-1}\left(\frac{M_1}{M_\odot}\right)^{0.5}\left(\frac{R_d}{10^{10}\text{cm}}\right)^{0.5}, \quad \text{(A.3)}$$

and,

$$\left(\frac{C_{\rm irr}}{T_{\rm irr}^4}\right) = (5.4 \times 10^6)\left(\frac{f_t}{10^{-12}\text{ergs}^{-1}\text{cm}^{-2}}\right)^{-1}\left(\frac{d}{\text{kpc}}\right)^{-2}\left(\frac{R_{\rm disc}}{10^{10}\text{cm}}\right)^{2}. \quad \text{(A.4)}$$

See Chapters 3 and 4 for a detailed derivation of these relations.

(b) *Construct the Hierarchical Framework:* By building a Bayesian hierarchical model, one can simultaneously constrain α_h and $C_{\rm irr}$ (using the above equations) using the outburst light-curve of a source. This is done for each outburst in an ensemble of sources. In the case of multiple outbursts for the same source, the same posterior distribution of binary properties is used, but different α_h and C_{irr} are derived. This methodology will build a custom hierarchical framework based on the following user specifications:

i. *Set Model Dimensions and Priors:* One has the option of setting a source sample containing X number of individual outbursts occurring in Y sources. X and Y can take any integer number. The total number of dimensions in the framework is determined by user specified prior knowledge of:

   - Compact Object Mass (M_1);
   - Mass Ratio ($q = M_2/M_1$); and
   - Orbital Period (P_{orb}),

   for the source/outburst sample. For M_1 and q, one has the option of (i) inputting a known estimate of the parameter (assumed to be a Gaussian distribution based on measurement and uncertainty)or (ii) choosing the observed Galactic distribution of the parameter, as a prior for each system in the sample. The default Galactic distributions used are the Ozel mass distribution (Ozel et al., 2010) and the observed mass ratio distribution for the dynamically confirmed BHs in the Galaxy (Tetarenko et al., 2016). However, the user has the option to specify a custom distribution or either parameter. For P_{orb}, one must specify a known estimate for each system in the sample to be used as a prior. Each unique prior for M_1, q, and P_{orb} contributes a single dimension to the framework.

ii. *Choose Ensemble of "Walkers":* One has the option of choosing the number of "walkers" used per dimension of the hierarchical framework created above. The default is 10 "walkers" per dimension

iii. *Set a Starting Point:* The initial positions of the ensemble of "walkers" used are set by the methodology to be the mean of the prior distributions defined above for M_1, q, and P_{orb}.

iv. *Define Individual Sampling Levels:* To approximate the posterior distributions of α_h and $C_{\rm irr}$ requires four levels of sampling. These levels are defined as follows:

- *Level 1:* The first level of the hierarchical framework involves sampling from (and obtaining approximations of) the posterior distribution of the circularization radius ($R_{\rm circ}$) and the radius of the compact object's Roche lobe (R_1) for each system in the sample. To do so, the methodology uses the analytical approximations (Frank et al., 2002),

  $$\frac{R_{\rm circ}}{a} = (1+q)\left(\frac{R_1}{a}\right)^4, \tag{A.5}$$

  and

  $$\frac{R_1}{a} = 0.5 - 0.227\log_{10}(q), \tag{A.6}$$

  where,

  $$a = (3.5\times10^{10})M_1^{1/3}(1+q)^{1/3}P_{\rm orb}^{2/3}\,{\rm cm}, \tag{A.7}$$

  is the orbital separation of the binary, and samples from the combination of prior distributions set for M_1, q, and $P_{\rm orb}$ by the user.

- *Level 2:* The second level of the hierarchical framework involves sampling from (and obtaining approximations of) the accretion disc radius of each system ($R_{\rm disc}$). The methodology accomplishes this task by sampling $R_{\rm disc}$ from a uniform distribution between $R_{\rm circ}$ and R_1, using the posterior distributions of these quantities obtained in Level 1.

- *Level 3:* The third level of the hierarchical framework involves sampling from (and obtaining approximations of) the α-viscosity parameter (α_h) for each individual outburst of each system in the sample. The methodology samples α_h from a combination of the posterior distribution for viscous timescale (τ_e) obtained from characterizing each outburst light-curve profile, the prior distributions set for M_1, and the posterior distribution of R_{disc} obtained in Level 2.

- *Level 4:* The fourth level of the hierarchical framework involves sampling from (and obtaining approximations of) the irradiation constant (C_{irr}) for each individual outburst of each system in the sample. The methodology samples C_{irr} from a combination of the posterior distribution for transition flux (f_t) obtained from characterizing each outburst light-curve profile, the prior distribution set for M_1, a user specified distance to each source (d; similar to the orbital parameters, a Gaussian distribution based on measurement and uncertainty is assumed), and the posterior distribution of R_{disc} obtained in Level 2.

(c) *Perform the Hierarchical Sampling:* Similar to the light-curve fitting algorithm presented above, the methodology uses the MCMC sampler, from the `emcee` PYTHON package (Foreman-Mackey et al., 2013), to perform each level of sampling sequentially. For each level, the MCMC sampler is first run for an initial 500 step "burn-in" phase. Then the MCMC sampler is restarted, with the "walkers" starting at the final position they acquired during the "burn-in" phase, and run until convergence. When the acceptance fraction reaches the range between 0.2–0.5, likelihood maximization for the level is considered complete. After all four levels have been sampled with this procedure, the final result is the posterior distributions of the α-viscosity parameter (α_h) and irradiation constant (C_{irr}) for each individual outburst of each source in the user established sample.

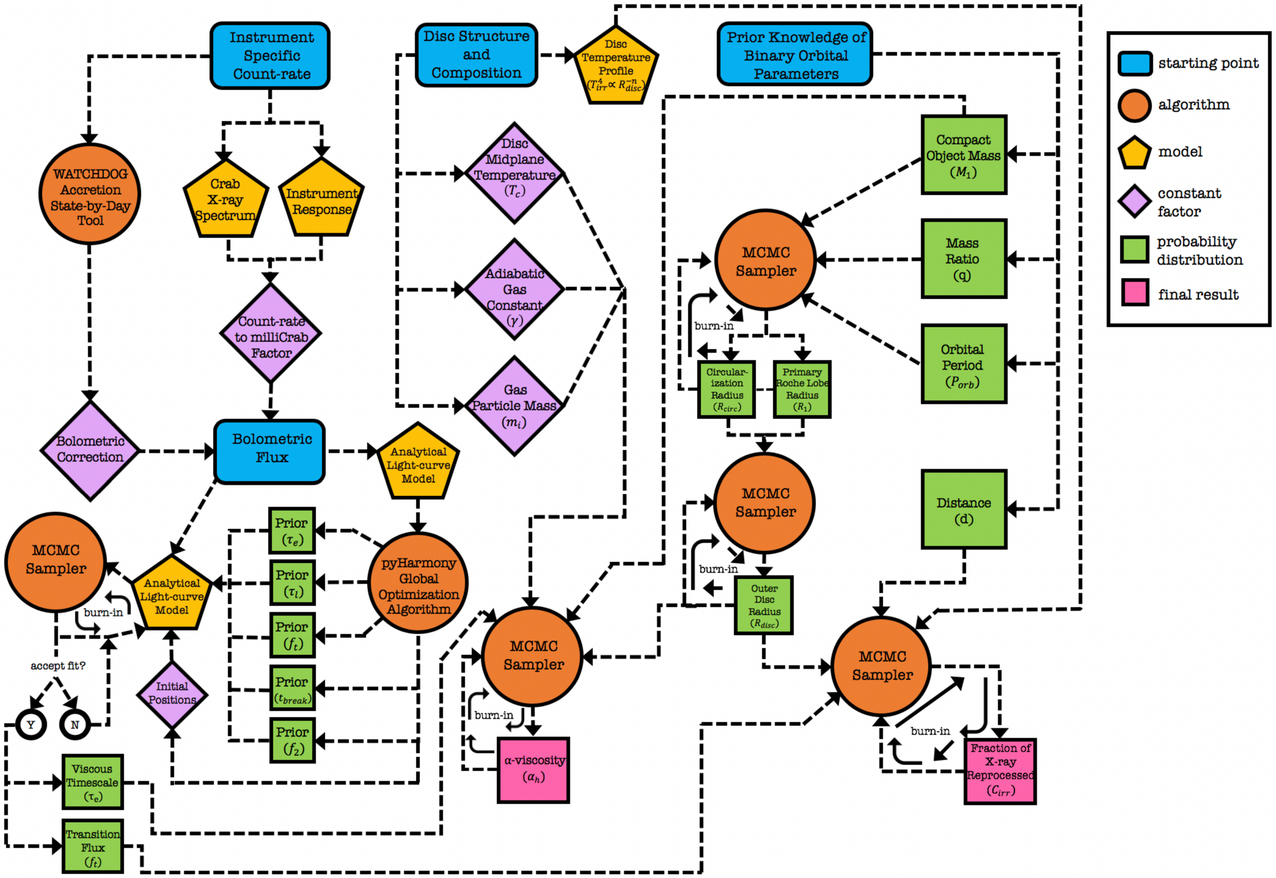

Figure A.1: The process involved in the Bayesian Hierarchical Methodology developed and used in Chapters 3–5.

Bibliography

Abramowicz, M., & Igumenshchev, I. 2001, ApJ, 554, L53

Al Qasim, A., AlMannaei, A., Russell, D. M., & Lewis, F. 2016, The Astronomer's Telegram, 9739

Al Qasim, A., AlMannaei, A., Russell, D. M., et al. 2017, The Astronomer's Telegram, 10075

Aref'ev, V. A., Revnivtsev, M. G., Lutovinov, A. A., & Sunyaev, R. A. 2004, AstL, 30, 669

Armas Padilla, M., Degenaar, N., Russell, D. M., & Wijnands, R. 2013, MNRAS, 428, 3083

Armas Padilla, M., Wijnands, R., Altamirano, D., et al. 2014, MNRAS, 439, 3908

Arnaud, K. A. 1996, in Astronomical Society of the Pacific Conference Series, Vol. 101, Astronomical Data Analysis Software and Systems V, ed. G. H. Jacoby & J. Barnes, 17

Augusteijn, T., Kuulkers, E., & Shaham, J. 1993, A&A, 279, L13

Bai, X.-N., & Stone, J. 2013, Astrophys. J., 767, 30

Balbus, S., & Hawley, J. 1991, Astrophys. J., 376, 214

—. 1998, Rev. Mod. Phys, 70, 1

Barthelmy, S. D., D'Avanzo, P., Deich, A., et al. 2018, GRB Coordinates Network, Circular Service, No. 22416, #1 (2018/February-0), 22416

Barthelmy, S. D., Barbier, L. M., Cummings, J. R., et al. 2005, Space Sci. Rev., 120, 143

Basak, R., & Zdziarski, A. 2016, MNRAS, 458, 2199

Begelman, M., & Mckee, C. 1983, ApJ, 271, 89

Belczynski, K., Kalogera, V., & Bulik, T. 2002, ApJ, 572, 407

Belczynski, K., Kalogera, V., Zezas, A., & Fabbiano, G. 2004, ApJ, 601, L147

Belloni, T., ed. 2010, Lecture Notes in Physics, Berlin Springer Verlag, Vol. 794, The Jet Paradigm

Belloni, T., Colombo, A. P., Homan, J., Campana, S., & van der Klis, M. 2002, A&A, 390, 199

Belloni, T., Mendez, M., van der Klis, M., et al. 1999, ApJ, 519, L159

Belloni, T., Parolin, I., Del Santo, M., et al. 2006, MNRAS, 367, 1113

Bernardini, F., Zhang, G., Russell, D. M., et al. 2017, The Astronomer's Telegram, 10325

Bianchi, S., Ponti, G., Muñoz-Darias, T., & Petrucci, P.-O. 2017, ArXiv e-prints, arXiv:1709.00860

Blandford, R., & Begelman, M. 1999, MNRAS, 303, L1

Blandford, R. D., & Königl, A. 1979, ApJ, 232, 34

Bradt, H., & McClintock, J. 1983, ARA&A, 21, 13

Bright, J., Staley, T., Fender, R., Motta, S., & Cantwell, T. 2017, The Astronomer's Telegram, 10110

Brocksopp, C., Bandyopadhyay, R. M., & Fender, R. P. 2004, New Ast., 9, 249

Brocksopp, C., Jonker, P. G., Fender, R. P., et al. 2001, MNRAS, 323, 517

Brocksopp, C., Jonker, P. G., Maitra, D., et al. 2010, MNRAS, 404, 908

Buat-Ménard, V., Hameury, J.-M., & Lasota, J.-P. 2001a, Astron. Astrophys., 366, 612

—. 2001b, A&A, 369, 925

Buning, A., & Ritter, H. 2004, A&A, 423

Burrows, D. N., Hill, J. E., Nousek, J. A., et al. 2000, in Proc. SPIE, Vol. 4140, X-Ray and Gamma-Ray Instrumentation for Astronomy XI, ed. K. A. Flanagan & O. H. Siegmund, 64–75

Burrows, D. N., Hill, J. E., Nousek, J. A., et al. 2005, Space Sci. Rev., 120, 165

Buxton, M. M., Bailyn, C. D., Capelo, H. L., et al. 2012, AJ, 143, 130

Cadolle Bel, M., Ribó, M., Rodriguez, J., et al. 2007, ApJ, 659, 549

Campana, S., Coti Zelati, F., & D'Avanzo, P. 2013, Mon. Not. R. Astron. Soc., 432, 1695

Cannizzo, J., Chen, W., & Livio, M. 1995, ApJ, 454, 880

Cannizzo, J. K. 1993, in Accretion Disks in Compact Stellar Systems, ed. J. C. Wheeler (World Scientific Publishing Co), 6–40

—. 2000, ApJL, 534, L35

Cannizzo, J. K., Wheeler, J. C., & Ghosh, P. 1985, in Proceedings of the Seventh North American Workshop, Vol. 113, Cataclysmic variables and low-mass X-ray binaries, ed. D. Lamb & J. Patterson (Cambridge, MA: Dordrecht, D. Reidel Publishing), 307–313

Capitanio, F., Bazzano, A., Ubertini, P., & Bird, A. J. 2006, in VI Microquasar Workshop: Microquasars and Beyond, 74

Capitanio, F., Belloni, T., Del Santo, M., & Ubertini, P. 2009, MNRAS, 398, 1194

Capitanio, F., Ubertini, P., Bazzano, A., & Del Santo, M. 2010, in The First Year of MAXI: Monitoring Variable X-ray Sources, 11P

Capitanio, F., Ubertini, P., Bazzano, A., et al. 2005, ApJ, 622, 503

Casares, J. 2016, ApJ, 822, 99

Cash, W. 1979, ApJ, 228, 939

Cassatella, P., Uttley, P., & Maccarone, T. J. 2012, MNRAS, 427, 2985

Chakravorty, S., Lee, J. C., & Neilsen, J. 2013, Mon. Not. R. Astron. Soc., 436, 560

Charles, P. A., & Coe, M. J. 2006, in Compact stellar X-ray sources, ed. W. H. G. Lewin & M. van der Klis (Cambridge University Press), 215–265

Chaty, S., Dubus, G., & Raichoor, A. 2011, A&A, 529, A3

Chen, W., Shrader, C., & Livio, M. 1997, Astrophys. J., 491, 312

Chiang, C. Y., Done, C., Still, M., & Godet, O. 2010, MNRAS, 403, 1102

Coleman, M., Kotko, I., Blaes, O., Lasota, J.-P., & Hirose, S. 2016, Mon. Not. R. Astron. Soc., 462, 3710

Corbel, S., Coriat, M., Brocksopp, C., et al. 2013, MNRAS, 428, 2500

Corbel, S., & Fender, R. P. 2002, ApJL, 573, L35

Corbel, S., Tomsick, J., & Kaaret, P. 2006, ApJ, 636, 971

Coriat, M., Fender, R., & Dubus, G. 2012, Mon. Not. R. Astron. Soc., 424, 1991

Corral-Santana, J. M., Casares, J., Muñoz-Darias, T., et al. 2016, A&A, 587, A61

Corral-Santana, J. M., Casares, J., Shahbaz, T., et al. 2011, MNRAS, 413, L15

Croton, D. J., Springel, V., White, S. D. M., et al. 2006, Mon. Not. R. Astron. Soc., 365, 11

Curran, P. A., & Chaty, S. 2013, A&A, 557, 45

Curran, P. A., Coriat, M., Miller-Jones, J. C. A., et al. 2014, MNRAS, 437, 3265

Davis, S. W., Stone, J. M., & Pessah, M. E. 2010, Astrophys. J., 713, 52

de Jong, J., van Paradijs, J., & Augusteijn, T. 1996, Astron. Astrophys., 314, 484

Debnath, D., Chakrabarti, S., & Nandi, A. 2013a, AdSpR, 52, 2143

Debnath, D., Mondal, S., & Chakrabarti, S. 2013b, arXiv:1306.3745v1

Deegan, P., Combet, C., & Wynn, G. 2009, MNRAS, 400, 1337

DePoy, D. L., Atwood, B., Belville, S. R., et al. 2003, in Proc. SPIE, Vol. 4841, Instrument Design and Performance for Optical/Infrared Ground-based Telescopes, ed. M. Iye & A. F. M. Moorwood, 827–838

Di Matteo, T., Springel, V., & Hernquist, L. 2005, Nature, 433, 604

Diaz Trigo, M., Migliari, S., Miller-Jones, J. C. A., & Guaninazzi, M. 2014, A&A, 571, A76

Done, C. 2010, in XXI Canary Islands Winter School of Astrophysics, ed. T. Shahbaz (Cambridge University Press), 184–226

Done, C., Gierlinski, M., & Kubota, A. 2007, A&ARv, 15, 1

Dubus, G., Hameury, J.-M., & Lasota, J.-P. 2001, Astron. Astrophys., 373, 251

Dubus, G., Lasota, J.-P., Hameury, J.-M., & Charles, P. 1999, Mon. Not. R. Astron. Soc., 303, 139

Dunn, R. J. H., Fender, R. P., Körding, E. G., Belloni, T., & Cabanac, C. 2010, MNRAS, 403, 61

Esin, A., Lasota, J.-P., & Hynes, R. 2000, A&A, 354, 987

Esin, A., McClintock, J., & Narayan, R. 1997, ApJ, 489, 865

Esin, A. A., Kuulkers, E., McClintock, J. E., & Narayan, R. 2000, ApJ, 532, 1069

Evans, P. A., Beardmore, A. P., Page, K. L., et al. 2009, Mon. Not. R. Astron. Soc., 397, 1177

Falcke, H., Kording, E., & Markoff, S. 2004, A&A, 414, 895

Faulkner, J., Lin, D. N. C., & Papaloizou, J. 1983, Mon. Not. R. Astron. Soc., 205, 359

Fender, R. 2010, in Lecture Notes in Physics, Berlin Springer Verlag, Vol. 794, Lecture Notes in Physics, Berlin Springer Verlag, ed. T. Belloni, 115

Fender, R., Belloni, T., & Gallo, E. 2004, MNRAS, 355, 1105

Fender, R., & Gallo, E. 2014, arXiv:1407.3674

Fender, R., Gallo, E., & Jonker, P. 2003, MNRAS, 343, 99

Fender, R. P. 2001, MNRAS, 322, 31

Ferrigno, C., Bozzo, E., Del Santo, M., & Capitanio, F. 2011, A&A, 537, L7

Fitzpatrick, E. L., & Massa, D. 1999, ApJ, 525, 1011

Foreman-Mackey, D., Hogg, D. W., Lang, D., & Goodman, J. 2013, Pub. Astron. Soc. Japan, 125, 306

Fragos, T., Kalogera, V., Belczynski, K., et al. 2008, ApJ, 683, 346

—. 2009, ApJ, 702, L143

Frank, F., King, A., & Raine, D. 2002, Accretion Power in Astrophysics, 3rd edn. (Cambridge Univ. Press)

Fraser, G. 2009, Detectors in X-ray Astronomy (Cambridge University Press)

Froning, C. S., Maccarone, T. J., France, K., et al. 2014, ApJ, 780, 48

Frontera, F., Zdziarski, A. A., Amati, L., et al. 2001, ApJ, 561, 1006

Gandhi, P., Rao, A., Johnson, M. A. C., Paice, J. A., & Maccarone, T. J. 2018, ArXiv e-prints, arXiv:1804.11349

Gandhi, P., Dhillon, V. S., Durant, M., et al. 2010, MNRAS, 407, 2166

Gandhi, P., Bachetti, M., Dhillon, V. S., et al. 2017, Nature Astronomy, 1, 859

Garcia, J., McClintock, J., Steiner, J., Remillard, R., & Grinberg, V. 2014, ApJ, 794, 73

Garcia, M. R., McClintock, J. E., Narayan, R., et al. 2001, ApJ, 553, L47

Geem, Z., Kim, J., & Loganathan, G. 2001, Simulation, 76, 60

Gehrels, N. 1986, ApJ, 303, 336

Gierliński, M., Done, C., & Page, K. 2009, MNRAS, 392, 1106

Gierlinski, M., & Newton, J. 2006, MNRAS, 370, 837

Gilfanov, M. 2010, in Lecture Notes in Physics, Berlin Springer Verlag, Vol. 794, Lecture Notes in Physics, Berlin Springer Verlag, ed. T. Belloni (Springer), 17

Goodman, J., & Weare, J. 2010, Comm. App. Math. Comp. Sci., 5, 65

Halpern, J. P. 2005, ATel, 549, 1

Hameury, J., King, A. R., & Lasota, J. 1986, A&A, 162, 71

—. 1987, A&A, 171, 140

—. 1988, A&A, 192, 187

—. 1990, ApJ, 353, 585

Hameury, J.-M., & Lasota, J.-P. 2014, A&A, 569, A48

Hameury, J.-M., Lasota, J.-P., McClintock, J. E., & Narayan, R. 1997, ApJ, 489, 234

Hameury, J.-M., Lasota, J.-P., & Warner, B. 2000, A&A, 353, 244

Hameury, J.-M. Menou, K., Dubus, G, ., Lasota, J.-P., & Hure, J.-M. 1998, MNRAS, 298, 1048

Harmon, B. A., Wilson, C. A., Paciesas, W. S., et al. 1994, ApJ, 425, L17

Harpaz, A., & Rappaport, S. 1991, ApJ, 383, 739

Haswell, C. A., & King, A. R. 2001, X-ray Astronomy: Stellar Endpoints, AGN, and the Diffuse X-ray Background, 599, 642

Haswell, C. A., King, A. R., Murray, J. R., & Charles, P. A. 2001, MNRAS, 321, 475

Heinke, C. O., Bahramian, A., Degenaar, N., & Wijnands, R. 2015, Mon. Not. R. Astron. Soc., 447, 3034

Heinke, C. O., Altamirano, D., Cohn, H. N., et al. 2010, ApJ, 714, 894

Hiemstra, B., Soleri, P., Méndez, M., et al. 2009, MNRAS, 394, 2080

Higginbottom, N., & Proga, D. 2015, Astrophys. J., 807, 107

Hirose, S., Blaes, O., Krolik, J., Coleman, M., & Sano, T. 2014, Astrophys. J., 787, 1

Hjellming, R. M., & Wade, C. M. 1971, Nature, 234, 138

Hog, D., Bovy, J., & Lang, D. 2010, arXiv:1008.4686v1

Homan, J., Buxton, M., Markoff, S., et al. 2005, ApJ, 624, 295

Huang, M., & Wheeler, J. 1989, Astrophys. J., 343, 229

Hynes, R. I. 2005, ApJ, 623, 1026

Hynes, R. I., Haswell, C. A., Chaty, S., Shrader, C. R., & Cui, W. 2002a, MNRAS, 331, 169

—. 2002b, MNRAS, 331, 169

Hynes, R. I., Mauche, C. W., Haswell, C. A., et al. 2000, ApJ, 539, L37

Hynes, R. I., Charles, P. A., Garcia, M. R., et al. 2004, ApJL, 611, L125

Ichimaru, S. 1977, ApJ, 217, 840

in't Zand, J. J. M., Markwardt, C. B., Bazzano, A., et al. 2002, A&A, 390, 587

Ivanova, N., Justham, S., Chen, X., et al. 2013, A&A Rev., 21, 59

Jahoda, K., Swank, J. an Giles, A., Stark, M., et al. 1996, in X-Ray, and Gamma-Ray Instrumentation for Astronomy VII, ed. O. Siegmund & M. Gummin, Vol. 2808, 59–70

Jonker, P., Miller-Jones, J., Homan, J., et al. 2012, MNRAS, 423, 3308

Jonker, P. G., & Nelemans, G. 2004, MNRAS, 354, 355

Kajava, J. J. E., Veledina, A., Tsygankov, S., & Neustroev, V. 2016, A&A, 591, A66

Kalemci, E., Tomsick, J. A., Rothschild, R. E., et al. 2006, ApJ, 639, 340

Kato, T. 2015, PASJ, 67, 108

Kawamuro, T., Negoro, H., Yoneyama, T., et al. 2018, The Astronomer's Telegram, 11399

Kawase, T., Negoro, H., Yoneyama, T., et al. 2018, The Astronomer's Telegram, 11323

Kim, S.-W., Wheeler, J. C., & Mineshige, S. 1999, PASJ, 51, 393

King, A. 1988, QJRAS, 29, 1

King, A., & Pounds, K. 2015, Ann. Rev. Astron. Astrophys., 53, 115

King, A. L., Miller, J. M., Raymond, J., et al. 2012, ApJL, 746, L20

King, A. R., Kolb, U., & Burderi, L. 1996, ApJ, 464, 127

King, A. R., Pringle, J. E., & Livio, M. 2007, Mon. Not. R. Astron. Soc., 376, 1740

King, A. R., & Ritter, H. 1998, MNRAS, 293, 42

Knevitt, G., Wynn, G. A., Vaughan, S., & Watson, M. G. 2014, MNRAS, 437, 3087

Kolehmainen, M., Done, C., & Díaz Trigo, M. 2014, MNRAS, 437, 316

Kotko, I., & Lasota, J.-P. 2012, Astron. Astrophys., 545, 115

Kotze, M. M., & Charles, P. A. 2012, MNRAS, 420, 1575

Kraft, R. P., Burrows, D. N., & Nousek, J. A. 1991, ApJ, 374, 344

Krimm, H. A., Holland, S. T., Corbet, R. H. D., et al. 2013, ApJSS, 209, 14

Kubota, A., & Makishima, K. 2004, ApJ, 601, 428

Kuulkers, E., Shaw, S. E., Paizis, A., et al. 2007, A&A, 466, 595

La Palombara, N., & Mereghetti, S. 2005, A&A, 430, 53

Landolt, A. U. 1992, AJ, 104, 340

Lasota, J.-P. 2001, New Astron. Rev, 45, 449

Lasota, J.-P., Dubus, G., & Kruk, K. 2008, A&A, 486, 523

Lasota, J.-P., King, A. R., & Dubus, G. 2015, Astrophys. J. (Letters), 801, 4

Lee, J. C., Reynolds, C. S., Remillard, R., et al. 2002, ApJ, 567, 1102

Lesur, G., Ferreira, J., & Ogilvie, G. I. 2013, Astron. Astrophys., 550, A61

Levine, A., Bradt, H., Cui, W., et al. 1996, ApJ, 469, L33

Lin, D. N. C., Papaloizou, J., & Faulkner, J. 1985, MNRAS, 212, 105

Lin, D. N. C., & Taam, R. E. 1984, in American Institute of Physics Conference Series, Vol. 115, American Institute of Physics Conference Series, ed. S. E. Woosley, 83–102

Lipunova, G. V., & Malanchev, K. L. 2017, Mon. Not. R. Astron. Soc., 468, 4735

Lipunova, G. V., & Shakura, N. I. 2000, A&A, 356, 363

Liu, B. F., Yuan, W., Meyer, F., Meyer-Hofmeister, E., & Xie, G. Z. 1999, ApJL, 527, L17

Liu, Q. Z., van Paradijs, J., & van den Heuvel, E. P. J. 2001, A&A, 368, 1021

—. 2007, A&A, 469, 807

Lund, N., et al. 2003, A&A, 411, 231

Maccarone, T. 2003, A&A, 409

—. 2005, MNRAS, 360, 68

—. 2014, SSRv, 183, 101

Maccarone, T., & Coppi, P. 2003, MNRAS, 338, 189

Maccarone, T. J., & Patruno, A. 2013, MNRAS, 428, 1335

Makishima, K., Maejima, Y., Mitsuda, K., et al. 1986, ApJ, 308, 635

Malzac, J., Belloni, T., Spruit, H. C., & Kanbach, G. 2003, A&A, 407, 335

Malzac, J., & Belmont, R. 2009, MNRAS, 392, 570

Matsuoka, M., Kawasaki, K., Ueno, S., et al. 2009, PASJ, 61, 999

McClintock, J., & Remillard, R. 2006, in Compact Stellar X-Ray Sources, ed. W. Lewin & M. van der Klis, 157–206

McClintock, J., Remillard, R., Rupen, M., et al. 2009, ApJ, 698, 1398

McClintock, J. E., Haswell, C. A., Garcia, M. R., et al. 2001, ApJ, 555, 477

Meier, D. 2005, Ap&SS, 300, 55

Menou, K., Hameury, J.-M., Lasota, J.-P., & Narayan, R. 2000, Mon. Not. R. Astron. Soc., 314, 498

Menou, K., Narayan, R., & J.P., L. 1999, ApJ, 513, 811

Meshcheryakov, A. V., Tsygankov, S. S., Khamitov, I. M., et al. 2018, MNRAS, 473, 3987

Meyer, F., Liu, B. F., & Meyer-Hofmeister, E. 2007, A&A, 463, 1

Meyer, F., & Meyer-Hofmeister, E. 1981, Astron. Astrophys., 104, 10

Meyer, F., & Meyer-Hofmeister, E. 1983, A&A, 121, 29

Meyer-Hofmeister, E. 2004, A&A, 423, 321

Migliari, S., & Fender, R. 2006, Mon. Not. R. Astron. Soc., 366, 79

Mihara, T., Nakajima, M., Sugizaki, M., et al. 2011, PASJ, 63, 623

Miller, J. M., Homan, J., & Miniutti, G. 2006, ApJL, 652, L113

Miller, J. M., Raymond, J., Fabian, A., et al. 2006, Nature, 441, 953

Miller, J. M., Raymond, J., Reynolds, C. S., et al. 2008, ApJ, 680, 1359

Miller, J. M., Raymond, J., Fabian, A. C., et al. 2004, ApJ, 601, 450

Miller, J. M., Raymond, J., Homan, J., et al. 2006, Astrophys. J., 646, 394

Miller-Jones, J. C. A., Sivakoff, G. R., Altamirano, D., et al. 2012, MNRAS, 421, 468

Mineshige, S., & Wheeler, J. 1989, ApJ, 343, 241

Mitsuda, K., Inoue, H., Koyama, K., et al. 1984, PASJ, 36, 741

Morgan, E., Swank, J., Markwardt, C., & Gehrels, N. 2005, ATel, 550, 1

Motta, S., Belloni, T., & Homan, J. 2009, MNRAS, 400, 1603

Motta, S., Muñoz-Darias, T., & Belloni, T. 2010, MNRAS, 408, 1796

Narayan, R., Barret, D., & McClintock, J. E. 1997, ApJ, 482, 448

Narayan, R., & Yi, I. 1994, ApJ, 452, 710

Negoro, H., Ishikawa, M., Ueno, S., et al. 2017, The Astronomer's Telegram, 10699

Neilsen, J. 2013a, AdSpR, 52, 732

—. 2013b, Advances in Space Research, 52, 732

Neilsen, J., & Homan, J. 2012, ApJ, 750, 27

Neilsen, J., & Lee, J. 2009, Nature, 458, 481

Neustroev, V. V., Gafton, E., Haanpaa, V.-J., et al. 2016, The Astronomer's Telegram, 9741

Neustroev, V. V., Veledina, A., Poutanen, J., et al. 2014, MNRAS, 445, 2424

Ohsuga, K., & Mineshige, S. 2011, Astrophys. J., 736, 2

Oosterbroek, T., van der Klis, M., van Paradijs, J., et al. 1997, A&A, 321, 776

Osaki, Y. 1974, Pub. Astron. Soc. Japan, 26, 429

—. 1985, A&A, 144, 369

—. 1996, PASP, 108, 39

Osaki, Y., & Kato, T. 2013, PASJ, 65, 50

Ozel, F., Psaltis, D., Narayan, R., & McClintock, J. 2010, Astrophys. J., 725, 1918

Paczynski, B. 1971, A&A, 9, 183

Page, M. J., Symeonidis, M., Vieira, J. D., et al. 2012, Nature, 485, 213

Paizis, A., Ebisawa, K., Takahashi, H., et al. 2009, PASJ, 61, 107

Palmer, D. M., Barthelmey, S. D., Cummings, J. R., et al. 2005, ATel, 546, 1

Patruno, A., Maitra, D., Curran, P. A., et al. 2016, ApJ, 817, 100

Phinney, E. S. 1982, MNRAS, 198, 1109

Plant, D. S., Fender, R. P., Ponti, G., Muñoz-Darias, T., & Coriat, M. 2014, MNRAS, 442, 1767

Plotkin, R., Gallo, E., Markoff, S., et al. 2015, MNRAS, 446, 4098

Plotkin, R. M., Miller-Jones, J. C. A., Jonker, P. G., et al. 2016, The Astronomer's Telegram, 9765

Plotkin, R. M., Bright, J., Miller-Jones, J. C. A., et al. 2017, ApJ, 848, 92

Podsiadlowski, P. 1991, Nature, 350, 136

Podsiadlowski, P., Rappaport, S., & Pfahl, E. 2002, ApJ, 565, 1107

Ponti, G., Fender, R. P., Begelman, M. C., et al. 2012, Mon. Not. R. Astron. Soc., 422, L11

Portegies Zwart, S., Dewi, J., & Maccarone, T. 2004, MNRAS, 355, 413

Powell, C., Haswell, C., & Falanga, M. 2007, Mon. Not. R. Astron. Soc., 374, 466

Pringle, J., & Rees, M. J. 1972, A&A, 21, 1

Rahoui, F., Tomsick, J. A., Coriat, M., et al. 2015, ApJ, 810, 161

Reis, R. C., Miller, J. M., Reynolds, M. T., Fabian, A. C., & Walton, D. J. 2012, ApJ, 751, 34

Remillard, R., & McClintock, J. 2006, ARA&A, 44, 49

Remillard, R., Sobczak, G., Muno, M., & McClintock, J. 2002, ApJ, 564, 962

Revnivtsev, M., Borozdin, K., Priedhorsky, W., & Vikhlinin, A. 2000a, ApJ, 530, 955

Revnivtsev, M., Sunyaev, R., & Borozdin, K. 2000b, A&A, 361, 37

Reynolds, M. T., Miller, J. M., Homan, J., & Miniutti, G. 2010, ApJ, 709, 358

Rodriguez, J., Cadolle Bel, M., Tomsick, J., et al. 2007, ApJ, 655, L97

Roming, P. W. A., Hunsberger, S. D., Mason, K. O., et al. 2004, in Proc. SPIE, Vol. 5165, X-Ray and Gamma-Ray Instrumentation for Astronomy XIII, ed. K. A. Flanagan & O. H. W. Siegmund, 262–276

Roming, P. W. A., Kennedy, T. E., Mason, K. O., et al. 2005, Space Sci. Rev., 120, 95

Rothschild, R. E., Blanco, P. R., Gruber, D. E., et al. 1998, ApJ, 496, 538

Rushton, A. P., Shaw, A. W., Fender, R. P., et al. 2016, MNRAS, 463, 628

Russell, D. M., AlMannaei, A., Qasim, A. A., et al. 2016, The Astronomer's Telegram, 9708

Russell, D. M., Fender, R. P., Hynes, R. I., et al. 2006, MNRAS, 371, 1334

Russell, D. M., Maitra, D., Dunn, R. J. H., & Markoff, S. 2010, MNRAS, 405, 1759

Russell, D. M., Markoff, S., Casella, P., et al. 2012, MNRAS, 429, 815

Russell, T. D., Soria, R., Miller-Jones, J. C. A., et al. 2014, MNRAS, 439, 1390

Rykoff, E. S., Miller, J. M., Steeghs, D., & Torres, M. A. P. 2007, ApJ, 666, 1129

Salvesen, G., Simon, J. B., Armitage, P. J., & Begelman, M. C. 2016, Mon. Not. R. Astron. Soc., 457, 857

Scepi, N., Lesur, G., Dubus, G., & Flock, M. 2017, ArXiv e-prints, arXiv:1710.05872

Shahbaz, T., Charles, P., & King, A. 1998, Mon. Not. R. Astron. Soc., 301, 382

Shahbaz, T., & Kuulkers, E. 1998, MNRAS, 295, L1

Shakura, N., & Sunyaev, R. A. 1973, A&A, 24, 337

Shaposhnikov, N., Jahoda, K., Markwardt, C., Swank, J., & Strohmayer, T. 2012, ApJ, 757, 159

Sharma, S. 2017, Annual Review of Astronomy and Astrophysics, 55, 213

Shaw, A. W., Charles, P. A., Casares, J., & Hernández Santisteban, J. V. 2016a, MNRAS, 463, 1314

Shaw, A. W., Tomsick, J. A., Bahramian, A., et al. 2016b, The Astronomer's Telegram, 9735

Shaw, A. W., Tomsick, J. A., Zhang, G., et al. 2017, The Astronomer's Telegram, 10288

Shaw, A. W., Charles, P. A., Bird, A. J., et al. 2013, MNRAS, 433, 740

Shaw, A. W., Gandhi, P., Altamirano, D., et al. 2016c, MNRAS, 458, 1636

Shaw, A. W., Tomsick, J. A., Clavel, M., et al. 2016d, The Astronomer's Telegram, 8782

Sidoli, L., Paizis, A., Mereghetti, S., Gotz, D., & Del Santo, M. 2011, MNRAS, 415, 2373

Simon, J. B., Beckwith, K., & Armitage, P. J. 2012, Mon. Not. R. Astron. Soc., 422, 2685

Simon, V., Bartolini, C., Piccioni, A., & Guarenieri, A. 2006, Mon. Not. R. Astron. Soc., 369, 355

Simonsen, M. 2011, Journal of the American Association of Variable Star Observers (JAAVSO), 39, 66

Skrutskie, M. F., Cutri, R. M., Stiening, R., et al. 2006, AJ, 131, 1163

Smak, J. 1983, Astrophys. J., 272, 234

—. 1984, Acta Astron., 34, 161

Smak, J. 1999, Acta Astronomica, 49, 383

—. 2000, New Astronomy Reviews, 44, 171

Sobczak, G., McClintock, J., Remillard, R., et al. 2000, ApJ, 544, 993

Soleri, P., Muñoz-Darias, T., Motta, S., et al. 2013, MNRAS, 429, 1244

Sturner, S. J., & Shrader, C. R. 2005, ApJ, 625, 923

Subasavage, J. P., Bailyn, C. D., Smith, R. C., et al. 2010, in Proc. SPIE, Vol. 7737, Observatory Operations: Strategies, Processes, and Systems III, 77371C

Suleimanov, V. F., Lipunova, G. V., & Shakura, N. I. 2008, A&A, 491, 267

Sunyaev, R. A., & Truemper, J. 1979, Nature, 279, 506

Swank, J. 1997, in Nuclear Physics B Proceedings Supplements, ed. L. Scarsi, H. Bradt, P. Giommi, & F. Fiore (Rome, Italy: astro–ph/9802188)

Swank, J., & Markwardt, C. 2001, in Astronomical Society of the Pacific Conference Series, Vol. 251, New Century of X-ray Astronomy, ed. H. Inoue & H. Kunieda, 94

Szkody, P., Albright, M., Linnell, A. P., et al. 2013, PASP, 125, 1421

Tanaka, Y., & Lewin, W. 1995, in X-Ray Binaries, ed. W. Lewin, J. van Paradijs, & P. van den Heuvel (Cambridge University Press), 126–174

Tanaka, Y., & Shibazaki, N. 1996, ARA&A, 34, 607

Tananbaum, H., Gursky, H., Kellogg, E., & Giacconi, R. 1972, ApJ, 177, L5

Tauris, T. M., & van den Heuvel, E. P. J. 2006, in Compact stellar X-ray sources, ed. W. H. G. Lewin & M. van der Klis (Cambridge University Press), 623–665

Tetarenko, A. J., Sivakoff, G. R., Miller-Jones, J. C. A., et al. 2017, MNRAS, 469, 3141

Tetarenko, B. E., Dubus, G., Lasota, J.-P., Heinke, C. O., & Sivakoff, G. R. 2018a, MNRAS, 480, 2

Tetarenko, B. E., Lasota, J.-P., Heinke, C. O., Dubus, G., & Sivakoff, G. R. 2018b, Nature, 554, 69

Tetarenko, B. E., Sivakoff, G. R., Heinke, C. O., & Gladstone, J. C. 2016, ApJS, 222, 15

Thorne, K., & Price, R. 1975, ApJ, 195, 101

Tody, D. 1986, in Society of Photo-Optical Instrumentation Engineers (SPIE) Conference Series, Vol. 627, Instrumentation in astronomy VI, ed. D. L. Crawford, 733

Tody, D. 1993, in Astronomical Society of the Pacific Conference Series, Vol. 52, Astronomical Data Analysis Software and Systems II, ed. R. J. Hanisch, R. J. V. Brissenden, & J. Barnes, 173

Tomsick, J., Corbel, S., Fender, R., et al. 2003, ApJ, 582, 933

Tomsick, J., Corbel, S., & Kaaret, P. 2001a, ApJ, 563, 229

Tomsick, J., Kalemci, E., & Kaaret, P. 2004, ApJ, 601, 439

Tomsick, J. A., Shaw, A., Gandhi, P., Rahoui, F., & Dincer, T. 2017, The Astronomer's Telegram, 10114

Tomsick, J. A., Smith, E., Swank, J., Wijnands, R., & Homan, J. 2001b, IAU Circ., 7575

Tomsick, J. A., Rahoui, F., Kolehmainen, M., et al. 2015, ApJ, 808, 85

Toor, A., & Seward, F. D. 1974, Astron. J., 79, 995

Torres, M. A. P., Jonker, P. G., Steeghs, D., et al. 2008, Astrophys. J., 672, 1079

Truss, M. R., Wynn, G. A., Murray, J. R., & King, A. R. 2002, Mon. Not. R. Astron. Soc., 337, 1329

Ubertini, P., Lebrun, F., Di Cocco, G., et al. 2003, A&A, 411, 131

Vadawale, S. V., Rao, A. R., Naik, S., et al. 2003, ApJ, 597, 1023 van Paradijs, J. 1983, in Accretion-Driven Stellar X-ray Sources, ed. W. H. G. Lewin & E. P. J. van den Heuvel, 189–260

van Paradijs, J. 1996, Astrophys. J. (Letters), 464, L139

van Paradijs, J., & McClintock, J. 1994, Astron. Astrophys., 290, 133

—. 1995, in X-Ray Binaries, ed. W. Lewin, J. van Paradijs, & P. van den Heuvel (Cambridge University Press), 58

Veledina, A., Gandhi, P., Hynes, R., et al. 2017, MNRAS, 470, 48

Veledina, A., Poutanen, J., & Vurm, I. 2013, MNRAS, 430, 3196

Verbunt, F., & Zwaan, C. 1981, A&A, 100, L7

Verner, D. A., Ferland, G. J., Korista, K. T., & Yakovlev, D. G. 1996, ApJ, 465, 487

Vrtilek, S., Raymond, J., Garcia, M. R., et al. 1990, A&A, 235, 165

Walter, R., Lubinski, P., Paltani, S., et al. 2007, A&A, 461, L17

Warner, B. 1995, Cambridge Astrophysics Series, 28

Webbink, R., Rapport, S., & Savonije, G. 1983, ApJ, 270, 678

White, N., & Holt, S. 1982, ApJ, 257, 318

White, N., Nagase, F., & Parmar, A. 1995, in X-Ray Binaries, ed. W. Lewin, J. van Paraijs, & E. van den Heuvel (Cambridge University Press), 1–57

Wijnands, R., & Miller, J. 2002, ApJ, 564, 974

Wilms, J., Allen, A., & McCray, R. 2000, ApJ, 542, 914

Winkler, C., Courvoisier, T. J.-L., Di Cocco, G., et al. 2003, A&A, 411, L1

Wu, Y. X., Yu, W., Li, T. P., Maccarone, T. J., & Li, X. D. 2010, Astrophys. J., 718, 620

Yan, Z., & Yu, W. 2015, Astrophys. J., 805, 87

—. 2017, MNRAS, 470, 4298

Zdziarski, A., Gierlinski, M., Mikolajewska, J., et al. 2004, MNRAS, 351, 791

Zhang, G., Qu, J., Zhang, S., et al. 2007, ApJ, 659, 1511

Zhang, G.-B., Russell, D. M., Bernardini, F., Gelfand, J. D., & Lewis, F. 2017, The Astronomer's Telegram, 10562

Zhou, J., Liu, Q., Chen, Y., et al. 2013, MNRAS, 421, 2285

Zurita, C., Durant, M., Torres, M. A. P., et al. 2008, ApJ, 681, 1458